ALTERNATIVES FOR NICKEL AS BARRIER COATING FOR INTERMETALLIC MIGRATION

KAM-MOON CHOW

M. PHIL.

THE HONG KONG POLYTECHNIC UNIVERSITY

1998

Alternatives for Nickel as Barrier Coating for Intermetallic Migration

A Thesis submitted in Fulfilment
of the Requirements
for the Degree of

Master of Philosophy

by

Kam-Moon Chow

at the

Department of Applied Biology and
Chemical Technology
The Hong Kong Polytechnic University

September 1997

ABSTRACT

The interdiffusion of electrodeposited Ni, Pd, Pd-Fe, Co, Co-W with Cu substrate were studied, at temperature ranging from 250°C to 800°C, using Energy Dispersive X-ray Spectroscopy (EDS). Chemical interdiffusion coefficients were calculated using the Boltzmann-Matano Analysis. Intermetallic phase formation was studied by X-ray Diffraction (XRD). Grain sizes of the electrodeposits were estimated by the particle size boardening method. Microstructures were observed by optical microscopy and scanning electron microscopy (SEM).

The higher interdiffusion coefficients observed for Cu/lamellar Ni to that of the Cu/columnar Ni couple might be due to having smaller initial grain size and different microstructure. The grain growth rate of the Cu/Ni couple at 500°C for the first 30 min. annealing was observed to be higher than after 48 hours annealing, resulting to higher diffusivities determined. A transition range at about 700-750°C was observed from the Arrhenius plot of diffusivities for the Cu/Ni systems indicating a transition between different diffusion mechanism.

Interdiffusion coefficients of the Cu/Pd system determined in the temperature range 300-700°C are higher than about one order of magnitude for those of Cu/Ni system. Interdiffusion of Cu/Pd was reduced when Fe was alloyed with Pd as 75wt%Pd-25wt%Fe alloy by electroplating. The as-deposited Pd-Fe coating consists of $FePd_3$ and FePd phases, and $PdCu_3$ was observed after heat treatment.

No remarkable interdiffusion was observed by EDS measurement for the Cu/Co and Cu/Co-W systems up to 800°C. However, after annealing ranging from 400-800°C for the Cu/Co/Ni system, accumulation of Cu atoms was found at the Co/Ni interface in which Cu had further diffused into the Ni electrodeposit. It is suggested that Cu atoms diffuse through the Co layer by the grain-boundary diffusion

mechanism. Alloying Co with W as 65wt% Co-35wt% W by electroplating reduced interdiffusion of Cu through Co to Ni. The structure of the Co-W coating has changed from a mixture of h.c.p. and f.c.c. Co-like structure to f.c.c. Co-like structure upon 1100°C annealing for 90 min. The diffusion barrier properties of Co and Co-W were compared with those of Ni. Results ascertain that Co is a more effective barrier than Ni for Cu diffusion up to 219 h at 400°C. Co-W alloy coating, of 36 wt.% W is a more effective barrier for Cu diffusion than Ni up to 72 h at 500°C. Co-W coating containing crystalline phases was found to be a more effective barrier than amorphous Co-W coating. The crystalline Co-W coating was found to be more effective as a diffusion barrier than Co coating at all investigated temperatures (400-800°C), whereas amorphous Co-W coating performs better than Co coating only at 500°C or lower. However, interpenetration of Cu through Co is more pronounced than diffusion of Cu through Ni for temperatures ranging from 500°C to 800°C. Interdiffusion of Cu through Co-36 wt.% W coating is more pronounced than diffusion of Cu through Ni for temperatures ranging from 600°C to 800°C.

Results of diffusion experiments on different Cu/barrier/Au systems showed that Co-35wt% W coating was confirmed to be the most effective barrier for Cu/Au interdiffusion at 400°C or lower among other electrodeposited coatings Co, Ni (lamellar/columnar), Pd and Pd-Fe. Corrosion properties of different electrodeposited coatings Ni (lamellar/columnar), Pd, Pd-Fe, Co and Co-W were evaluated by AC impedance and D.C. polarisation measurements with 3 % NaCl electrolyte, in which polarisation resistances (R_p) were determined.

ACKNOWLEDGEMENTS

Many people have given helps and guidance to the author during the course of this research work and the author would like to mention some of them here. The most concrete assistance came from the author's supervisor Dr. Wing-Yan Ng who provided many insightful suggestions and comments and provided the author with a whole range of new emotions and experiences that the author could not have previously anticipated and understood.

The author would also like to express his gratitude to Prof. Chun-chun Xu in Beijing University of Chemical Technology for her encouragement to the author during her stay at the Hong Kong Polytechnic University last year.

Together, Mr. Stephen Yue-Shing Sin and Mr. Chi-Lam Chan also deserve special thanks for their help on the operation of scanning electron microscope in the Materials Research Centre of this University.

The author would also like to thank all the staff members of the Chemical and Metallurgy Division at the Hong Kong Productivity Council for their help and cooperation throughout the author's stay at their Quality Control and Testing Laboratory.

The assistance of Mr. William Chi-Yuen Chan, graduate student of Department of Electronic Engineering at this University, in the editing of all graphs and figures of this thesis is gratefully acknowledged.

The financial support from the Industry Department of Hong Kong Government in the form of a Teaching Company Scheme via The Hong Kong Polytechnic University and the Hong Kong Productivity Council, which was essential for the author's graduate studies, is gratefully acknowledged.

The award of a Tuition Scholarship granted from the Hong Kong Polytechnic University is gratefully acknowledged, which provided the financial support for the author's graduate studies.

Finally, many thanks are due to all the graduate students for providing a conductive atmosphere to do the present research work.

TABLE OF CONTENTS

LIST OF TABLES

LIST OF FIGURES

Chapter 1 Introduction

1.1 Introduction

Gold coating has been extensively utilized for the manufacturing of electrical and electronic components. Gold exhibits many of the desirable qualities such as minimal electrical contact resistance and bulk resistivity, good solderability and good corrosion resistance. Because of economical reason, thin gold plating is plated instead. The Cu/barrier coating/Au system is commonly used in the jewelry industries. Without the barrier coating, surface contamination resulting from diffusion of basis metal through the gold deposit adversely affects the decorative appearance.

Nickel has been used as an effective barrier to reduce the penetration of copper through gold electrodeposits [1, 2]. Pickering *et al* [2] observed that Ni and its alloys, for example, Ni-8 wt% phosphorous and cobalt deposits can withstand copper diffusion at 400°C for 19 days. However, the potential of nickel as an allergen and carcinogeneity of specific nickel compounds has aroused concerns for some surface finishers to re-assess its uses [3, 4]. In view of this, the utilization of nickel coating as the diffusion barrier for metal-metal interdiffusion was proposed to be controlled by the Commission of the European Union (EU) in 1994 [5]. For articles with direct contact to human bodies, releasing more than 0.5 $\mu m/cm^2$/week of Ni^2 are prohibited. The draft Directive has now been passed back to the European parliament for approval. The objective of the Directive is to protect consumers against the allergic reactions likely to be caused in certain nickel-sensitive people by jewelry and personal items coming into contact with their skin. Canada and USA have not implemented

similar controls, but for a long term planning it is desirable to eliminate the use of nickel either as the diffusion barrier or colouring purpose of the top decorative coating of jewelry.

This project is to investigate the effectiveness of different electrodeposited materials as the diffusion barrier between copper and gold. As an effective barrier interdiffusion between it and the copper substrate should be minimized.

Many investigators [1-3, 13-14] have studied the effects of certain plating conditions on the grain size of nickel electrodeposit. They found that grain size of the nickel coating affects the effectiveness of nickel as a diffusion barrier, but few investigation has been reported on the effects of additives of the plating bath on the diffusion barrier properties of the electrodeposit. For example, the brightener changing the structure of the nickel electrodeposit may affect the diffusion barrier properties of the Ni coating. In this study, we examine the interactions of Cu/Ni (columnar structure), Cu/Ni (lamellar structure) systems and compare the interdiffusivities of both systems with the effects of grain sizes and microstructure.

The use of palladium as the alternative for nickel has been expanding in the jewelry business. Many investigations have been done on electrodeposited Pd and Pd alloys systems [1, 6-8] and its function as a diffusion barrier for electronic applications [9-10]. The cost of Pd is about 1/3 of gold. Manufacturers always look for a cheaper substitute for Pd. Diffusion experiment results on the Cu/Pd-Fe system help us evaluate its suitability as one the alternatives for Pd.

Cobalt has been suggested as a good substitute for, and even better than nickel as the diffusion barrier material between copper and gold on the basis of their mutual insolubility at low temperatures, as indicated by the Cu-Co phase diagram. It prevents Cu from diffusing through the Co crystal grains [1]. In this work, we would show that

Cu diffused through Co by grain boundary diffusion and accumulated at the Co/Ni interface for the Cu/Co/Ni system after heat treatment.

Wheeler *et al* [11] reported a study on electrodeposited Co-W as a diffusion barrier coating for graphite fiber and observed that coating of 5-10.5 at-% W, is an effective diffusion barrier for carbon and nickel in graphite fiber/nickel composites for up to 24 hours at 800°C. Admon *et al.* [12] studied the microstructure of the Co-W thin films and concluded that the Co-W deposits were either amorphous or crystalline consisted of h.c.p., f.c.c. or mixed Co-like phases.

Because of the mutual insolubility between Cu and Co (and Co-W), few data are available from the literature featuring its capability as effective diffusion barrier for copper. This project initiates a study on the transfer process of Cu in Co, Co-W and Ni electrodeposits. The structural change of the electrodeposits upon heat treatment which leads to a change of diffusion barrier properties of the coating is reported. A semi-quantitative method is developed to compare the performance of Co and Co-W as diffusion barrier with those of Ni. An *apparent* interdiffusion coefficient for the Cu/Co/Ni and Cu/Co-W/Ni systems is introduced so that an evaluation and comparison of the barrier properties among Co, Co-W, Ni (lamellar/columnar), Pd and Pd-Fe becomes possible.

Finally, results from the diffusion experiment of Cu/barrier coating couples and Cu/Co(or Co-W)/Ni systems will be compared and confirmed with results of diffusion experiment of different Cu/barrier/Au systems.

When Pd-Fe coating is used as the barrier in the manufacturing of jewelry, the corrosion property is an important factor in evaluating its suitability. Corrosion properties of different electrodeposited coatings will be evaluated by both AC impedance and DC polarization methods.

1.2 Objective of the Present Study

The intent of this study was to evaluate interdiffusion kinetics of potential diffusion barrier materials with copper substrates. Influence of electroplating conditions and the microstructure of electrodeposits on the interdiffusion barrier behaviour has also been studied. Diffusion barrier properties of different electrodeposits were compared with that of nickel to evaluate their suitability as an alternative to nickel as diffusion barrier for copper diffusion.

Chapter 2

Literature and Theory Review

To prevent or at least retard the interdiffusion of copper base metal with gold deposit, a diffusion barrier is inserted between the substrate and the gold electrodeposit. As an effective barrier material, the transport rates between Cu and Au across the barrier material should be small. Moreover, the loss of barrier material into either Cu or Au should be minimized. It should also have good thermal stability and strong adhesion with both Cu substrate and Au overplated.

As a first step to evaluate different potential diffusion barriers, interdiffusion between copper substrate and the potential barrier material should be studied. Interdiffusion of the different metallic couples has been the subjects of many investigations. The followings are a survey of literature for the interdiffusion studies of different Cu/electrodeposit by some investigators.

2.1 Copper-Nickel System

Interdiffusion in the copper-nickel system has been studied by many investigators. Nakahara and Felder [13] investigated the effect of certain plating conditions on the microstructure of nickel electrodeposits from sulfate baths and concluded that the bath efficiency, the grain size, and the defect density are dependent on the temperature and pH of the plating bath. Kaja [1] discovered that nickel deposited from a sulfmate bath at pH 4.2 provided a better diffusion barrier against

grain boundary diffusion below 350°C than finer-grained nickel deposited at pH 1.15. Katz [14] electroplated nickel from Watts, all-chloride and chloride-free baths onto copper substrates. He observed that grain boundary diffusion was the dominant diffusion mode at or below 700°C for all three electrodeposits and the apparent diffusivity decreased with time at a constant temperature due to grain growth. He also concluded that recrystallized large grained electrodeposits were more effective barriers than the fine grains ones, because of the reduction of the rate of interdiffusivity.

Chin-An Chang [15] studied the interactions between gold and copper across a nickel barrier layer using Rutherford backscattering spectrometry and Auger spectroscopy and suggested that the Ni/Cu interactions were low because copper had very low solubility in nickel below 400°C and the distribution of gold into the copper lattice was very likely dominated by grain boundary diffusion through nickel with a much reduced lattice diffusion in the absence of an intimate Au-Cu interface, in which all metal layers were deposited by vacuum electron-beam evaporation. R. Venos *et al* [16-17] investigated grain boundary diffusion in vacuum evaporated polycrystalline Ni-Cu multilayer films in the temperature range 250-400°C and Cu/Ni bilayers in the temperature range 130-330°C using Auger electron depth profiling technique; in which grain boundary and volume diffusion coefficients were separated for the Ni-Cu multilayer systems by using a diffusion model proposed by K. Roll [18] and surface accumulation method was used to separate the grain boundary diffusion coefficients of copper and nickel in the Cu-Ni bilayer system. They also concluded that the low activation energy for lattice diffusion of Cu-Ni was due to the high defect density in the grains of the evaporated films.

2.2 Copper-Palladium System

J. L. Martin and M. P. Toben [9] made a historical review on the usage of palladium plating for the electronics industry and stated that microcracking because of codeposited hydrogen and intrinsic catalytic properties of pure palladium limited its reliability for connector applications. Sobha Jayakrishnan *et al* [19] compared the physical properties of palladium electrodeposited by three ammine complexes baths based on palladous ammine nitrite, palladous ammine chloride and palladous ammine bromide and concluded that the chloride and bromide baths gave pore- and crack-free deposits with higher thickness and lower internal stress to that of the nitrite bath. R. Le Penven et al [20] studied the electrochemistry of solutions of palladous ammine complexes and defined the importance of oxygen reduction, hydrogen absorption and hydrogen evolution as competing cathode reactions under various conditions. Graham *et al* [21] studied various properties of palladium and palladium-nickel deposits and found that these deposits had better ductility, superior resistance to corrosion-product creep, and lower porosity than hard gold deposits. E. J. Kudrak *et al* [7] investigated the porosity of palladium and palladium-nickel electrodeposits and showed that certain process variables such as current density, agitation and certain proprietary additives can exert considerable effect on the porosity of electrodeposits. I. Boguslavsky *et al* [6] confirmed that gold-flashed palladium-nickel deposits have good corrosion resistance after heat treatment and low porosity and believed this is due to the property of Pd-Ni layer as an excellent intermetallic diffusion barrier. Kaja [1] studied the diffusion characteristics of both electroplated and wrought palladium-copper diffusion couples in the temperature range 550°C-900°C and observed that

plated palladium displayed a higher diffusivity, which was associated with the finer grain size of the electrodeposit.

2.3 Copper/Palladium-Iron System

Apparently, interdiffusion studies between copper and palladium-iron coating has not been studied. For the electrodeposition of the Pd-Fe alloy coating, P. Juzikis *et al* [25] proposed an ammoniacal bath containing palladium(II) and iron(III) chlorides, with sulfosalicylic acid as a complexing agent. He found that depending on the composition of the alloy, the coating can be in crystalline or multiphase structure, with at least one phase being exceptionally distorted. He also investigated magnetic properties of the as-deposited Pd-Fe alloy and concluded that coercive force exhibit a maximum near 75 wt. percent Pd. The coercive forces of the as-deposited alloys are near 100-150 Oe.

G. Battaglin *et al* [38] characterised the phases of ion-beam-mixed (using 200 keV Kr^2 ions) and thermally reacted Fe/Pd thin film bilayers using X-ray diffraction (XRD) and transmission electron microscopy (TEM). He found that, in the ion-mixed sample, iron migrates into the palladium layer to form $FePd_3$. The remaining iron film is heavily damaged by irradiation and its α-Fe structure is heavily distorted. After the 550°C annealing he detected the formation of FePd equilibrium phase in the unirradiated sample, while in the ion-mixed sample subjected to the same thermal treatment, evolution towards the equilibrium situation was slower.

2.4 Copper/Cobalt System

Kaja [1] observed that negligible interdiffusion between copper and electrodeposited cobalt was measured by the electron probe. He concluded that cobalt is an effective diffusion barrier. Peter Madakson *et al* [35, 37] studied the interdiffusion of Cu/Co, Cu/Co/Au and Cr/Cu/Co/Au thin films, using Rutherford backscattering spectroscopy and Auger analysis, in which deposition was carried out by electron beam evaporation at a vacuum pressure of about 10^{-7} Torr. He concluded that cobalt is a very effective diffusion barrier between Cu and Au at temperatures lower than 400°C. Above this temperature, Co breaks down and massive interdiffusion of Cu and Au thin films occurs. Complete interdiffusion of Cu and Au, in the Cu/Co/Au thin-film system, occurs at about 450°C.

2.5 Copper/Cobalt-Tungsten System

While interdiffusion studies between copper and cobalt-tungsten coating has not been studied, Wheeler *et al.* [11] reported a study on electrodeposited Co-W as a diffusion barrier coating for graphite fiber and observed that coating of 5-10.5 at-% W, is an effective diffusion barrier for carbon and nickel interdiffusion in graphite fiber/nickel composites for up to 24 hours at 800°C. Lattice expansion was also observed after heat treatment at 800°C for 24 hours. Admon *et al* [12] studied the microstructure of the Co-W thin films prepared from a basic bath (pH=8.5) containing Rochelle salt and $(NH_4)_2SO_4$ and concluded that the Co-W deposits were either amorphous or crystalline consisted of h.c.p., f.c.c. or mixed Co-like phases. Polukarov

[32] reported that the formation of crystalline Co_3W intermetallic phases was possible when under conditions of high W concentration and cathode potential. The occurrence of Co_3W phases was not reported by Admon *et al.* and Wheeler *et al.*

2.6 Determination of interdiffusion coefficients by the Boltzmann-Matano Method

Interdiffusion of different Cu/electrodeposit couples were studied by determination of the concentration-distance profile after heat treatment at different temperatures. The problems associated with diffusion in a concentration gradient can be handled by the Boltzmann-Matano method [22]. A chemical interdiffusion coefficient D is introduced which varies along the concentration gradient in the diffusion zone of the Cu/electrodeposit couple. Hence, chemical diffusivities were calculated from the concentration versus distance data at different copper concentration. Arrhenius plots (log diffusivity versus reciprocal temperature) can be constructed.

Heat treatment at temperature T leads to planar interdiffusion at the interface between two metals layers A and B. As interdiffusion proceeds, metal A will develop a profile of fractional atomic concentration $c_A(x)$. $D_{AB}(x)$ describes the progress of A atoms at a particular depth x measured from the original interface, where the host matrix is a mixture of A and B atoms in the proportion $c_A(x) : c_B(x)$. Exchange of two A atoms does not contribute to the observed diffusing flux of species A. However, in a random vacancy diffusion process, the probability of a successful replacement of a B atom with one type A will be proportional to $c_B(x)$. Thus, the effective transport of species A from the interface, due to the combined migration of both A and B atoms, is described by $D_{AB}(x)$, where

$$\tilde{D}_{AB}(x) = D_A\, c_B(x) + D_B\, c_A(x) \qquad (2.6.1)$$

D_A and D_B can be deduced by measuring D_{AB} at several known concentrations (c_A, c_B) and then solve for D_A and D_B, for which the variation in D_{AB} with varying concentration can be handled by a method first proposed by Boltzmann. Fick's second law for one-dimensional diffusion is generalized to allow explicitly for the variation in D by writing it in the form below

$$\frac{\partial c}{\partial t} = \frac{\partial}{\partial x}\left(D \frac{\partial c}{\partial x}\right) = D \frac{\partial^2 c}{\partial x^2} + \frac{\partial D(c)}{\partial c}\left(\frac{\partial c}{\partial x}\right)^2 \qquad (2.6.2)$$

Assume a solution of the form

$$c = c(xt^{-1/2}) \qquad (2.6.3)$$

and define $y = x\, t^{-1/2}$. Now by differentiation we obtain

$$\frac{\partial c}{\partial t} = \frac{dc}{dy}\frac{\partial y}{\partial t} = -\frac{1}{2}\frac{x}{t^{3/2}}\frac{dc}{dy} = -\frac{y}{2t}\frac{dc}{dy}$$

$$\frac{\partial c}{\partial x} = \frac{dc}{dy}\frac{\partial y}{\partial x} = t^{-1/2}\frac{dc}{dy}$$

$$\frac{\partial^2 c}{\partial x^2} = \frac{1}{t}\frac{\partial^2 c}{\partial y^2}$$

$$\frac{\partial D}{\partial x} = t^{-1/2}\frac{dD}{dy} \qquad (2.6.4)$$

Substituting into (A.1) we obtain

$$\frac{\partial c}{\partial t} = \frac{D}{t}\frac{\partial^2 c}{\partial y^2} + \frac{1}{t}\frac{dD}{dy}\frac{dc}{dy} = -\frac{y}{2t}\frac{dc}{dy} \qquad (2.6.5)$$

or in another form

$$\frac{d\left(D\frac{dc}{dy}\right)}{dy} = -\frac{y}{2}\frac{dc}{dy}$$

solving for D and substituting for y, we obtain

$$\tilde{D} = -\frac{1}{2}\frac{dy}{dc}\int_{c_o}^{c} y\,dc = \frac{1}{2t}\frac{dx}{dc}\int_{c}^{c_o} x\,dc \qquad (2.6.6)$$

The interdiffusion coefficient, $\tilde{D}$, reflects the average of the overall movement of all constituents diffusing in a concentration gradient.

Imagine two homogeneous semi-infinite cylinders of different chemical composition, which are intimately joined at a mutual planar interface. For such a configuration it becomes obvious that at $x = \pm\infty$, $dc/dx = 0$ and hence, equation 2.6.6 is undetermined as a result of the fact that $c = 0$ or $c = c_o$ for each of the arbitrary number of constituents.

Consequently, we can now write

$$\frac{1}{2}\int_{c_o}^{c'} y\,dc = \tilde{D}\frac{dc}{dy} = -\frac{1}{2}\int_{c_o}^{c'} x\,dc \qquad (2.6.7)$$

hence

$$\tilde{D} = -\frac{1}{2}\frac{dy}{dc}\int_{c_o}^{c'} x\,dc \qquad (2.6.8)$$

However, x must run from -∞ to ∞ for equation 2.6.8 to be valid, and $x = 0$ must define a surface such that the depletion of a particular constituent to the left of it must exactly equal the accumulation on the right. This is simply the requirement of the existence of a conservation of mass surface, which is called the Matano interface. As a result of this condition, we now write for t equal to a constant

$$\int_{c_o}^{c_1} x\,dc - \int_{c'}^{c_1} x\,dc = 0 \qquad (2.6.9)$$

or

$$\int_{c_o}^{c_1} x\,dc = \int_{c'}^{c_1} x\,dc \qquad (2.6.10)$$

This situation is shown graphically in Fig. 2.6.1. When the diffusion coefficient is independent of composition, $c_1 = c_o/2$ and the Matano interface after corrections for change in molar volumes corresponds to the original interface. This is seldom if ever

the case, although this condition is closely approached when the two members of the diffusion couple are of nearly the same composition. In actual practice, different elements diffuse with different velocities and furthermore are dependent upon composition. Values of D are computed graphically; e.g., dc/dx is determined by drawing the tangent to the experimental measured diffusion profile at c'_1, the composition of interest, and the integration performed graphically:

$$D_{c=c'_1} = \frac{1}{2t}\frac{dx}{dc}\bigg|_{c=c'_1} \int_{c'}^{c_1} x\,dc$$

This method may be extended to other concentrations if one component is far more mobile than the rest by applying the graphical method shown in Fig. 2.6.2. Hence we get:

$$D_{c=c'_1} = -\frac{1}{2t}\frac{dx}{dc}\bigg|_{c=c'_1} \int_{0}^{c_1} x\,dc \qquad (2.6.11)$$

By repetition of the process at a series of temperatures, Arrhenius plots for D_{AB}, D_A and D_B may be obtained, leading to experimental values for activation energies Q_{AB}, Q_A and Q_B.

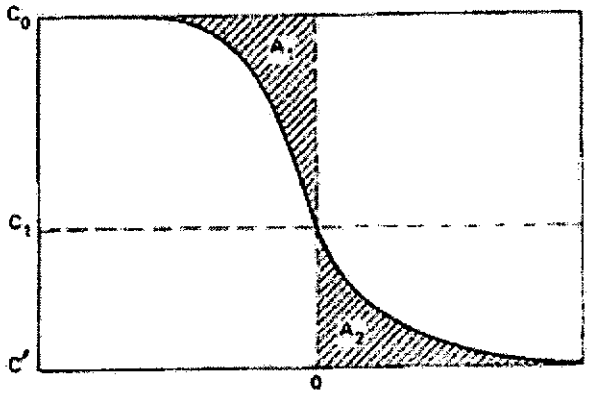

Fig. 2.6.1 Illustrating the Matano interface as defined by the areas A_1=A_2 for a specific constituent.

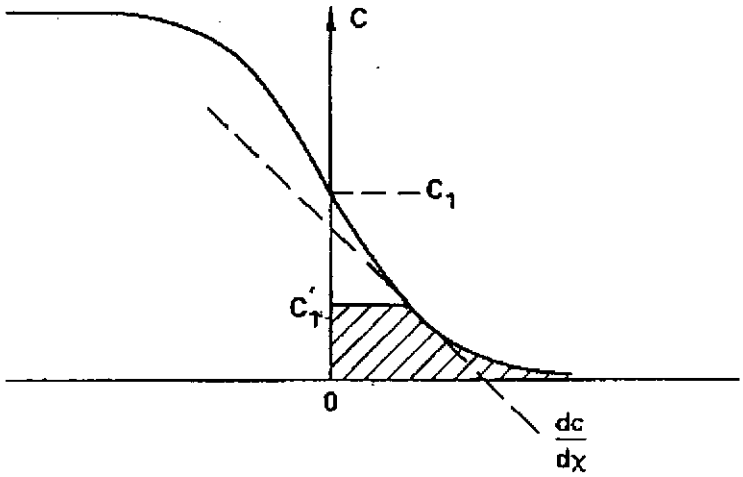

Fig. 2.6.2 Calculation of the chemical diffusion coefficient when only one constituent is appreciably mobile.

2.7 Determination of lattice-parameter and identification of crystalline phases by X-ray diffraction (XRD)

It is generally observed that the interdiffusion property between two different metal layers behaves differently upon heat treatment at different specific temperature range. This is due to the structural changes and intermetallic phases formation of the electrodeposit upon heat treatment, which affect the interdiffusion behaviour for the copper/electrodeposit couple. Formation of lattice vacancies and change of grain boundaries density result to higher interdiffusion coefficients.

X-ray diffraction techniques are used to identify the phases present in samples and to provide information on the grain size, texture and lattice parameter.

High-energy (20 kV) electron beam is directed into a water-cooled target for generation of X-rays. As electrons are decelerated in the target, most of the electron beam energy is lost in collisions that set the atoms in motion and produce heat, which must be dissipated through the cooling water. The decelerated electrons caught in the electric fields of the atom produces X-rays of a continuum of all energies between zero and the excitation potential, and is termed as white radiation. Some target electrons are knocked out of their orbitals, and the stored energy is released as the electrons from other orbitals drop into the vacant orbital, for which these electron transitions are quantized and have specific wavelengths. Therefore, x-rays exiting the target have a few strong characteristic concentrations of specific wavelengths superimposed on the white radiation. Copper is used as the target because the Kα characteristic radiation is a useful wavelength, 0.15406nm, and the target is easily cooled for high efficiency. For copper radiation, a nickel foil absorbs most of the white radiation and the other characteristic peaks, transmitting essentially pure Kα

radiation. In our case, a flat graphite crystal monochromator is used since it monochromates the X-ray beam better than nickel foil filter. The crystal monochromator also suppresses the effects of sample fluorescence. A proportional detector filled with Xe gas is used for detection of X-rays as it is particularly good for detecting radiation that has the wavelength of Cu or longer.

Characteristics of a sample can be determined from the collection of angles at which diffracted X-ray beams are detected. The lattice of the sample reflects the size and shape of the unit cells and their periodic arrangement in space. The lattice is fundamental to the geometry of any diffraction experiment. Interference of the scattered x-rays in most directions results in cancellation and absence of detectable beams; however, in a few selected directions, reinforcement of all the scattered rays occurs, and a strong beam results. These are the diffracted beams. Because the crystal is periodic in three dimension, the lattice sites act as the scattering centers. Each scattering center emits rays in all directions, and the resulting diffracted rays define a family of cones in space. The three-dimensional lattice of scattering centers restricts a diffraction experiment severely, and diffraction can only occur when the incident beam makes precisely the correct angle relative to the crystal.

For simplicity, the lattice is considered to be planes of lattice points (Figure 2.7.1), and the X-ray beam acts as if it reflects off these planes. Constructive interference occurs only when the incidence angle and diffraction angle θ satisfy the condition:

$$\lambda = 2d \sin\theta \qquad (2.7.1)$$

where d is the perpendicular spacing between the lattice planes and is a function of lattice parameters a, b, c and Miller indices h, k, l and the lattice angles α, β and γ. The angle θ is the Bragg angle. This condition identifies diffraction as scattering and interference from the periodically arranged unit cells. Table 2.1 are the expressions for determining the possible d values for some specific lattices.

Table 2.1 Formulas for calculating interplanar spacing d_{hkl}

Crystal system	Axial translations	Axial angles	d_{hkl}
Cubic	a = b = c	$\alpha = \beta = \gamma = 90°$	$a(h^2 + k^2 + l^2)^{-1/2}$
Tetragonal	a = b ≠ c	$\alpha = \beta = \gamma = 90°$	$[(h^2/a^2) + (k^2/a^2) + (l^2/c^2)]^{-1/2}$
Hexagonal	a = b ≠ c	$\alpha = \beta = 90°$ $\gamma = 120°$	$[(4/3a^2)(h^2 + k^2 + hk) + (l^2/c^2)]^{-1/2}$

Lattice constants can be determined by solving one of the d-spacing equations in Table 2.1. The lattice constants of a crystal may be sufficient to identify an unknown compound when it is compared to a tabulation of the lattice data of all known compounds. For example, the Powder Diffraction File (PDF). Using the PDF, identification may be possible based only on the d spacings without knowledge of lattice constants.

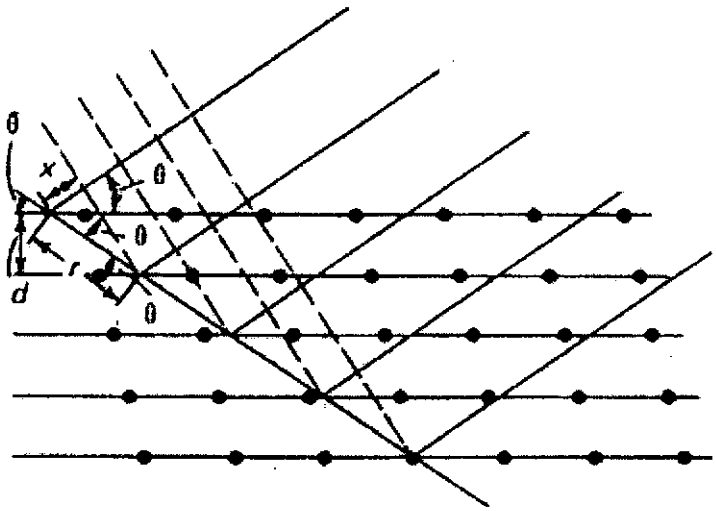

Fig. 2.7.1 Diffraction in a crystal lattice and the derivation of the Bragg equation

$$n\lambda = r - x$$

$$r = \frac{d}{\tan\theta} = d\,\frac{\cos\theta}{\sin\theta}$$

$$x = r\cos 2\theta = d\,\frac{\cos\theta\cos 2\theta}{\sin\theta}$$

$$\begin{aligned} n\lambda &= d\left(\frac{\cos\theta}{\sin\theta}\right)(1-\cos 2\theta) \\ &= d\left(\frac{\cos\theta}{\sin\theta}\right)(1-\cos^2\theta+\sin^2\theta) \\ &= d\left(\frac{\cos\theta}{\sin\theta}\right)(2\sin^2\theta) = 2d\sin\theta \end{aligned}$$

2.8 DC Polarization and AC Electrochemical Impedance Spectroscopy Studies

The corrosion resistance of different electrodeposits should also be a key factor for considering their suitability as diffusion barriers. To evaluate the corrosion resistance of metal coatings, conventional test methods such as Salt Spray Testing, which entails a salt spray exposure of hundreds of hours. This procedure is rather time consuming, the results are highly interpretive, and therefore relatively imprecise. Techniques that determine the coating weight per unit area after prolonged immerse of the specimen in the corrosion media such as seawater could be useful, but these techniques are not sensitive to flaws such as porosity or the presence of contaminants in the coating (i.e. the composition of the alloy coating). The DC Polarization and Electrochemical Impedance Spectroscopy provide rapid nondestructive testings of electrodeposited coatings.

2.8.1 Determination of Corrosion Rates from Polarization Resistance Measurements

Electrochemical methods are useful for determining the corrosion rates of metals in a short period of time. Since application of high potentials to operating systems may be risky, linear polarization techniques with low current-potential applications around corrosion potential values are the most widely used electrochemical methods.

This technique is one of the most used techniques for studying corrosion [38]. The potential would be scanned linearly around E_{corr} as a function of time and the current monitored as the potential changes. When the potential is plotted as a function

of the log of the current, portions of both the anodic and cathodic regions may be linear and follow a Tafel behaviour. In such cases, it is possible to extrapolate these linear regions to where they should intersect, at the corrosion potential (E_{corr}), and obtain a value for the corrosion current (I_{corr}).

The basis of the polarization resistance technique is the relation:

$$I_{Corr} = \frac{b_a b_c}{2.3(b_a + b_c)}\left(\frac{dI}{d\phi}\right)_{\phi_{Corr}} = \frac{b_a b_c}{2.3(b_a + b_c)}\frac{1}{R_p} = \frac{B}{R_p} \qquad (2.8.1)$$

Which is valid as long as the relation between current (I) and potential (ϕ) can be expressed as:

$$I = I_{Corr}\left\{\exp\frac{2.3(\phi - \phi_{Corr})}{b_a} - \exp\frac{-2.3(\phi - \phi_{Corr})}{b_c}\right\} \qquad (2.8.2)$$

In Equations (1) and (2), I_{corr} and ϕ_{corr} are corrosion current and corrosion potential, b_a and b_c are anodic and cathodic Tafel slopes, and $Rp = (d\phi/dI)\phi_{corr}$ is the slope of a potential-current plot at the corrosion potential. Rp is often called polarization resistance, which is equivalent to the charge transfer resistance on the metal/electrolyte interface for the activation-controlled corrosion reactions.

Where in equation (2.8.1):

$$B = \frac{b_a b_c}{2.3(b_a + b_c)}$$

It is desirable to obtain simultaneously the Tafel slopes (b_a and b_c) and polarization resistance (R_p) in order to determine the corrosion current (I_{corr}). In doing so, one could accurately determine I_{corr} as a function of time, electrolyte composition, temperature, or other parameters.

Analysis of polarization curves is summarized in the following.

Combination of Equations (2.8.1) and (2.8.2) leads to:

$$I = \frac{1}{2.3}\frac{b_a b_c}{b_a + b_c}\frac{1}{R_p}\left\{\exp\left(\frac{2.3(\phi - \phi_{corr})}{b_a}\right) - \exp\left(-\frac{2.3(\phi - \phi_{corr})}{b_c}\right)\right\}, \qquad (2.8.3)$$

Which can be written after rearrangement as:

$$2.3R_p I = \frac{b_a b_c}{b_a + b_c}\left\{\exp\left(\frac{2.3\Delta\phi}{b_a}\right) - \exp\left(-\frac{2.3\Delta\phi}{b_c}\right)\right\} \qquad (2.8.4)$$

Where $\Delta\phi = \phi - \phi_{corr}$.

The corrosion current (I_{corr}) can then be calculated from the measured polarization curve in the following four steps which are based on Equations (1) and (2):

(1) Determine the polarization resistance R_p from:

$$\left(\frac{dI}{d\phi}\right)_{\phi_{corr}} = R_p^{-1}$$

By drawing a tangent at $\Delta\phi = 0$.

(2) Multiply the current I measured at a certain value $\Delta\phi$ by 2.3 R_p and plot 2.3 R_p I Vs $\Delta\phi$.

(3) Determine from this plot the Tafel slopes (b_a and b_c) by curve fitting using theoretical curves calculated for various values of b_a and b_c.

(4) Calculate I_{corr} from Equation (1) using the R_p value determined in Step 1 and the Tafel slopes determined in Step 3.

Several examples of computer programs have been described in the literature [40-41], where the application of statistics permit an automatic analysis of experimental data to obtain Tafel constants and calculate I_{corr} according to the Tafel extrapolation technique for measurement of corrosion kinetic parameters introduced by Stern [42] and Stern and Geary [43]. A commercial corrosion testing software is employed for the current studies [44].

2.8.2 Evaluation of Polarization Resistance by AC Impedance Technique

Electrochemical Impedance Spectroscopy has been successfully applied to the study of corrosion system for year's [45].

The smallest potential applied will disturb the structure of the double layer at the metal/electrolyte interface. The natural corrosion conditions will be disturbed. The metal surface will behave differently under direct current applied conditions than under natural conditions.

The application of AC instead of direct current in determining the corrosion rates is expected that more reliable currents can be obtained by applying high frequency very small alternative current by the AC impedance technique since this will not disturb the electrode properties to be measured, the possibility of studying corrosion reactions and measuring corrosion rates in low conduction media where traditional DC methods fail, and the fact the polarization resistance as well as double layer capacitance data can be obtained in the same measurement.

The simplest type of corrosion process would be the combination of a corrosion reaction and a double layer. One example of this type of process is uniform corrosion involving one chemical reaction. For example, the corrosion of carbon steel in 1 molar (M) sulfuric acid falls into this category. The reaction

$$Fe + 2H^{+} \rightarrow H_2 + Fe^{+2}$$

describes the corrosion reaction. This reaction can be represented by a simple resistor. The double layer is created by the fact that the surface of a metal in contact with any oxidizing agent, such as water or oxygen, is itself an oxide or hydroxide. The latter component would tend to ionize in water so that the surface becomes charged. Counter-ions would be present in the liquid layer adjacent to the metal surface to balance the surface charge. This structure responds to an AC voltage signal in a way analogous to a capacitor. If the real component Z' and the negative of the imaginary component Z'', measured as a function of frequency, are plotted against each other for this type of simple corrosion process, the plot would appears as in Fig. 2.8.1. This method of plotting is called the *Nyquist plot.*

The model circuit is shown in Fig. 2.8.2. The circuit is a resistor, R_p, in parallel with a capacitor, C. The entire parallel circuit is in series with another resistor, R_s. The utility of AC impedance lies in the fact that R_s equals the solution

resistance uncompensated by the potentiostat and R_p equals the polarization resistance. R_p is inversely proportional to the corrosion rate. Use of R_p with Tafel slopes allows the corrosion rate to be estimated. Thus, the AC impedance technique enables the corrosion rate to be estimated rapidly in the absence of uncompensated solution resistance and at the corrosion potential.

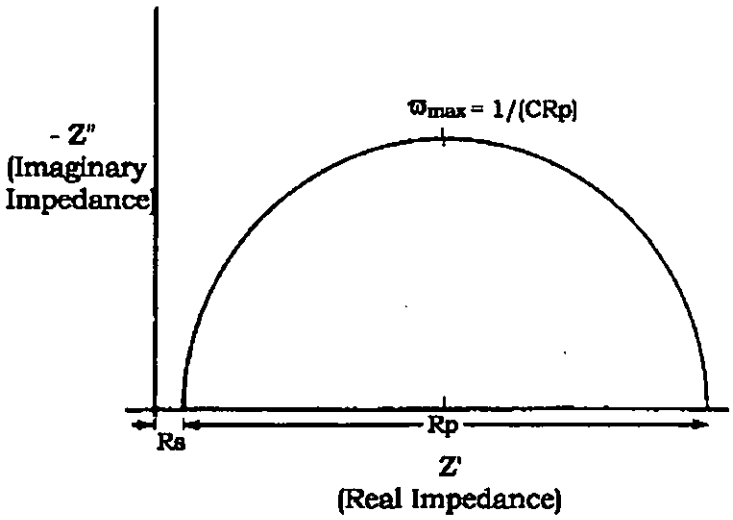

Fig. 2.8.1. Nyquist plot of simple charge transfer corrosion process.

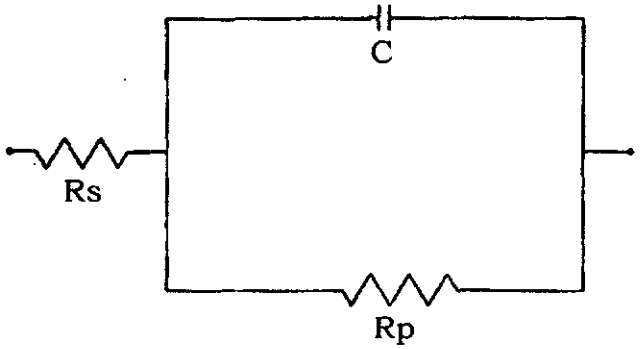

Fig. 2.8.2 Circuit that models impedance in Fig. 2.8.1.

The plot shown in Fig. 2.8.1 can be described by the relation

$$Z = R_s + \frac{R_p}{1+\omega^2 R_p^2 C^2} - \frac{j\omega R_p^2 C}{1+\omega^2 R_p^2 C^2}$$

When the first two terms in the right hand side of the equation are defined as real impedance (Z') and the last term is defined as complex impedance (Z''), ω is eliminated and the following equation of semi-circular is obtained:

$$\left[Z' - \left(R_s + \frac{R_p}{2}\right)\right]^2 + (Z'')^2 = \left(\frac{R_p}{2}\right)^2$$

which is the equation of a circle with a radius of ½ R_p, the center of which lies on the Z'-axis at $Z'_o = R_s + ½ R_p$. At the apex of the semicircle, $\omega_{max} = 1/(CR_p)$.

By examining the impedance at appropriate frequency limits, values of R_s, R_p and C can be obtained.

While the calculation of polarization resistance from AC impedance data is relatively straightforward for many applications, difficulties in data interpretation are still an important obstacle to making practical and routine use of the testing technique [46].

Chapter 3

Experimental Procedure

3.1 Pretreatment Procedure

Copper panels with dimensions of 6.5 x 10 cm were electrocleaned in alkaline soak cleaner. Samples were bright dipped and lightly etched by sulphuric acid 45%, nitric acid 22%, hydrochloric acid 0.1% and distilled water 32.9%. They were then activated in a 10% aqueous solution of hydrochloric acid before electroplating. All substrates were rinsed thoroughly by deionised water between each step.

3.2 Copper/(Columnar/Lamellar) Nickel Systems

3.2.1 Electrodeposition of Columnar/Lamellar Nickel coatings

Watts nickel containing 300g/l of $NiSO_4 \cdot 6H_2O$, 50g/l of $NiCl_2 \cdot 6H_2O$, and 40g/l of boric acid was electroplated on pre-cleaned and surface activated copper substrate with and without additives. The additives contain 1 g/l 2-butyne-1,4-diol and 0.05g/l sodium dodecylsulpahte. The solution pH was adjusted to 3.2-3.4 and the temperature was maintained at 50°C. The current density ranged from 1.8 to 5.6 A/dm^2; and with nickel electrodeposits thickness of 5 to 15μm. The current efficiency of the Watts Nickel plating bath was calculated at different current density conditions

by measuring the weight of the deposits and using the following equation;

$$Current\ efficiency = \frac{Weight\ of\ Ni\ Electrodeposit \times 96500 \times 2}{Current(A) \times Time(s) \times Atomic\ Weight\ of\ Ni} \times 100\%$$

3.2.2 Diffusion Experiment

The plated samples were cut into 1 cm×1 cm. They were heat treated at temperatures ranging from 250°C-900°C in an evacuated quartz tube. The samples were heat treated for time interval ranging from 0.5 to 284 hours. After heat treatment, samples were micro-sectioned with 120, 320 and 600 grit silicon carbide papers and polished successively using 5μm, 1μm and 0.3μm alumina powder. Samples were cleaned ultrasonically between each successive polishing step.

The microstructures were examined with optical microscopy and scanning electron microscopy (SEM) (Leica stereoscan-440). Samples were etched by 30/70/0.5 mixture of nitric acid, acetic acid and hydrochloric acid prior to optical microscopy examination. Energy Dispersive X-ray Spectroscopy (EDS) (Oxford Link ISIS) was employed for obtaining characteristic X-rays of the samples being scanned by the incident electron beam along a line across the diffusion zone, operating at 20 keV with working distance between the electron probe to the sample of 20 mm. The electron probe was calibrated with reference to a 70-30 Cu-Ni standard. Raw X-ray intensity values were then converted to chemical composition values by employing Link ISIS program [23] in which ZAF corrections were made for atomic number effects, absorption and fluorescence effects. Linescan concentration-versus-distance profiles were obtained.

The chemical interdiffusion coefficients were calculated using the Boltzmann-Matano method [22] (for details see Chapter 2). With this analysis the value of $\tilde{D}$ is determined as a function of concentration and is given as:

$$D_{c=c_1} = -\frac{1}{2t}\frac{dx}{dc}\bigg|_{c=c_1}\int_0^{c_1} x\,dc$$

where t = time of diffusion, $\left(\frac{dx}{dc}\right)_{c_1}$ = reciprocal slope of the concentration-distance profile evaluated at c_1, $\int_0^{c_1} xdc$ = area between the profile and the Matano interface from c = 0 to c = c_1 concentration lines and c_1 = any concentration between 0 to 100%. Concentration-distance data points with different diffusion times were fitted into a polynomial curve. Then the position of the Matano interface and evaluation of the Matano solution at different concentration level were calculated numerically. (An example of a Pascal program calculating the Matano interface and solution is put in Appendix I).

Heat treatment temperature and times for the Cu/lamellar Ni and Cu/columnar Ni diffusion couples are listed in Table 3.1 and 3.2 respectively.

Table 3.1. Heat Treatment Schedule for Copper/Lamellar Nickel Diffusion Couples

Sample Designation	Annealing Temperature (°C)	Annealing Time (h)
ni/cu33	250	2568
ni/cu 31	300	96
ni/cu31b	300	284
ni/cu 26	350	48
ni/cu 27	350	48
ni/cu 2	400	72
ni/cu 4	400	72
ni/cu 14	400	96
ni/cu 16	450	24
ni/cu 17	450	24
ni/cu 18	450	24
ni/cu 20	500	24
ni/cu 21	500	24
ni/cu 6	500	48
ni/cu 22	550	18
ni/cu 13	550	36
ni/cu 30	600	10
ni/cu 3	600	18
ni/cu 24	650	6
ni/cu 12	650	12
ni/cu 9	700	5
ni/cu 5	750	3
ni/cu 1	800	0.75
ni/cu 10	850	0.25
ni/cu 11	850	0.25
ni/cu 29	900	0.17

Table 3.2 Heat Treatment Schedule for Copper/Columnar Nickel Diffusion Couples

Annealing Temp. (°C)	Annealing Time (h)	Sample Ref.
250	2568	ni-64-18
300	96	ni-64-14
300	284	ni-64-15
350	48	ni-64-16
350	72	ni-64-16b
350	96	ni-64-9
400	72	ni-64-13
450	48	ni-64-16
450	48	ni-64-4
500	24	ni-64-10
600	13.22	ni-64-11
650	6	ni-64-6
700	5	ni-64-12
700	6	ni-64-1
750	3	ni-64-2
800	0.75	ni-64-3
850	0.28	ni-64-7
900	0.183	ni-64-8

3.2.3 X-ray diffraction studies

A Philips X-ray diffractometer (XRD) with a high intensity Cu tube was operated at 40 kV and 35 mA with the monochromated incident radiation of CuKα (λ=0.15406 nm) for measuring the lattice parameter at room temperature. The diffracted rays were detected with a Xe gas filled proportional detector; and a step-by-step technique was employed with steps of 0.02°. XRD spectra were recorded in the Bragg-Brentano geometry in the 2θ interval. A schematic diagram is shown in Figure 3.1 for the X-ray diffraction measurement.

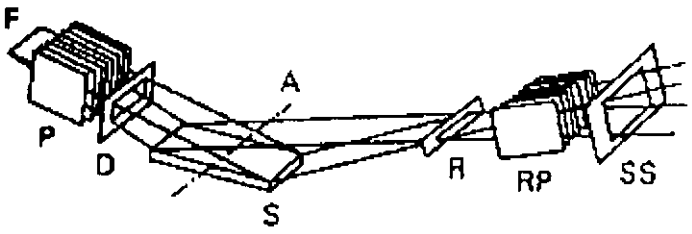

Fig.3.1 Geometry of the Bragg-Brentano diffractometer

F, line source of X-rays from the anode of the X-ray tube;
P, soller slits (collimator); D, divergent slit;
A, axis about which sample and detector rotate;
S, sample; R, receiving slit; RP, receiving soller slits; SS, scatter slit.

The width of the Ni(111) peak were used to provide an estimate of the apparent grain size using the Warren-Scherrer method [24], in which the apparent crystallite dimension D can be determined by the equation for particle-size broadening,

$$D = \frac{k\lambda}{\beta \cos\theta}$$

where β is a measure of the amount to which a line is broadened by particle-size widening, if the line is for a reflection at Bragg angle θ with wavelength λ, and k is a constant of the order of unity. β is taken to be the width in radians of a diffraction peak at half peak height above background intensity. Actually, k may be between 0.8 to 1.2 for various particle shapes. The value of k was assumed to be 1.0 in our studies.

3.3 Copper/Palladium system

3.3.1 Electrodeposition of Palladium coatings

Pretreatment procedures are the same as described in the previous section. Palladium was electroplated in a bath contains 30g/l of $Pd(NH_3)Cl_2$ and 23g/l of NH_4Cl, with current density 0.5 A/dm^2. The solution pH was adjusted to 8.9-9.1 with ammonia solution (NH_3 25%). The temperature was maintained at 25°C.

Structure and surface morphology of the palladium electrodeposit was studied by optical microscopy and SEM. Etchants were prepared by mixing 60% HCL and 40% HNO_3 which was heated before use.

3.3.2 Diffusion Experiment

Diffusion annealing schedule ranging from 250°C to 850°C of the Cu/Pd system is listed at Table 3.3. Chemical interdiffusion coefficients for the temperatures ranging from 250°C to 700°C were calculated by Matano-Boltzman Method. The procedures followed after the diffusion annealing were similar to those described in the previous section for the copper-nickel systems.

Table 3.3. Heat Treatment Schedule of Copper/Palladium (12μm) Diffusion Couples

Sample Ref.	Anneal. Temp. (°C)	Anneal. Time (h)	Remarks
Cu-Pd-1	700	4	40 wt% of Cu was observed on the surface
Cu-Pd-2	750	2	40 wt% of Cu was observed on the surface
Cu-Pd-3	800	0.5	25 wt% of Cu was observed on the surface
Cu-Pd-4	850	0.25	30 wt% of Cu was observed on the surface
Pd2-10	300	15	negligible interdiffusion
Pd2-8	350	5	very little interdiffusion
Pd2-17	250	980	
Pd2-11	300	87.42	
Pd2-16	300	91.5	
Pd2-15	300	91.5	
Pd2-12	300	12	negligible interdiffusion
Pd2-14	350	71	
Pd2-2	400	3	
Pd2-6	450	1	
Pd2-7	450	1	
Pd2-3	500	1	
Pd2-4	550	0.25	
Pd2-5	550	0.25	
Pd2-1	700	0.5	

3.3.3 Evaluation of Interdiffusion Coefficient by X-ray Diffraction

Offering the same current density 0.5 A/dm^2 , five samples were electroplated with palladium having average thickness of only 0.67μm, in which the electrodeposit thickness was determined by a X-ray Fluorescence coating thickness meter (Fischer Instrumentation). Samples were annealed at 400°C for 30 min to 120 min. The changes in integrated intensity of the Pd(111) peak during annealing were used as a measure of the degree of interdiffusion between Cu and Pd. The decrease in the integrated intensity of the Pd(111) peak can be attributed to the interdiffusion between

Cu and Pd. It is assumed that the (111)Pd integrated intensity is directly proportional to the thickness of the Pd film, the measured integrated intensities could be related to the apparent thickness of Pd. As palladium and copper atoms were being interdiffused, the apparent thickness of Pd was decreasing.

3.4 Copper/Palladium-Iron System

3.4.1 Electrodeposition of Palladium-Iron coatings

Pd-Fe alloy was electroplated with current density of 0.5A/dm^2 in a bath contained 4.43g/l of $PdCl_2$, 10.15g/l of $Fe_2(SO_4)_3$, 25.42g/l of sulfosalicylic acid and 19.80g/l of $(NH_4)_2SO_4$. The pH was adjusted to 8.0-8.5 with ammonia. The plating temperature was 40°C. Composition of the Pd-Fe alloy coating for diffusion experiment was measured by energy dispersion spectrometer (EDS) to be Pd 75wt%/Fe 25wt%. Some Pd-Fe coatings were plated with current density ranging from 0.5 to 10.0 A/dm^2 to observe any dependence of composition on plaint parameters.

3.4.2 Diffusion Experiment

Diffusion annealing schedule is listed in Table 3.4.

Table 3.4. Heat treatment Schedule of Copper/Palladium-Iron (10μm) Diffusion Couples

Sample Designation	Annealing Temperature (°C)	Annealing Time (h)	Remarks
Cu/Pd-Fe-1	600	1	40wt% Cu on surface
Cu/Pd-Fe-2	700	0.5	60wt% Cu on surface
Cu/Pd-Fe-3	800	0.17	70wt% Cu on surface
Cu/Pd-Fe-11	500	0.6	apparent interdiff. coefficient calculated
Cu/Pd-Fe-9	450	1	apparent interdiff. coefficient. calculated
Cu/Pd-Fe-4	400	1	negligible diffusion
Cu/Pd-Fe-8	400	3.5	apparent interdiff. coefficient. calculated
Cu/Pd-Fe-7	350	12	little interdiffusion
Cu/Pd-Fe-10	350	66.2	apparent interdiff. coefficient calculated
Cu/Pd-Fe-5	300	7	negligible diffusion
Cu/Pd-Fe-12	300	91.5	apparent interdiff. coefficient calculated
Cu/Pd-Fe-13	250	980	apparent interdiff. coefficient calculated

Interdiffusion coefficients regarding Cu and Pd-Fe as two species interdiffusing with each other were determined at the temperatures ranging from 250°C to 500°C by

Boltzman-Matano method. Surface morphology of the Pd75%/Fe25% electrodeposit plated at 0.5 A/dm^2 is revealed by SEM.

3.4.3 X-ray diffraction

To gain more understanding for the Cu/Pd-Fe system, XRD analysis of untreated as-deposited samples and samples heat treated at 500°C for 1 h were investigated. Any intermetallic phases can be identified by the XRD spectra recorded in the Bragg-Brentano geometry in the 2θ interval.

3.5 Copper/Cobalt System

3.5.1 Electrodeposition of Cobalt coatings

Cobalt was electroplated on pre-cleaned and surface activated copper substrate in a bath containing 100g/l of cobalt chloride ($CoCl_2 \cdot 6H_2O$) and 60g/l of boric acid (H_3BO_3) with current density ranging from 3.2 to 3.8 A/dm^2. The solution pH was adjusted to 2.5-3.5. The temperature was maintained at 50°C.

3.5.2 Diffusion Experiment

Diffusion annealing temperatures and times are listed in Table 3.5. The procedures followed after the diffusion annealing were similar to the copper-nickel systems. For optical microscopy examination of the cobalt deposit, etchants

containing 10% HNO_3 and 90% Methanol (95%) was used to reveal the structure of the cobalt coating.

Table 3.5 Heat Treatment Schedule for Copper/Cobalt Diffusion Couples

Sample Designation	Annealing Temperature (°C)	Annealing Time (h)
Cu-Co-1	600	24
Cu-Co-2	700	14
Cu-Co-3	800	6
Cu-Co-4	600	50
Cu-Co-5	700	24
Cu-Co-6	700	48
Cu-Co-7	900	3
Cu-Co-8	900	15

3.5.3 X-ray Diffraction

XRD spectra of the as-deposited cobalt coating were recorded in the Bragg-Brentano geometry in the 2θ interval between 40° and 100°.

3.6 Copper/Cobalt-Tungsten System

3.6.1 Electrodeposition of Cobalt-Tungsten coatings

Co-W alloy for diffusion experiment was electroplated at 65°C with current density 1.2 A/dm^2 in a bath containing 58.5g/l of $CoSO_4 \cdot 7H_2O$, 68.0g/l of $Na_2WO_4 \cdot 2H_2O$, 65.0g/l of citric acid and 20g/l of Ethylene diamine tetraocetic disodium salt (EDTA). The pH was adjusted to about 7 with NH_3 solution. The composition of the electrodeposit was determined by EDS detector.

The composition of the Co-W layer depends on the deposition parameters as well as on the variation of electrolyte concentrations. The tungsten content in the electrolyte was kept constant at 0.2 M. Cobalt content varied from 0.1 to 0.3 M and the current densities were adjusted from 1 to 5 A/dm^2. The plating temperature and pH of the solution were kept constant at 65°C and 7, respectively. The alloy compositions were then determined by EDS.

3.6.2 Diffusion Experiment

The Cu/65wt%Co-35wt%W samples were annealed at 500°C for 6 hours and 800°C for 45 min respectively. The concentration-distance profiles after annealing were obtained by EDS. The cross-sectioned structure and surface morphology of the Co-W electrodeposit were studied by SEM.

3.6.3 X-ray Diffraction

XRD patterns of the as-deposited and Cu/Co-W samples having annealed at 500°C, 800°C and 1100°C were obtained for phases and structure identification for the Co-W coatings.

3.7 Copper/Cobalt(barrier)/Nickel and Copper/Cobalt-Tungsten (barrier)/Nickel systems

3.7.1 Electrodeposition of Co/Ni and Co-W/Ni Coatings

In order to evaluate the performance of cobalt and cobalt-tungsten being a diffusion barrier for copper, cobalt layers of thickness 0.5μm and 1.5μm were electroplated respectively on copper substrates using the cobalt plating bath as described in Section 3.5, in which the same plating conditions and pre-treatment procedure of the copper substrate were followed. Electroplated copper/cobalt samples were then surface activated. Using a Watts nickel bath with the same plating conditions of Section 3.2, the Cu/Co samples were electroplated with nickel layers of thickness more than 10μm. Cobalt-35wt%tungsten layers of thickness 1.5μm were electroplated on copper substrates using the cobalt-tungsten plating bath as described in Section 3.7. The same plating conditions and pre-treatment procedure of the copper substrate were followed. Electroplated copper/cobalt-tungsten samples were then surface activated. Using a Watts nickel bath with the same plating condition to that of Section 3.2, Cu/Co-W samples were electroplated with nickel layers of thickness more than 10μm.

3.7.2 Diffusion Experiment

Diffusion experiment of the Cu/Co(barrier)/Ni and Cu/Co-W(barrier)/Ni systems were conducted for samples having Co or Co-W thickness of 0.5μm and 1.5μm at temperatures ranging from 400°C to 800°C. Concentration-distance profiles were obtained by EDS and results were compared with the Cu/Ni system.

3.8 Copper/Barriers/Gold Systems

3.8.1 Electrodeposition of Barriers and Gold coatings

To evaluate the effectiveness of different electrodeposited coatings as diffusion barrier for Cu/Au interdiffusion, electrodeposited coatings of columnar Ni, lamellar Ni, Co, Pd, Co-W, Pd-Fe of thickness 1μm were electroplated respectively on pre-cleaned copper substrates. Gold coatings were then electroplated on the copper/barrier samples in a bath containing 13.6g/l of $KAu(CN_2)$, 50g/l of $(NH_4)_2C_6H_6O_7$. The pH was adjusted to 4.8-5.2 with citric acid. The current density was kept within the range of 0.32-0.35A/dm^2. The temperature was maintained at 60°C.

3.8.2 Diffusion Experiment

Diffusion experiment of the Cu/Barriers(1μm)/Au systems were conducted at 400°C for 24 h and 48 h respectively. Concentration–distance profiles were then obtained by EDS after heat treatments.

3.9 DC Polarization and AC Electrochemical Impedance Measurements

DC polarization and AC electrochemical impedance measurements were carried out on Watts nickel (columnar/lamellar), cobalt, palladium, cobalt-tungsten and palladium-iron electrodeposits of 1 cm^2 geometric area in a cell containing 3% sodium chloride solution of pH 5-6 at 25°C. A schematic diagram of the cell is shown in Fig. 3.9.1.

Fig. 3.9.1 Schematic Diagram of the Flat Cell used for AC Impedance and Linear Polarisation Measurements

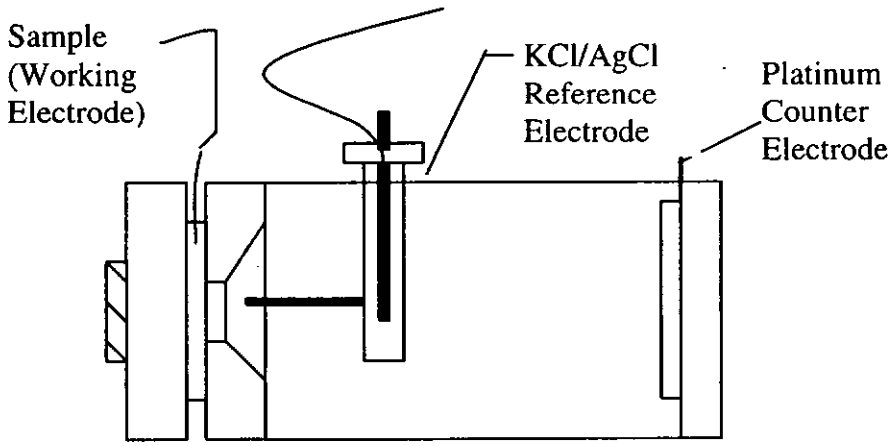

The test cell consisted of a platinum counter electrode and a saturated KCl/AgCl reference electrode. The reference electrode is housed in a Luggin well,

with a fixed Teflon Luggin capillary protruding from the bottom of the well. A Teflon gasket exposes a 1 cm^2 area of the working electrode to the cell solution. The Luggin capillary is positioned at the proximity to the center of the working electrode (the exposed 1 cm^2 part of the sample).

Prior to testing, each specimen was polished to 500 grit then degreased with acetone and cleaned in 10% HCl solution; they were washed thoroughly with distilled water before each experimental run.

Impedance measurements were made with Solartron 1255 HF Frequency Response Analyzer and EG & G PARC Model 273A Potentiostat. A constant perturbating signal amplitude $|\Delta E|$=10 mV was used over the frequency range 10 mHz – 10kHz. During the experiments, the metal was kept at corrosion potential. The real and imaginary parts of the impedance were recorded for various samples. An Electrochemical Impedance Software (EG & G Model 398) was used to analyze the ac impedance measurement data.

DC polarization studies were carried out using an EG & G PARC Model 273 Potentiostat. The potential scans were taken place within ±250 mV of E_{corr} for each specimen with a scan rates of 0.166 mV/s. The resulting Tafel plots and potential *versus* current polarization plots for different samples were obtained. A Corrosion Measurement & Analysis Software (EG & G Model 352) was used to analyze the DC polarization measurement results.

Chapter 4

Results and Discussion on Diffusion Experiments

4.1 Copper/Nickel Systems

4.1.1 Copper/Nickel (lamellar) System

4.1.1.1 Microstructural Observations

Metallographic studies were conducted by both optical microscope and SEM on the as-deposited and annealed samples to determine if there were any structural changes of the nickel electrodeposits. Figures 4.1.1 and 4.1.2 show that for the nickel coating electroplated from a bath containing 2-butyne-1,4-diol has a lamellar structure. The lamellar structure became blurred after heat treatment at 400°C for 1 hour (Fig. 4.1.3) and completely disappeared when the nickel sample was heat treated at 500°C for 1 hour (Fig.4.1.4). The surface of the lamellar nickel electrodeposit is shown in Figure 4.1.5.

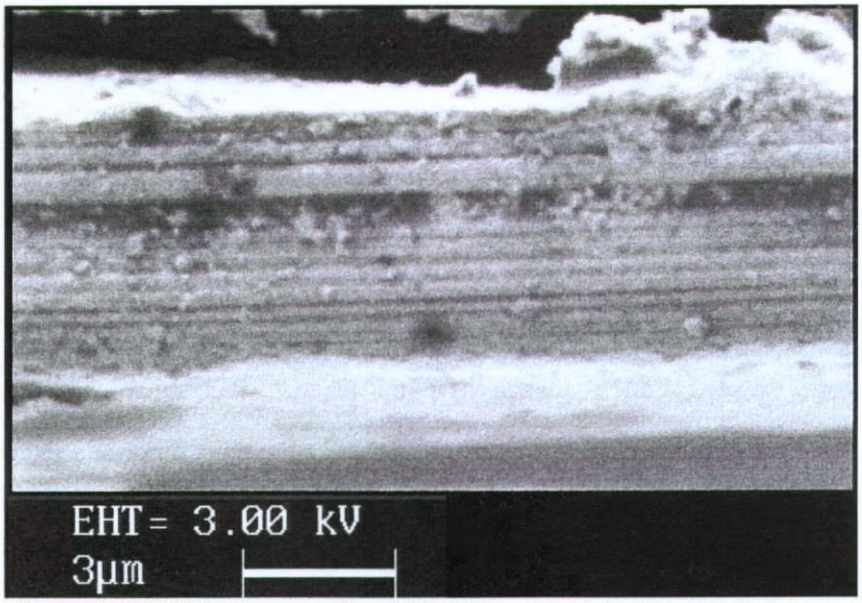

Fig. 4.1.1 SEM micrograph of Cu/Ni system electroplated from a bath containing 2-butyne-1,4-diol shows a lamellar structure.

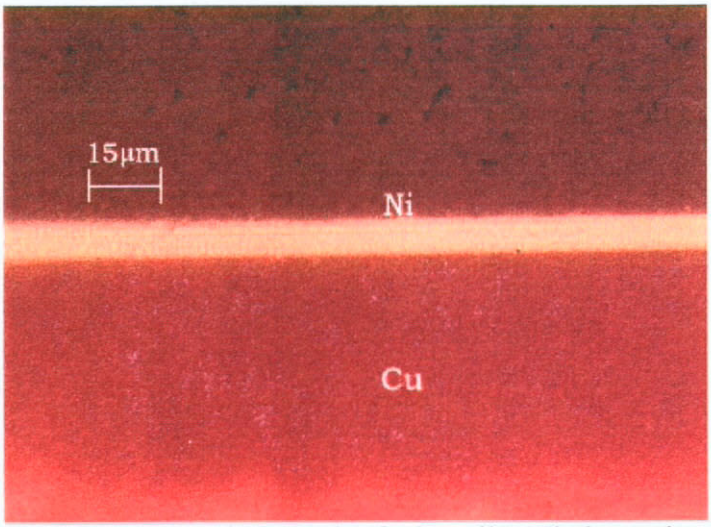

Fig. 4.1.2 Optical micrograph of a lamellar Ni electrodeposit plated from a bath containing 2-butyne-1,4-diol.

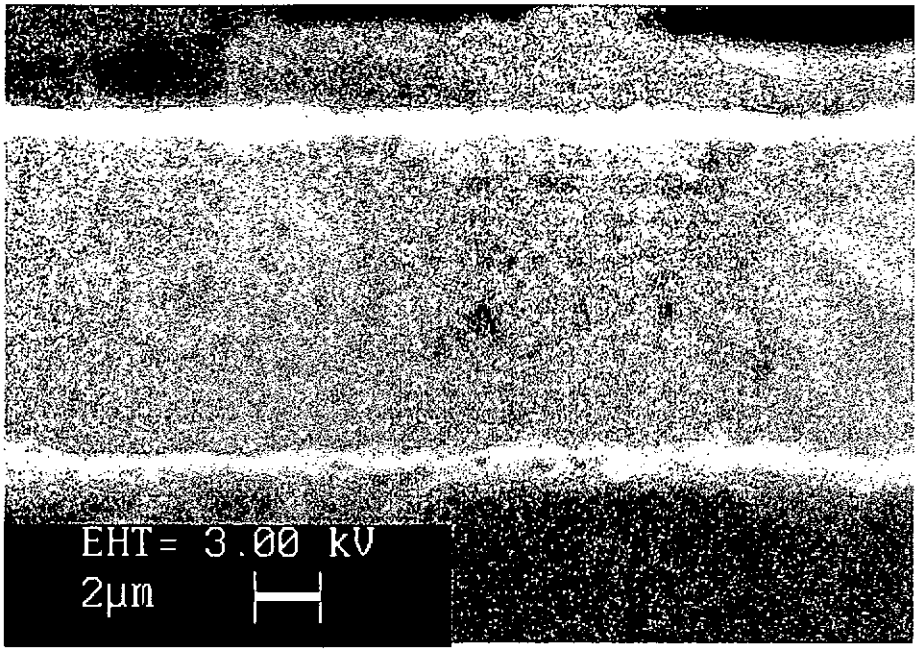

Fig. 4.1.3 The lamellar structure of the Ni coating becomes blurred after heat treatment at 400 °C for 1 h.

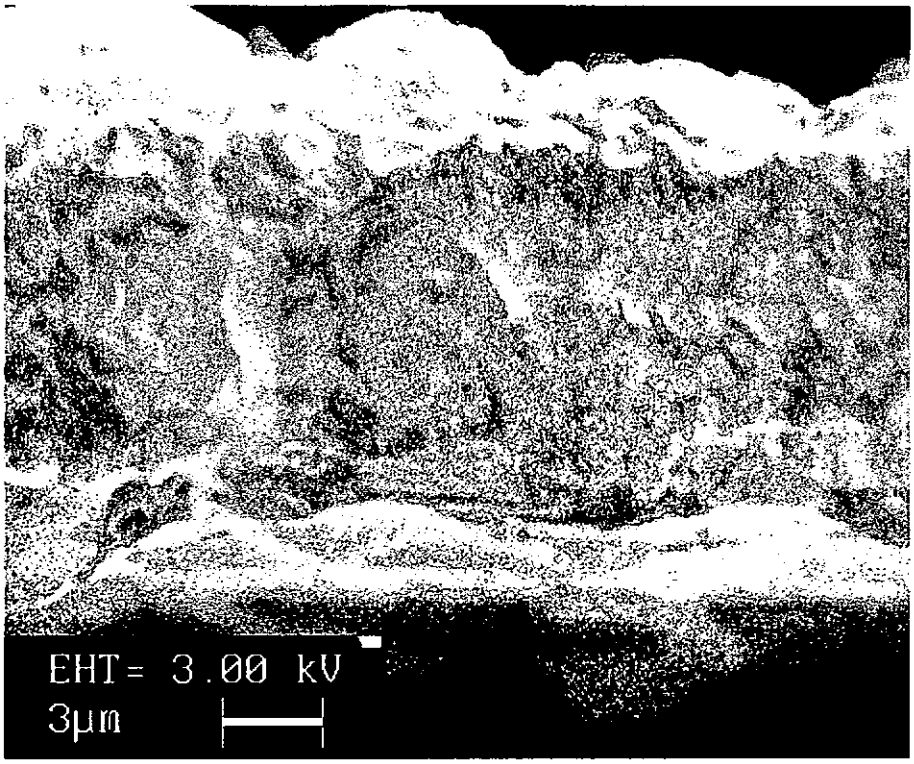

Fig. 4.1.4 The lamellar structure of the Ni coating has disappeared after heat treatment at 500 °C for 1 h.

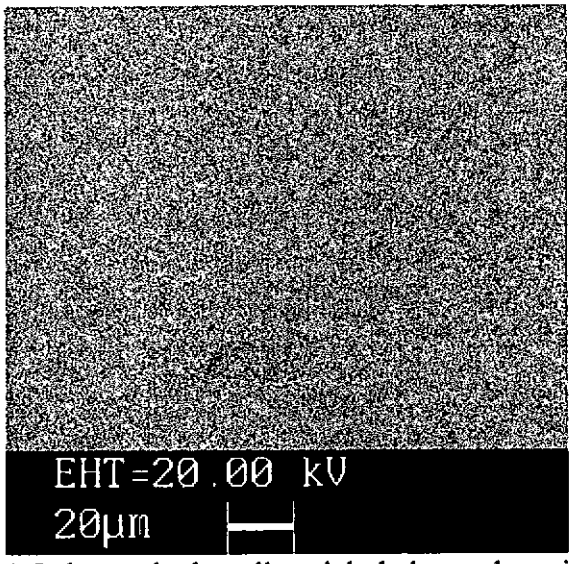

Fig. 4.1.5 shows the lamellar nickel electrodeposit has a good surface smoothness.

4.1.1.2 X-ray Diffraction Studies

XRD spectra were recorded in the Bragg-Brentano geometry in the 2θ interval between 40° and 100°, where the most relevant diffraction peaks of the nickel deposit are present, as shown in Figure 4.1.6. The lattice parameters, the interplanar lattice spacing and the Bragg angles (2θ) where reported in Table 4.1.1. The presence of the copper substrate lowers the intensity ratio of the signals originated by the nickel deposit, thus only the most intense reflections due to nickel deposit could be recorded.

Table 4.1.1. Data obtained from the analysis of the XRD patterns.

Crystalline phase	*Crystalline structure*	*Lattice parameters (nm)*	*Interplanar lattice spacing (nm)*	*(hkl)*	*2θ*
Ni	f.c.cubic	a=0.3522	0.2033	(111)	44.54°
		a=0.3510	0.1755	(200)	52.05°
		a=0.3521	0.1245	(220)	76.43°
		a=0.3512	0.1059	(311)	93.25°
		a=0.3523	0.1017	(222)	98.47°
Cu	f.c.cubic	a=0.3621	0.2091	(111)	43.23°
		a=0.3622	0.1811	(200)	50.33°
		a=0.3618	0.1279	(220)	74.04°
		a=0.3618	0.1091	(311)	89.81°

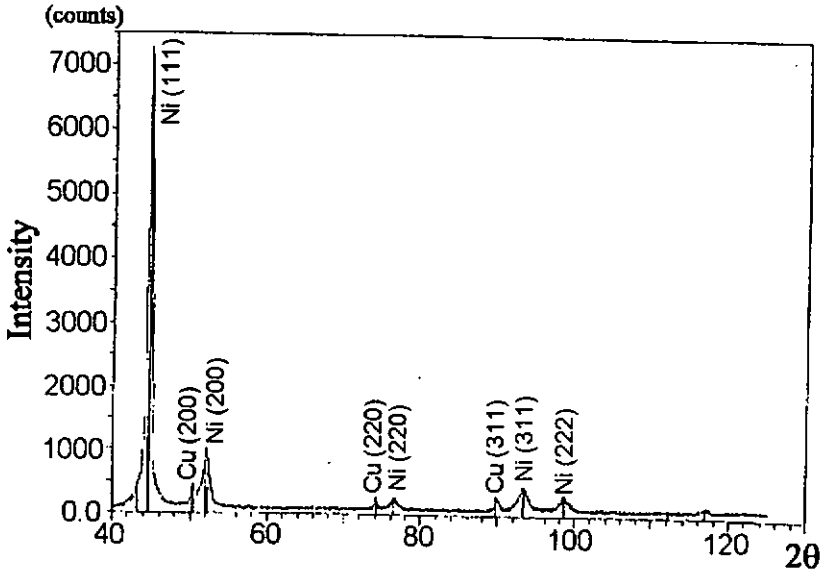

Fig. 4.1.6 XRD spectra of as-deposited lamellar nickel coating.

XRD spectra of lamellar nickel coatings plated at 3.6 A/dm^2 at 50°C after heat treatment at 500°C for 0, 24, 48 and 96 hours respectively were obtained. Fig. 4.1.7 shows the Ni (111) peaks of the as-deposited and heat treated (at 500°C for 24 h) lamellar nickel coating. Apparent grain sizes of the as-deposited lamellar Ni coatings and after heat treatment at 500°C for 30 min. to 96 hours were determined from the

Ni(111) peak by the Warren-Scherrer method [24] (Table 4.1.2). Fig. 4.1.8 illustrates the change of grain size at 500°C with time.

Table 4.1.2. Apparent Grain Size *D* for Seven Heat Treated Lamellar Nickel Samples Plated at 3.6 A/dm^2.

Annealing Temp. (°C)	Annealing Time (h)	Peak Width (degree)	*D* (nm)
500	0	0.667	14.3
500	0.5	0.386	24.7
500	6.5	0.354	26.9
500	15.25	0.334	28.6
500	24	0.300	31.8
500	48	0.2857	33.4
500	96	0.2727	35.0

The grain sizes increases rapidly in the initial 30min and gradually levels off.

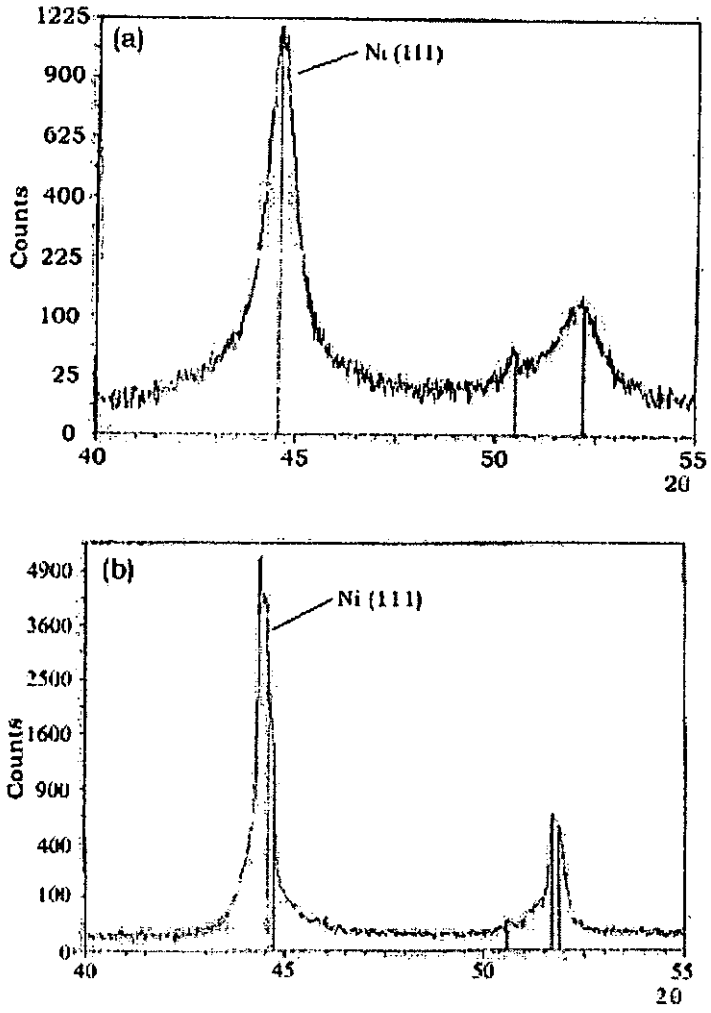

Fig. 4.1.7 XRD spectra show the Ni(111) peak of the (a) as-deposited (b) heat treated at 500°C for 24 h lamellar nickel electrodeposit.

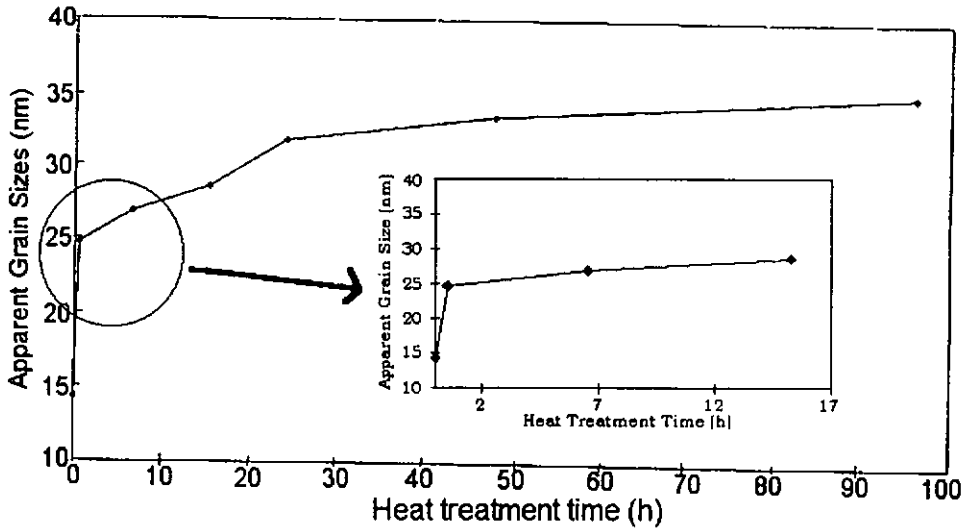

Fig. 4.1.8 Variation of apparent grain sizes of lamellar nickel electrodeposit treated at 500°C with time.

4.1.1.3 Diffusivity Values

Figures 4.1.9 to 4.1.11 shows the EDS concentration-distance profiles at the diffusion zone for the 300°C, 400°C and 900°C heat treated Cu/lamellar Ni couples respectively. There is some interdiffusion at 300°C for 284 h, and at 400°C both Ni and Cu have notably interdiffused after 96 h heat treatment. At 900°C Ni and Cu interdiffuse rapidly within the time interval of 10 min.

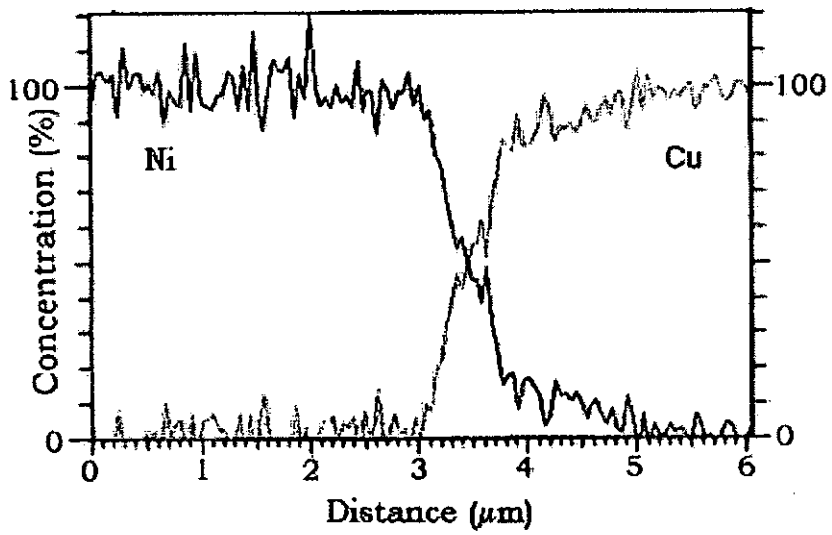

Fig. 4.1.9 Concentration-distance profile of Cu/lamellar Ni couple after heat treatment at 300°C for 284h.

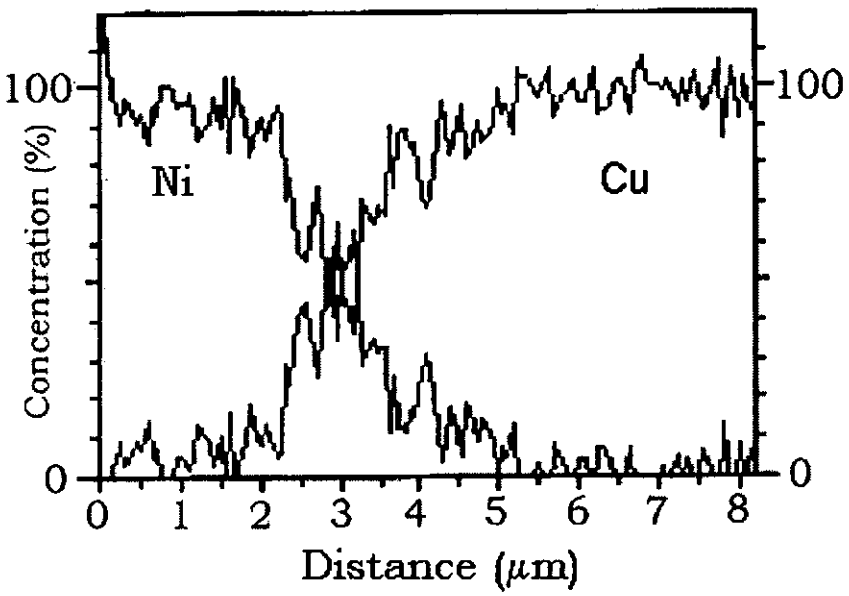

Fig. 4.1.10 Concentration-distance profile of Cu/lamellar Ni couple after heat treatment at 400°C for 96h.

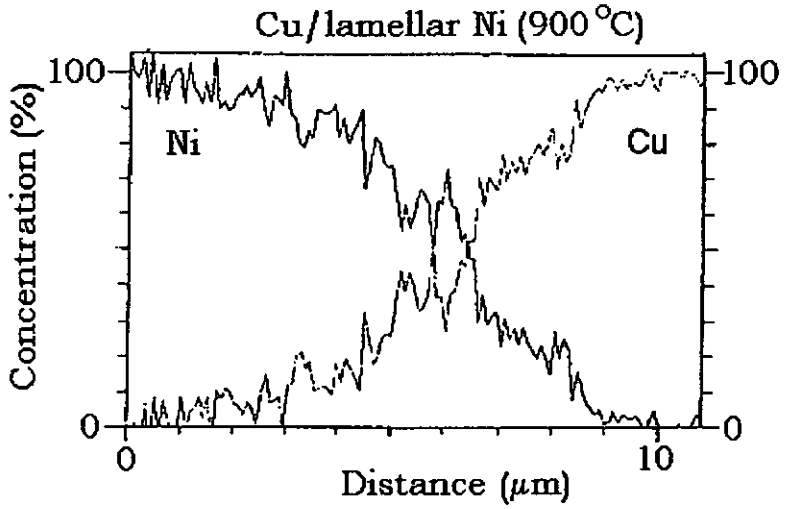

Fig. 4.1.11 Concentration-distance profile of Cu/lamellar Ni couple after heat treatment at 900°C for 10 min.

The chemical interdiffusion coefficient $\tilde{D}$ was found to be a function of concentration. Diffusion coefficients at different temperatures and copper concentrations are shown in Table 4.1.3. A curve of $log\,\tilde{D}$ as a function of concentration for each of the temperatures investigated is plotted in Fig. 4.1.12.

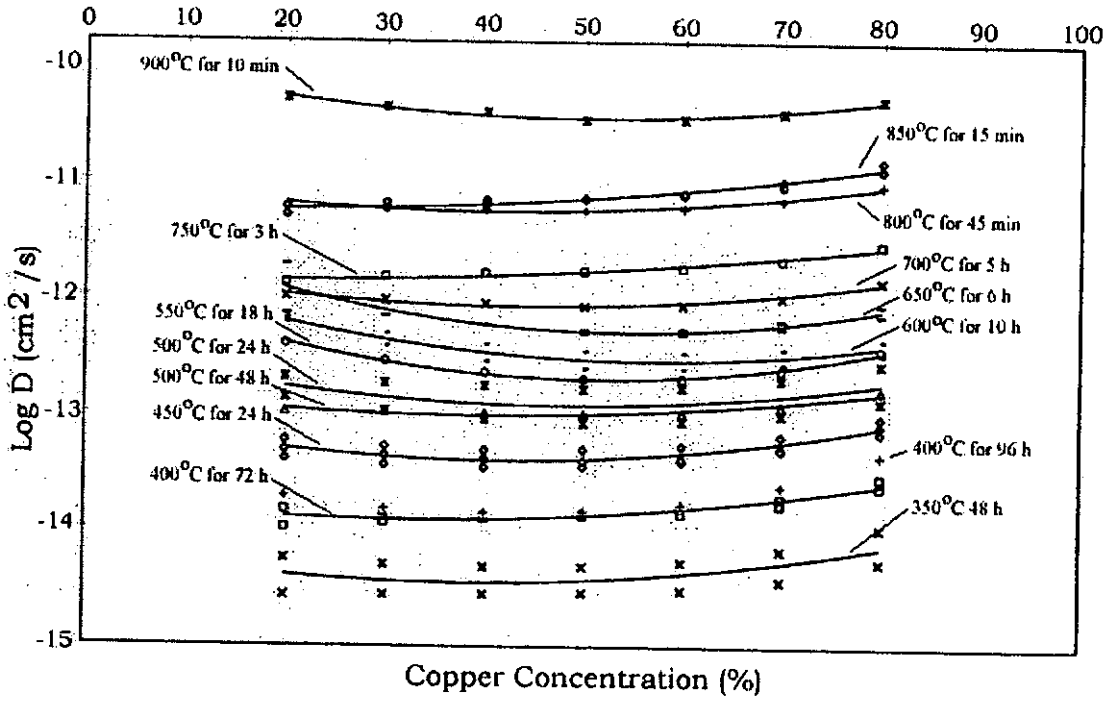

Fig. 4.1.12 Variation of D with Copper Concentration for Different Heat Treatment Conditions

Table 4.1.3. Chemical Diffusion Coefficients of Cu/lamellar Ni Couples at Different Temperatures and Copper Concentrations calculated by Boltzman-Matano Method.

Temperature (°C)	Anneal Time (h)	D at 20% of Cu (cm^2/s)	D at 30% of Cu (cm^2/s)	D at 40% of Cu (cm^2/s)	D at 50% of Cu (cm^2/s)	Sample ref.
250	2568	1.510×10^{-15}	1.429×10^{-15}	1.454×10^{-15}	1.562×10^{-15}	ni/cu33
300	96	negligible	inter-	diffusion		ni/cu31
300	284	8.119×10^{-16}	8.712×10^{-16}	9.245×10^{-16}	9.776×10^{-16}	ni/cu31
350	48	2.729×10^{-15}	2.756×10^{-15}	2.809×10^{-15}	2.901×10^{-15}	ni/cu26
350	48	5.654×10^{-15}	5.035×10^{-15}	4.839×10^{-15}	4.850×10^{-15}	ni/cu27
400	72	1.486×10^{-14}	1.410×10^{-14}	1.354×10^{-14}	1.325×10^{-14}	ni/cu2
400	72	1.040×10^{-14}	1.155×10^{-14}	1.256×10^{-14}	1.366×10^{-14}	ni/cu4
400	96	1.948×10^{-14}	1.532×10^{-14}	1.417×10^{-14}	1.454×10^{-14}	ni/cu14
450	24	4.071×10^{-14}	3.625×10^{-14}	3.472×10^{-14}	3.519×10^{-14}	ni/cu16
450	24	4.844×10^{-14}	4.382×10^{-14}	4.116×10^{-14}	3.950×10^{-14}	ni/cu17
450	24	5.912×10^{-14}	5.259×10^{-14}	4.868×10^{-14}	4.953×10^{-14}	ni/cu18
500	0.5	2.779×10^{-13}	2.259×10^{-13}	1.993×10^{-13}	1.867×10^{-13}	ni/cu32
500	24	2.041×10^{-13}	1.846×10^{-13}	1.747×10^{-13}	1.635×10^{-13}	ni/cu20
500	24	1.357×10^{-13}	1.051×10^{-13}	9.058×10^{-14}	8.372×10^{-14}	ni/cu21
500	48	1.034×10^{-13}	1.046×10^{-13}	1.014×10^{-13}	9.969×10^{-14}	ni/cu6
550	18	3.951×10^{-13}	2.847×10^{-13}	2.272×10^{-13}	1.988×10^{-13}	ni/cu22
550	36	2.331×10^{-13}	3.203×10^{-13}	2.663×10^{-13}	2.058×10^{-13}	ni/cu13
600	10	6.046×10^{-13}	4.866×10^{-13}	3.971×10^{-13}	3.461×10^{-13}	ni/cu30
600	18	6.530×10^{-13}	3.810×10^{-13}	2.841×10^{-13}	2.470×10^{-13}	ni/cu3
650	6	1.925×10^{-12}	8.770×10^{-13}	5.873×10^{-13}	4.939×10^{-13}	ni/cu24
650	12	7.244×10^{-13}	6.942×10^{-13}	5.875×10^{-13}	5.284×10^{-13}	ni/cu12
700	5	1.015×10^{-12}	9.558×10^{-13}	8.947×10^{-13}	8.444×10^{-13}	ni/cu9
750	3	1.325×10^{-12}	1.509×10^{-12}	1.624×10^{-12}	1.687×10^{-12}	ni/cu5
800	0.75	6.260×10^{-12}	5.978×10^{-12}	5.796×10^{-12}	5.623×10^{-12}	ni/cu1
850	0.25	5.947×10^{-12}	6.571×10^{-12}	6.985×10^{-12}	7.242×10^{-12}	ni/cu10
850	0.25	5.129×10^{-12}	5.818×10^{-12}	6.447×10^{-12}	7.082×10^{-12}	ni/cu11
900	0.17	5.135×10^{-11}	4.376×10^{-11}	3.982×10^{-11}	3.415×10^{-11}	ni/cu29

Table 4.1.3. (Continue) Chemical Diffusion Coefficients of Cu/lamellar Ni Couples at Different Temperatures and Copper Concentrations calculated by Boltzman-Matano Method.

Temperature (°C)	Annealing Time (h)	D at 60% of Cu (cm^2/s)	D at 70% of Cu (cm^2/s)	D at 80% of Cu (cm^2/s)	Sample ref.
250	2568	1.783×10^{-15}	2.320×10^{-15}	4.148×10^{-15}	ni/cu33
300	284	1.048×10^{-15}	1.268×10^{-15}	1.898×10^{-15}	ni/cu31
350	48	3.056×10^{-15}	3.688×10^{-15}	5.382×10^{-15}	ni/cu26
350	48	5.303×10^{-15}	6.767×10^{-15}	1.058×10^{-14}	ni/cu27
400	72	1.389×10^{-14}	1.673×10^{-14}	2.406×10^{-14}	ni/cu2
400	72	1.521×10^{-14}	1.900×10^{-14}	2.899×10^{-14}	ni/cu4
400	96	1.675×10^{-14}	2.406×10^{-14}	4.469×10^{-14}	ni/cu14
450	24	3.941×10^{-14}	5.120×10^{-14}	8.132×10^{-14}	ni/cu16
450	24	4.124×10^{-14}	4.947×10^{-14}	7.082×10^{-14}	ni/cu17
450	24	5.343×10^{-14}	6.568×10^{-14}	9.466×10^{-14}	ni/cu18
500	0.5	1.974×10^{-13}	2.385×10^{-13}	3.394×10^{-13}	ni/cu31
500	24	1.703×10^{-13}	2.000×10^{-13}	2.733×10^{-13}	ni/cu20
500	24	8.662×10^{-14}	9.961×10^{-14}	1.297×10^{-13}	ni/cu21
500	48	1.020×10^{-13}	1.186×10^{-13}	1.623×10^{-13}	ni/cu6
550	18	2.022×10^{-13}	2.423×10^{-13}	3.619×10^{-13}	ni/cu22
550	36	1.915×10^{-13}	2.182×10^{-13}	3.106×10^{-13}	ni/cu13
600	10	3.387×10^{-13}	3.676×10^{-13}	4.435×10^{-13}	ni/cu30
600	18	2.462×10^{-13}	2.723×10^{-13}	3.330×10^{-13}	ni/cu3
650	6	4.908×10^{-13}	5.552×10^{-13}	7.233×10^{-13}	ni/cu24
650	12	5.423×10^{-13}	6.408×10^{-13}	8.788×10^{-13}	ni/cu12
700	5	8.696×10^{-13}	1.024×10^{-12}	1.424×10^{-12}	ni/cu9
750	3	1.791×10^{-12}	2.139×10^{-12}	2.903×10^{-12}	ni/cu5
800	0.75	5.906×10^{-12}	7.000×10^{-12}	9.450×10^{-12}	ni/cu1
850	0.25	7.764×10^{-12}	9.338×10^{-12}	1.296×10^{-11}	ni/cu10
850	0.25	7.979×10^{-12}	1.031×10^{-11}	1.536×10^{-11}	ni/cu11
900	0.17	3.473×10^{-11}	3.967×10^{-11}	5.148×10^{-11}	ni/cu29

Since the chemical diffusion coefficient is a function of concentration, its dependence on temperature must be represented by a family of curves. Curves of $\log_{10}\tilde{D}$ vs. $1/T$ for concentrations of 20 to 80 % Cu are plotted in Figures 4.1.13 through 4.1.19, respectively. For all the three concentrations, the general shapes of the curves are identical. At higher temperatures (750°C to 900°C) the data conform to an Arrhenius equation $D = D_o \exp(-Q/RT)$. where D_o is the frequency factor, Q is apparent activation energy for diffusion and R is gas constant 8.32 $Jmol^{-1}K^{-1}$ (1.98719 cal $mol^{-1}K^{-1}$). In the mid temperature range of 350°C to 700°C all data points fall above the curve extrapolated from the higher temperatures, thus indicating that a low temperature diffusion mechanism predominates.

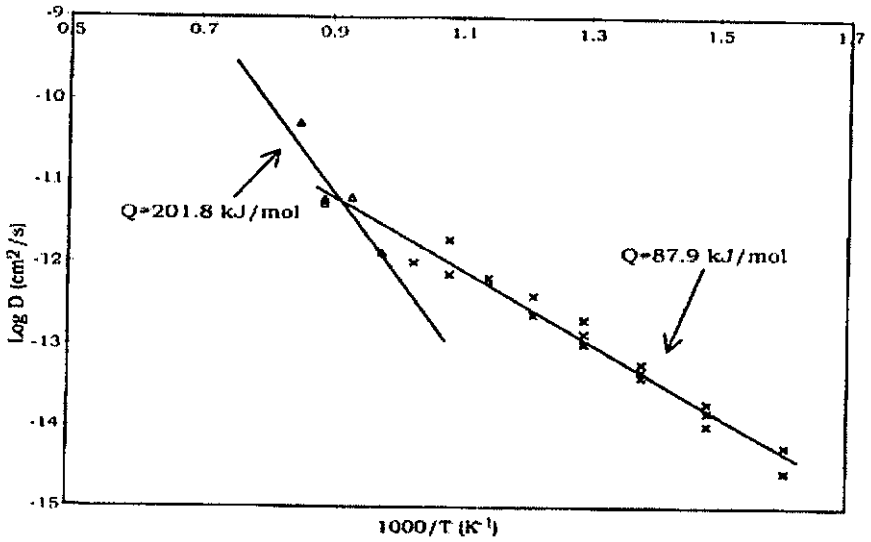

Fig. 4.1.13 The Arrhenius plot of diffusivities at 20% copper

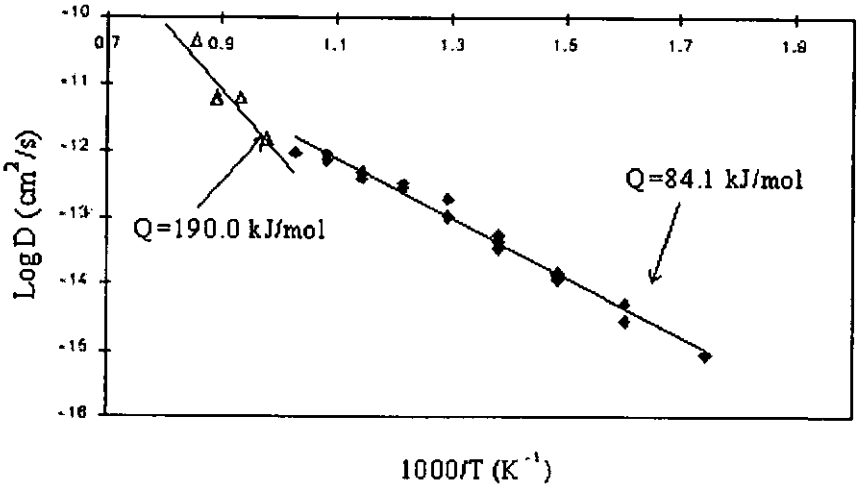

Fig. 4.1.14 The Arrhenius plot of diffusivities at 30% copper

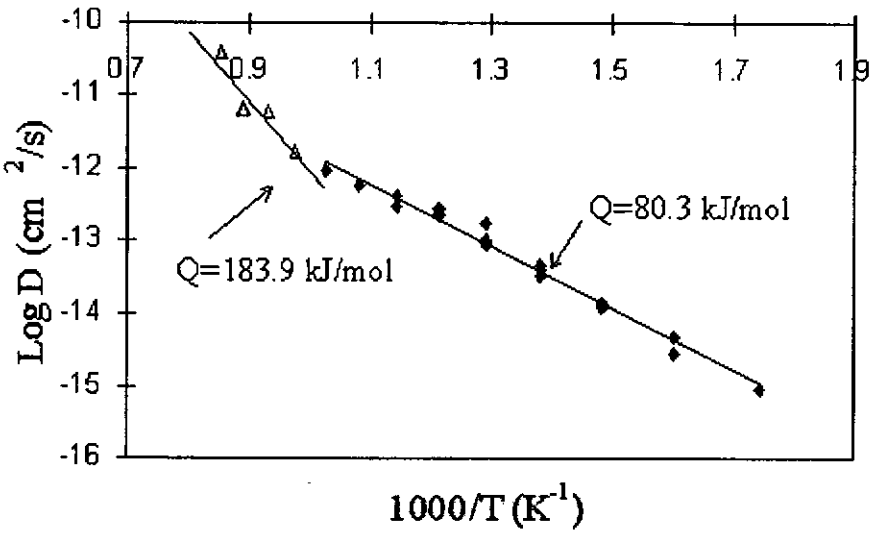

Fig. 4.1.15 The Arrhenius plot of diffusivities at 40% copper

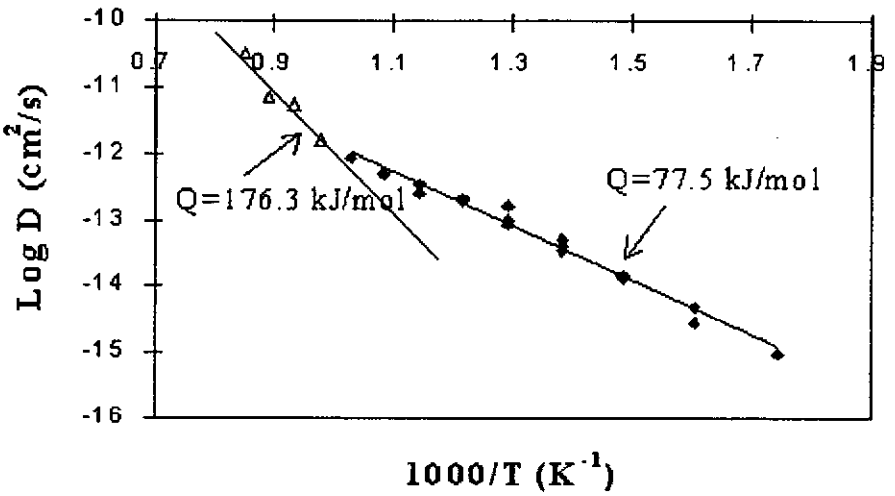

Fig. 4.1.16 The Arrhenius plot of diffusivities at 50% copper

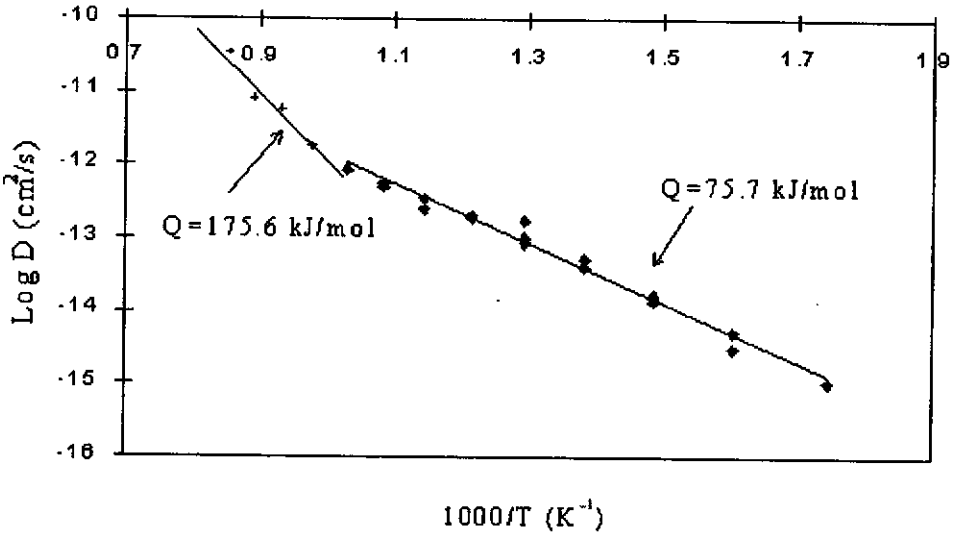

Fig. 4.1.17 The Arrhenius plot of diffusivities at 60% copper

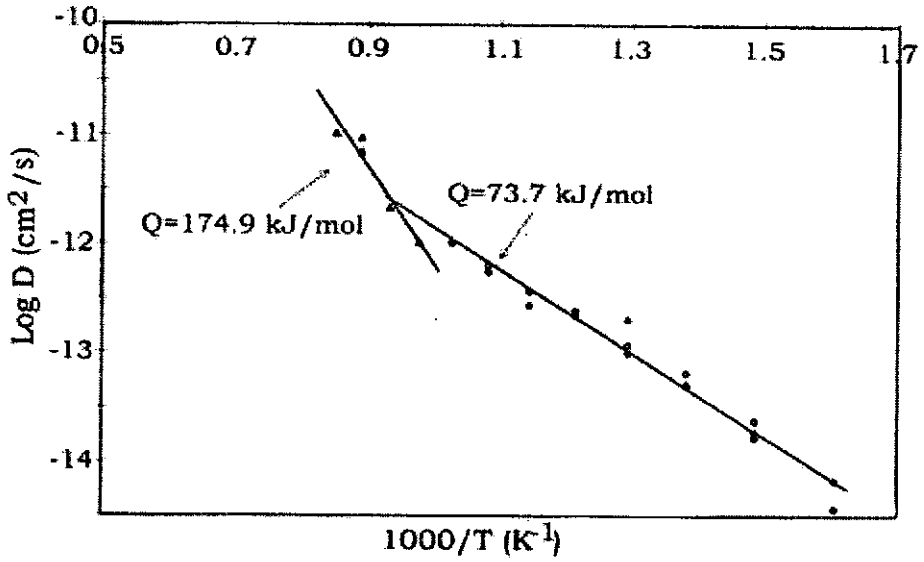

Fig. 4.1.18 The Arrhenius plot of diffusivities at 70% copper

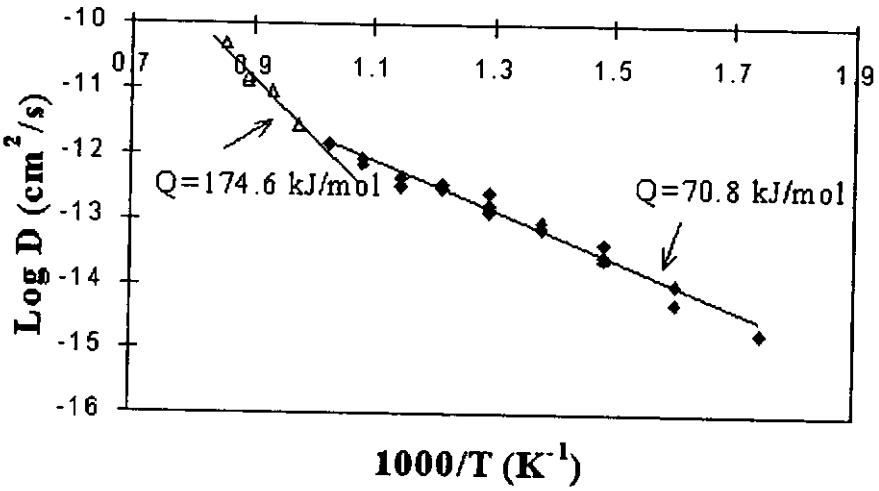

Fig. 4.1.19 The Arrhenius plot of diffusivities at 80% copper

Apparent activation energies for diffusion were calculated from the curves in Figures 4.1.13 through 4.1.19. In the high temperature range the value of Q decreases from 201.8 kJ/mol to 174:6 kJ/mol as the copper concentration increases from 20 to 80 %. In the mid temperature range the value of Q is seen to be approximately one-half that of Q at the higher temperatures. Variations of Q as a function of copper concentrations are shown in Figures 4.1.20 and 4.1.21; and variation of logarithm of frequency factor D_o as function of copper concentrations for higher temperatures range (700°C to 900°C) and lower temperatures range (350°C to 700°C) are given in Figures 4.1.22 and 4.1.23 respectively.

Extrapolating these graphs to 0 and 100 % the activation energy and frequency factors for the impurity self diffusion coefficients of Ni and Cu are obtained. For example, for the lower temperature range 350°C to 700°C the self diffusion coefficients of Nickel in Copper at 400°C and 550°C are 1.13×10^{-14} cm^2/s and 2.26×10^{-13} cm^2/s, respectively, with an activation energy of 92.1 kJ/mol and a frequency factor of 1.57×10^{-7} cm^2/s. The self diffusion coefficients of copper in nickel were 2.61×10^{-14} cm^2/s and 2.15×10^{-13} cm^2/s at 400°C and 550°C, respectively, with an activation energy of 64.9 kJ/mol and a frequency factor of 2.8×10^{-9} cm^2/s. For the higher temperature range 700°C to 900°C, the self activation energy and frequency factor of nickel are 203.9 kJ/mol and 0.048 cm^2/s while copper has the self activation energy of 161.2 kJ/mol and frequency factor of 1.39×10^{-4} cm^2/s. Figures 4.1.24 and 4.1.25 shows the variation of self diffusion coefficients of nickel and copper for both temperature ranges. It was found that the self diffusion coefficients of nickel and copper always have the same orders of magnitude at all investigated temperatures.

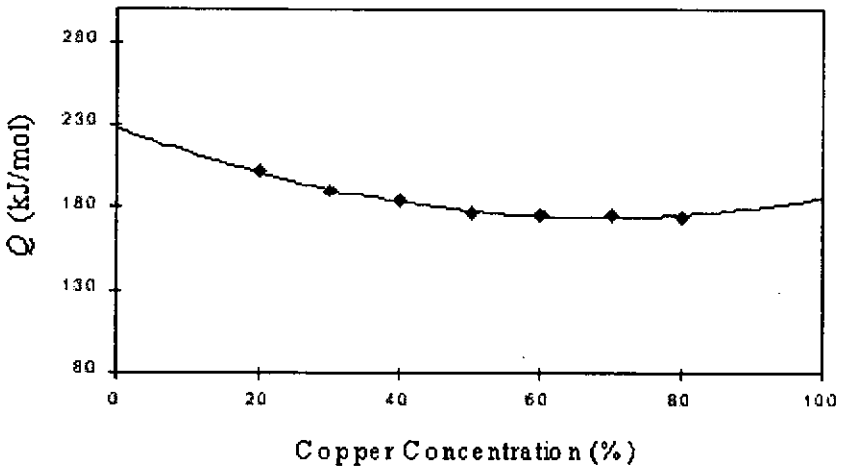

Fig. 4.1.20 Variation of Activation Energy with copper concentration in the temperature range 700-900°C

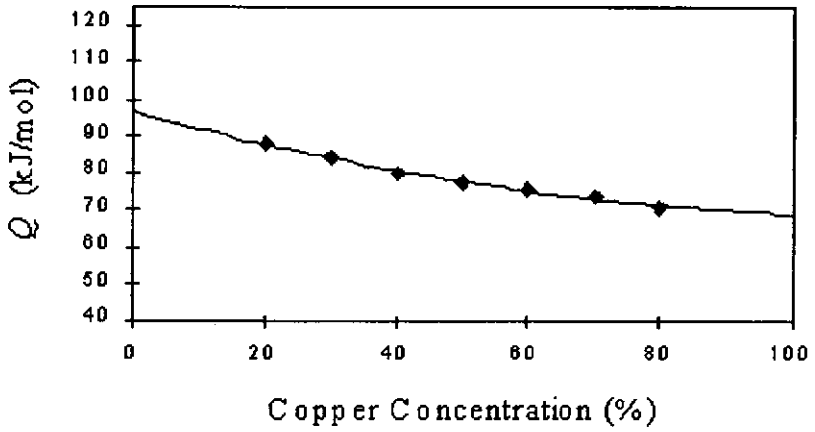

Fig. 4.1.21 Variation of Activation Energy with copper concentration in the temperature range 350-700°C

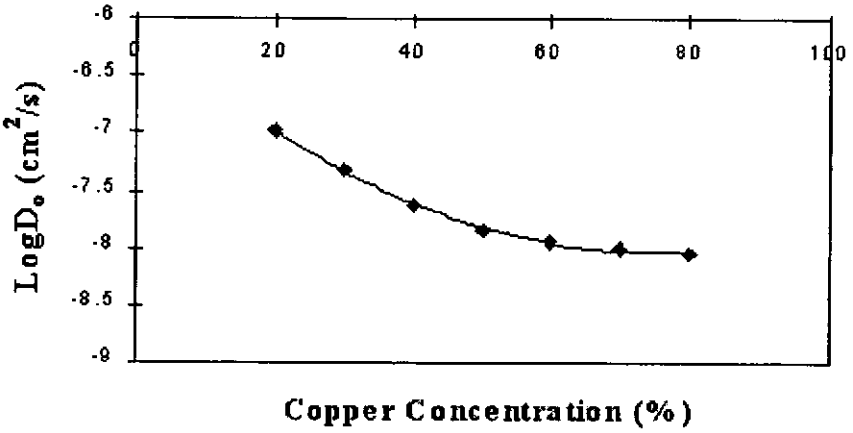

Fig. 4.1.22 Variation of Frequency Factors with copper concentration in the temperature range 350-700°C

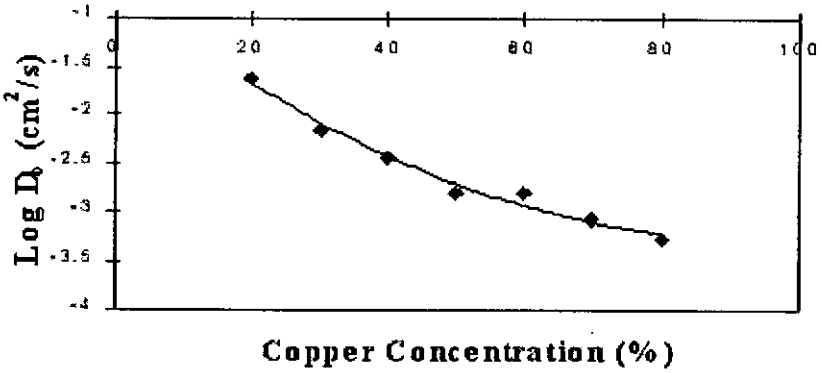

Fig. 4.1.23 Variation of Frequency Factors with copper concentration in the temperature range 700-900°C

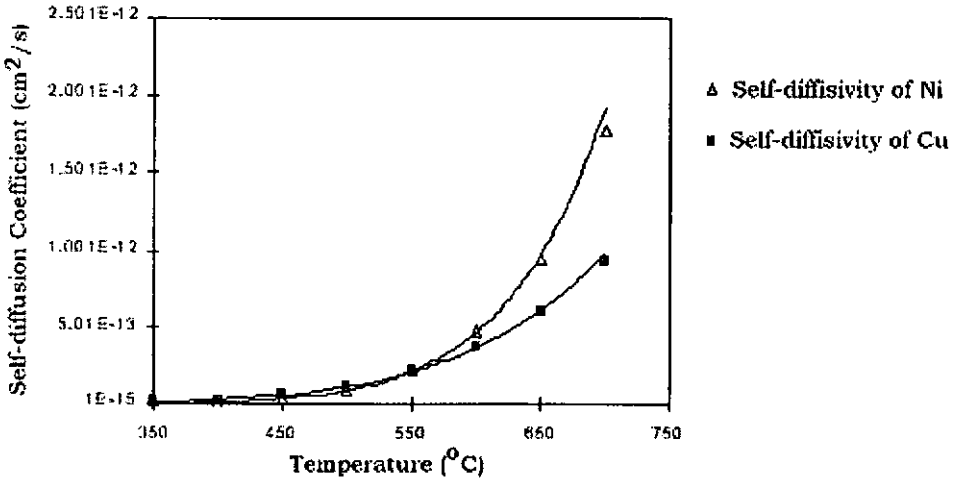

Fig. 4.1.24 Variation of Self-diffusion coefficients of Nickel (D_{Ni}) and Copper (D_{Cu}) in the temperature range 350-700°C

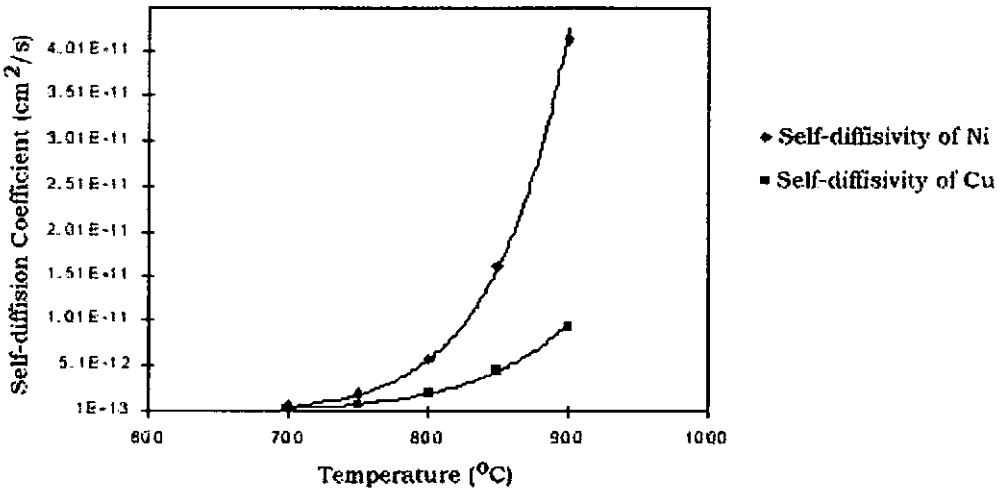

Fig. 4.1.25 Variation of Self-diffusion coefficients of Nickel (D_{Ni}) and Copper (D_{Cu}) in the temperature range 700-900°C

For all concentration levels, the apparent activation energy Q is seen to be approximately one-half that of Q at the higher temperatures. Defect diffusion such as diffusion along grain boundaries and dislocation has a smaller activation energy than that for the bulk diffusion. Clearly, a gradual transition range must exist where the dominance shifts from one mechanism to the other [1, 2]. Results of this study indicate that the transition range is about 700°C to 750°C for the copper/lamellar nickel system. It was found that the self diffusion coefficients of nickel and copper always have the same orders of magnitude at all investigated temperatures because the interdiffusion coefficients are only slightly concentration dependence resulting a lesser self diffusion coefficients differences between Ni and Cu.

It is also found that diffusivities determined at 500°C for 0.5h are higher than those measured after 24 and 48h heat treatment at the same temperature (Table 4.1.4). During heat treatment, recrystallization and grain boundary motion enhance effective volume diffusion. If all of the migration occurs during the first 24h of heat treatment, then it will give rise to higher diffusivity values than those measured for longer than 24h heat treatment.

Table 4.1.4 Chemical interdiffusion coefficients determined after heat treatment for different time intervals at 500°C for the Cu/lamellar Ni system.

Anneal Time	*D* at 20% ($\times 10^{-13}$ cm^2/s)	*D* at 30% ($\times 10^{-13}$ cm^2/s)	*D* at 40% ($\times 10^{-13}$ cm^2/s)	*D* at 50% ($\times 10^{-13}$ cm^2/s)	*D* at 60% ($\times 10^{-13}$ cm^2/s)	*D* at 70% ($\times 10^{-13}$ cm^2/s)	*D* at 80% ($\times 10^{-13}$ cm^2/s)	*appar. grain size D (nm)*
0.5h	2.779	2.259	1.993	1.867	1.974	2.385	3.394	24.7
24h	2.041	1.846	1.747	1.635	1.703	2.000	2.733	31.8
48h	1.034	1.046	1.014	0.997	1.020	1.186	1.623	33.4

The initial apparent grain size of the lamellar nickel deposit is 14.3nm. The apparent sizes increased from 14.3nm to 24.7nm after heat treatment for 0.5h (about 10nm differences); and increased from 24.7nm to 31.8nm after further 23.5h heat treatment (about 7nm differences); and increased from 31.8nm to 33.4nm after further 24h heat treatment (about 1.5nm differences). The larger the differences of the apparent grain sizes the higher the rate of grain growth, resulting to a higher extent of grain boundaries migrations and a higher effective volume diffusion arising from grain boundary transport. It was observed that the interdiffusion coefficients were the highest for annealing time of 0.5h, as diffusion by grain boundaries migrations due to grain growth was the highest during that period. This phenomenon has also been observed by Kaja [1], who called it Diffusion Induced Grain Boundary Migration (DIGM). Moreover, the higher interdiffusion coefficient determined after 0.5h heat treatment is also due to having comparatively smaller grain size 24.7nm (higher amount of grain boundary diffusion). Interdiffusion coefficients with heat treatment time for 24h were slightly smaller than those determined at 0.5h heat treatment as it had lesser grain boundary migrations and having comparatively larger grain size 31.8nm. Obviously, the interdiffusion coefficients determined after 48h heat treatment had shown noticeable decrease. Because the grain sizes had reached a steady value (Fig. 4.1.8), diffusion enhanced by grain boundaries migration had also reached a steady state. However, interdiffusion coefficients determined for all heat treatment time had the same order of magnitude, which suggests that volume diffusion is the controlling migration mechanism.

It is interesting to note that the interdiffusion coefficients of the Cu/lamellar Ni couple at 250°C is higher than those at 300°C. This can be attributed to the

recrystallization kinetics. Grain growth rate or recrystallization at 300°C takes place in a relatively short period of time as compared to the total heat treatment time. Grain boundary diffusion dominates at temperatures below 300°C. Grain boundaries have been greatly reduced after the comparatively long heat treatment time for the Cu/lamellar Ni couple at 300°C. For the 250°C heat treatment, it has taken much longer time for recrystallization, thus giving a faster rate of diffusion via grain boundaries and resulting to a higher overall diffusion rate. In general, recrystallization and grain growth process take place over a shorter period of time at higher temperatures. At higher temperatures, volume diffusion dominates because of having higher internal volume to boundary-defect volume ratio. For low temperature annealing, grain growth process is much slower, thus having a higher diffusivity via grain boundary diffusion.

4.1.2 Copper/Nickel (columnar) System

4.1.2.1 Current Efficiency

The nickel plating solution we have used has a good current efficiency in general. The current efficiency increases from 95% at 1.8 A/dm^2 to above 99% at 11 A/dm^2 at 50°C and pH 3.3. Cathode efficiency increases with current density for the Watts nickel bath. The result is presented in Fig. 4.1.26.

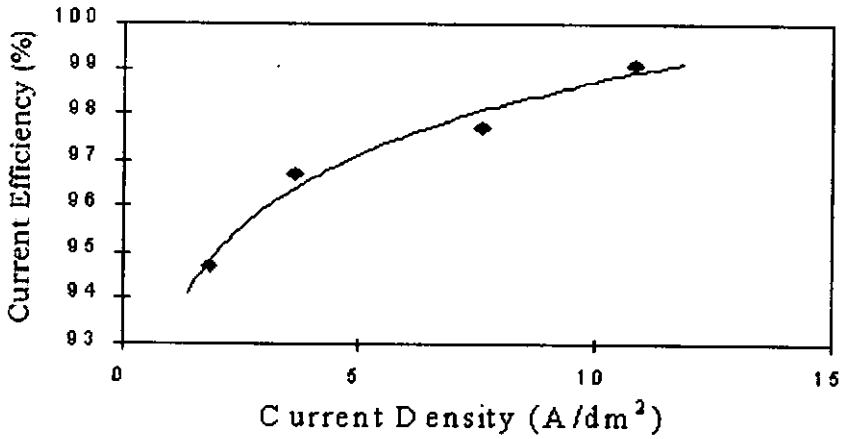

Fig. 4.1.26 Current efficiency of Watts nickel plating bath with increasing current density at 50°C and pH 3.3.

The high current efficiency of the nickel plating bath reduces the cost for its extensive use in the electroplating industry.

4.1.2.2 Microstructural Observations

Metallographic studies were conducted on both the as-deposited and heat treated samples to determine if there were any structural changes of the nickel electrodeposits. Fig. 4.1.27 reveals that structure of the as-deposited nickel coating is

basically columnar. The structure has changed via recrystallization and grain growth with the increasing annealing temperatures. Figures 4.1.28 and 4.1.29 show that the deposit structure has coarsened after heat treatment at temperatures of 700°C and 800°C respectively. The nickel deposit surface is shown in Fig. 4.1.30, in which the surface smoothness is poorer than that of the lamellar nickel deposit plated in a bath containing 2-butyne-1,4-diol.

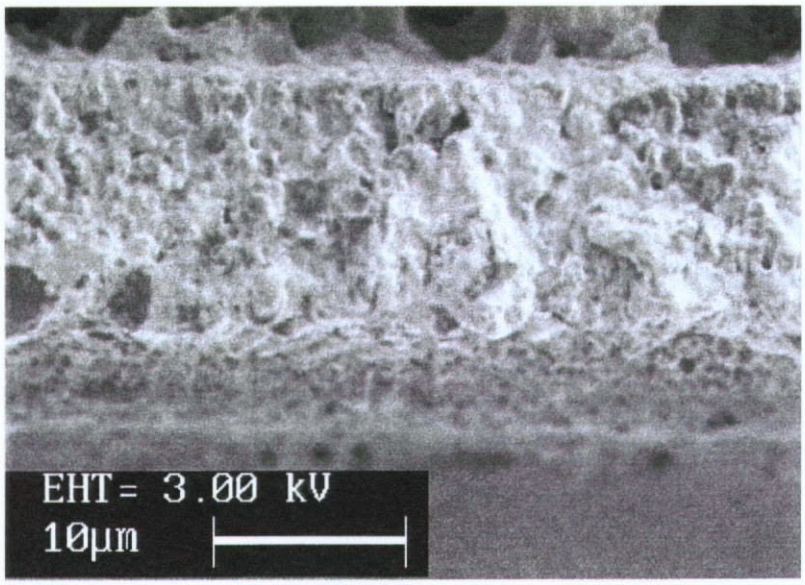

Fig. 4.1.27(a) SEM reveals the columnar structure of a Watts nickel coating electroplated at 5.1A/dm^2.

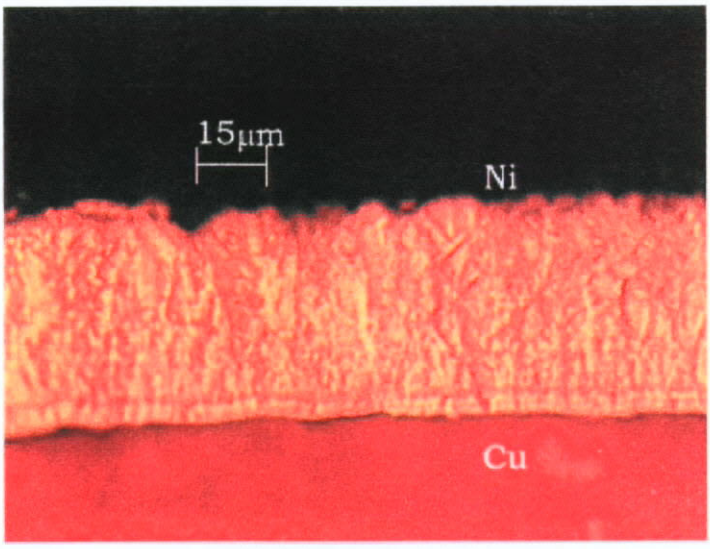

Fig. 4.1.27(b) Optical micrograph shows the columnar structure of a Watts nickel coating electroplated at 5.1A/dm^2.

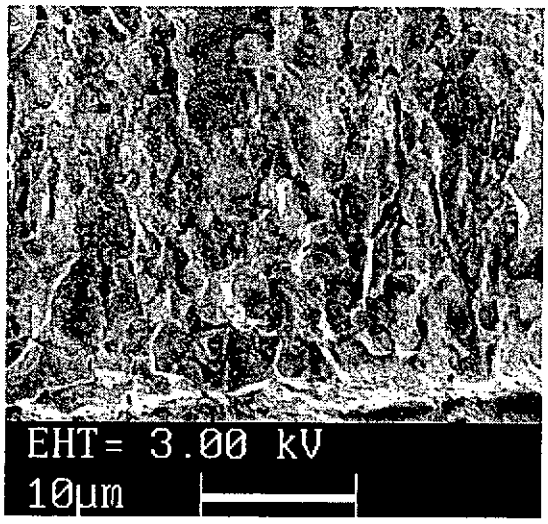

Fig. 4.1.28 SEM shows the coarsened columnar structure of a Watts nickel electrodeposit after heat treatment at 700°C for 1 h.

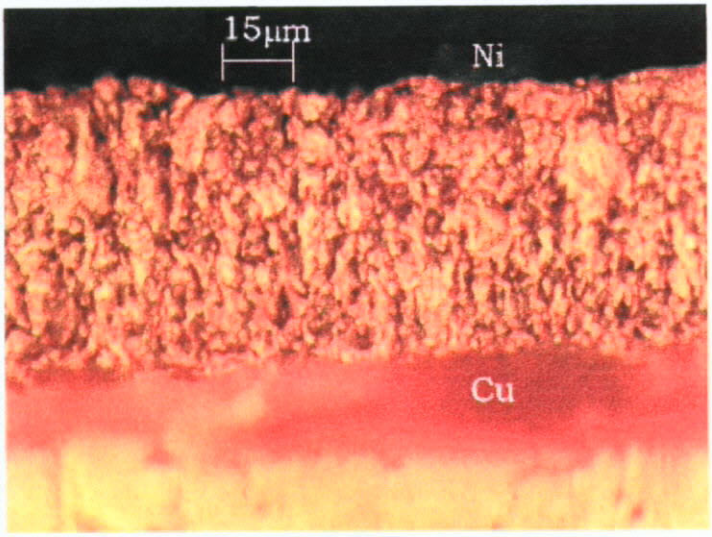

Fig. 4.1.29(a) Optical micrograph shows the coarsened columnar structure of a Watts nickel electrodeposit after heat treatment at 800°C for 1 h.

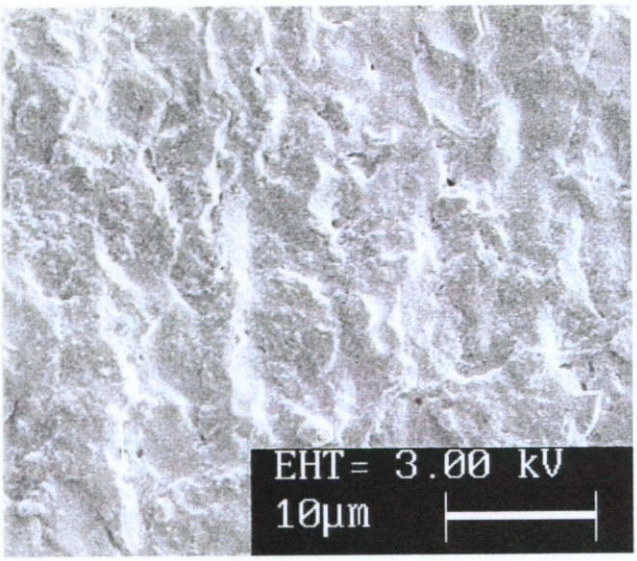

Fig. 4.1.29(b) SEM shows the coarsened columnar structure of a Watts nickel electrodeposit after heat treatment at 800°C for 1 h.

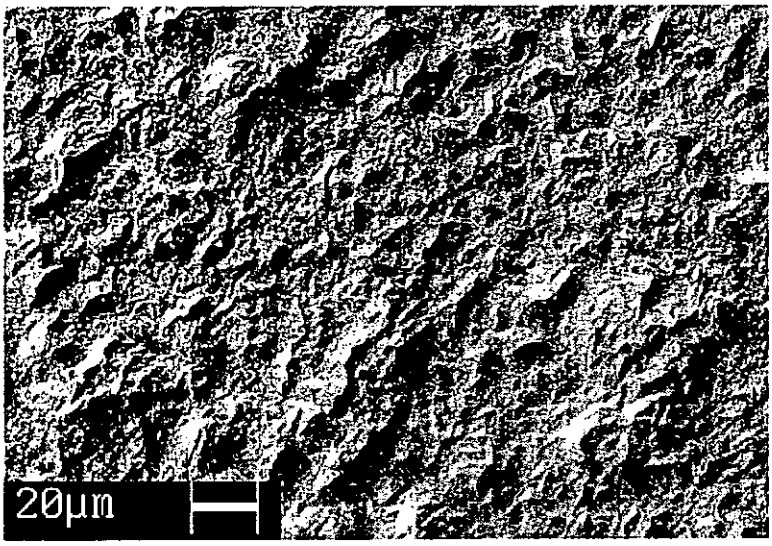

Fig. 4.1.30 SEM shows the surface of the as-deposited Watts nickel coating.

4.1.2.3 X-ray Diffraction Study

XRD spectra for Watts nickel coatings plated with different current densities were recorded. Fig. 4.1.31 shows the Ni (111) peaks of the Watts nickel electrodeposit plated at 3.6 and 18.2 A/dm^2 respectively. Apparent grain size were also determined and shown in Table 4.1.5.

Table 4.1.5. Apparent grain size *D* for Watts nickel coatings electrodeposited at different current density.

Current Density (A/dm^2)	Peak Width (degree)	*D* (nm)
0.9	0.267	35.7
1.8	0.400	23.9
3.6	0.417	22.9
7.6	0.467	20.4
11.4	0.433	22.0
18.2	0.433	22.0

There are little changes of grain sizes when the nickel coatings were plated with the current density ranging from 1.8-7.6 A/dm^2. No general relationship of current density and grain size could be concluded from our observation; with the exception that when the deposits was plated at a lower current density of 0.9 A/dm^2, the as-plated deposit grain size is more than fifty percent larger than 20 nm. Moreover, the grain size determined (around 20 nm) for our Watts nickel electrodeposits plated at current density ranging from 1.8-18.2 A/dm^2 have the similar values of that of the nickel film of the Ni-Cu multilayer films deposited by electron gun evaporation in high vacuum (10^{-8}-10^{-7}) on glass substrates reported by R. Venos *et al* [16]. The average grain size for their nickel films were determined by TEM.

On the whole, the grain sizes of the Watts nickel electrodeposits are not so dependent to the plating current density ranging from 1.8-18.2 A/dm^2.

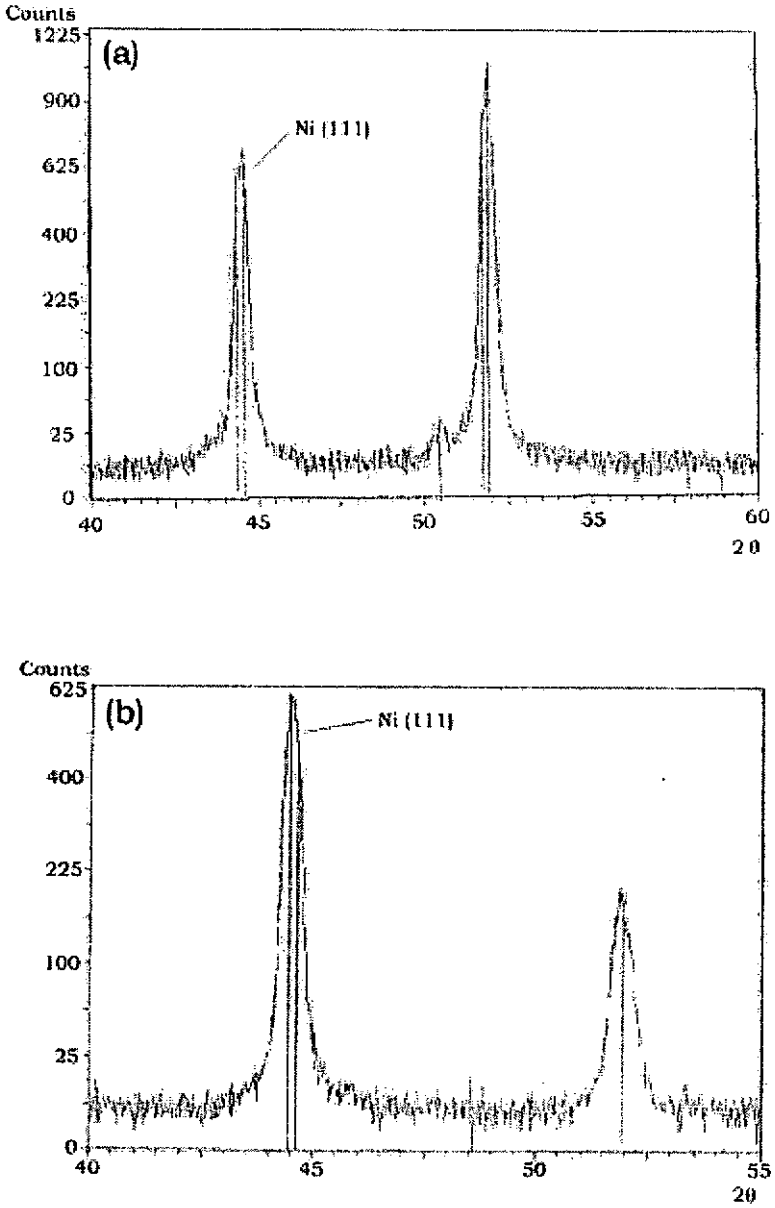

Fig. 4.1.31 XRD spectra show the Ni (111) peaks of the Watts nickel electrodeposits plated at (a) 3.6 A/dm^2 (b) 18.2 A/dm^2

4.1.2.4 Diffusivity Values of Cu/columnar Ni couples and Comparison with Cu/lamellar Ni couples

Fig. 4.1.32 shows the EDS concentration-distance profiles at the diffusion zones of both the Cu/lamellar Ni and Cu/columnar Ni couples after heat treatment at 250°C for 107 days (2568 h). Concentration-distance profiles were monitored by using discrete scan method with step of 0.5μm. For the Cu/columnar Ni couple, both Ni and Cu have not interdiffused significantly after 107 days heat treatment as indicated by the sharp changes in metal concentrations at the Cu/Ni interface (Fig. 4.1.32(a)). However, for the Cu/lamellar Ni couple after heat treatment under identical conditions, both Ni and Cu have notably interdiffused as shown with their far less sharp concentration changes at the Cu/Ni interface (Fig. 4.1.32(b)). The smaller initial grain size of the lamellar Ni results to a higher extent of grain boundary diffusion, which contributes a higher rate of the overall diffusion.

Fig. 4.1.33 shows the concentration-distance profiles of the Cu/columnar Ni and Cu/lamellar Ni couples after heat treatment at 900°C for 10 min. At 900°C Ni and Cu interdiffused so rapidly within the time interval of 10 min heat treatment that both Cu/lamellar Ni and Cu/columnar Ni couples bear similar behaviour. The different extent of interdiffusion for the Cu/lamellar Ni and Cu/columnar Ni couples at low temperature (250°C) depicts the mechanisms for re-crystallization and diffusion for lamellar Ni are different to that of columnar Ni under heat treatment. In turns, different crystalline structure affects the overall transport rate.

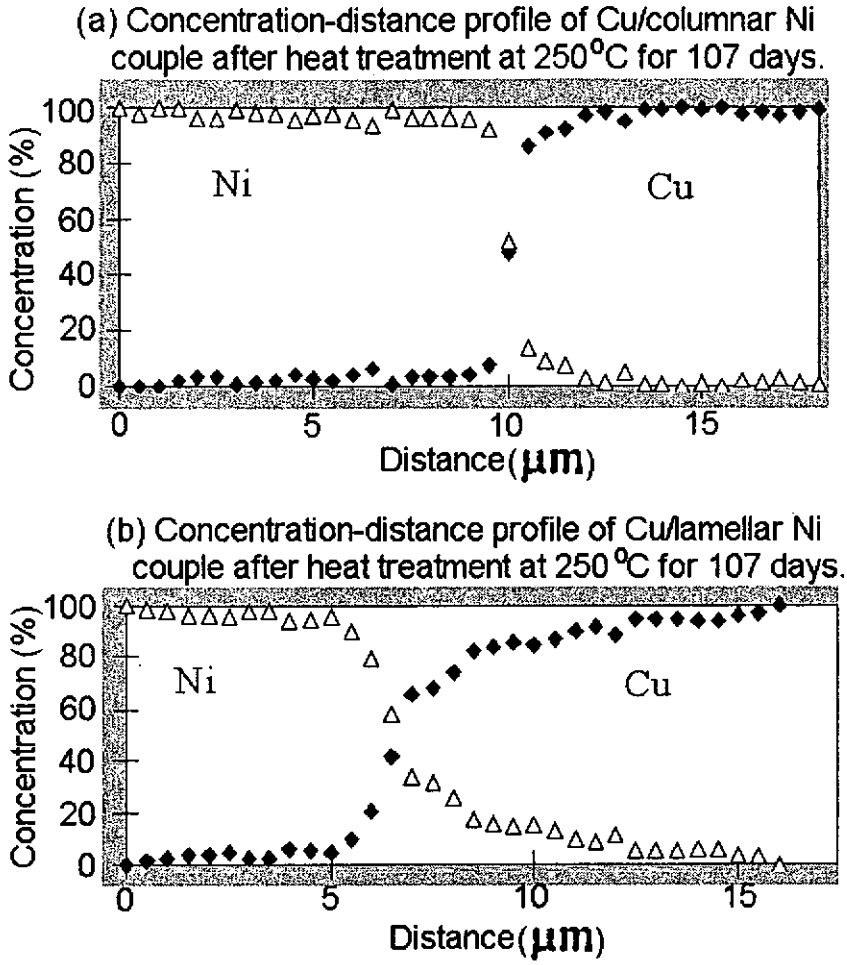

Fig. 4.1.32 Concentration-distance profiles of (a) Cu/columnar Ni (b) Cu/lamellar Ni couples after heat treatment at 250°C for 107 days

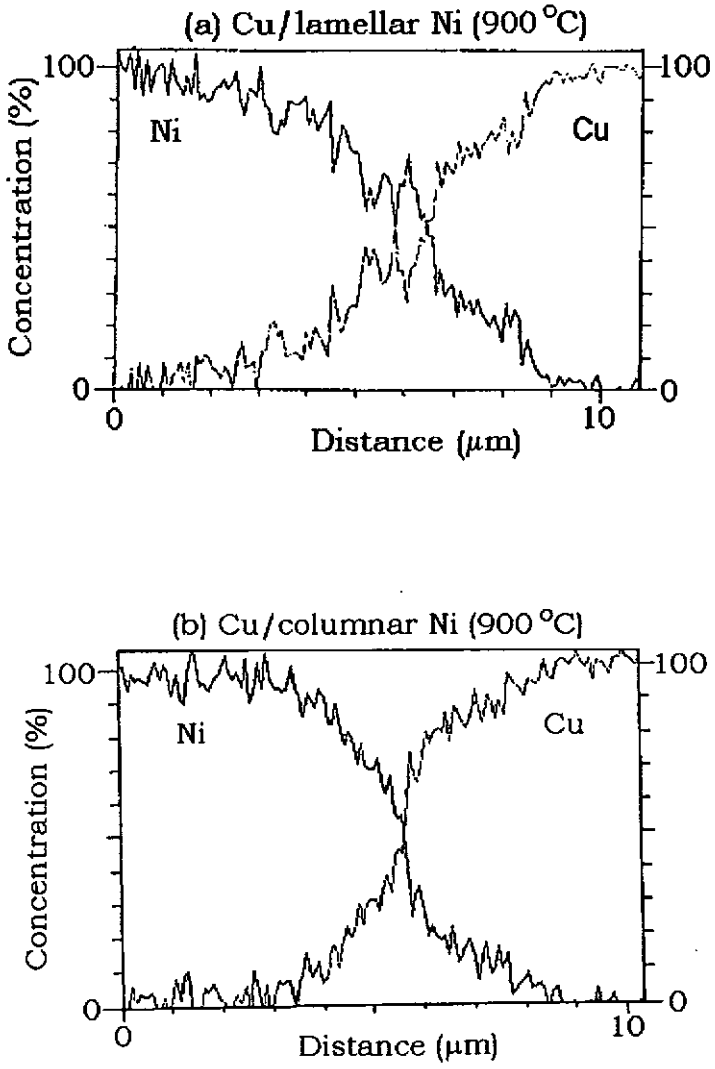

Fig. 4.1.33 Concentration-distance profiles of (a) Cu/lamellar Ni (b) Cu/columnar Ni couples after heat treatment at 900°C for 10 min.

Interdiffusion coefficients at different heat treatment temperatures and copper concentrations of the Cu/columnar Ni couples are shown in Table 4.1.6.

Table 4.1.6. Chemical interdiffusion coefficients of copper/columnar nickel couples at different temperatures and copper concentrations calculated by Boltzman-Matano Method.

Anneal. Temp. (°C)	Anneal. Time (h)	D at 20% Cu (cm^2/s)	D at 30% Cu (cm^2/s)	D at 40% Cu (cm^2/s)	D at 50% Cu (cm^2/s)	Sample Ref.
250	2568	2.370×10^{-16}	2.281×10^{-16}	2.297×10^{-16}	2.402×10^{-16}	ni-64-18
300	96	negligible	inter-	diffusion		ni-64-14
300	284	negligible	inter-	diffusion		ni-64-15
350	48, 72	negligible	inter-	diffusion		ni-64-17
350	96	9.935×10^{-15}	8.890×10^{-15}	8.624×10^{-15}	8.865×10^{-15}	ni-64-9
400	72	8.636×10^{-15}	8.261×10^{-15}	8.455×10^{-15}	9.022×10^{-15}	ni-64-13
450	48	6.191×10^{-15}	6.067×10^{-15}	6.652×10^{-15}	7.666×10^{-15}	ni-64-16
450	48	7.144×10^{-15}	6.910×10^{-15}	7.189×10^{-15}	7.879×10^{-15}	ni-64-4
500	24	8.054×10^{-14}	7.012×10^{-14}	6.294×10^{-14}	5.799×10^{-14}	ni-64-10
600	13.22	2.131×10^{-13}	1.571×10^{-13}	1.244×10^{-13}	1.102×10^{-13}	ni-64-11
650	6	4.437×10^{-13}	2.712×10^{-13}	2.019×10^{-13}	1.754×10^{-13}	ni-64-6
700	5	8.234×10^{-13}	5.336×10^{-13}	4.377×10^{-13}	4.278×10^{-13}	ni-64-12
700	6	1.358×10^{-12}	1.524×10^{-12}	1.280×10^{-12}	1.253×10^{-12}	ni-64-1
750	3	4.549×10^{-12}	1.613×10^{-12}	1.061×10^{-12}	9.223×10^{-13}	ni-64-2
800	0.75	7.659×10^{-12}	5.930×10^{-12}	4.710×10^{-12}	3.981×10^{-12}	ni-64-3
850	0.28	1.025×10^{-11}	8.884×10^{-12}	8.144×10^{-12}	7.698×10^{-12}	ni-64-7
900	0.183	1.663×10^{-11}	1.380×10^{-11}	1.256×10^{-11}	1.206×10^{-11}	ni-64-8

Table 4.1.6. (Continue) Chemical interdiffusion coefficients of copper/columnar nickel couples at different temperatures and copper concentrations calculated by Boltzman-Matano Method.

Annealing Temp. (°C)	Anneal. Time (h)	D at 60% Cu (cm^2/s)	D at 70% Cu (cm^2/s)	D at 80% Cu (cm^2/s)	Sample Ref.
250	2568	2.672×10^{-16}	3.451×10^{-16}	5.533×10^{-16}	ni-64-18
350	96	9.644×10^{-15}	1.263×10^{-14}	2.236×10^{-14}	ni-64-9
400	72	9.995×10^{-15}	1.311×10^{-14}	2.166×10^{-14}	ni-64-13
450	48	9.187×10^{-15}	1.242×10^{-14}	2.003×10^{-14}	ni-64-16
450	48	9.359×10^{-15}	1.305×10^{-14}	2.304×10^{-14}	ni-64-4
500	24	5.958×10^{-14}	7.010×10^{-14}	9.855×10^{-14}	ni-64-10
600	13.22	1.102×10^{-13}	1.233×10^{-13}	1.570×10^{-13}	ni-64-11
650	6	1.763×10^{-13}	2.020×10^{-13}	2.721×10^{-13}	ni-64-6
700	5	4.799×10^{-13}	6.245×10^{-13}	1.012×10^{-12}	ni-64-12
700	6	1.379×10^{-12}	1.691×10^{-12}	2.388×10^{-12}	ni-64-1
750	3	9.680×10^{-13}	1.183×10^{-12}	1.716×10^{-12}	ni-64-2
800	0.75	3.900×10^{-12}	4.521×10^{-12}	6.653×10^{-12}	ni-64-3
850	0.28	8.079×10^{-12}	9.708×10^{-12}	1.389×10^{-11}	ni-64-7
900	0.183	1.291×10^{-11}	1.629×10^{-11}	2.621×10^{-11}	ni-64-8

Figures 4.1.34 and 4.1.35 give the $\mathrm{Log}_{10}\tilde{D}$ vs. $1/T$ for 40 and 80% Cu of the Cu/columnar Ni and Cu/lamellar Ni couples respectively. For all copper concentrations, the shapes of the curves bear similar behaviour. The interdiffusion rates for both Cu/columnar Ni and Cu/lamellar Ni show a sharp change in the slope at 700 to 750°C. This indicates that a grain boundary diffusion mechanism predominates for temperatures below 700°C. The activation energy of diffusion for temperatures above 700°C is roughly double to that for temperatures below 700°C. The transition range (700 to 750°C) is similar to the findings of Kaja [1] for the diffusion of Cu in sulfamate columnar Ni electrodeposit.

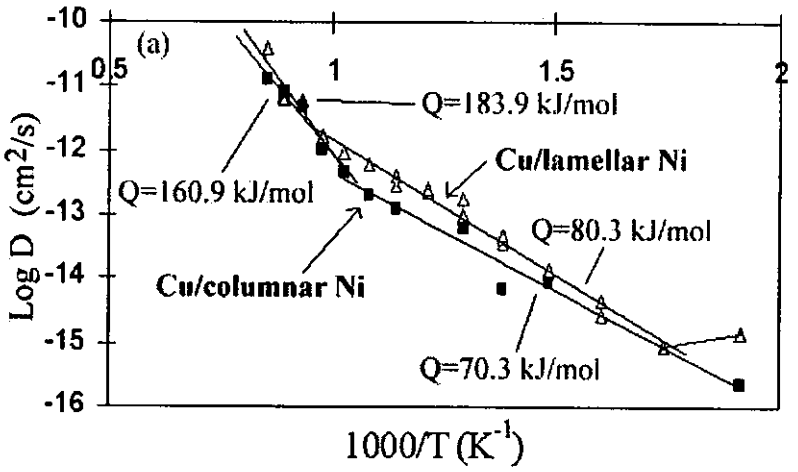

Fig. 4.1.34 Arrhenius plots at 40% Cu of Cu/lamellar Ni and Cu/columnar Ni couples

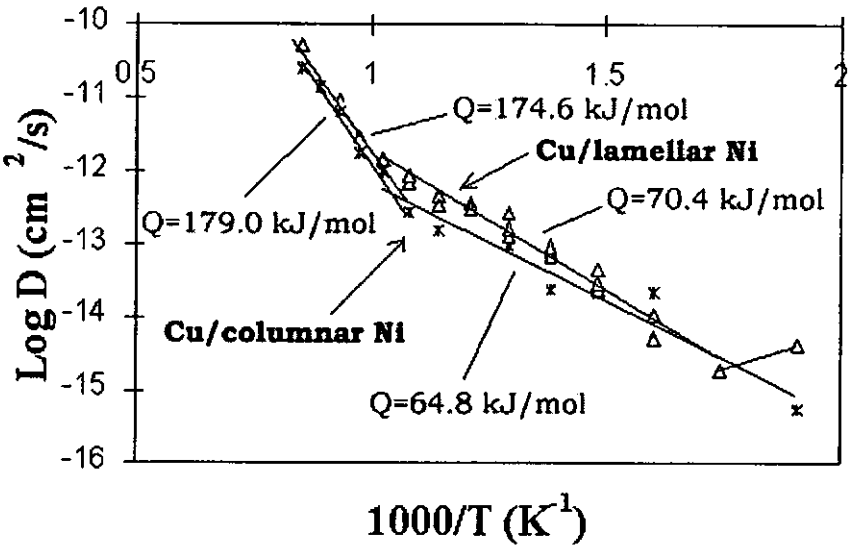

Fig. 4.1.35 Arrhenius plots at 80% Cu of Cu/lamellar Ni and Cu/columnar Ni couples

The interdiffusion coefficients for the Cu/columnar Ni couples have the same order of magnitude to those of Cu/lamellar Ni couples. Both Cu/lamellar Ni and Cu/columnar Ni have similar interdiffusion coefficients for temperatures above 300°C, indicating that lattice diffusion is the dominating diffusion mechansim. When the temperature was lowered to 250°C for 107 days, interdiffusion coefficients for the Cu/lamellar Ni couples had an order of magnitude of 10^{-15} cm^2/s while interdiffusion coefficients for the Cu/columnar Ni couples had an order of magnitude of 10^{-16} cm^2/s. The difference in interdiffusion coefficients for the Cu/lamellar Ni and Cu/columnar Ni couples at lower temperatures (250°C, say) is due to their different initial structure and grain sizes.

The total diffusional flux of a metal through polycrystalline Ni is the sum of the grain boundary diffusion and lattice diffusion processes. For the Cu/lamellar Ni couples, the Ni coating electroplated at 3.6 A/dm^2 has initial grain size of 14.3nm; whereas the Ni coating electroplated at the same current density has initial grain size of 23.0nm for the Cu/columnar Ni couples. The smaller initial grain size for the Cu/lamellar couple results to a higher extent of grain boundary diffusion, which gives higher interdiffusion coefficients. As the temperature increases, the lamellar structure begins to diminish (Figures 4.1.3 and 4.1.4), and grain size of the Ni coating increases; thus, the extent of grain boundary diffusion decreases and results in numerically closer interdiffusion coefficients with those of the Cu/columnar Ni couples.

4.2 Copper/Palladium System

4.2.1 Microstructural Observations

Fig. 4.2.1 shows the optical micrograph of the columnar structure palladium coating electrodeposited at 0.5A/dm^2 at 25°C. The surface morphology is revealed by SEM in Fig. 4.2.2.

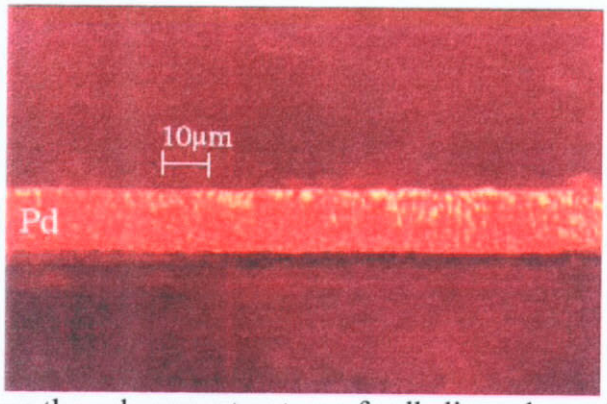

Fig. 4.2.1 shows the columnar structure of palladium electrodeposit.

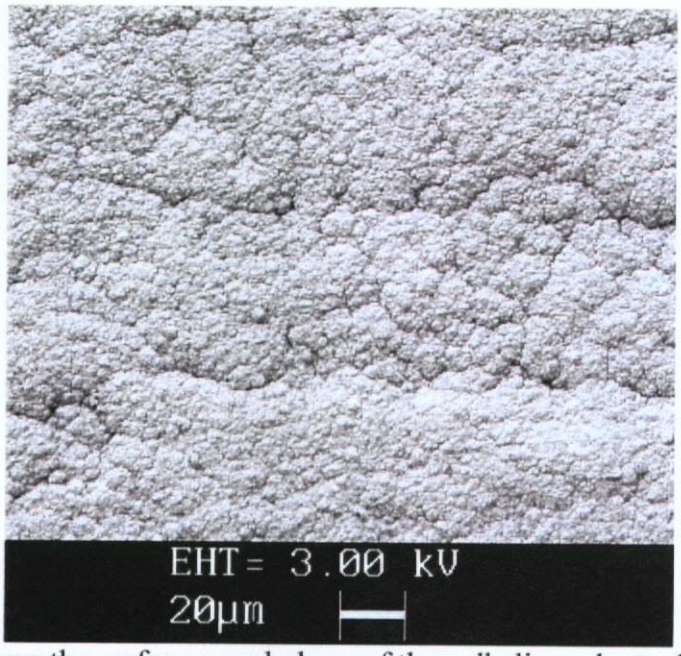

Fig. 4.2.2 shows the surface morphology of the palladium electrodeposit.

4.2.2 Diffusion Experiment

In Fig. 4.2.3, Cu and Pd interdiffused at 300°C for 90 h. Similar extent of interdiffusion of the Cu/Pd couple was observed after heat treatment at 450°C for 1h (Fig. 4.2.4). The Cu/Pd couples have higher interdiffusion coefficients than those of the Cu/Ni (lamellar/columnar) systems. Moreover, it is interesting to note that interdiffusion coefficients of the Cu/Pd system in the temperature range 400 to 700°C are higher than those of the Cu/Ni (lamellar/columnar) systems by about one order of magnitude. Diffusion experiment results ranging from 250°C to 850°C and the corresponding chemical interdiffusion coefficients of the Cu/Pd couples are listed in Table 4.2.1.

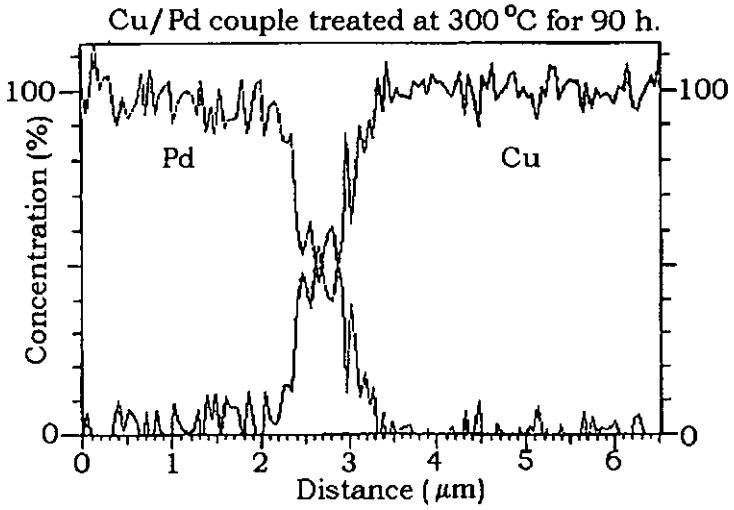

Fig. 4.2.3 Concentration-distance profile of Cu/Pd couple after heat treatment at 300°C for 90h.

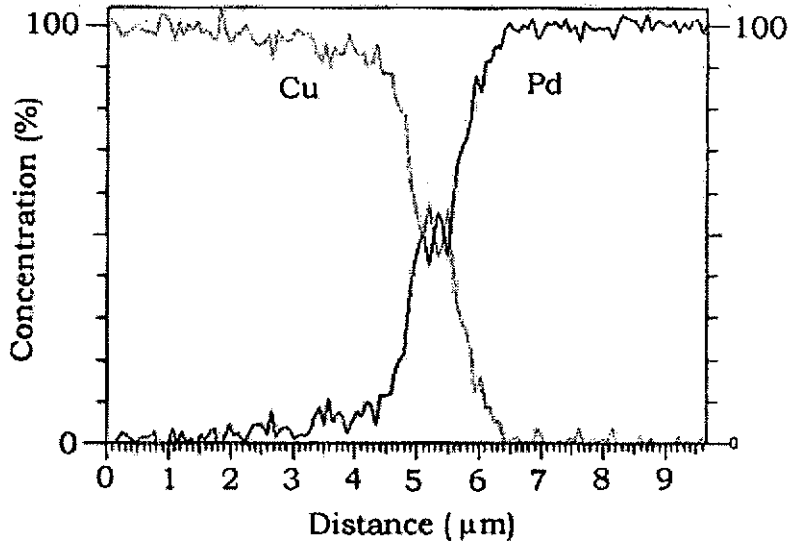

Fig. 4.2.4 Concentration-distance profile of Cu/Pd couple after heat treatment at 450°C for 1h.

Table 4.2.1. Chemical interdiffusion coefficients of copper / palladium (12μm) couple

Sample Ref.	Anneal. Temp. (°C)	Anneal. Time (h)	D at 20% Copper (cm^2/s)	D at 30% Copper (cm^2/s)	D at 40% Copper (cm^2/s)	Remarks
Cu-Pd-1	700	4	–	–	–	40 wt% of Cu was observed on the surface
Cu-Pd-2	750	2	–	–	–	40 wt% of Cu was observed on the surface
Cu-Pd-3	800	0.5	–	–	–	25 wt% of Cu was observed on the surface
Cu-Pd-4	850	0.25	–	–	–	30 wt% of Cu was observed on the surface
Pd2-10	300	15	–	–	–	negligible interdiffusion
Pd2-8	350	5	–	–	–	very little interdiffusion
Pd2-17	250	980	2.650×10^{-15}	2.519×10^{-15}	2.585×10^{-15}	
Pd2-11	300	87.4	6.862×10^{-15}	5.215×10^{-15}	4.368×10^{-15}	
Pd2-16	300	91.5	5.359×10^{-15}	5.132×10^{-15}	5.002×10^{-15}	
Pd2-15	300	91.5	2.365×10^{-15}	2.711×10^{-15}	3.563×10^{-15}	
Pd2-12	300	12				little interdiffusion
Pd2-14	350	71	3.576×10^{-14}	4.115×10^{-14}	4.689×10^{-14}	
Pd2-2	400	3	1.718×10^{-13}	1.750×10^{-13}	1.844×10^{-13}	
Pd2-6	450	1	1.097×10^{-12}	9.923×10^{-13}	9.182×10^{-13}	
Pd2-7	450	1	1.332×10^{-12}	1.198×10^{-12}	1.094×10^{-12}	
Pd2-3	500	1	1.003×10^{-11}	1.319×10^{-11}	1.194×10^{-11}	
Pd2-4	550	0.25	8.719×10^{-12}	6.832×10^{-12}	8.532×10^{-12}	
Pd2-5	550	0.25	1.273×10^{-11}	1.023×10^{-11}	8.623×10^{-12}	
Pd2-1	700	0.5	3.085×10^{-11}	3.664×10^{-11}	5.178×10^{-11}	

Table 4.2.1. (Continue) Chemical interdiffusion coefficients of copper / palladium (12μm) couple

Sample Ref.	Anneal. Temp. (°C)	Anneal. Time. (h)	D at 50% Copper (cm^2/s)	D at 60% Copper (cm^2/s)	D at 70% Copper (cm^2/s)	D at 80% Copper (cm^2/s)
Pd2-17	250	980	2.761×10^{-15}	3.280×10^{-15}	4.415×10^{-15}	6.787×10^{-15}
Pd2-11	300	87.4	4.082×10^{-15}	4.333×10^{-15}	5.205×10^{-15}	7.314×10^{-15}
Pd2-16	300	91.5	4.914×10^{-15}	5.234×10^{-15}	6.270×10^{-15}	8.578×10^{-15}
Pd2-15	300	91.5	4.490×10^{-15}	4.588×10^{-15}	4.660×10^{-15}	5.511×10^{-15}
Pd2-14	350	71	5.195×10^{-14}	5.639×10^{-14}	5.934×10^{-14}	6.440×10^{-14}
Pd2-2	400	3	1.911×10^{-13}	2.082×10^{-13}	2.520×10^{-13}	3.470×10^{-13}
Pd2-6	450	1	8.708×10^{-13}	9.153×10^{-13}	1.060×10^{-12}	1.363×10^{-12}
Pd2-7	450	1	1.022×10^{-12}	1.055×10^{-12}	1.192×10^{-12}	1.472×10^{-12}
Pd2-3	500	1	7.926×10^{-12}	6.324×10^{-12}	5.975×10^{-12}	6.438×10^{-12}
Pd2-4	550	0.25	8.299×10^{-12}	8.920×10^{-12}	1.038×10^{-11}	1.311×10^{-11}
Pd2-5	550	0.25	7.643×10^{-12}	7.649×10^{-12}	8.477×10^{-12}	1.041×10^{-11}
Pd2-1	700	0.5	6.097×10^{-11}	4.656×10^{-11}	4.028×10^{-11}	4.129×10^{-11}

A family of curves of $\log_{10}\tilde{D}$ vs. $1/T$ for concentrations of 20, 50 and 80 % Cu are plotted in Fig. 4.2.5.

Unlike Cu/Ni couple, the Arrhenius plots of the Cu/Pd system show no transition region. The apparent activation energies for diffusion Q vary from 97.9 kJ/mol to 106.4 kJ/mol in the temperature range 250 to 700°C.

Some Cu/Pd samples were subjected to peel off when the annealing temperature was increased above 700°C. This may be attributed to the codeposition of atomic hydrogen at interstitial sites in the growing palladium lattice. Subsequent diffusion of the codeposited hydrogen through the palladium causes simultaneous volume expansions and contractions in adjacent areas of the lattice structure. Moreover, as copper atoms diffuse into the palladium layer, inhomogeneities in the Cu concentration, which cause local strains may further adversely affect the situation. The volume dismatch between the Cu and Pd layers resulting in undermining the adhesion power between two layers.

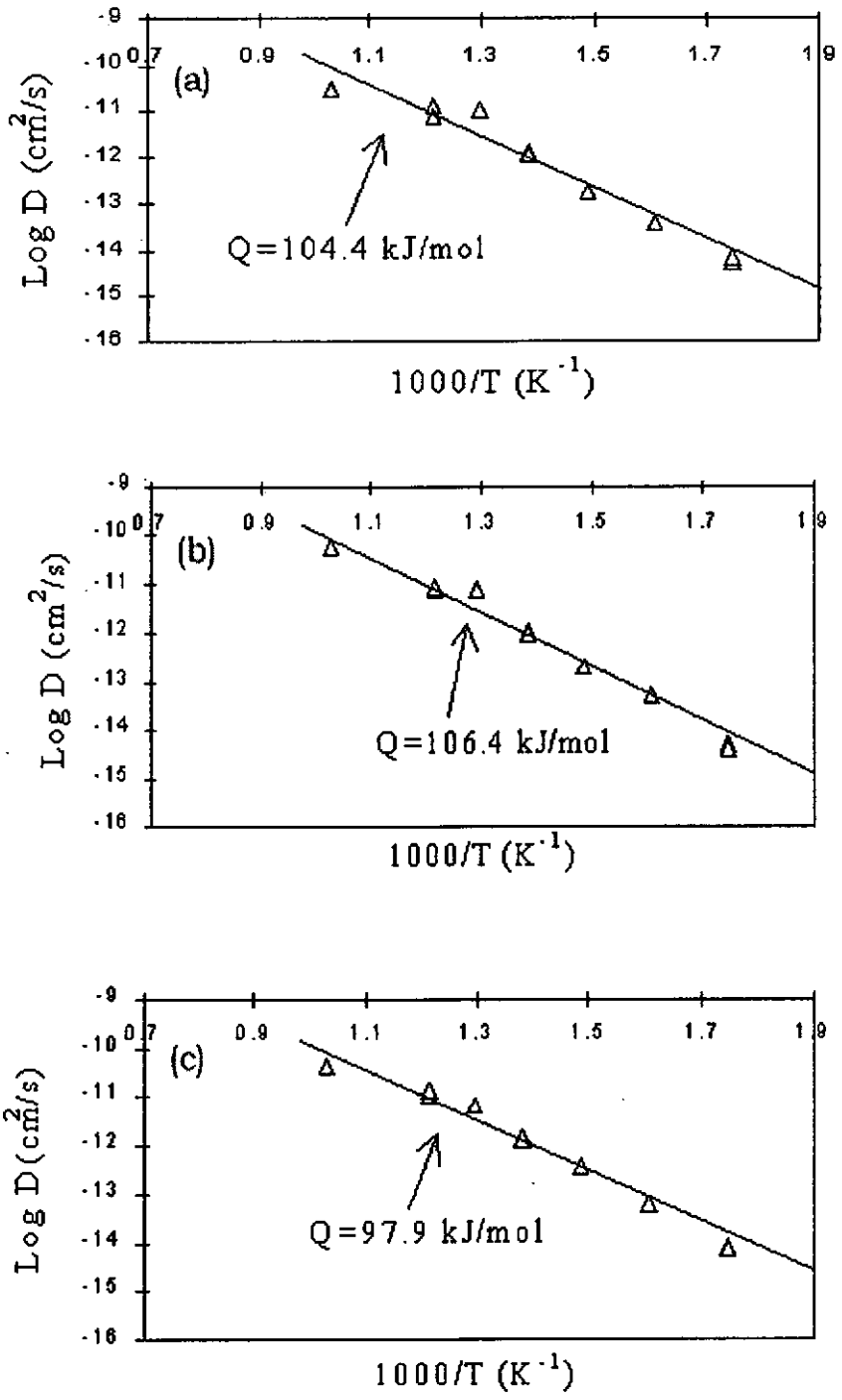

Fig. 4.2.5 Arrhenius plots of interdiffusion coefficients at (a) 20%, (b) 50%, (c) 80% copper for the Cu/Pd couple

For instance, $\tilde{D}$ of the Cu/Pd system at 500°C at 50% copper is 7.93×10^{-12} cm^2/s where $\tilde{D}$ of the Cu/lamellar Ni system at the same temperature is 8.37×10^{-14} cm^2/s. This observation seems to imply that palladium is not a suitable alternative for nickel as diffusion barrier. However, it is also noted that the interdiffusion coefficient $\tilde{D}$ of the Cu/Pd system at 250°C has been dropped substantially to 2.76×10^{-15} cm^2/s at 50% copper, which is close to the $\tilde{D}$ value of the Cu/lamellar Ni system at 250°C which is 1.56×10^{-15} cm^2/s. At lower temperatures, say 250°C the $\tilde{D}$ value of the Cu/Pd system are comparable to those of the Cu/lamellar Ni system. Palladium still can be used as an alternative to nickel as a diffusion barrier, as for most applications the working temperatures are normally below 300°C.

4.2.3 X-ray Diffraction Study

XRD spectra were recorded in the Bragg-Brentano geometry in the 2θ interval between 20° and 125°, where the most relevant diffraction peaks of the palladium deposit are present, as shown in Fig. 4.2.6 where the lattice parameters, the interplanar lattice spacing and the Bragg angles (2θ) were reported in Table 4.2.2. It is noted that some peaks come from the copper substrate

Table 4.2.2. Data obtained from the XRD analysis of the palladium electrodeposit

Crystalline phase	*Crystalline structure*	*Lattice parameter (nm)*	*Lattice Interplanar spacing (nm)*	*(hkl)*	*2θ (°)*
Pd	f.c.c.	a=0.3886	0.2244	(111)	40.15
		a=0.3894	0.1947	(200)	46.61
		a=0.3895	0.1377	(220)	68.04
		a=0.3890	0.1173	(311)	82.11
		a=0.3883	0.1121	(222)	86.79

Besides, apparent grain size of the as-deposited Pd plated at 0.5 A/dm^2 was also determined to be 12.5 nm by measuring the peak width of the Pd (111) diffraction peak.

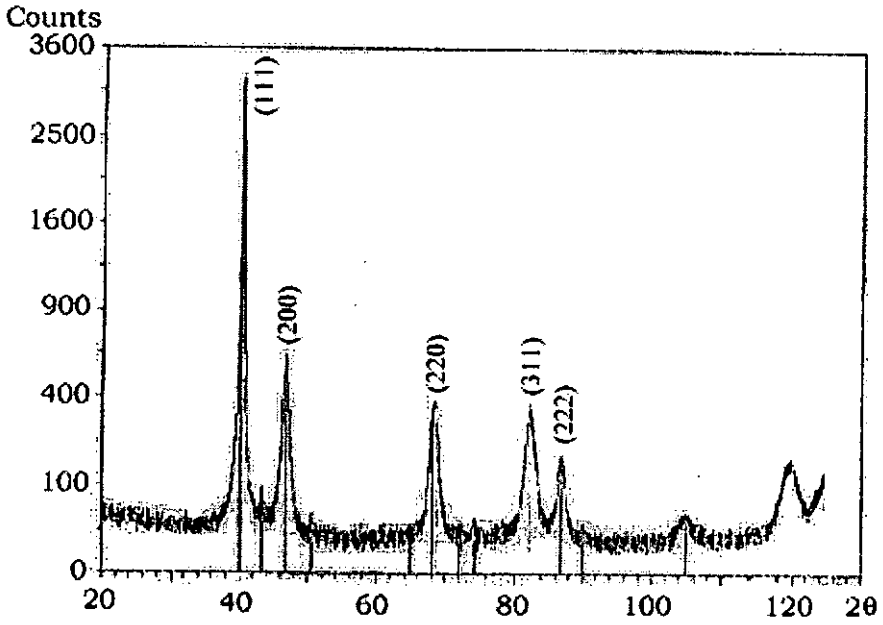

Fig. 4.2.6 XRD spectra of the Pd electrodeposit plated at 0.5A/dm^2

4.2.4 Estimation of Diffusion Coefficient D by X-ray Diffraction

Four Cu/Pd samples with average Pd thickness of 0.67μm after heat treatment at 400°C for 30 min to 60 min were taken for XRD examination. The apparent grain sizes of each sample after having annealed for 30 min to 60 min were determined (Table 4.2.3).

Interdiffusion coefficient of Cu/Pd at 400°C was determined by the following method proposed by Lau *et al.* [52]. The integrated intensity of Pd(111) peaks from the samples annealed at 400°C for 30 min to 120 min were plotted against the square root of the annealing time (Fig. 4.2.7). Since the integrated intensities of Pd (111)

peaks were found to decrease with the square root of annealing time, the reduction of the effective Pd film thickness is therefore expected to follow a diffusion mechanism. Extrapolating the linear portion of the measured integrated intensities in Fig. 4.2.7 to zero, a critical time (t_c) is obtained which corresponds to the time when there should not be any more homogeneous Pd remaining on the copper substrate. Thus, at the critical time the effective thickness of Pd should have decreased to zero.

Using the simple diffusion equation $x^2=2 \cdot D\ t$, the apparent diffusion coefficient (D) can be calculated assuming it is independent of the composition of the alloy film; where x the original Pd thickness (0.67μm) is taken as the diffusion distance and critical time (t_c) is substituted for t. The calculated coefficient which can be considered only as convenient approximation for comparison with the results obtained by EDS detector in which interdiffusion coefficients were calculated by Matano-Boltzman method. The calculated apparent diffusion coefficient (D) at 400°C is $\underline{2.84\times10^{-13}\ cm^2/s}$ which has the same order of magnitude to the interdiffusion coefficients calculated at 400°C by Matano-Boltzman method (see Table 4.2.1).

Table 4.2.3. Apparent grain size of the palladium electrodeposit (0.67μm) after heat treatment at 400°C.

Annealing Time (min)	*2θ*	Peak Width (degree)	*D* (nm)
0	40.30°	0.591	15.9
30	40.06°	0.546	17.2
60	40.06°	0.500	18.8

The interdiffusion coefficient estimated by this X-ray diffraction method has provided a fast mean for supporting our EDS result. However, the present method cannot determine the concentration dependent interdiffusion coefficients and cannot give the concentration-distance profile at the diffusion zone of the Cu/Pd couple. Only

a simple diffusion equation $x^2=2 \cdot D\ t$ was used for a rough estimation of D at 400°C. To determine the concentration-distance profile of the thin-film diffusion couple by X-ray diffraction technique, some more elegant methods should be employed [53-55]. X-ray diffracted peaks from both the bottom and top films should be strong enough, in which those peaks width and intensity change notably with heat treatment time. However, those methods are limited to the interdiffusion studies of thin-films. For the interdiffusion studies of electrodeposits, the electrodeposited coatings are not thin enough so that we cannot obtain the X-ray diffracted peaks from both the substrate and the electrodeposited coating with notable change of peaks width and intensity simultaneously after heat treatment. Thus, in our present studies, EDS method was used instead for the determination of concentration-distance profiles of the diffusion electrodeposited couples.

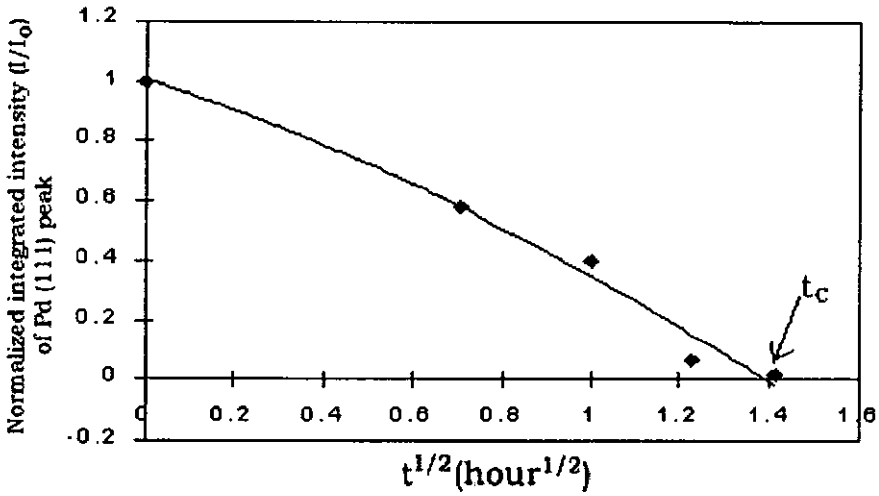

Fig. 4.2.7 Integrated intensity of Pd (111) peak vs. square root of heat treatment time

4.3 Copper/Palladium-Iron System

4.3.1 Microstructural Observations

Surface morphology of the Pd-25wt%Fe electrodeposit plated at 0.5A/dm^2 is revealed by SEM in Fig. 4.3.1. Fig. 4.3.2 shows the cross-sectioned view of the Pd-25wt.%Fe coating. Micro-cracks can be observed from both figures.

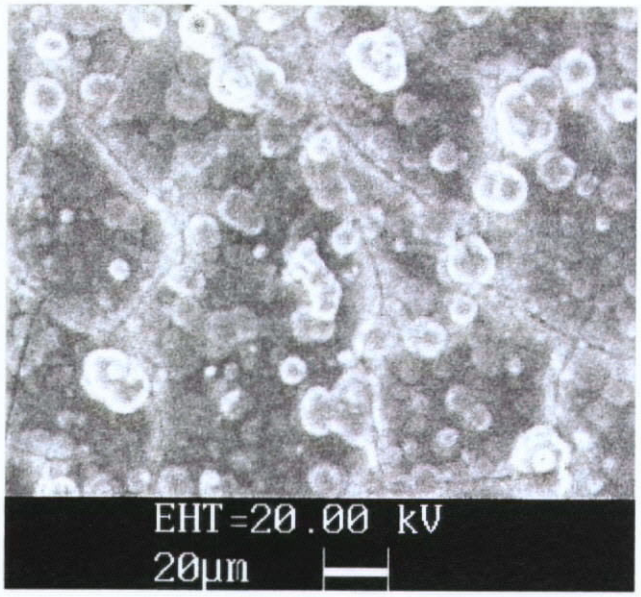

Fig. 4.3.1 SEM shows the surface morphology of Pd-25wt%Fe electrodeposit

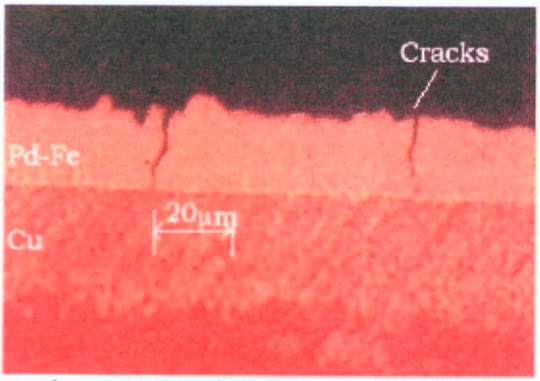

Fig. 4.3.2 shows the cross-sectional view of the Pd-Fe coating

4.3.2 Effect of Deposition Parameter

Fig. 4.3.3 shows the variation of alloy composition of Pd-Fe with increasing plating current density. It is noted that with other plating parameters being unchanged, the Pd content of the coating decreases with increasing current density.

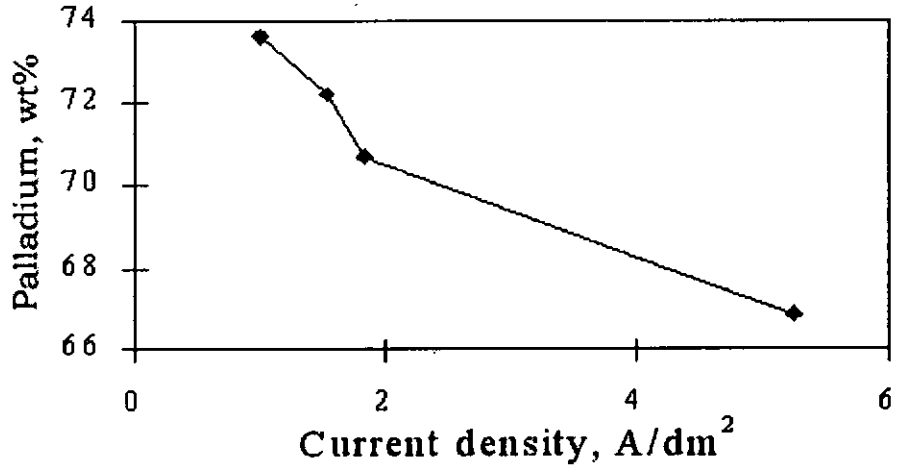

Fig. 4.3.3 Influence of plating current density on Pd-Fe composition.

A few Pd-Fe coatings with different composition were taken for AC impedance measurement. Results are presented in Chapter 5.

4.3.3 Diffusion Experiment

Diffusion Experiments were carried out on Cu/Pd-25wt%Fe couples. Concentration-distance profiles in the diffusion zones without cracks were obtained. Figures 4.3.4 and 4.3.5 give the concentration-diffusion profiles of Cu/Pd and Cu/Pd-Fe couples after heat treatment at 250°C for 980h and at 300°C for 90h respectively. Substantial interdiffusion of Cu is observed for the Cu/Pd-Fe couple after heat treatment at 500°C for 35 min, as shown in Fig. 4.3.6. It is noted that for the Cu/Pd-Fe couple, Cu is less penetrative into the Pd-Fe coating than that for the Cu/Pd couple

into the Pd phase at all investigated temperatures (250-500°C). Interdiffusion coefficients of the Cu/Pd-Fe couples at all Cu concentration are lower than those of the Cu/Pd couples at all investigated temperatures, as shown in Table 4.3.1.

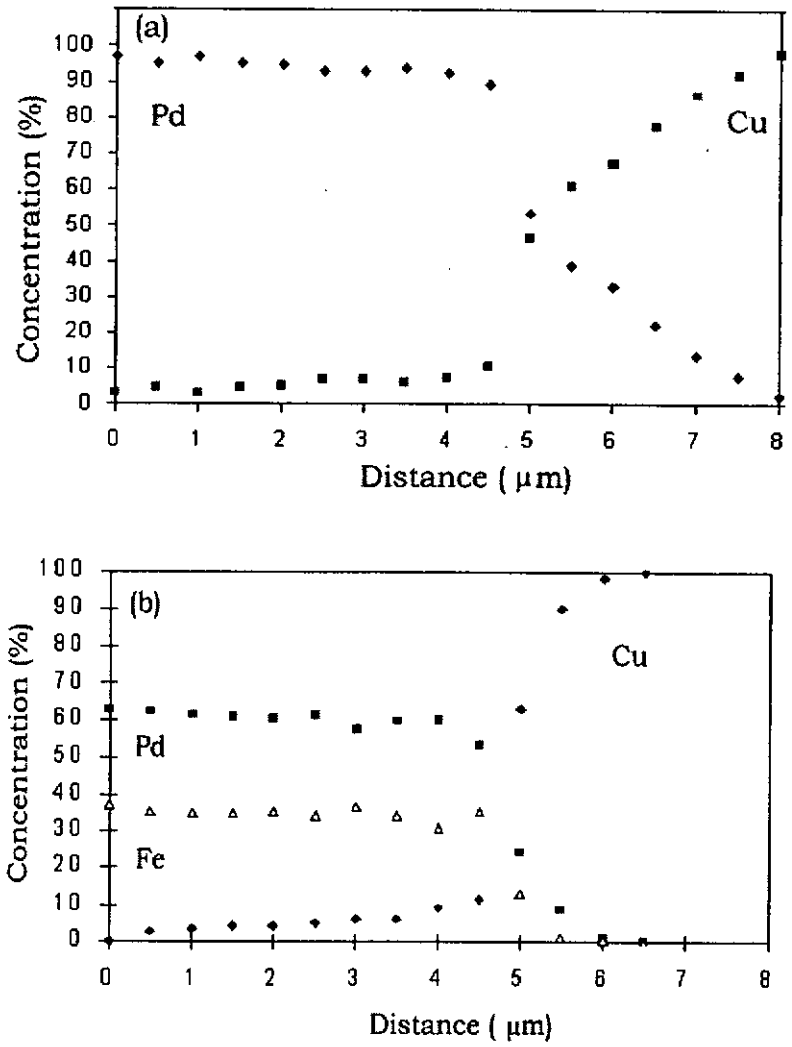

Fig. 4.3.4 Concentration-distance profiles of (a) Cu/Pd, (b) Cu/Pd-Fe couples after heat treatment at 250°C for 980h

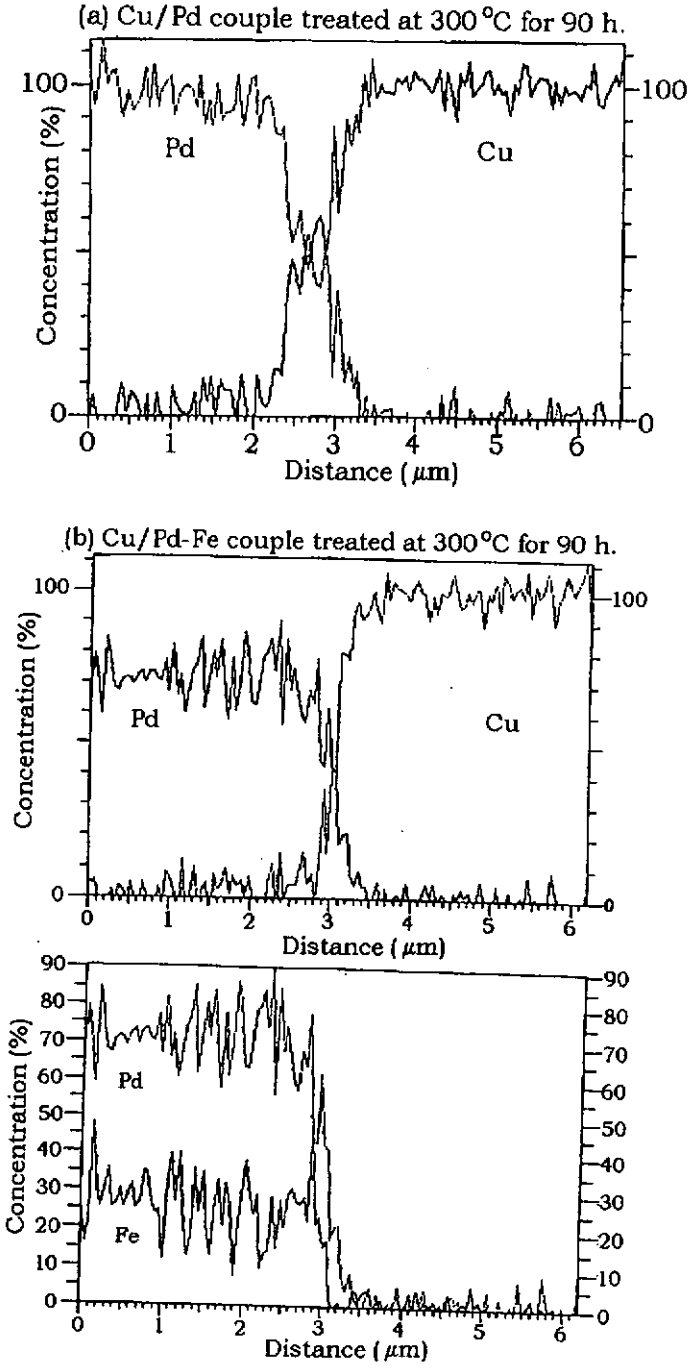

Fig. 4.3.5 Concentration-distance profiles of (a) Cu/Pd couple, (b) Cu/Pd-Fe couple after heat treatment at 300°C for 90h

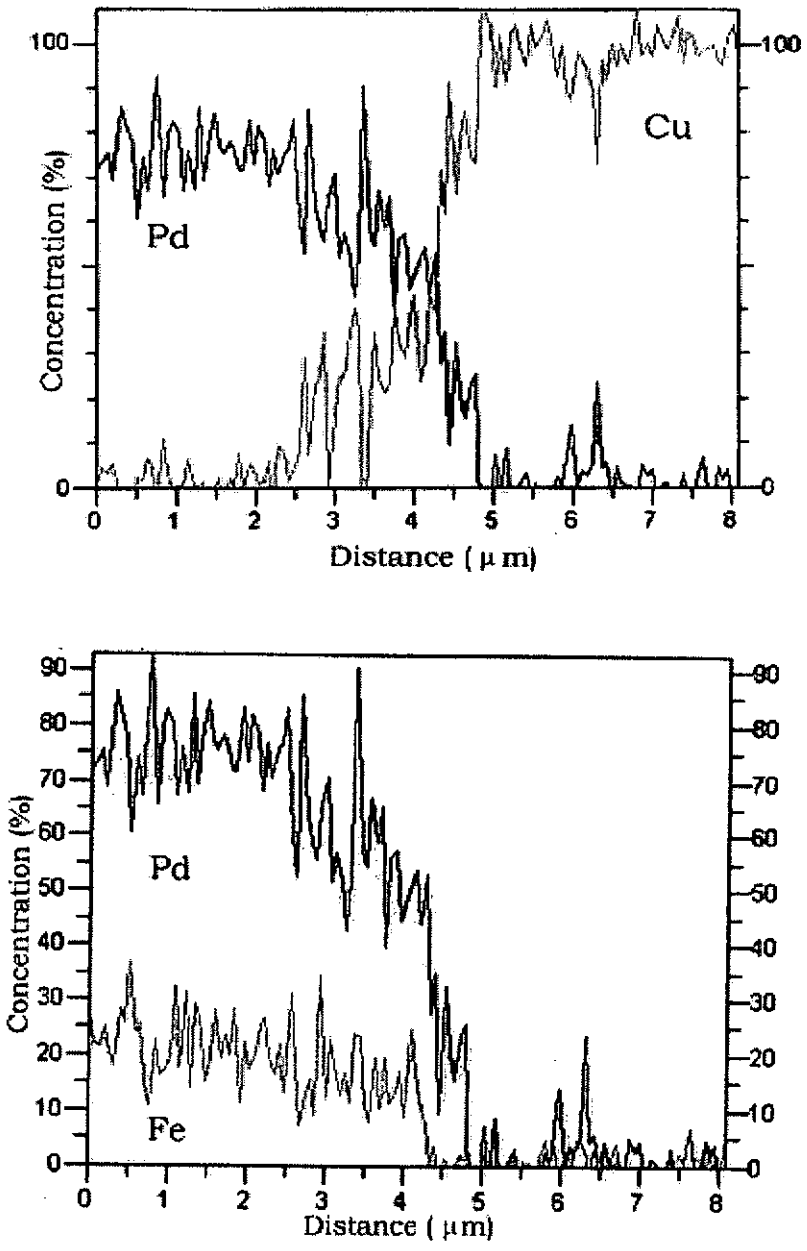

Fig. 4.3.6 Concentration-distance profiles of the Cu/Pd-Fe couple after heat treatment at 500°C for 35 min.

Table 4.3.1 Chemical interdiffusion coefficients of Cu/Pd and Cu/Pd-Fe systems at different Cu concentrations

Annealing Temp. (°C)	D at 20% Cu (cm^2/s)		D at 30% Cu (cm^2/s)		D at 40% Cu (cm^2/s)		D at 50% Cu (cm^2/s)	
	Pd	Pd-Fe	Pd	Pd-Fe	Pd	Pd-Fe	Pd	Pd-Fe
700	3.085×10^{-11}	-	3.664×10^{-11}	-	5.178×10^{-11}	-	6.097×10^{-11}	-
550	1.273×10^{-11}	-	1.023×10^{-11}	-	8.623×10^{-12}	-	8.299×10^{-12}	-
500	1.003×10^{-11}	4.201×10^{-12}	1.319×10^{-11}	3.142×10^{-12}	1.194×10^{-11}	1.631×10^{-12}	7.926×10^{-12}	1.330×10^{-12}
450	1.332×10^{-12}	1.240×10^{-12}	1.198×10^{-12}	7.988×10^{-13}	1.094×10^{-12}	6.791×10^{-13}	1.022×10^{-12}	6.623×10^{-13}
400	1.718×10^{-13}	1.488×10^{-13}	1.750×10^{-13}	1.102×10^{-13}	1.844×10^{-13}	8.991×10^{-14}	1.911×10^{-13}	8.022×10^{-14}
350	3.576×10^{-14}	1.679×10^{-14}	4.115×10^{-14}	1.419×10^{-14}	4.689×10^{-14}	1.263×10^{-14}	5.195×10^{-14}	1.154×10^{-14}
300	2.365×10^{-15}	1.020×10^{-15}	2.711×10^{-15}	9.158×10^{-16}	3.563×10^{-15}	8.776×10^{-16}	4.490×10^{-15}	8.485×10^{-16}
250	2.650×10^{-15}	8.411×10^{-16}	2.519×10^{-15}	5.929×10^{-16}	2.585×10^{-15}	4.976×10^{-16}	2.761×10^{-15}	4.856×10^{-16}

Table 4.3.1 (Continue) Chemical interdiffusion coefficients of Cu/Pd and Cu/Pd-Fe systems at different Cu concentrations

Annealing Temp. (°C)	D at 60% Cu (cm^2/s)		D at 70% Cu (cm^2/s)		D at 80% Cu (cm^2/s)	
	Pd	Pd-Fe	Pd	Pd-Fe	Pd	Pd-Fe
700	4.656×10^{-11}	-	4.028×10^{-11}	-	4.129×10^{-11}	-
550	7.649×10^{-12}	-	8.477×10^{-12}	-	1.041×10^{-11}	-
500	6.324×10^{-12}	1.328×10^{-12}	5.975×10^{-12}	1.521×10^{-12}	6.438×10^{-12}	1.990×10^{-12}
450	1.055×10^{-12}	7.790×10^{-13}	1.192×10^{-12}	1.108×10^{-12}	1.472×10^{-12}	1.188×10^{-12}
400	2.082×10^{-13}	8.061×10^{-14}	2.520×10^{-13}	9.258×10^{-14}	3.470×10^{-13}	1.231×10^{-13}
350	5.639×10^{-14}	1.186×10^{-14}	5.934×10^{-14}	1.368×10^{-14}	6.440×10^{-14}	1.808×10^{-14}
300	4.588×10^{-15}	8.943×10^{-16}	6.270×10^{-15}	1.073×10^{-15}	8.578×10^{-15}	1.561×10^{-15}
250	3.280×10^{-15}	5.345×10^{-16}	4.415×10^{-15}	6.614×10^{-16}	6.787×10^{-15}	9.681×10^{-16}

Fig. 4.3.7 compares the logarithm of interdiffusion coefficients of Cu/lamellar Ni, Cu/Pd and Cu/Pd-Fe systems at 20%, 50% and 80% Cu with temperatures. Fig. 4.3.7 illustrates that interdiffusion coefficients of the Cu/Pd-Fe system are lower than those of the Cu/Pd system at all Cu concentrations. For example, the apparent interdiffusion coefficient of the Cu/Pd-Fe system at 400°C is smaller than that of the Cu/Pd system approximately by a factor of 2. Interdiffusion coefficients of the Cu/Pd-Fe system are still higher than those of the Cu/Ni system for temperatures above 300°C. When the temperature is in the region of 300°C, interdiffusion coefficients of the Cu/Pd-Fe system are comparable to those of the Cu/Ni system. For instance, at 250°C interdiffusion coefficients of the Cu/Pd-Fe system are comparable to those of the Cu/lamellar Ni system.

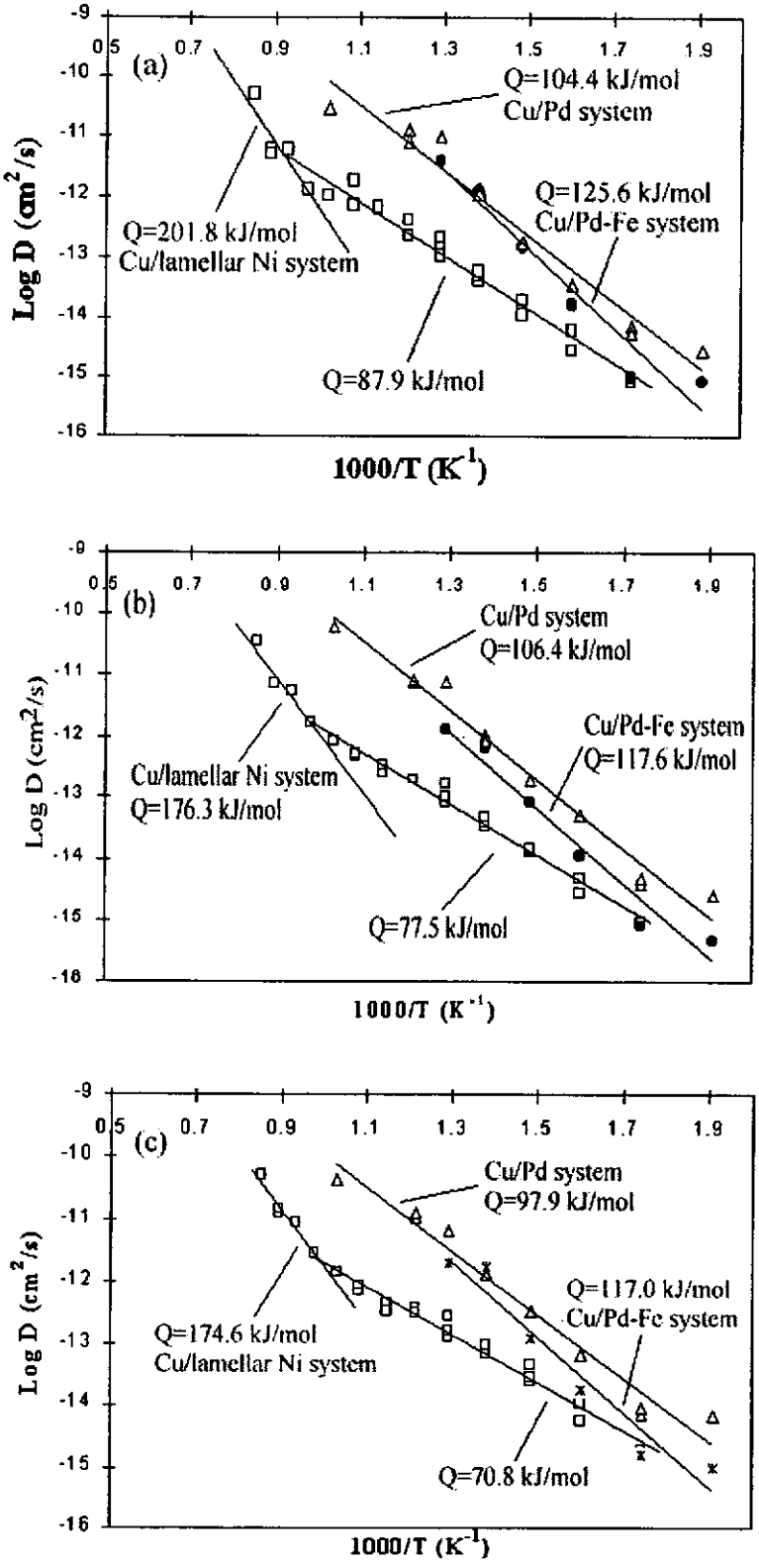

Fig. 4.3.7 Arrhenius plots of interdiffusion coefficients at (a) 20%, (b) 50%, (c) 80% Cu for Cu/lamellar Ni, Cu/Pd and Cu/Pd-Fe systems

Apparent activation energies Q for diffusion for the Cu/Pd-Fe system were calculated from the curves in Fig. 4.3.7. In the temperature range 250°C to 500°C, the value of Q for the Cu/Pd-Fe system varies from 117.0 kJ/mol to 125.6 kJ/mol. Apparent activation energies Q for diffusion of the Cu/Pd-Fe system are higher than those of the Cu/Pd system in the temperature range 250°C to 700°C. The comparatively higher values of Q for the Cu/Pd-Fe system reflect that interdiffusion of the Cu/Pd-Fe system is less pronounced than that of the Cu/Pd system.

4.3.4 X-ray Diffraction Study

To gain more understanding on the Cu/Pd-Fe system, XRD analysis of untreated sample and sample heat treated at 500°C for 1 h were investigated. From the X-ray diffraction data (Fig. 4.3.8(a)), where different phases of the Pd-Fe electrodeposit are present, where the lattice parameters, the interplanar lattice spacing and the Bragg angles (2θ) were reported in Table 4.3.2. It is noted a Cu (111) peak was also recorded because of the substrate. As the X-ray mass-absorption coefficients for Pd (205.5 m^2kg^{-1}) and Fe (307.3 m^2kg^{-1}) are both large, intensities of those peaks received are relatively low.

Table 4.3.2 Data obtained from XRD analysis of the Pd-Fe as-deposit

Crystalline phase	*Crystalline structure*	*Lattice parameter (nm)*	*Lattice Interplanar spacing (nm)*	*(hkl)*	*2θ*
$FePd_3$	f.c.c.	a=0.3856	0.2227	(111)	40.48°
FePd	f.c.tetragonal	a=0.3869	0.2194	(111)	41.12°
FePd	f.c.tetragonal	c=0.3670	0.1935	(200)	46.93°
Cu (from substrate)	f.c.c.	a=0.3615	0.2087	(111)	43.32°

We observed that the untreated Pd-Fe coating is a mixture of tetragonal FePd and f.c.c. $FePd_3$ phases when the composition is Pd 75wt%-Fe 25wt%. This composition falls on the transition interface between the FePd and $FePd_3$ regions in the Fe-Pd Phase diagram (Fig. 4.3.9) [56].

As a consequence of the thermal treatment at 500°C for 1 h, f.c.c. $FePd_3$ phase transforms towards the tetragonal FePd phase. The broad (111) peak of the FePd phase for the Pd-Fe as-deposit indicates small crystallites. Larger grains can be expected for the heat treated Pd-Fe sample with narrower (111) peak. (Table 4.3.3 and Fig. 4.3.8 (b)).

Table 4.3.3 Data obtained from XRD spectra of the 75%Pd-25%Fe deposit heat treated at 500°C for 1 h.

Crystalline phase	*Crystalline structure*	*Lattice parameter (nm)*	*Lattice Interplanar spacing (nm)*	*(hkl)*	*2θ*
FePd	f.c.tetragonal	a=0.3803	0.2195	(111)	41.09°
FePd	f.c.tetragonal	c=0.3799	0.1901	(200)	47.80°
$PdCu_3$	f.c.c.	a=0.3682	0.1841	(200)	49.47°

Moreover, the intermetallic phase of $PdCu_3$ was observed, indicating some copper atoms had diffused into the Pd-Fe coating. The FePd (200) peak was shifted due to the diffused copper and formation of $PdCu_3$ phase. Transformation of $FePd_3$ phase towards equilibrium FePd phase is also due to consumption of Pd atom for the formation of $PdCu_3$ phase resulting to the lowered Pd weight fraction in the Pd-Fe system phase diagram.

Rapid interdiffusion of Cu and Pd-Fe was observed at 500°C (Fig. 4.3.6). This is attributed to the formation of $PdCu_3$ compound which promotes the generation of vacancies [26], thus further enhance the rate of diffusion. No α-Fe phase was detected implying that the Pd weight fraction had not decreased below 65 wt% while some Pd

atoms formed intermetallic phases with copper; otherwise, α-Fe phase would be precipitated if weight fraction of Pd was lower than 65 wt%.

On the contrary, Cu/Pd-Fe couples give the lower interdiffusivities than those of Cu/Pd couples, which can be attributed to the information shown in the Cu-Fe phase diagram (Fig. 4.3.10) [57]. Cu has a low solubility in Fe (about 2.2 wt% Cu) while Cu forms solid solution with Pd. Thus, copper probably diffuses more slowly in FePd than in Pd.

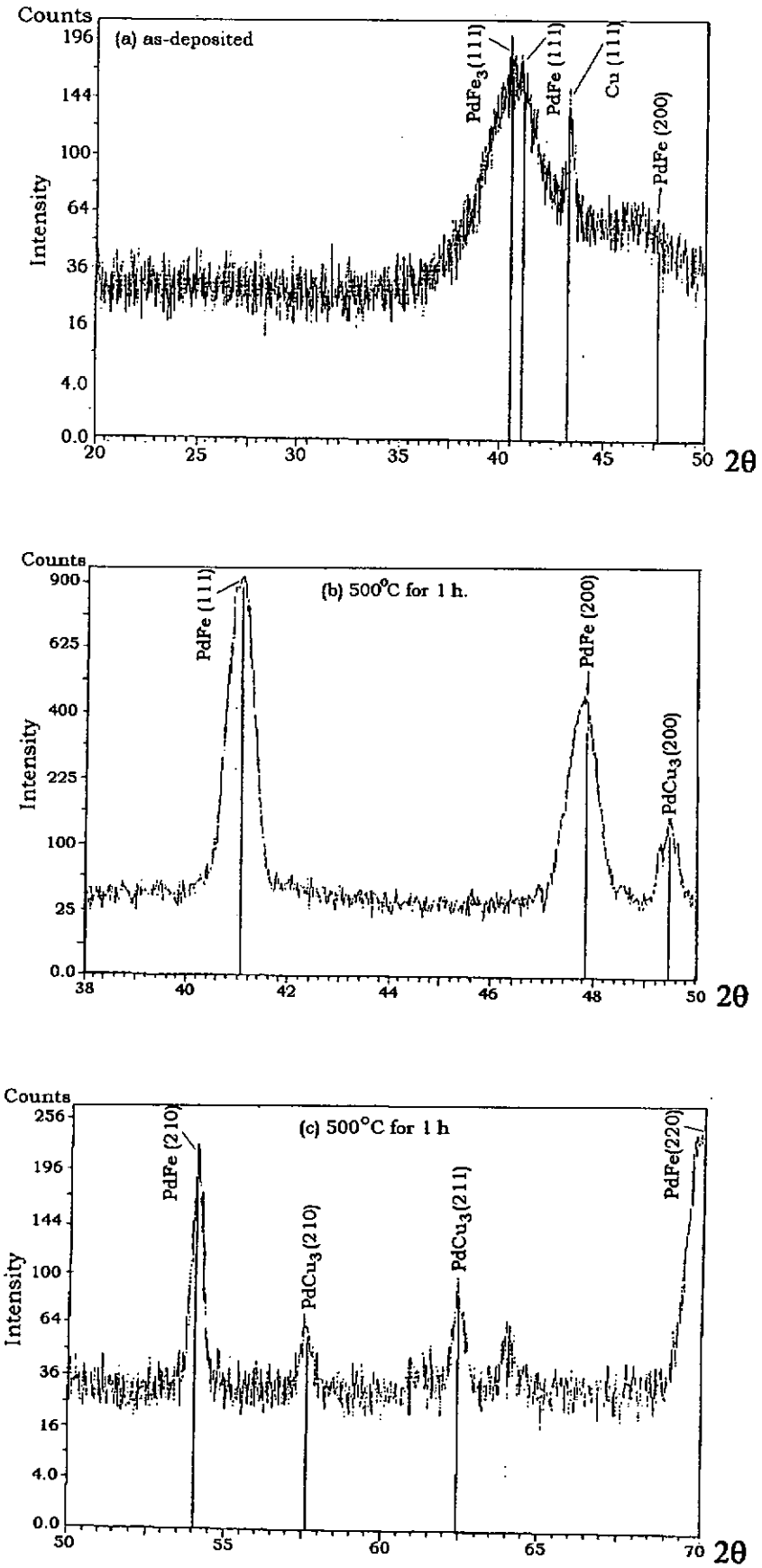

Fig. 4.3.8 XRD spectra of Pd-Fe coating; (a) as-deposited Pd-Fe coating,
(b) after heat treatment at 500°C for 1h,
(c) after heat treatment at 500°C for 1h (continue)

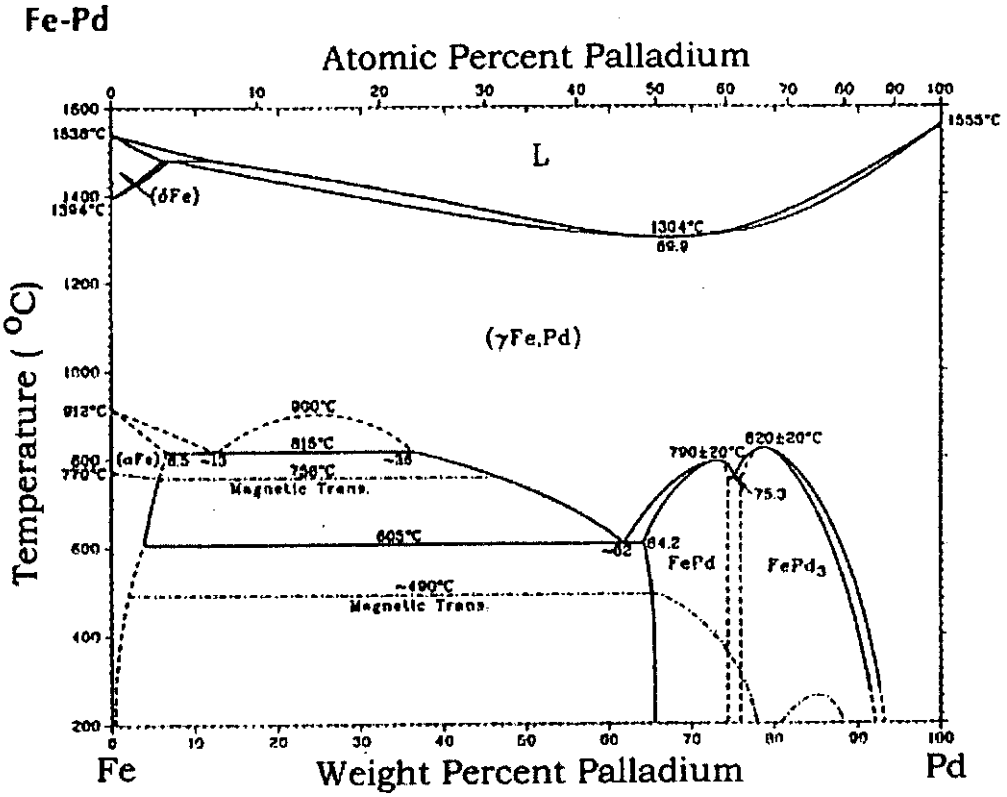

Fig. 4.3.9 Phase Diagram of the Fe-Pd alloy system

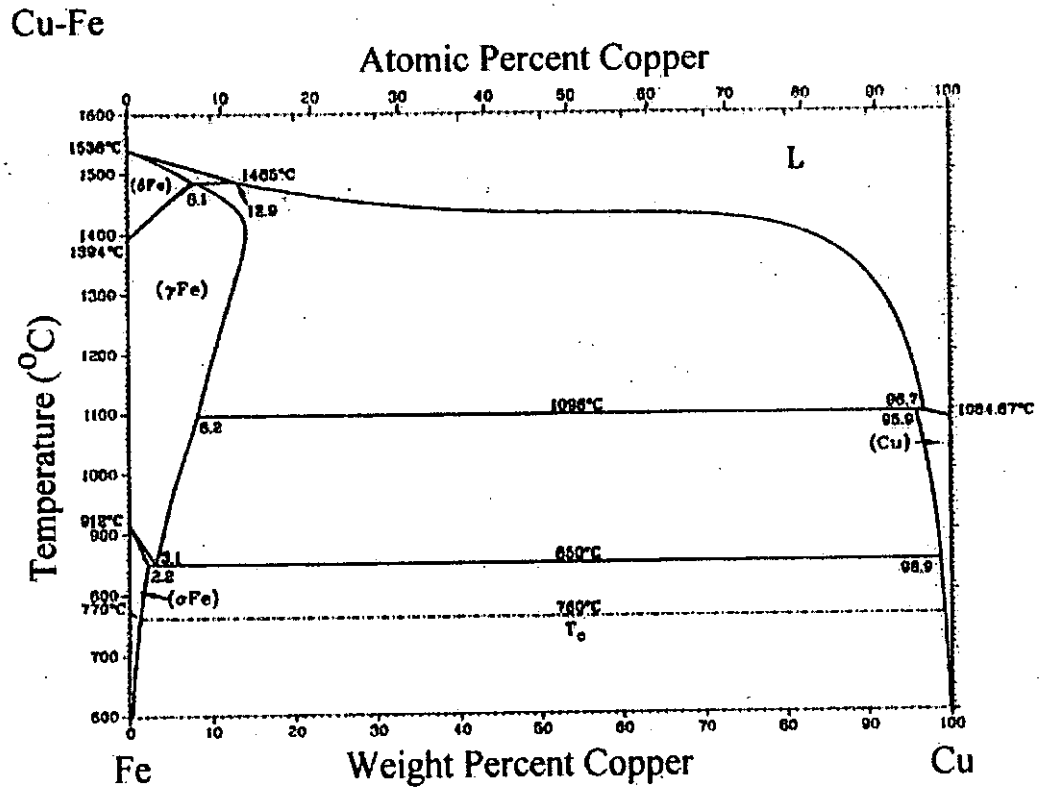

Fig. 4.3.10 Phase Diagram of the Cu-Fe alloy system.

4.4 Copper/Cobalt System

4.4.1 Current Efficiency

The current efficiency of the cobalt plating bath was calculated at different current density conditions by measuring the weight of the deposits before and after plating. A plot of current efficiency with increasing current density was shown in Fig. 4.4.1. It shows that the current efficiency of the cobalt plating bath at 50°C pH 2.1 increases from 72.9% at 1.67A/dm^2 to 88.7% at 16.7A/dm^2.

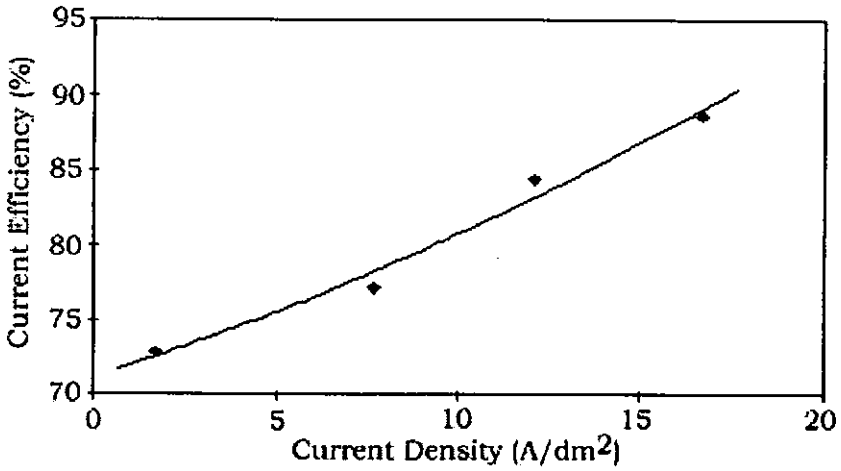

Fig. 4.4.1 Variation of current efficiency of the cobalt plating bath at 50°C pH 2.1 with current density

It is noted that the current efficiency of the cobalt plating bath is lower than that of the Watts nickel bath. Presumably, if cobalt is used as diffusion barrier coatings in the electroplating industry, the operation cost of cobalt plating should be higher than nickel plating.

4.4.2 Microstructural Observations

Structure of a cobalt deposit electroplated at 3.6A/dm^2 at 50°C is shown in the optical photograph (Fig. 4.4.2), which has a fine grain structure. The structure is also revealed by SEM as shown in Fig. 4.4.3.

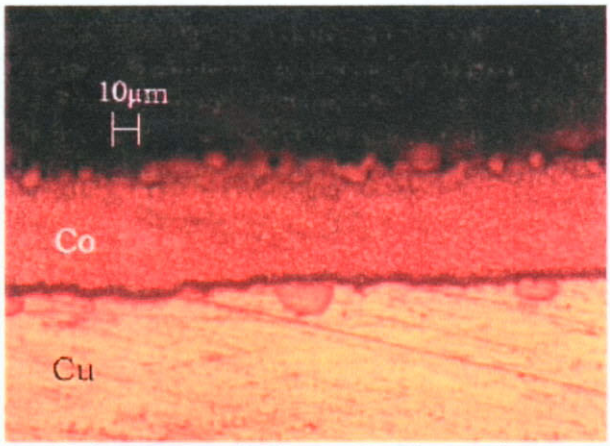

Fig. 4.4.2 Optical photograph shows the fine grain structure of the cobalt electrodeposit

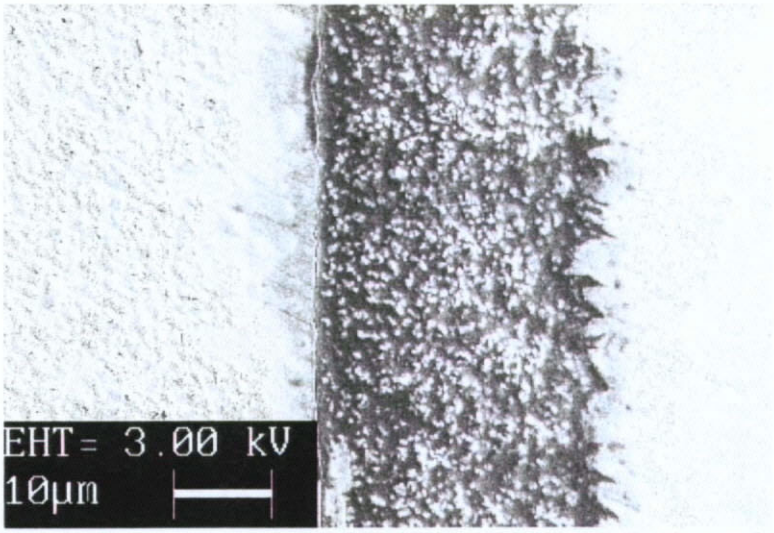

Fig. 4.4.3 SEM shows the cross-sectional view of the cobalt electrodeposit

4.4.3 X-ray Diffraction Study

XRD spectra were recorded in the Bragg-Brentano geometry in the 2θ interval between 40° and 100°, where the most relevant diffraction peaks of the h.c.p. cobalt

deposit are present, as shown in Fig. 4.4.4, where the lattice parameters, the interplanar lattice spacing and the Bragg angles (2θ) where reported in Table 4.4.1.

Apparent grain size was also determined to be 15.7nm by measuring the peak width of Co (002) diffraction peak.

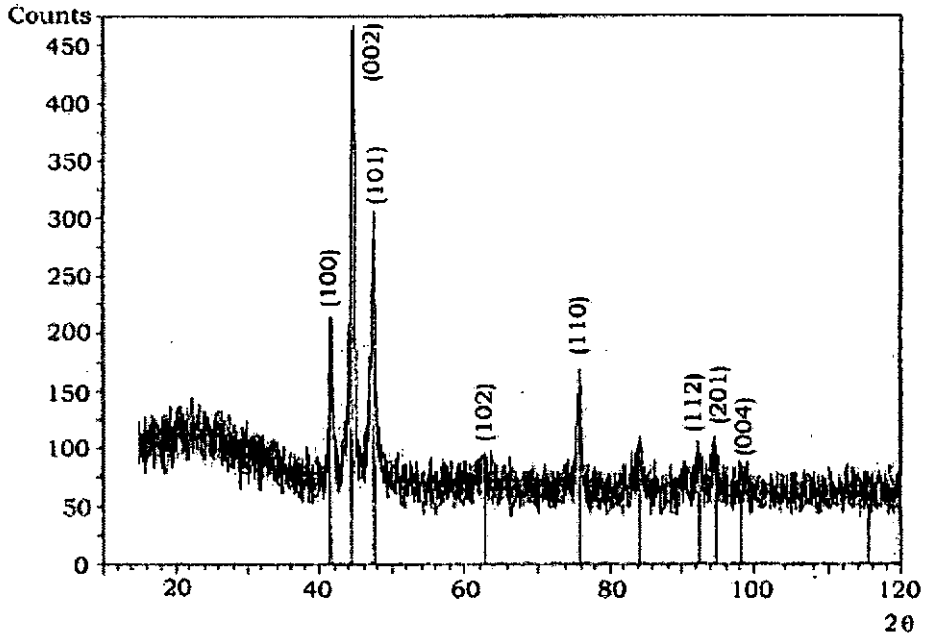

Fig. 4.4.4 XRD spectra of the cobalt electrodeposit

Table 4.4.1. Data obtained from the analysis of XRD pattern of cobalt deposit

Crystalline phase	*Crystalline structure*	*Lattice parameters (nm)*	*Interplanar spacing (nm)*	*(hkl)*	*2θ*
Co (α-phase)	hexagonal	a=0.2506 c=0.4076	0.2038	(002)	44.41°
			0.2173	(100)	41.53°
			0.1917	(101)	47.38°
			0.1478	(102)	62.83°
			0.1253	(110)	75.87°
			0.1019	(004)	98.28°
			0.1068	(112)	92.30°
			0.1048	(201)	94.66°

4.4.4 Diffusion Experiment

Fig. 4.4.5 shows the concentration-distance profiles of the Cu/Co system after heat treatment at 600°C for 50 h and 800°C for 6 h respectively. No significant interdiffusion was detected at all investigated temperatures (500°C to 900°C). Diffusion heat treatment results are summarized in Table 4.4.2.

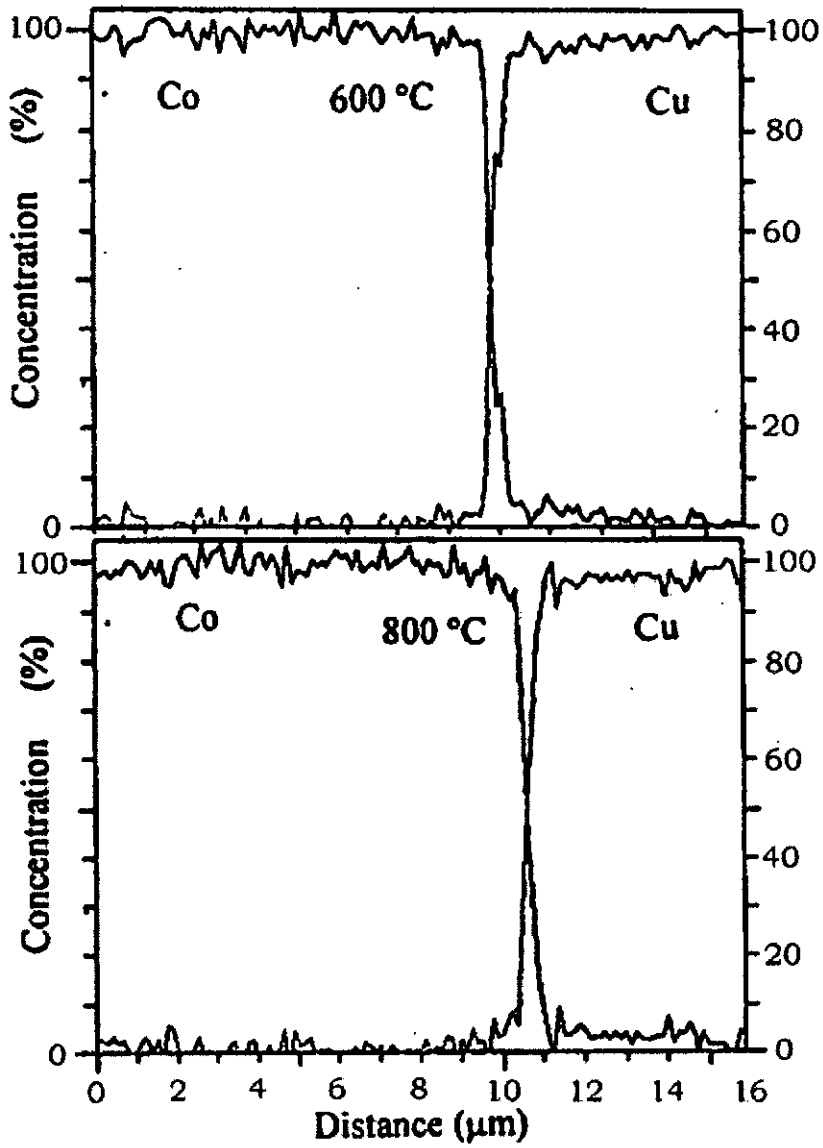

Fig. 4.4.5 Concentration-distance profiles of Cu/Co couples after heat treatment at (a) 600°C for 50 h, (b) 800°C for 6 h.

Table 4.4.2. Heat treatment results for the copper/cobalt system

Sample Designation	Annealing Temperature (°C)	Annealing Time (h)	Remarks
Cu-Co-1	600	24	negligible diffusion
Cu-Co-2	700	14	negligible diffusion
Cu-Co-3	800	6	negligible diffusion
Cu-Co-4	600	50	negligible diffusion
Cu-Co-5	700	24	negligible diffusion
Cu-Co-6	700	48	negligible diffusion
Cu-Co-7	900	3	negligible diffusion
Cu-Co-8	900	15	negligible diffusion

The width of the diffusion profiles for the Copper/Cobalt system was very narrow even at the highest temperature investigated, 900°C. In fact, it is believed that any apparent intermixing of the two metals indicated by the data was due to the error associated with the finite beam size of the microprobe. For the ideal case, when no interdiffusion has occurred, the curve is a step function. The corresponding concentration profiles obtained seem to indicate that some diffusion had taken place. Because of the finite size of the microprobe beam , when it passes over the interface between the two metals, it will excite both metals at once; thus, there is a slight broadening of the step profile. However, when a large amount of diffusion has taken place, the effect of the beam can be ignored.

Because of the mutual insolubility of copper and cobalt, apparently no significant concentrations of copper in cobalt or vice versa can be detected by microprobe measurements. Therefore, lattice diffusion of copper in cobalt may not occur. If there is any copper diffusion in cobalt it may be grain boundary diffused.

The reason for copper in cobalt not being detected by electron microprobe can be attributed to the resolution of it. The resolving power depends on factors such as the diameter of the incident electron beam (the electron probe diameter) before it reaches the specimen surface, the spot size of the diffused electron beam penetrated into the specimen, the spot size of the diffused characteristic X-ray source.

Firstly, the effective electron beam diameter is the diameter of the Gaussian probe spot with corrections by mainly the result of spherical aberration, chromatic aberration, and electron diffraction effects [27]. For our SEM operating at 20 kV, the effective primary electron beam diameter (d_e) is around 15 nm.

Moreover, when electrons penetrate in to the specimen, they interact with outer shell electrons and are scattered by elastic and inelastic collisions. Before losing all the energies during traveling, they produces secondary electrons, backscattering electrons and the most important for EDS study the X-ray generation. Thus, it is important to know quantities such as the range of an electron [28-29], which can travel before being absorbed or stopped by the material. The electron penetration range can be calculated by the equation:

$$R = \frac{4120}{\rho} E^{(1.265-0.0954 \ln E)}$$

where R = penetration in microns, E = primary electron energy in MeV, ρ = absorber density, in g/cm^3.

In our case, cobalt has density of 8.9 g/cm^3 and copper has density of 8.96 g/cm^3; for E = 20keV the electron penetration range calculated are 0.763μm (for cobalt) and 0.757μm (for copper) respectively. The spot shape of the diffused electron beam is assumed to be a sphere with the Gaussian distribution of electron beam intensity, which has the size of the same order of magnitude of the electron penetration range.

As the energy of electrons having decreased to that of critical potential of X-ray generation, the electron will soon be stopped, the spot size of the X-ray source is nearly equal to that of the diffused electron beam. If δd is the spot size of the X-ray source corresponding to an extremely narrow beam (diameter of the initial electron beam becomes zero) and assuming a Gaussian distribution of the X-ray source, the spot size of the characteristic X-ray source excited by a finite electron beam is given by $d = 2[(d_e/2)^2+(\delta d/2)^2]^{1/2}$. If we take d_e = 15 nm (the effective primary electron beam diameter) and δd=0.76μm (the electron penetration range), then X-ray source spot size is approximately equals to 0.76μm. Thus, the factor which plays the most important role in resolution is not the aberration originated from electron optics but that due to electron diffusion.

For simplicity, we may conclude that the X-ray source spot size is in the order of magnitude of 1μm. Assuming a polycrystal consisting of closely packed spherical grains model developed by Bokshtein *et al* [10], the volume fraction of the grain boundaries can be expressed as $g= \pi r_g\delta /(\pi r_g\delta + \pi r_g^2)$ where r_g is radius of the grain and δ is the grain boundary width. Since the grain boundary is not more than two to three atomic dimensions thick, we assume it be 3 angstrom (3×10^{-10} m). The apparent grain size of the as-deposited cobalt determined by X-ray diffraction is around 15.7nm. Considering the X-ray source spot volume of $(4/3)\pi(d/2)^3$, where d=0.76μm,

the X-ray source spot volume is $2.298\times10^{-19}m^3$. The volume fraction for the grain boundary concentrated copper atoms is only 0.036; nearly 4% of the total volume in which X-rays emit. Moreover, the real density of packing of grains is expected to be higher since the shape of the grains is different in general, and the grains size of cobalt and copper are increasing during heat treatment at an elevated temperature; thus the volume fraction for the grain boundary concentrated copper atoms is further lowered and must be less than 4%. Hence, less than 4% in volume of the diffused electron beam interacts with the diffused elements inside the grain boundaries producing characteristic X-rays. Most of the detected X-rays are originated from the bulk material. Thus, for the Cu diffused Co specimen, most characteristic X-rays detected by EDS are originated from the bulk Co.

For this system some kind of permeation experiment would better characterize the barrier capabilities of cobalt. Diffusion experiment of a Cu/Co(barrier)/Ni system was studied, in which details will be discussed in Section 4.6.

4.5 Copper/Cobalt-Tungsten System

The tungsten composition of the Co-W electrodeposit of the Cu/Co-W couple for diffusion experiment was measured by EDS was Co-36 wt.% W (Fig. 4.5.1). The Co-W layer was electroplated at 1.2 A/dm^2 in the citrate bath with W/(W+Co) ions ratio of 1/2.

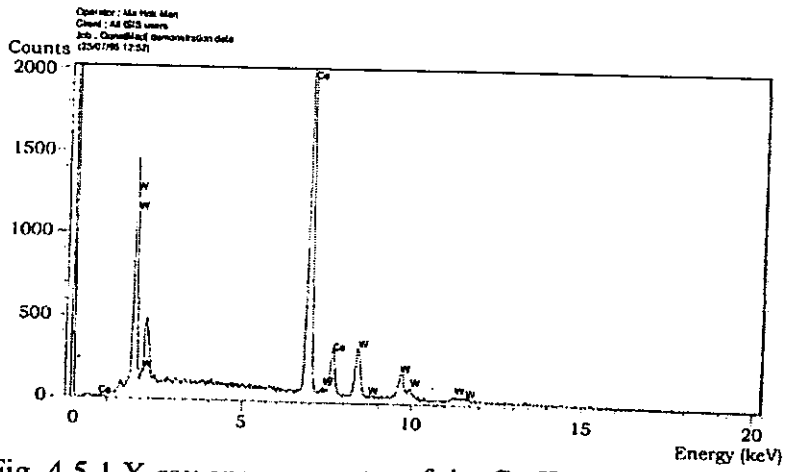

Fig. 4.5.1 X-ray energy spectra of the Co-W electrodeposit

4.5.1 Effects of Deposition Parameters

The composition of Co-W layer varies with the deposition parameters such as current density as well as on the electrolyte concentrations. Fig. 4.5.2 shows that alloys with constant tungsten content are formed over a range of current density when the W/(W+Co) ions ratio of the electrolyte is between 1/2 and 2/3. When the W/(W+Co) ions ratio is dropped to 2/5, the alloy composition becomes current density dependent. There is a substantial drop of the tungsten composition from 37 wt% to below 30 wt%, when the current density is lowered to below 2 A/dm^2. On the whole, the tungsten composition increases with the W/(W+Co) ions ratio.

Several Co-W electrodeposits with different composition were taken for DC polarization and AC electrochemical impedance measurements. Results will be discussed in Chapter 5.

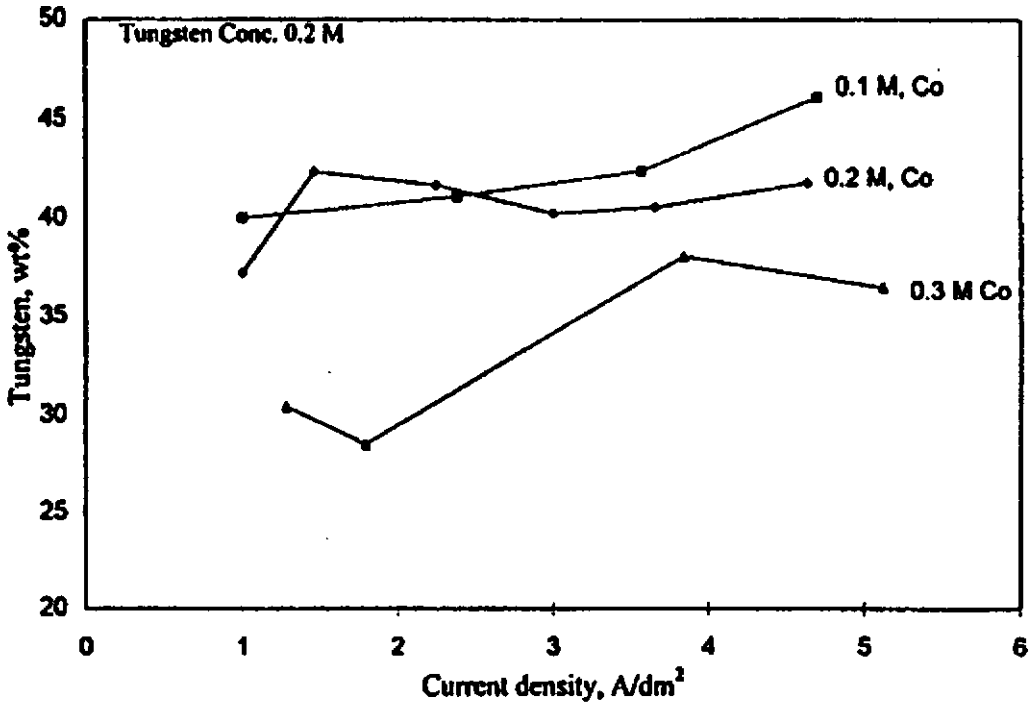

Fig. 4.5.2 Influence of electrolyte concentration and current density on alloy composition.

4.5.2 Microscopic Observation

The surface morphology of the Co-W electrodeposit is shown in Fig. 4.5.3 by SEM. Fig. 4.5.4 shows the lamellar structure of the Co-W electrodeposit.

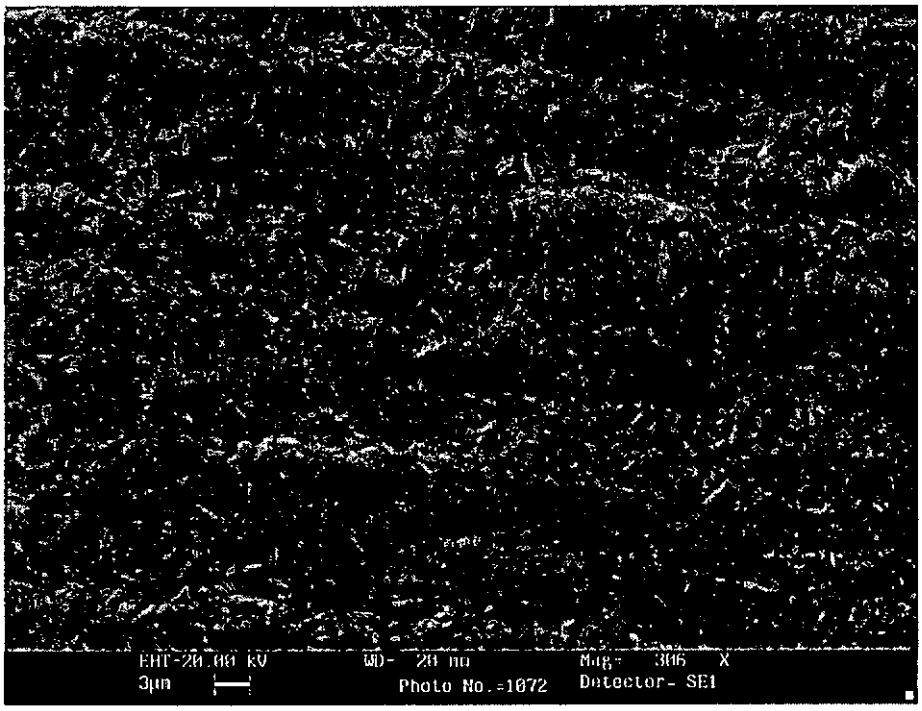

Fig. 4.5.3 SEM micrograph of the surface of the Co-W coating electrodeposited at 1.2 A/dm^2 in the citrate bath with W/(W+Co) ions ratio of ½.

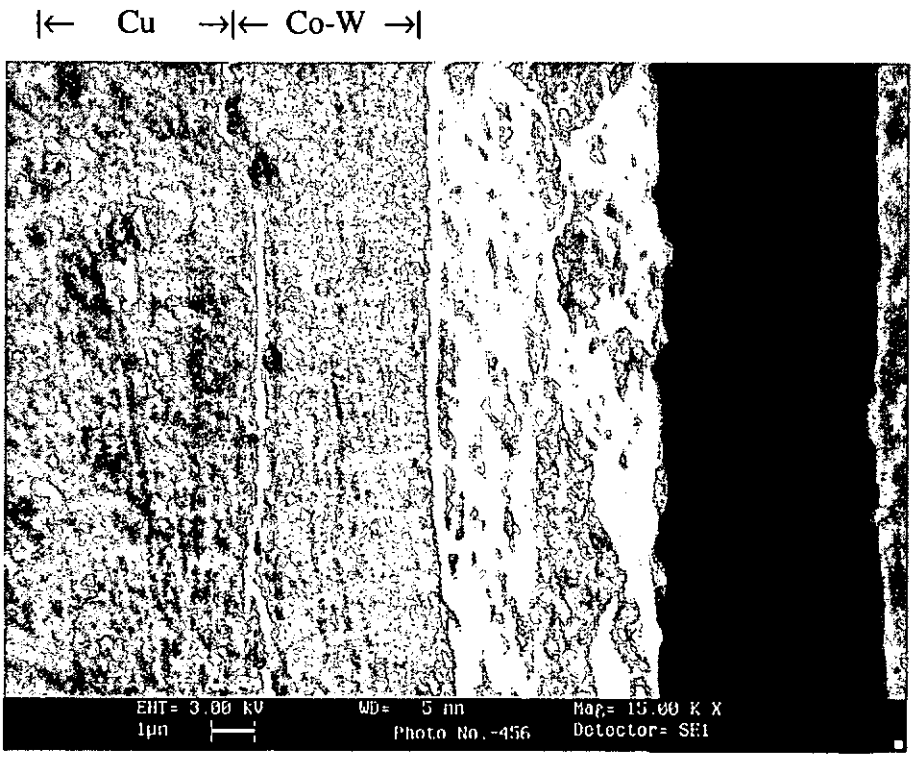

Fig. 4.5.4 SEM micrograph of Co-W electrodeposited at 1.2 A/dm^2 in the citrate bath with W/(W+Co) ions ratio of 1/2, which has a lamellar structure.

4.5.3 *X-ray Diffraction Study*

The XRD patterns of the as-deposited Cu/Co-W sample plated in a bath with W/(W+Co) ions ratio of 1/2 at 1.2 A/dm^2 shows the (200), (201), (400) and (401) peaks of h.c.p. Co_3W phase, which indicates the presence of crystalline Co_3W phase in the coating (Fig. 4.5.5 (a)). Some anticipated peaks are missing. The disappearance of those peaks reflects the relatively low crystallinity and textured properties of the Co-36 wt.% W electrodeposit.

The h.c.p. cobalt structure was not observed. Similar XRD pattern which was slightly shifted due to lattice expansion was obtained for the sample treated at 500°C for 1 hour, as shown in Fig. 4.5.5 (b). After treating at 800°C for 1.5 hour, the Co-W coating gives a mixture of cobalt-like h.c.p. and f.c.c. phases, as illustrated in Fig. 4.5.5 (c). Some peaks indicate the formation of cobalt oxide and cobalt tungsten oxide during heat treatment. These oxides might be derived from reaction of trace oxygen and trace citrate at high temperatures. Upon heat treatment at 1100°C for 1.5 hour, the coating was converted to f.c.c. cobalt structure, as shown in Fig. 4.5.5 (d). Comparing with the spectra of pure f.c.c. cobalt, peaks shifting are observed. This indicates lattice expansion, resulting from the inclusion of tungsten and diffused copper atoms in the cobalt lattice. The lattice parameter for the 1100°C heat-treated coating was 0.358 nm, which is larger than the value for pure f.c.c. cobalt [31] (0.3545 nm). Our result is consistent with the lattice parameter results of 0.357 nm; reported by Wheeler *et al.* [11] Tungsten is present in the Co f.c.c. phase as a solid solution giving a slightly larger lattice.

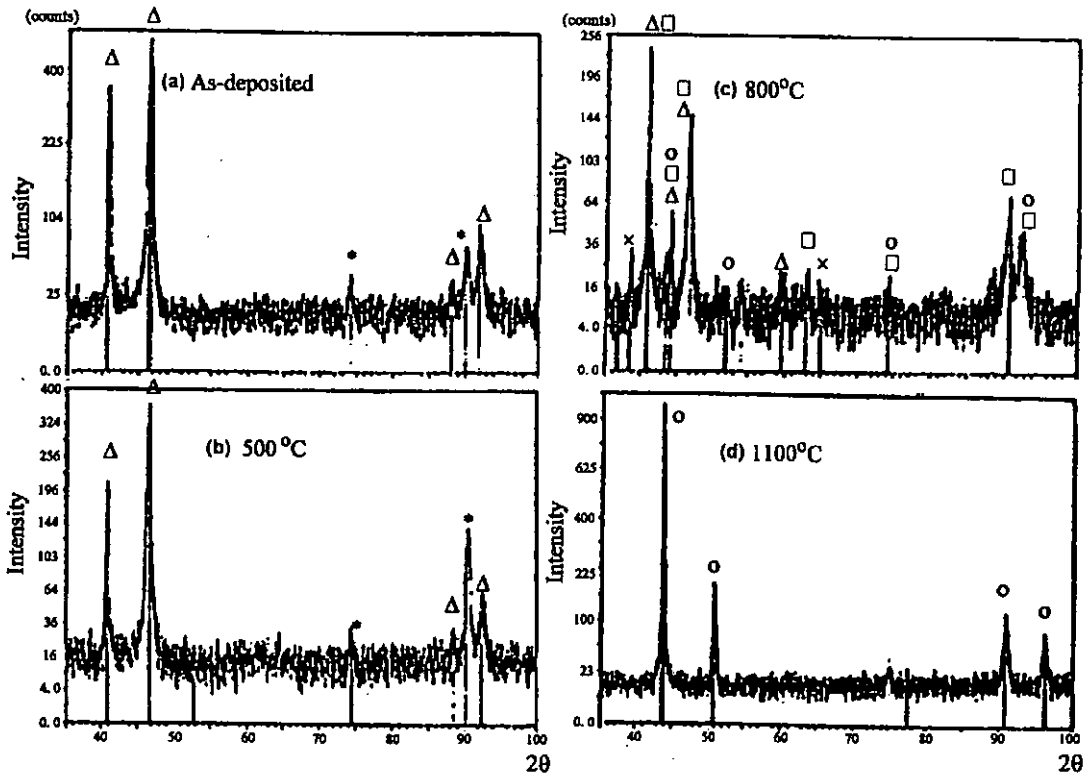

Fig. 4.5.5. XRD spectra of Co-W coating plated in a bath with W/(W+Co) ions ratio of 1/2 at 1.2 A/dm^2:
a) untreated, b) treated at 500°C for 1 h
c) at 800°C for 1.5 h, d) at 1100°C for 1.5 h
Δ-Co_3W intermetallic phase, -h.c.p. Co-like phase,
o-f.c.c. Co-like phase, *-peak from Cu substrate,
×-cobalt tungsten oxide ($CoWO_4$)

Fig. 4.5.6 (a) shows the X-ray diffraction patterns of the Co-W electrodeposit plated from a citrate bath with W/(W+Co) ions ratio of 1/2 at current density of 5.1 A/dm^2. A typical diffraction pattern for amorphous alloys is observed. There is no significant change of the amorphous diffraction pattern after the Co-W sample being heat-treated at 500°C for 1 hour (Fig. 4.5.6 (b)). After treating at 800°C for 1.5 hours, sharp peaks were observed indicating a crystalline structure of Co_3W intermetallic phases as shown in Fig. 4.5.6 (c). Some peaks of cobalt tungsten oxide are also observed. Upon heat treatment at 1100°C for 1.5 hours, the coating consisted of a mixture of crystalline h.c.p. Co_3W phase and h.c.p. and f.c.c. Co-like phases in which the f.c.c. cobalt phase had indicated a lattice expansion. (Fig. 4.5.6 (d))

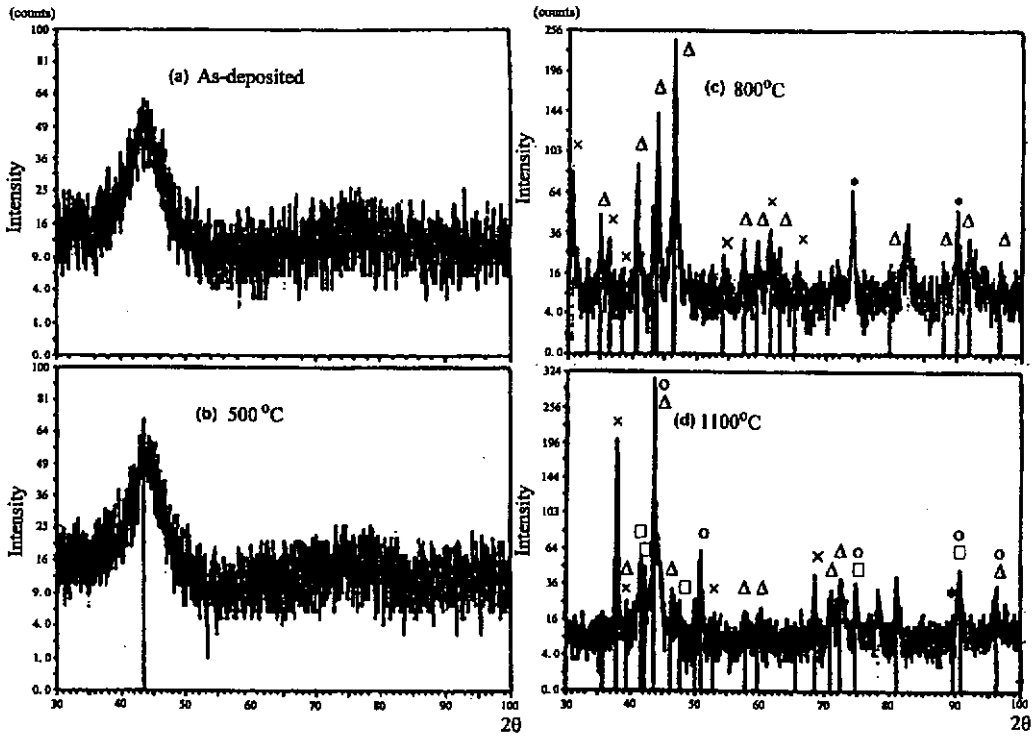

Fig. 4.5.6. XRD spectra of Co-W coating plated in a bath with W/W+Co ions ratio of 1/2 at 5.1 A/dm^2:
a) untreated, b) treated at 500°C for 1 h
c) at 800°C for 1.5 h, d) at 1100°C for 1.5 h
Δ-Co_3W intermetallic phase, -h.c.p. Co-like phase,
o-f.c.c. Co-like phase, *-peak from Cu substrate,
×-cobalt tungsten oxide ($CoWO_4$)

Similar results were obtained for the Co-W coating electrodeposited from a citrate bath with W/(W+Co) ions ratio of 2/3 at current densities of 1.2 and 5.1 A/dm^2 respectively. These coatings after electrodeposition were amorphous and became recrystallized upon heat treatment at 800°C and 1100°C.

Our results show close similarity with those reported by Admon *et al.* [12] They prepared their Co-W films from a basic bath (pH=8.5) containing $(NH_4)_2SO_4$ and Rochelle salt ($NaKC_4H_4O_6.6H_2O$). They observed that the texture was most pronounced when preparing within 50°C -90°C and 50% for the W/(W+Co) ions ratio. At higher W ion ratio the crystallinity and concurrently the texture were gradually destroyed. From our observations, XRD missing peaks for the Co-W coating prepared in a bath containing citric acid and with W/(W+Co) ions ratio of

50% at 1.2 A/dm^2 indicates a textured coating. When the W/(W+Co) ions ratio was increased to 66%, the Co-W coatings became amorphous. It is interesting to note that an amorphous coating can also be obtained by increasing the current density to 5.1 A/dm^2, and keeping the W/(W+Co) ions ratio 50% and temperature at 65°C unchanged.

Polukarov [32] reported that the formation of crystalline Co_3W intermetallic phase was possible when under conditions of high W concentration and cathode potential. In our studies, intermetallic phase of Co_3W were not observed for the as-deposited Co-W coating plated in a bath with a higher W/(W+Co) ions ratio of 2/3. However, intermetallic phase of Co_3W was observed upon heat treatment at 800°C for 1.5 hours. The occurrence of Co_3W phase was not reported by Admon *et al* [12] and Wheeler *et al* [11] for the as-deposited or heat treated Co-W coatings. The structure of Co-W deposits depends on a complex influence of the process variables, such as bath composition, pH, temperature and current density, resulting in yielding unique properties on the coatings as observed by different investigators using different plating baths. Table 4.5.1 summarizes our observations on the dependence of the phase composition with plating conditions and heat treatments.

Table 4.5.1. Variations of phase composition with plating conditions and heat treatment.

Current density (A/dm^2)	W/W+Co ions ratio	as-deposited coating	Heat treatments		
			500°C for 1 h	800°C for 1.5 h	1100°C for 1.5 h
1.2	1/2	crystalline h.c.p.Co_3W phase with missing peaks	No significant phase change	h.c.p and f.c.c. Co-like phases.	f.c.c. Co-like phase
5.1	1/2	Amorphous	No significant phase change	crystalline h.c.p.Co_3W phase	mixture of h.c.p. Co_3W and; h.c.p. and f.c.c. Co-like phases
1.2	2/3	Amorphous	No significant phase change	crystalline h.c.p.Co_3W phase	mixture of h.c.p. Co_3W and; h.c.p. and f.c.c. Co-like phases
5.1	2/3	Amorphous	No significant phase change	crystalline h.c.p.Co_3W phase	mixture of h.c.p. Co_3W and; h.c.p. and f.c.c. Co-like phases

4.5.4 Diffusion Experiment

Because of the solubility factor, similar results to those of the Cu/Co systems were observed for the Cu/Co-W systems. Fig. 4.5.7 shows the concentration-distance profiles of the Cu/Co-W system after heat treatment at temperatures ranging from 500°C to 800°C. Negligible interdiffusion of Co-W and Cu was detected.

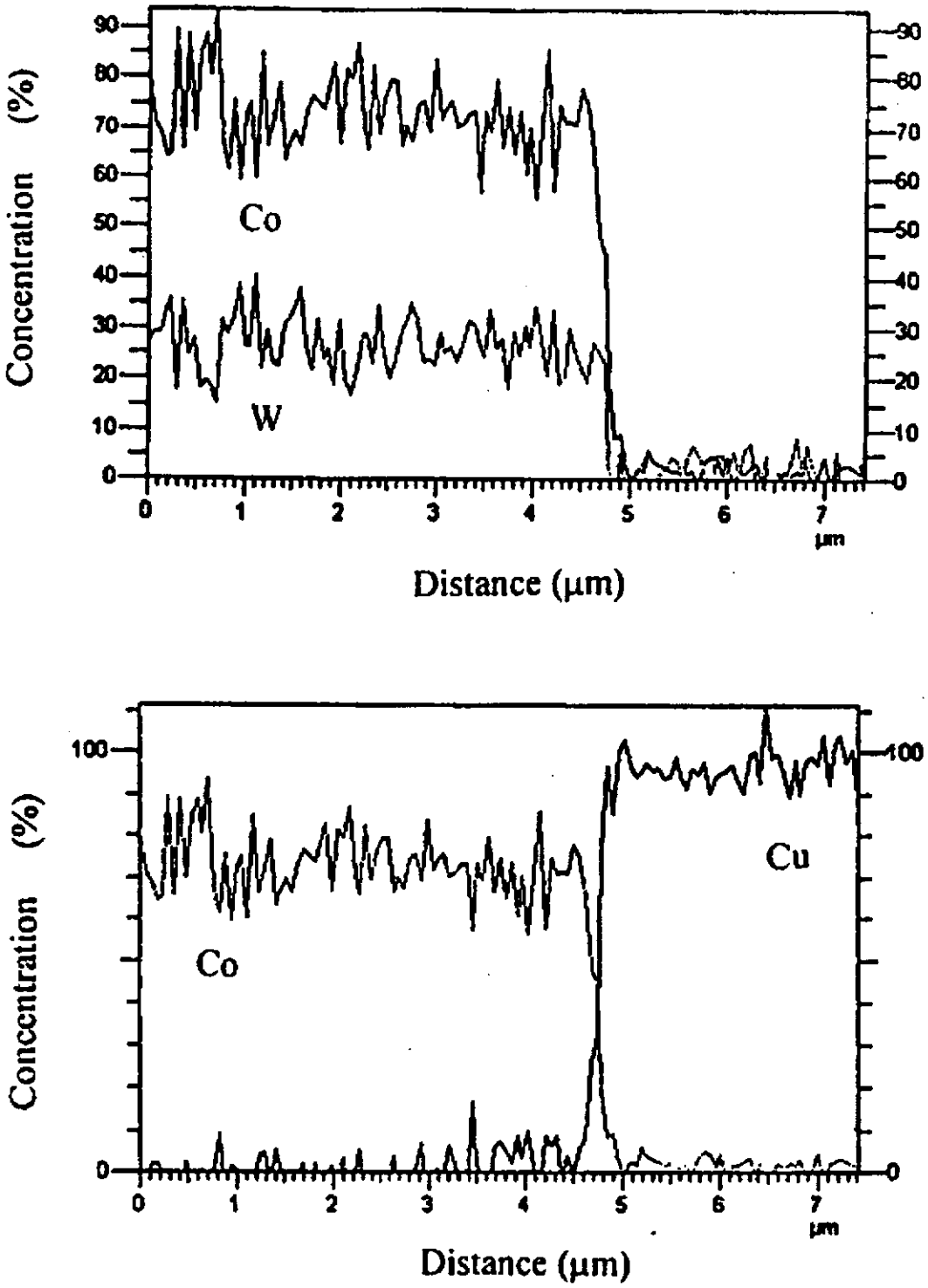

Fig. 4.5.7 (a) Concentration-distance profiles of Cu/Co-W couple after heat treatment at 500 °C for 6 h.

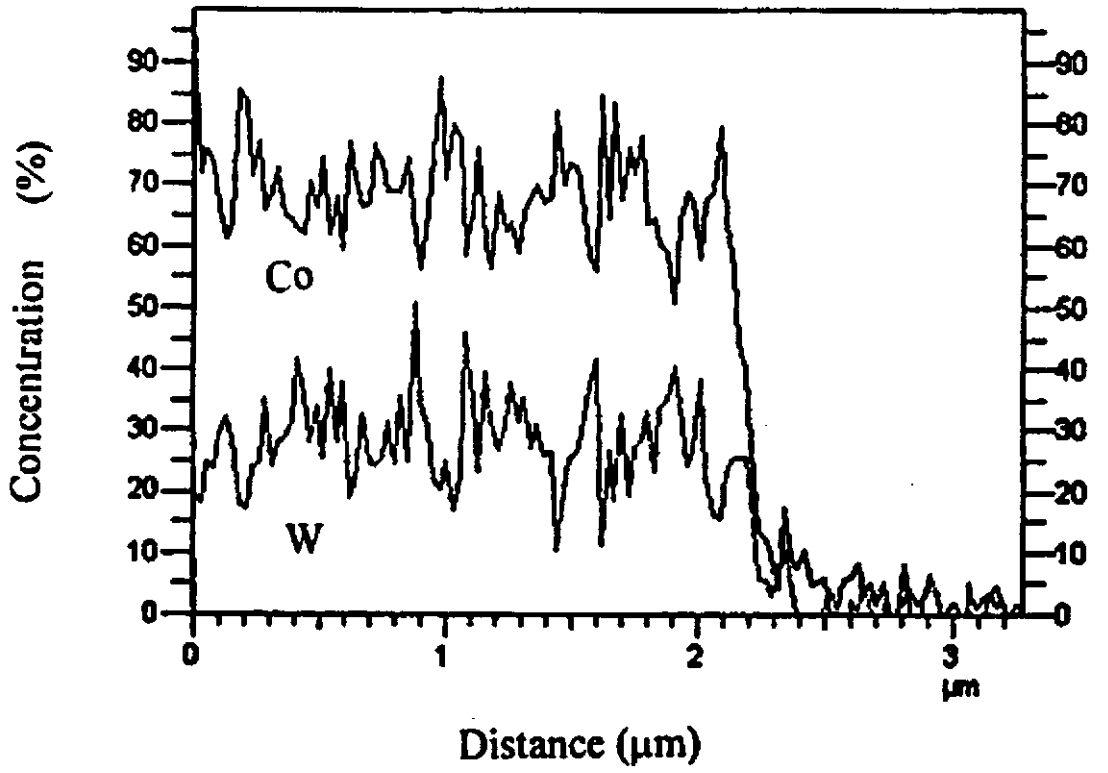

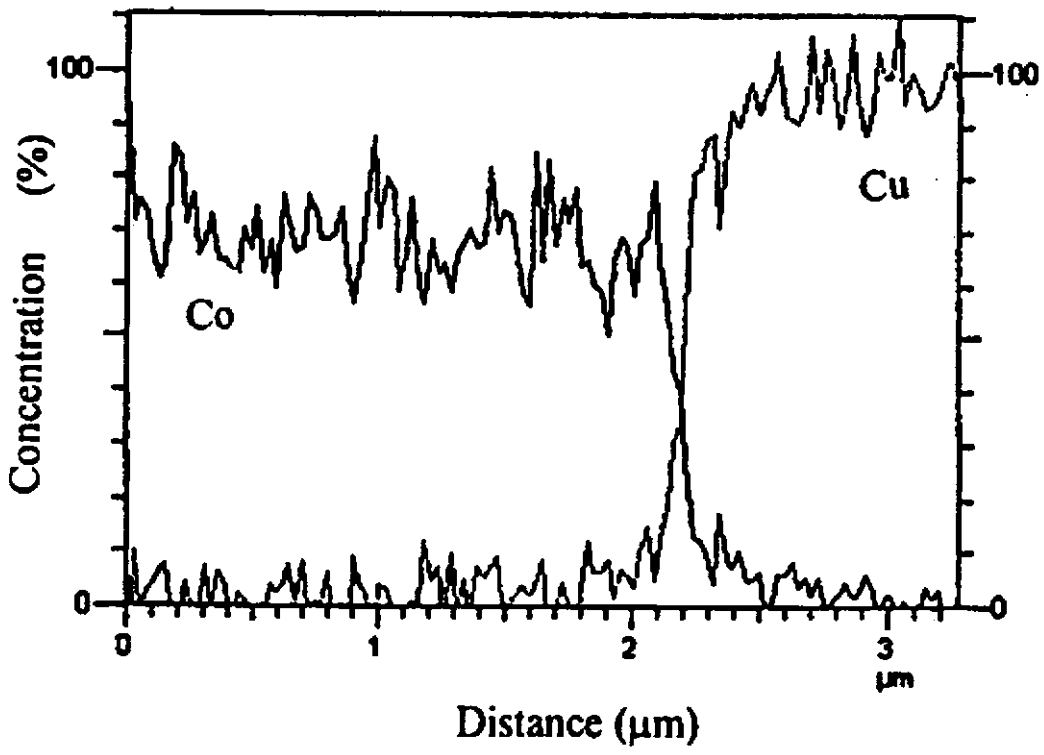

Fig. 4.5.7 (b) Concentration-distance profiles of Cu/Co-W couple after heat treatment at 800°C for 45 min.

4.6 Copper/Cobalt (barrier)/Nickel and Copper/Cobalt-Tungsten (barrier)/Nickel systems

4.6.1 Diffusion Experiment

To evaluate the diffusion barrier properties of cobalt and cobalt-tungsten, interdiffusion of a Cu/Co (barrier)/Ni and Cu/Co-36wt% W (barrier)/Ni systems were studied. Two different Co-W barrier coatings were electroplated. The first one was electroplated in a bath with W/(W+Co) ions ratio of 1/2 at 1.2 A/dm^2. Another was electroplated in a bath with W/(W+Co) ions ratio of 2/3 at 5.0 A/dm^2. We designate the Co/Co-W (barrier)/Ni system with the Co-W coating plated by the bath with W/(W+Co) ions ratio of ½ as system "A", whereas the one with W/(W+Co) ions ratio of 2/3 as system "B". Cu/Co/Ni and Cu/Co-W/Ni samples of thickness 0.5μm and 1.5μm were heat treated at temperatures ranging from 400°C to 800°C.

Figures 4.6.1 to 4.6.3 show the concentration-distance profiles for the Cu/Co (barrier)/Ni and Cu/Co-W (barrier) (coating A or B)/Ni samples after heat treatment at 400°C for 219h. There is little evidence of interdiffusion for all samples at 400°C. For heat treatment at 500°C for 72h, for the Cu/Co/Ni system and the Cu/Co-W (coating B)/Ni system, both Ni and Cu have interdiffused while there is negligible interdiffusion for the Cu/Co-W (coating A)/Ni sample (Figures 4.6.4 to 4.6.6).

Copper penetrates cobalt (the barrier) into the nickel layer, notwithstanding the mutual insolubility between Cu and Co. Copper has migrated into the nickel layer through the grain boundaries of the cobalt barrier and become segregated on the cobalt/nickel interface. These copper atoms continue to migrate into the nickel layer.

Taking into consideration the developed intergrain surface of the metallic vacuum condensates [33], Cu can penetrate the Co layer at the grain boundaries in a

similar way as interpenetration of atoms for the Cu-Cr system, whose mutual solubility is almost zero [34]. This phenomenon is similar to the diffusion behavior of copper through electroplated silver leadframes reported by Wakabayashi *et al.* [30] Because of the low mutual solubility between copper and silver, copper was only detected on the silver surface diffused through the grain boundaries of the silver.

Madakson *et al* [35] suggested that complete interdiffusion of Cu and Au in the Cu/Co (0.15μm)/Au thin film system occurred after heat treatment at 450°C for 30min. We have observed that, for the Cu/Co (1.5μm)/Ni electroplated system, significant interdiffusion between Cu substrate and Ni overlayer occurs after heat treatment at 500°C for 72h. For the Cu/Co-36 wt.% W (1.5μm-coating A)/Ni system, interdiffusion between Cu and Ni occurred after heat treatment at 600°C for 13.6h (Fig. 4.6.7(b)). It is also observed that the rate of diffusion of Cu for the Cu/Co (1.5μm)/Ni and Cu/Co-W (1.5μm-coating B)/Ni systems are even higher than that of the Cu/Co-W (1.5μm-coating A)/Ni system. (Fig. 4.6.7(a) and Fig. 4.6.8)

As the Co and Co-W barrier coatings in our systems have the thickness of about 10 times to that of Madakson's, we can predict from our observations that for the Cu/Co (0.15μm)/Ni system, interdiffusion between Cu substrate and Ni overlayer occurs after heat treatment at 500°C for 7.2h. For the Cu/Co-W (0.15μm-coating A)/Ni system, in which the Co-W coatings is electroplated in a bath with W/(W+Co) ions ratio of 1/2 at 1.2 A/dm^2, interdiffusion between Cu and Ni occurs after heat treatment at 600°C for about 1.4 h.

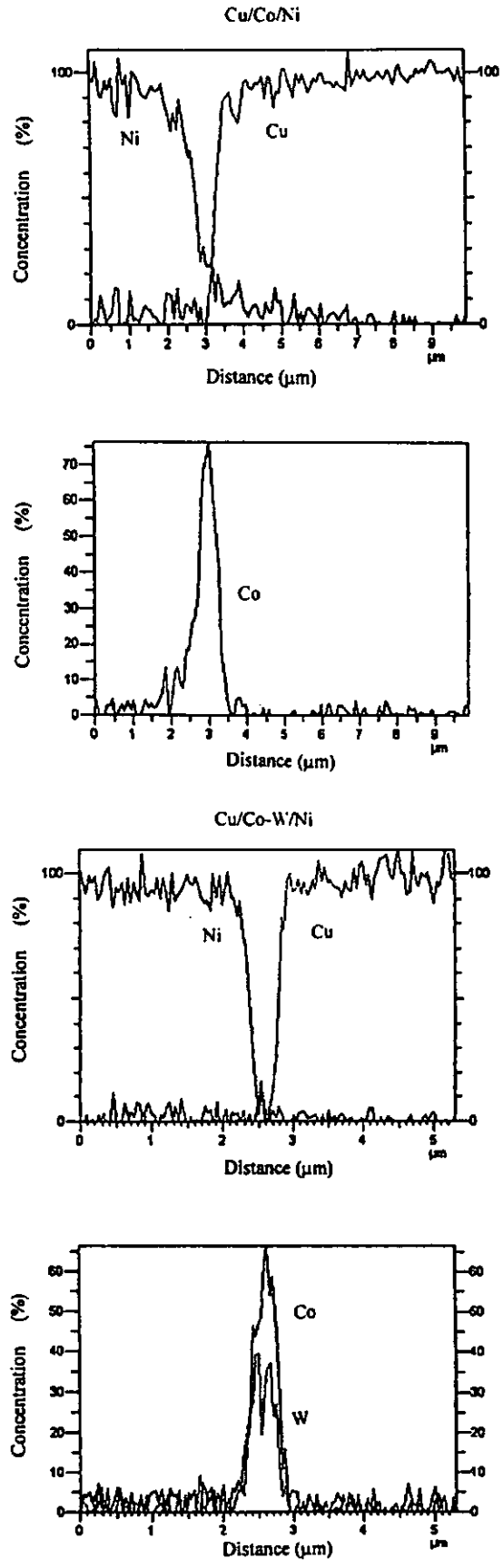

Fig. 4.6.1 and 4.6.2 Concentration-distance profiles of the Cu/Co (barrier)/Ni and Cu/Co-W (barrier-"A")/Ni systems after heat treatment at 400°C for 219 h.

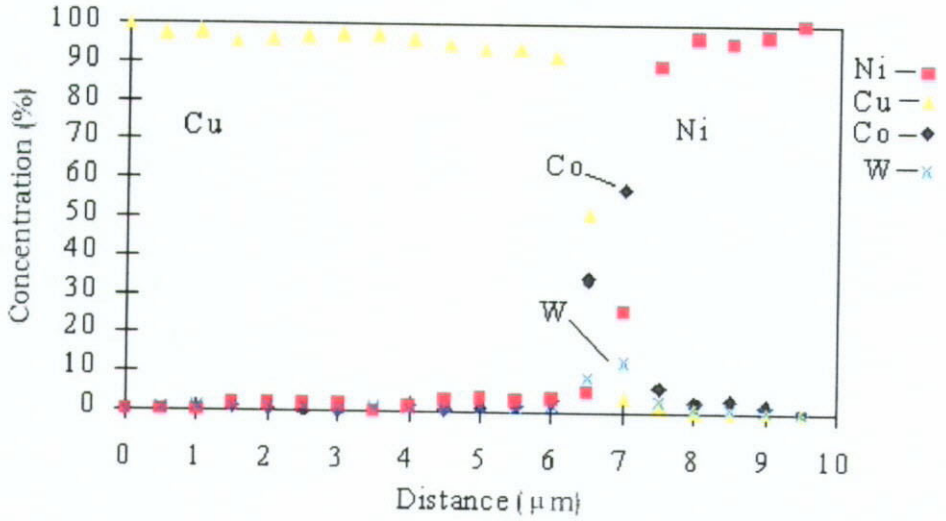

Fig. 4.6.3 Concentration-distance profiles of the Cu/Co-W (barrier-"B")/Ni system obtained by discrete EDS scan method after heat treatment at 400°C for 219 h.

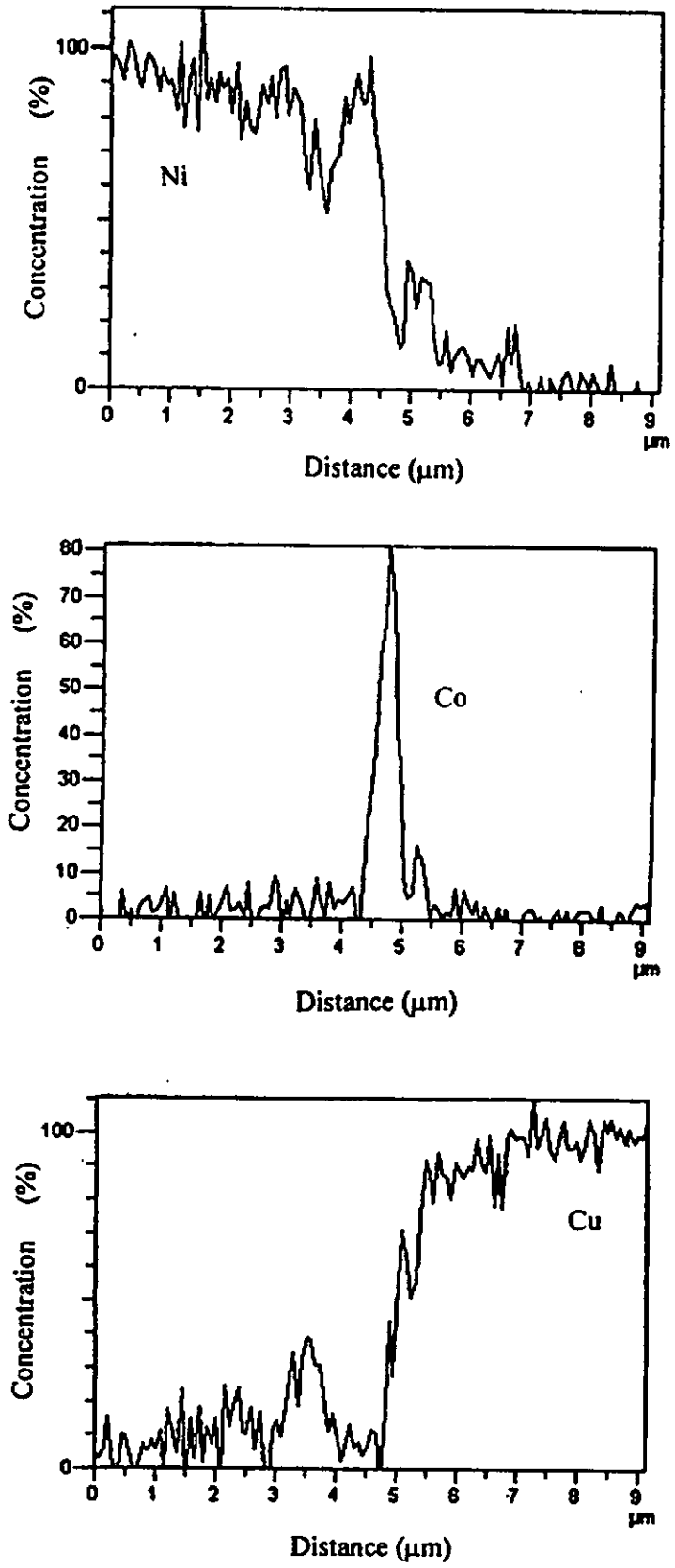

Fig. 4.6.4 Concentration–distance profiles of the Cu/Co/Ni system after heat treatment at 500°C for 72 h.

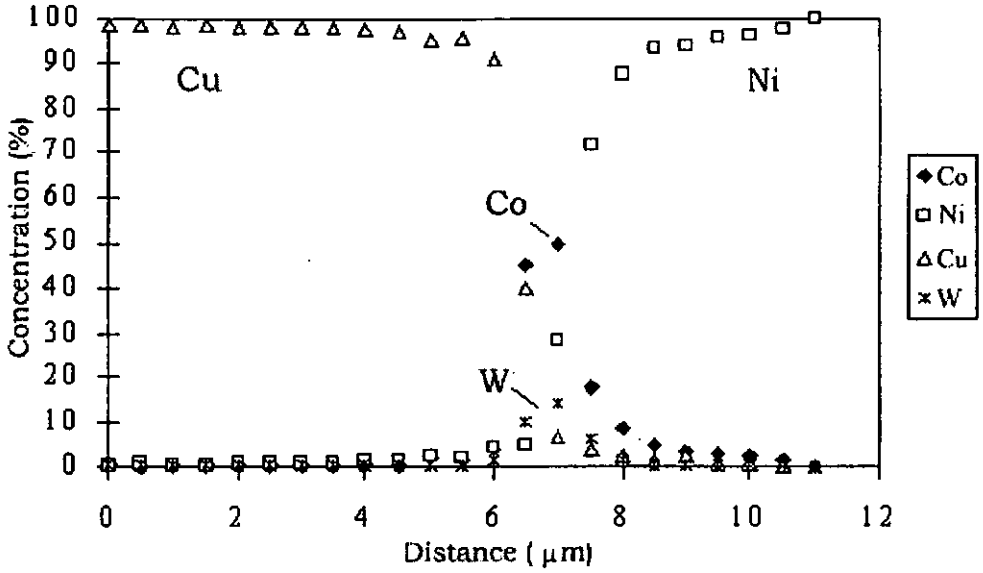

Fig. 4.6.5 Concentration–distance profiles of the Cu/Co-W (barrier-"B")/Ni system obtained by discrete EDS scan method after heat treatment at 500°C for 72 h.

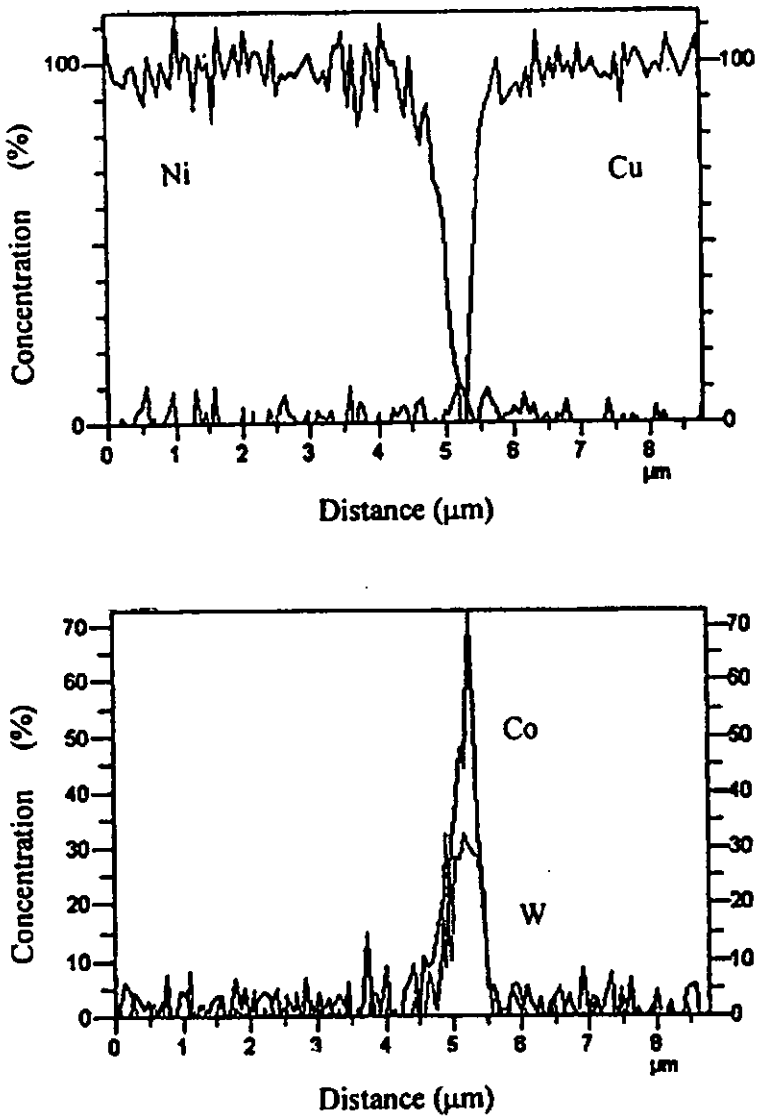

Fig. 4.6.6 Concentration-distance profiles of Cu/Co-W (barrier-"A")/Ni system after heat treatment at 500°C for 72 h.

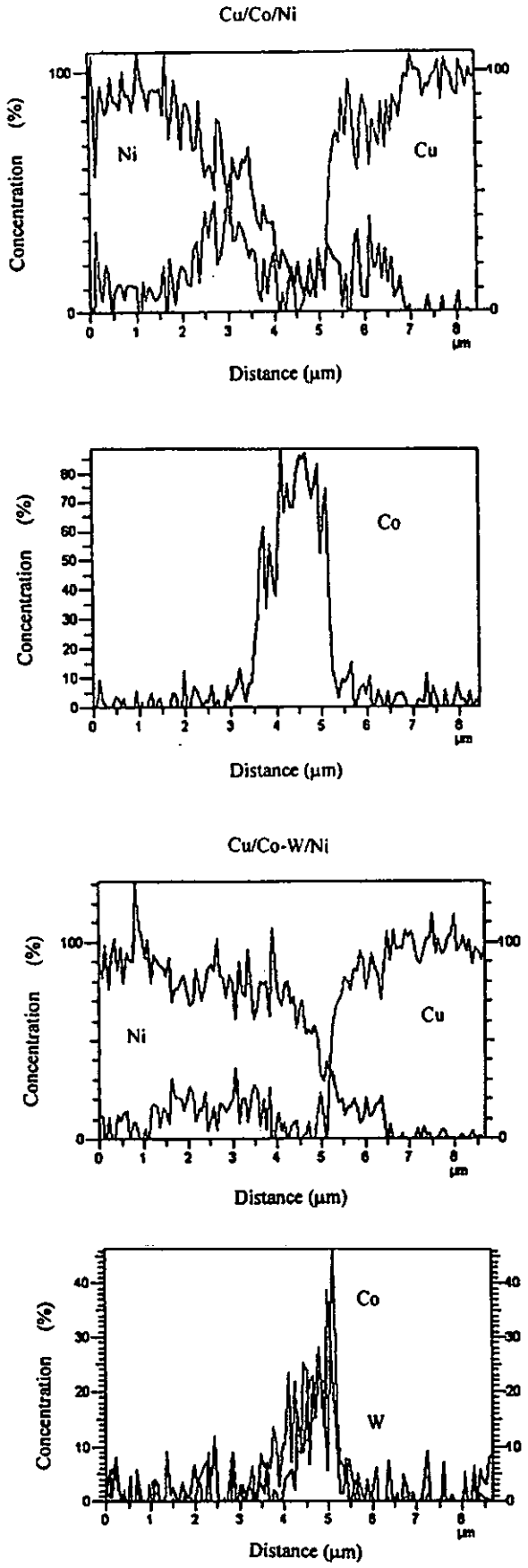

Fig. 4.6.7 Concentration-distance profiles of Cu/Co (barrier)/Ni and Cu/Co-W (barrier-"A")/Ni systems after heat treatment at 600°C for 13.6 h.

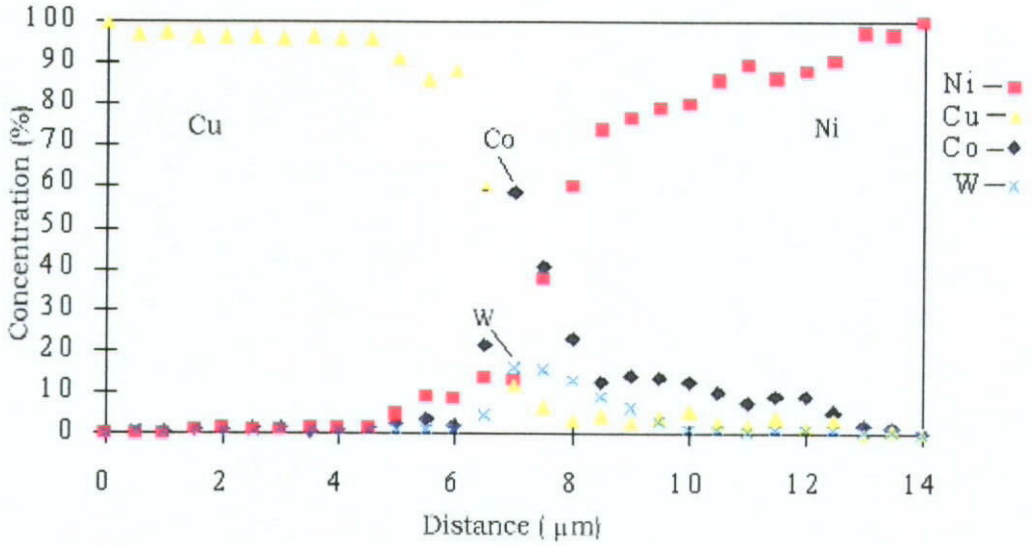

Fig. 4.6.8 Concentration-distance profiles of the Cu/Co-W (barrier-"B")/Ni system obtained by discrete EDS scan method after heat treatment at 600°C for 13.6 h.

Because of the mutual insolubility between Cu and Co, Cu was not detected by EDS in the Co or Co-W barrier coatings. The performance of cobalt and cobalt-tungsten as a diffusion barrier was determined by a semi-quantitative method. The *apparent* interdiffusion coefficient between Cu/barrier/Ni is determined by joining the two discontinued points of copper concentration on both sides of the Co or Co-W barrier, as illustrated in Fig. 4.6.9. Then the Cu concentration profiles were calculated by using Matano-Boltzman Method. The *apparent* interdiffusion coefficient between Cu and Ni would be lowered if the cobalt barrier had delayed interdiffusion between Cu and Ni. Conversely, the *apparent* interdiffusion coefficient between Cu and Ni would be increased if copper atoms diffuse into the cobalt layer with a faster speed than diffusing into nickel. The *apparent* interdiffusion coefficients of the Cu/Co (barrier)/Ni system and Cu/Co-W (barrier)/Ni systems are shown in Tables 4.6.1 to 4.6.3 respectively.

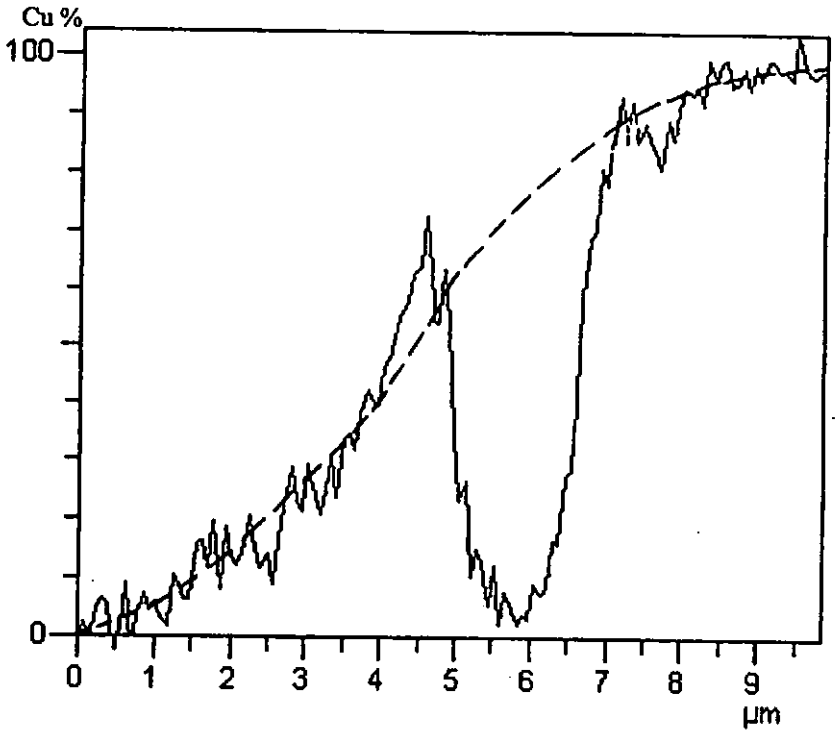

Fig. 4.6.9 Concentration-distance profile of Cu of the Cu/Co (barrier)/Ni system treated at 800°C for 45 min.; *apparent D* is determined by joining the discontinued points of the Cu concentration profile.

Table 4.6.1 *Apparent* interdiffusion coefficients of Cu/Ni for the Cu/Co (barrier)/Ni system after heat treatment at different temperatures.

Annealing temperature (°C)	Annealing time (h)	Cobalt barrier thickness (μm)	D at 20% copper (cm^2/s)	D at 30% copper (cm^2/s)	D at 40% copper (cm^2/s)	D at 50% copper (cm^2/s)
800	0.75	0.5	6.69×10^{-12}	8.21×10^{-12}	9.82×10^{-12}	1.12×10^{-11}
800	0.75	1.0	1.01×10^{-11}	8.21×10^{-12}	5.43×10^{-12}	4.26×10^{-12}
700	5	1.5	1.75×10^{-12}	1.82×10^{-12}	1.83×10^{-12}	1.80×10^{-12}
600	13.6	1.5	4.43×10^{-13}	5.49×10^{-13}	6.77×10^{-13}	8.50×10^{-13}
500	72	1.5	1.48×10^{-13}	1.27×10^{-13}	1.00×10^{-13}	8.24×10^{-14}
500	72	0.5	1.01×10^{-13}	7.92×10^{-14}	5.97×10^{-14}	4.74×10^{-14}
400	219	0.5	negligible	diffusion		
400	219	1.5	negligible	diffusion		

Annealing temperature (°C)	Annealing time (h)	Cobalt barrier thickness (μm)	D at 60% copper (cm^2/s)	D at 70% copper (cm^2/s)	D at 80% copper (cm^2/s)
800	0.75	0.5	1.17×10^{-11}	1.22×10^{-11}	1.35×10^{-11}
800	0.75	1.5	4.53×10^{-12}	9.50×10^{-12}	2.03×10^{-11}
700	5	1.5	1.88×10^{-12}	2.19×10^{-12}	2.86×10^{-12}
600	13.6	1.5	1.11×10^{-12}	1.47×10^{-12}	1.71×10^{-12}
500	72	1.5	7.85×10^{-14}	8.73×10^{-14}	1.17×10^{-13}
500	72	0.5	4.46×10^{-14}	4.84×10^{-14}	6.22×10^{-14}

Table 4.6.2 *Apparent* interdiffusion coefficients of Cu/Ni for the Cu/Co-35%W (barrier - "A")/Ni system after heat treatment at different temperatures.

Annealing temperature (°C)	Annealing time (h)	Cobalt-Tungsten barrier thickness (μm)	D at 20% copper (cm^2/s)	D at 30% copper (cm^2/s)	D at 40% copper (cm^2/s)	D at 50% copper (cm^2/s)
400	219	0.5	negligible	diffusion		
400	219	1.0	negligible	diffusion		
500	72	0.5	negligible	diffusion		
500	72	1.5	negligible	diffusion		
600	13.6	1.5	7.60×10^{-13}	5.74×10^{-13}	3.74×10^{-13}	3.04×10^{-13}
700	5	1.5	1.04×10^{-12}	1.26×10^{-12}	1.51×10^{-12}	1.80×10^{-12}
700	5	1.5	1.12×10^{-12}	1.32×10^{-12}	1.49×10^{-12}	1.84×10^{-12}
800	0.75	1.5	3.36×10^{-12}	3.51×10^{-12}	3.87×10^{-12}	4.03×10^{-12}

Annealing temperature (°C)	Annealing time (h)	Cobalt-Tungsten barrier thickness (μm)	D at 60% copper (cm^2/s)	D at 70% copper (cm^2/s)	D at 80% copper (cm^2/s)
600	13.6	1.5	2.95×10^{-13}	3.25×10^{-13}	4.05×10^{-13}
700	5	1.5	2.13×10^{-12}	2.62×10^{-12}	3.20×10^{-12}
700	5	1.5	1.84×10^{-12}	2.21×10^{-12}	2.69×10^{-12}
800	0.75	1.5	4.26×10^{-12}	9.01×10^{-12}	1.01×10^{-11}

Table 4.6.3 *Apparent* interdiffusion coefficients of Cu/Ni for the Cu/Co-35%W (barrier – "B")/Ni system after heat treatment at different temperatures.

Annealing temperature (°C)	Annealing time (h)	Cobalt-Tungsten barrier thickness (μm)	D at 20% copper (cm^2/s)	D at 30% copper (cm^2/s)	D at 40% copper (cm^2/s)	D at 50% copper (cm^2/s)
400	219	0.5	negligible	diffusion		
400	219	1.0	negligible	diffusion		
500	72	1.5	3.77×10^{-15}	2.84×10^{-15}	2.44×10^{-15}	2.17×10^{-15}
600	13.6	1.5	8.09×10^{-12}	6.50×10^{-12}	5.39×10^{-12}	4.71×10^{-12}
700	5	1.5	1.44×10^{-11}	1.26×10^{-11}	1.11×10^{-11}	1.01×10^{-11}
800	0.75	1.5	7.40×10^{-11}	8.80×10^{-11}	9.91×10^{-11}	1.07×10^{-10}

Annealing temperature (°C)	Annealing time (h)	Cobalt-Tungsten barrier thickness (μm)	D at 60% copper (cm^2/s)	D at 70% copper (cm^2/s)	D at 80% copper (cm^2/s)
500	72	1.5	2.20×10^{-15}	2.56×10^{-15}	3.65×10^{-15}
600	13.6	1.5	4.66×10^{-12}	5.12×10^{-12}	6.21×10^{-12}
700	5	1.5	1.01×10^{-11}	1.12×10^{-11}	1.38×10^{-11}
800	0.75	1.5	1.19×10^{-10}	1.44×10^{-10}	1.83×10^{-10}

To compare the diffusion barrier properties with Ni, the *apparent* interdiffusion coefficients for the Cu/Co (barrier)/Ni and Cu/Co-W (barrier coating A & B)/Ni systems at Cu concentrations of 40% and 80% Cu are summarised in Table 4.6.4. These values are useful for the evaluation on the barrier properties of Co and Co-W alloy electrodeposits.

Table 4.6.4 Interdiffusion coefficients of Cu/Ni at 40% Cu with and without Co or Co-W barriers after heat treatment at different temperatures.

Annealing temperature (°C)	Anneal. time (h)	D at 40% copper (cm^2/s) Cu/Ni	Cu/Co/Ni		Cu/Co-W(coating A)/Ni	
			Co barrier thickness 0.5μm	Co barrier thickness 1.5μm	Co-W barrier 0.5μm	Co-W barrier 1.5μm
800	0.75	4.71×10^{-12}	-	5.43×10^{-12}	-	3.87×10^{-12}
700	5	4.38×10^{-13}	-	1.83×10^{-12}	-	1.49×10^{-12}
600	13.6	1.24×10^{-13}	-	6.77×10^{-13}	-	3.74×10^{-13}
500	72	6.29×10^{-14}	5.97×10^{-14}	1.00×10^{-13}	Negligible interdiffusion	
400	219	8.46×10^{-15}	Negligible interdiffusion		Negligible interdiffusion	

Annealing temperature (°C)	Anneal. time (h)	D at 40% copper (cm^2/s) Cu/Ni	Cu/Co/Ni		Cu/Co-W(coating B)/Ni	
			Co barrier thickness 0.5μm	Co barrier thickness 1.5μm	Co-W barrier 0.5μm	Co-W barrier 1.5μm
800	0.75	4.71×10^{-12}	-	5.43×10^{-12}	-	9.91×10^{-11}
700	5	4.38×10^{-13}	-	1.83×10^{-12}	-	1.11×10^{-11}
600	13.6	1.24×10^{-13}	-	6.77×10^{-13}	-	5.39×10^{-12}
500	72	6.29×10^{-14}	5.97×10^{-14}	1.00×10^{-13}	-	2.44×10^{-15}
400	219	8.46×10^{-15}	Negligible interdiffusion		Negligible interdiffusion	

Table 4.6.4 (continue) Interdiffusion coefficients of Cu/Ni at 80% Cu with and without Co or Co-W barriers after heat treatment at different temperatures.

Annealing temperature (°C)	Anneal. time (h)	D at 80% copper (cm^2/s) Cu/Ni	Cu/Co/Ni		Cu/Co-W(coating A)/Ni	
			Co barrier thickness 0.5μm	Co barrier thickness 1.5μm	Co-W barrier 0.5μm	Co-W barrier 1.5μm
800	0.75	6.65×10^{-12}	-	2.03×10^{-11}	-	1.01×10^{-11}
700	5	1.01×10^{-12}	-	2.86×10^{-12}	-	2.69×10^{-12}
600	13.6	1.57×10^{-13}	-	1.71×10^{-12}	-	4.05×10^{-13}
500	72	9.86×10^{-14}	6.22×10^{-14}	1.17×10^{-13}	Negligible interdiffusion	
400	219	2.17×10^{-14}	Negligible interdiffusion		Negligible interdiffusion	

Annealing temperature (°C)	Anneal. time (h)	D at 80% copper (cm^2/s) Cu/Ni	Cu/Co/Ni		Cu/Co-W(coating B)/Ni	
			Co barrier thickness 0.5μm	Co barrier thickness 1.5μm	Co-W barrier 0.5μm	Co-W barrier 1.5μm
800	0.75	6.65×10^{-12}	-	2.03×10^{-11}	-	1.83×10^{-10}
700	5	1.01×10^{-12}	-	2.86×10^{-12}	-	1.38×10^{-11}
600	13.6	1.57×10^{-13}	-	1.71×10^{-12}	-	6.21×10^{-12}
500	72	9.86×10^{-14}	6.22×10^{-14}	1.17×10^{-13}	-	3.65×10^{-15}
400	219	2.17×10^{-14}	Negligible interdiffusion		Negligible interdiffusion	

Results of the diffusion experiments show that Co and Co-W are stable upon heat treatment at 400°C. Negligible interdiffusion was observed. Fig. 4.6.10 shows the optical micrograph of the Cu/Co-W (barrier)/Ni system after heat treatment at 400°C for 219h, in which there is no observable change for the Co-W barrier coating. It is noted that 0.5μm of Co or Co-W coatings can suppress interdiffusion of Cu and Ni at 400°C for more than 200 h. Co and Co-W show the better diffusion barrier properties than that of Ni for Cu interpenetration at 400°C and below. Our results also suggest that Co-W barrier coating-A can withstand Cu penetration at 500°C for 72 h, in which negligible interdiffusion was observed. There is no observable change for the Co-W barrier coating-A after heat treatment at 500°C for 72h, as shown in Fig. 4.6.11. Hence, it is superior to Ni and Co as a diffusion barrier at 500°C. Although interdiffusion occurred for the Cu/Co-W (barrier coating-B)/Ni system after heat treatment at 500°C for 72h, those D values are still smaller than those of the Cu/Co (barrier)/Ni and Cu/Ni systems. Thus, Co-W barrier coating-B also has more superior diffusion barrier properties than that of Ni and Co for Cu diffusion at 500°C.

It is interesting to note that as the temperature increases to 500°C, the Co barrier coating seems to enhance the interdiffusion of Cu and Ni. This leads to higher apparent interdiffusion coefficients of the Cu/Ni system. When the Co barrier thickness increases from 0.5 μm to 1.5 μm a much higher apparent interdiffusion coefficients of Cu/barrier/Ni is obtained. Cu atoms penetrate into Co with a faster speed than that of Ni at temperatures of 500°C or higher. Apart from the observation of concentration-distance profiles which shows interdiffusion of Cu and Ni for the Cu/Co (barrier)/Ni system at 500°C, the degradation of the Co barrier can also be revealed by the optical micrograph (Fig. 4.6.12). The breakdown of the Co barrier

properties may be related to the allotropic transformation transition of Co from h.c.p. to f.c.c structure at about 450°C (Fig. 4.6.13).

Similar trend was also observed for the Co-W coatings at 600°C. The Co-W coating of the Cu/Co-W (coating A)/Ni system had a blurred appearance after heat treatment at 600 for 13.6h, as shown in Fig. 4.6.14. Increasing the Co-W barrier coating thickness between Cu and Ni to 1.5 μm increases the apparent interdiffusion coefficient of Cu/Co-W (barrier)/Ni. Cu penetrates the Co-W barrier coatings (A and B types) with a higher rate than that of Ni at 600°C. Nevertheless, it is clearly noted that Co-W coating-A is a better diffusion barrier than that of Co at all temperatures investigated (400-800°C). The Cu/Co-W (coating-A)/Ni system gives smaller apparent interdiffusion coefficients. They are nearly 2 times smaller than those of the Cu/Co/Ni system.

Besides, Co-W (coating-B) also shows better diffusion barrier properties than that of the Co and Ni for temperatures below 500°C. Its diffusion barrier properties declines substantially when the temperature is increased to 600°C or above.

We can conclude that the crystalline Co-W barrier coating-A is a much better diffusion barrier to that of the amorphous Co-W barrier coating-B, especially at 600°C or above. For temperatures below 500°C, the comparatively better diffusion barrier properties of both the Co-W (A and B) coatings to that of Co and Ni can be attributed to their thermal stability below 500°C. It has already been shown that there is no noticeable change for the XRD spectra (Figures 4.5.5 (b) and 4.5.6 (b)) for the Co-W coatings (A and B types) after heat treatment at 500°C. This suggests Co-W coatings have a thermally stable structure up to 500°C. Rapid interdiffusion of Cu and Ni through the Co-W coating at temperatures higher than 500°C may be related to the

structural change of the Co-W coatings (A and B types) upon heat treatment at higher temperatures (Figures 4.5.5 (c), (d) and 4.5.6 (c), (d)).

A summary of a comparison among Ni, Co, Co-W (coating A) and Co-W (coating B) for their diffusion barrier properties is given in Table 4.6.5.

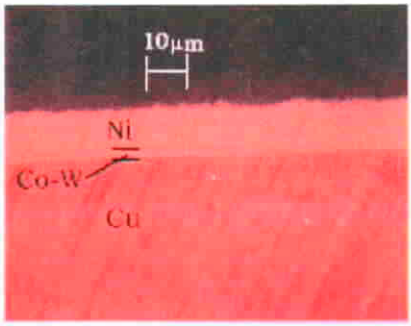

Fig. 4.6.10 Optical photograph shows a cross-sectional view of the Cu/Co-W (coating A)/Ni system after heat treatment at 400°C for 219 h.

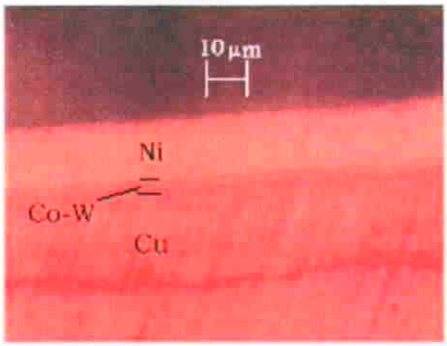

Fig. 4.6.11 Optical photograph shows a cross-sectional view of the Cu/Co-W (coating A)/Ni system after heat treatment at 500°C for 72 h.

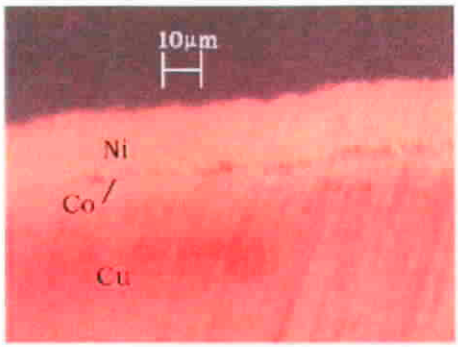

Fig. 4.6.12 Optical photograph shows a cross-sectional view of the Cu/Co/Ni system after heat treatment at 500°C for 72 h.

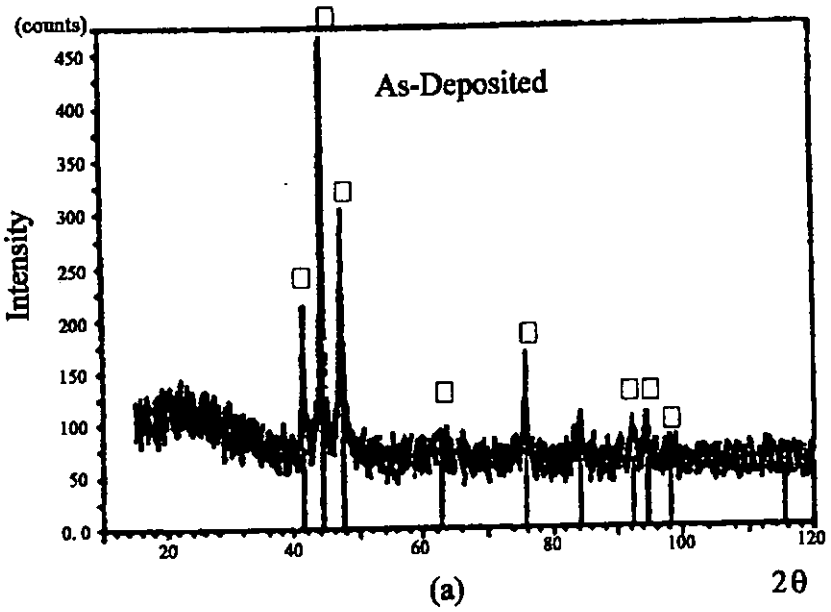

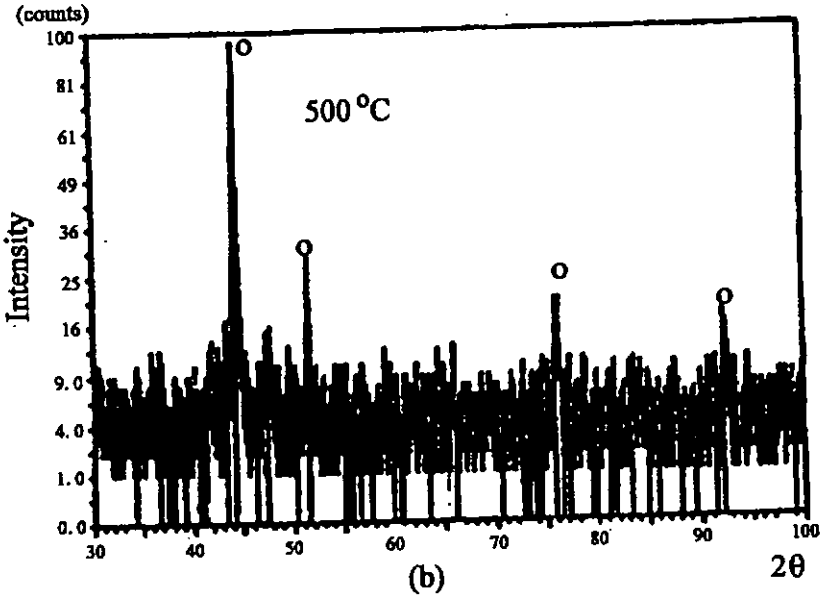

Fig. 4.6.13 XRD spectra of the cobalt coating electrodeposited at 3.6 A/dm^2.
(a) as-deposited (b) after heat treatment at 500°C for 1 hour.

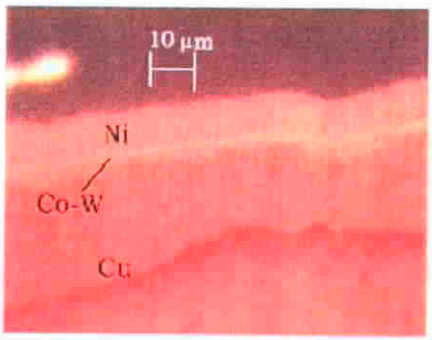

Fig. 4.6.14 Optical photograph shows a cross-sectional view of the Cu/Co-W(coating A)/Ni system after heat treatment at 600°C for 13.6 h.

Table 4.6.5 A summary of a comparison for the diffusion barrier properties of Ni, Co and Co-W (coatings A and B)

Temperature	Ability for withstanding Cu diffusion (in ascending order)
400°C	Ni < Co, Co-W (coatings A and B)
500°C	Ni ≈ Co < Co-W (coating B) < Co-W (coating A)
600-800°C	Co-W(coating B) < Co < Co-W (coating A) < Ni

Main observations for the investigation on the Co and Co-W coatings:

1. Co is a more effective barrier for Cu diffusion than Ni for up to 219 hours at 400°C while Co-W alloy coating , composed of 36 wt.% W, is a more effective barrier for Cu diffusion than Ni for up to 72 hours at 500°C.
2. Interpenetration of Cu through Co is more pronounced than diffusion of Cu through Ni for temperatures ranging from 500°C to 800°C; and interdiffusion of Cu through Co-36 wt.% W coatings (either amorphous or crystalline) is more pronounced than diffusion of Cu through Ni for temperatures ranging from 600°C to 800°C whereas crystalline Co-36wt% W is a more effective barrier than Co for Cu diffusion at all investigated temperatures (400-800°C).

3. The as-electrodeposited Co-W coating plated in a citrate bath with W/(W+Co) ratio of 1/2 at 1.2 A/dm^2 contains textured Co_3W phases and have no significant structural change up to 1 hour at 500°C. The coating composed of a mixture of Co-like f.c.c. and h.c.p. phases upon annealing at 800°C for 1.5 hours and transforms entirely to f.c.c. Co-like crystals with a certain lattice expansion upon annealing at 1100°C for 1.5 hours
4. An amorphous Co-W coating can be obtained either by increasing the W/(W+Co) ratio to 2/3 or increasing the current density to 5.1 A/dm^2. There is no significant structural change up to 1 hour at 500°C. It recrystallizes upon heat treatment at 800°C for 1.5 hour. Crystalline Co_3W phase were then observed.
5. The good diffusion barrier properties of Co and Co-W coatings (either amorphous or crystalline) are due to their good thermal stability below 500°C. Their effectiveness decline when temperature is increased to 600°C or above. These can be attributed to their structural and phase transformations as shown by their changed XRD spectra upon heat treatment.
6. Crystalline Co-W coating plated in a bath with W/(W+Co) ratio of ½ shows better diffusion barrier properties than that of the amorphous Co-W coating plated in a bath with W/(W+Co) ratio of 2/3 at all investigated temperatures. The amorphous Co-W coating is a more effective barrier than Co at 500°C or below, but it shows a poorer barrier capability than Co at 600°C or above.

4.7 Copper/Barrier/Gold Systems

To evaluate the effectiveness of different barrier coating and to measure the extent of diffusion of the copper into the gold electrodeposit upon heat treatment, a "copper penetration" (d_{Cu}) was arbitrarily defined as the distance on the copper concentration profile from the mid-plane of the barrier coating to the 10 atomic per cent copper composition plane, as shown in Fig. 4.7.1. This particular treatment of data, though biased in the direction of giving a penetration distance shorter than actual penetrations by 1.0 to 2.0 μm, provided a mean for comparison of the diffusion barrier properties among different electrodeposited coatings. This data treatment method had also been used by Marx *et al.* [58].

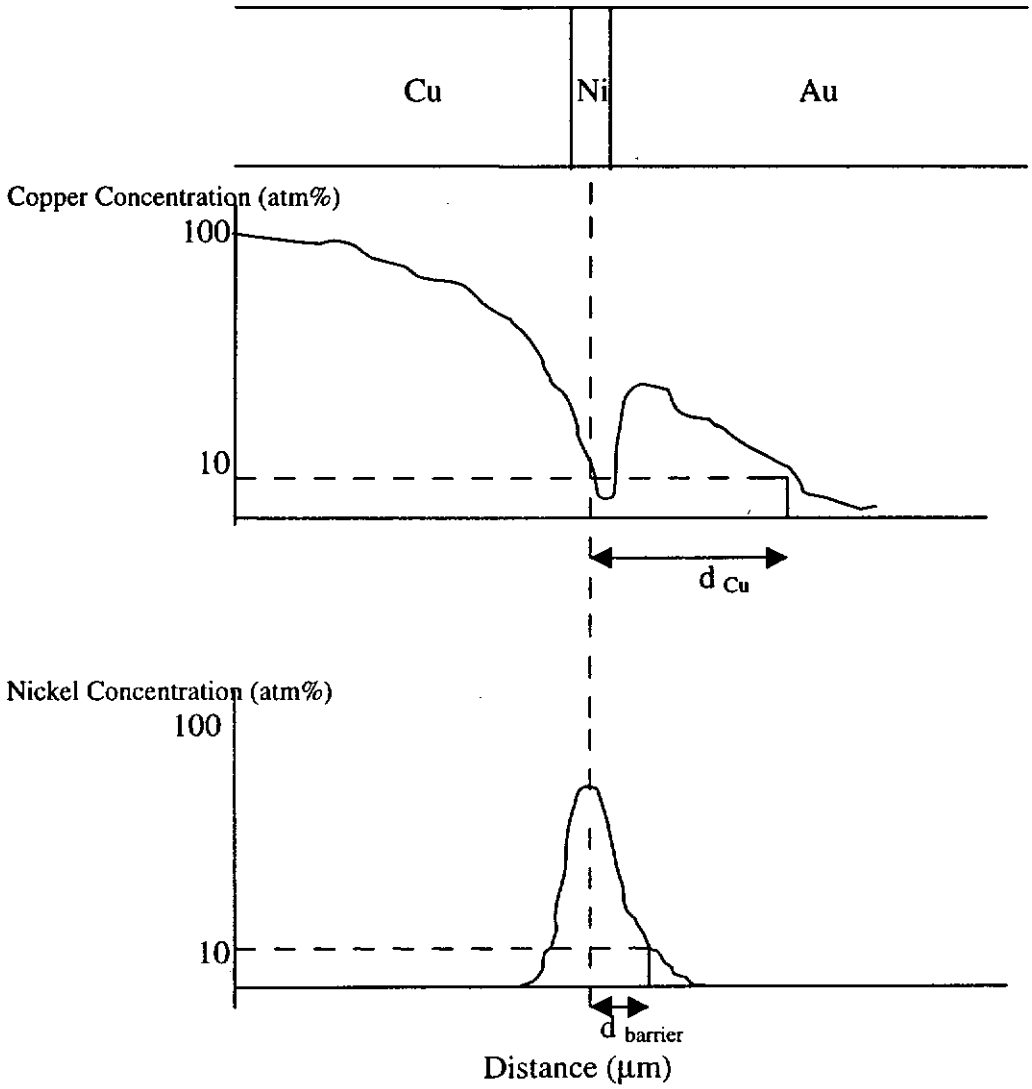

Fig. 4.7.1 illustrates the concentration-distance profiles for copper and nickel (barrier) after a diffusion heat treatment.

To be an effective barrier, diffusion of the barrier material itself to either the copper substrates or gold overplating should be small. To measure the extent of diffusion of barrier material into the gold electrodeposit upon heat treatment, a "barrier coating penetration" ($d_{barrier}$) was also defined as the distance on the barrier materials concentration profile from the central of the barrier coating to 10 atomic per cent of that barrier material.

All barrier coatings for our studies are 1μm in thickness. For example, Fig. 4.7.2 shows the cross-sectional view of the Cu/Co (1μm)/Au system by optical microscopy. Copper penetration values are presented in Table 4.7.1 for different Cu/barrier/Au specimens. To evaluate the relative effectiveness of one barrier *vs* another, comparisons were drawn between copper penetration values obtained from specimens given the same diffusion heat treatment. The values of copper penetration should be corrected within ±1 μm. The barrier material penetration distance was recorded only when it was larger than 1 μm. Negligible penetration was claimed when the penetration distance was lesser than 1 μm.

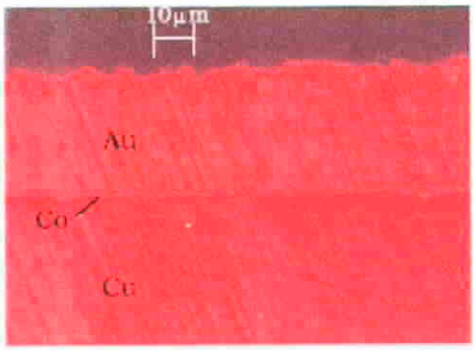

Fig. 4.7.2 Optical photograph shows the cross-sectional view of the Cu/Co (1μm)/Au system.

Table 4.7.1 Copper penetration values of different Cu/barrier/Au specimens upon heat treatment at 400°C for 24 and 48 h respectively.

Barrier	Thickness (μm)	Copper Penetration (μm)		Barrier material Penetration (μm)	
		400°C 24 h	400°C 48 h	400°C 24 h	400°C 48 h
Ni (lamellar)	1 μm	4.5	8	ND	1
Ni (columnar)	1 μm	6.5	7.5	ND	1
Pd	1 μm	8.5	9	3.5	3.5
Pd-Fe	1 μm	9.5	10.5	1	1
Co	1 μm	1.5	2	1	1
Co-W	1 μm	1	1	ND	ND

Co-W barrier plated specimens, as shown in Table 4.7.1, showed the best performance among other barrier coatings. Co-W barriers with thickness of 1 μm after heat treatments at 400°C for 24 h and 48 h respectively decreased the copper penetration distance to less than 1 μm (Fig. 4.7.3 and Fig. 4.7.4). The thermal stability of the Co-W barrier at 400°C is also good such that negligible diffusion of Co and W atoms to gold overlayer was observed. These results agree with our evaluation of the effectiveness of Co-W as diffusion barrier for copper diffusion for the Cu/Co-W/Ni systems.

Co barrier plated specimens also showed good performance as a diffusion barrier for copper diffusion. With Co barrier thickness of 1 μm, values of copper penetration are 1.5 μm and 2 μm after heat treatment at 400°C for 24 h and 48 h respectively (Fig. 4.7.5 and 4.7.6). The Co barrier penetration value to gold is about 1μm so that Co barrier also has a good thermal stability at 400°C as predicted by our evaluation of the Cu/Co/Ni systems.

Ni barrier with lamellar structure and 1 μm thickness has a smaller copper penetration value (4.5 μm) (Fig. 4.7.7) to that of the nickel barrier with columnar structure (6.5 μm) (Fig. 4.7.8) after heat treatment at 400°C for 24 h. Both nickel barriers have the similar copper penetration values after heat treatment at 400°C for 48 h (Fig. 4.7.9 and 4.7.10). The differences of copper penetration values of both barriers is due to their different initial structures. After 48h heat treatment, the nickel barrier with lamellar structure had transformed completely to columnar structure; thus both nickel barriers show similar diffusion barrier properties after a prolonged heat treatment period. Both nickel barriers also show good thermal stability at 400°C, such that they have small barrier material penetration value ($d_{barrier}$).

Copper penetration values determined from the specimens with palladium (Fig. 4.7.10 and 4.7.11) and palladium-iron (Fig. 4.7.12 and 4.7.13) barriers thickness of 1μm indicate these metals are not so effective in retarding the penetration of copper compared with Co, Co-W and Ni barriers. It is interested to note that the thermal stability of the Pd-Fe barrier is better than that of Pd barrier, for which the barrier penetration value ($d_{barrier}$) of Pd-Fe is smaller than that of the Pd barrier.

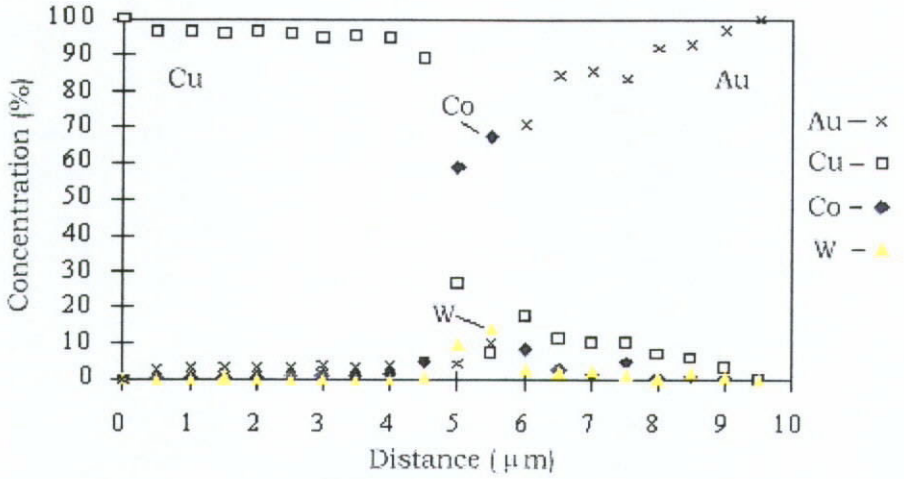

Fig. 4.7.3 Concentration-distance profile of the Cu/Co-W (1μm)/Au system obtained by discrete EDS scan method after heat treatment at 400°C for 24 h.

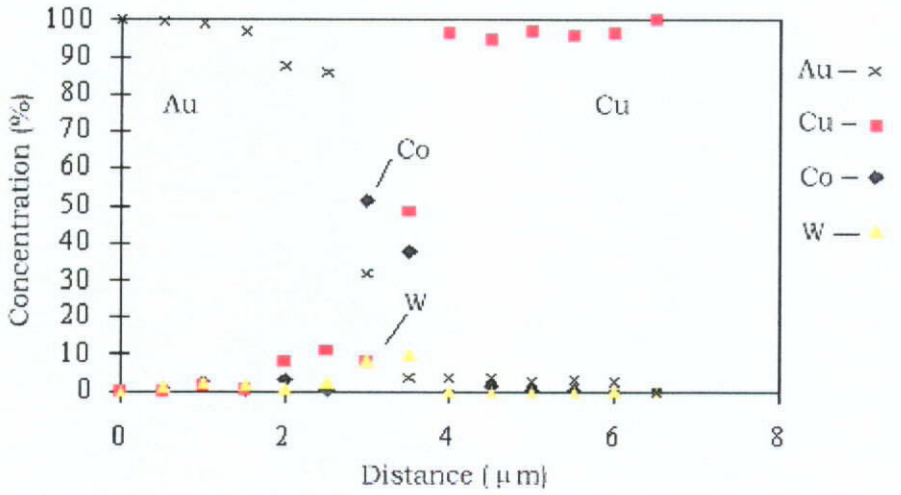

Fig. 4.7.4 Concentration-distance profile of the Cu/Co-W (1μm)/Au system obtained by discrete EDS scan method after heat treatment at 400°C for 48 h.

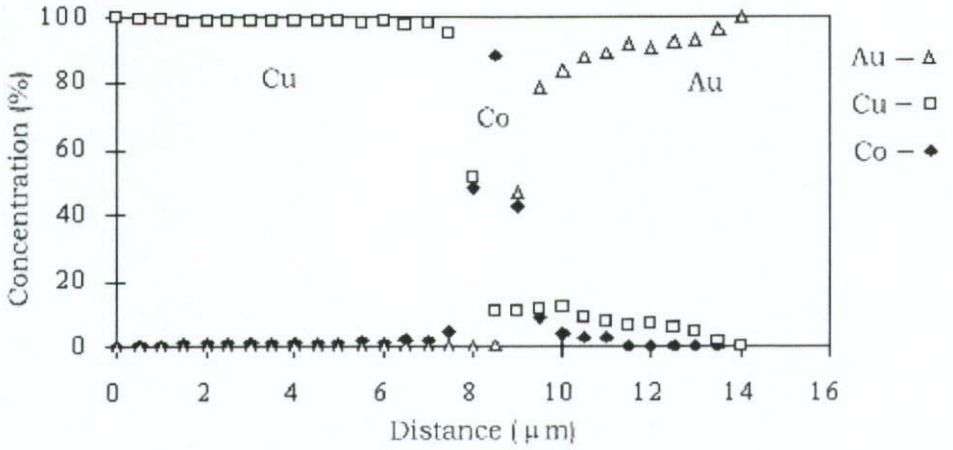

Fig. 4.7.5 Concentration-distance profile of the Cu/Co (1μm)/Au system obtained by discrete EDS scan method after heat treatment at 400°C for 24 h.

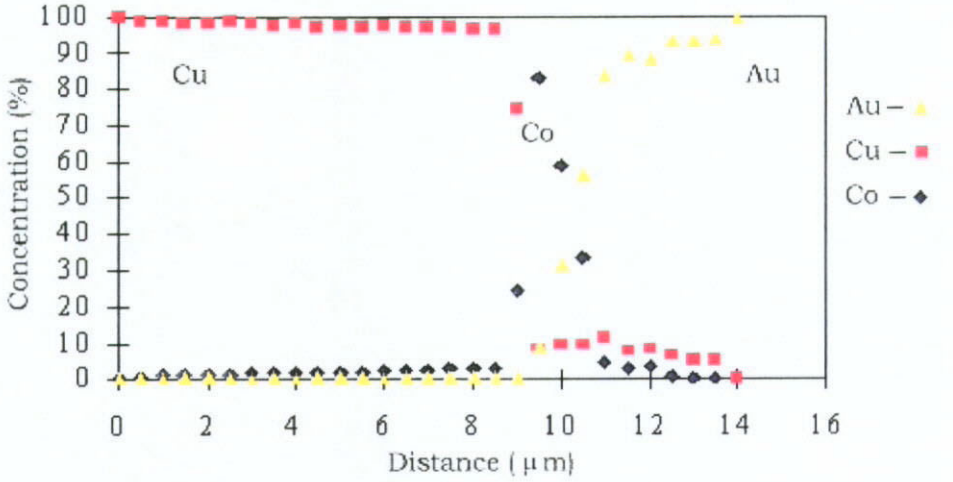

Fig. 4.7.6 Concentration-distance profile of the Cu/Co (1μm)/Au system obtained by discrete EDS scan method after heat treatment at 400°C for 48 h.

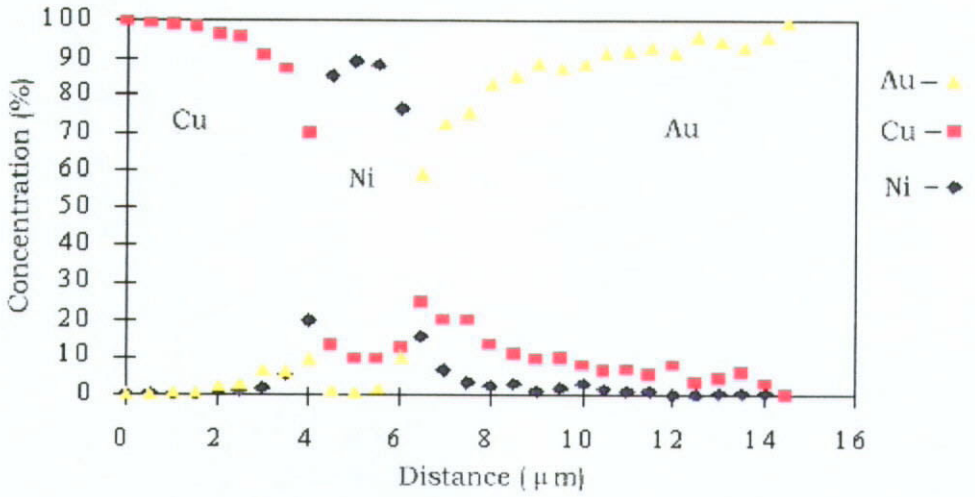

Fig. 4.7.7 Concentration-distance profile of the Cu/lamellar Ni (1μm)/Au system obtained by discrete EDS scan method after heat treatment at 400°C for 24 h.

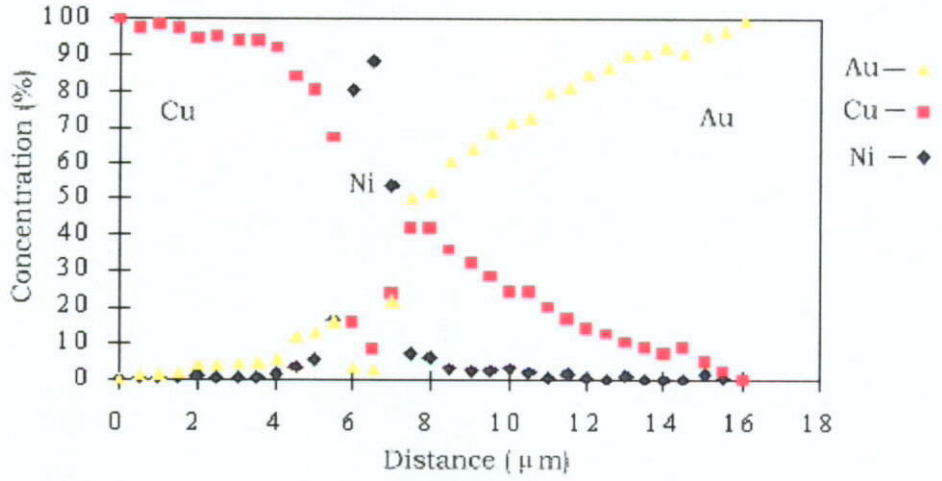

Fig. 4.7.8 Concentration-distance profile of the Cu/columnar Ni (1μm)/Au system obtained by discrete EDS scan method after heat treatment at 400°C for 24 h.

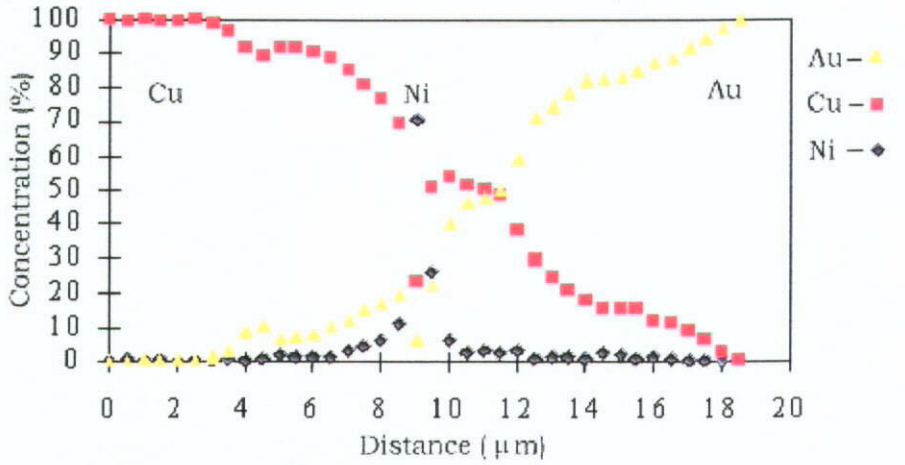

Fig. 4.7.9 Concentration-distance profile of the Cu/lamellar Ni (1μm)/Au system obtained by discrete EDS scan method after heat treatment at 400°C for 48 h.

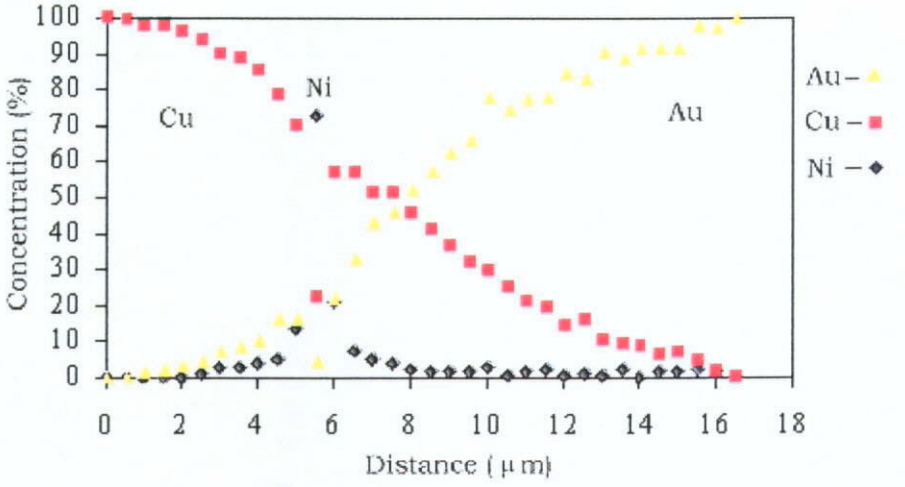

Fig. 4.7.10 Concentration-distance profile of the Cu/columnar Ni (1μm)/Au system obtained by discrete EDS scan method after heat treatment at 400°C for 48 h.

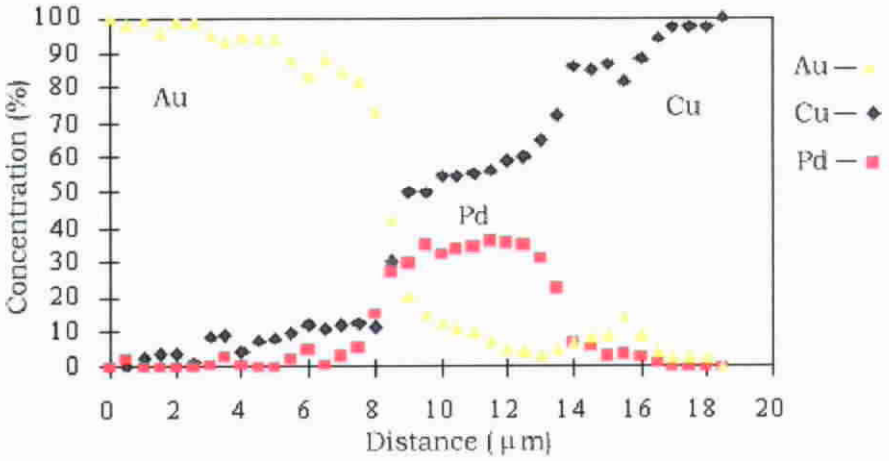

Fig. 4.7.11 Concentration-distance profile of the Cu/Pd (1μm)/Au system obtained by discrete EDS scan method after heat treatment at 400°C for 24 h.

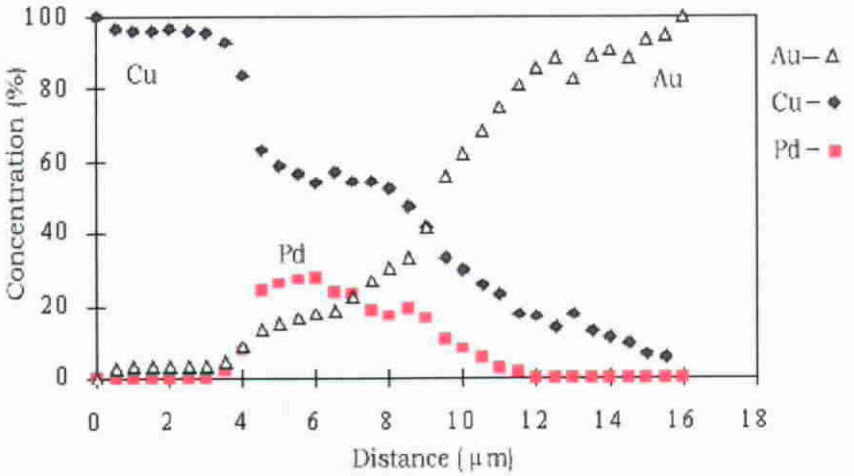

Fig. 4.7.12 Concentration-distance profile of the Cu/Pd (1μm)/Au system obtained by discrete EDS scan method after heat treatment at 400°C for 48 h.

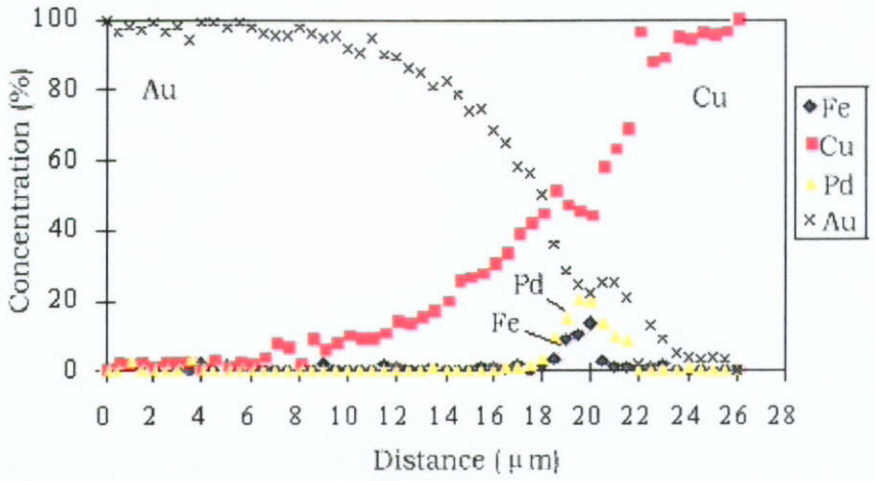

Fig. 4.7.13 Concentration-distance profile of the Cu/Pd-Fe (1μm)/Au system obtained by discrete EDS scan method after heat treatment at 400°C for 24h

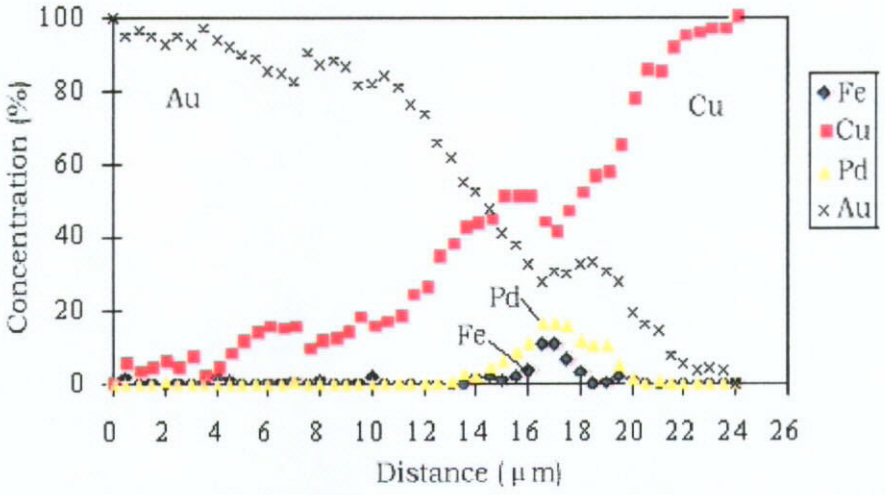

Fig. 4.7.14 Concentration-distance profile of the Cu/Pd-Fe (1μm)/Au system obtained by discrete EDS scan method after heat treatment at 400°C for 48h

Results indicate that Co-W and Co are the most effective metallic barriers studied in retarding the interdiffusion of copper and gold. From the diffusion experiments of Cu/Co/Au and Cu/Co-W/Au systems, it is also noted that cobalt-tungsten alloy is a more effective barrier than cobalt and have a better thermal stability. This observation confirms our prediction from the evaluation of the Cu/Co/Ni and Cu/Co-W/Ni systems that Co-W and Co have better diffusion barrier properties than Ni for Cu diffusion at 400°C.

From the results of the interdiffusion studies of the Cu/barrier/Au systems at 400°C, diffusion barrier capability for different electrodeposited coatings for Cu/Au interdiffusion can be ranked in ascending order as: palladium, palladium-iron, lamellar/columnar nickel, cobalt, cobalt-tungsten.

Chapter 5

Results and Discussion on DC Polarization and AC Impedance Measurements

5.1 Impedance data analysis

Assuming that a simple RC circuit validly represents a metallic surface exposed to electrolytic corrosion, the polarization resistance (R_p) for all samples were obtained by finding the arc diameter of the impedance plot. The classical Stern Geary approximation can then serve to transform these R_p's into corrosion rates. Because the adherence to this simple model is often limited to only a few data points (frequencies points), the interpretation of experimental curves are semi-quantitative only. For some cases, an Electrochemical Impedance Software (EG & G Model 398) was employed for extrapolating data points to calculate the projected arc centres

Figures 5.1 and 5.2 represent the impedance measurements made with a palladium and cobalt coating being immersed in 3% NaCl respectively. The a.c. impedance patterns for the Pd and Co coatings obtained fits the RC model reasonably well.

Since it is difficult to determine the correct semicircle through experiment points, especially if there is a significant scatter in the data. A Bode plot of log |Z| vs log f could be useful to determine R_p. At very high and very low frequency, |Z| becomes independent of frequency. Hence R_p+R_Ω can be determined by extrapolating

the low frequency data to the |Z| axis. Figures 5.3 and 5.4 show the Bode plots for the Pd and Co coatings respectively.

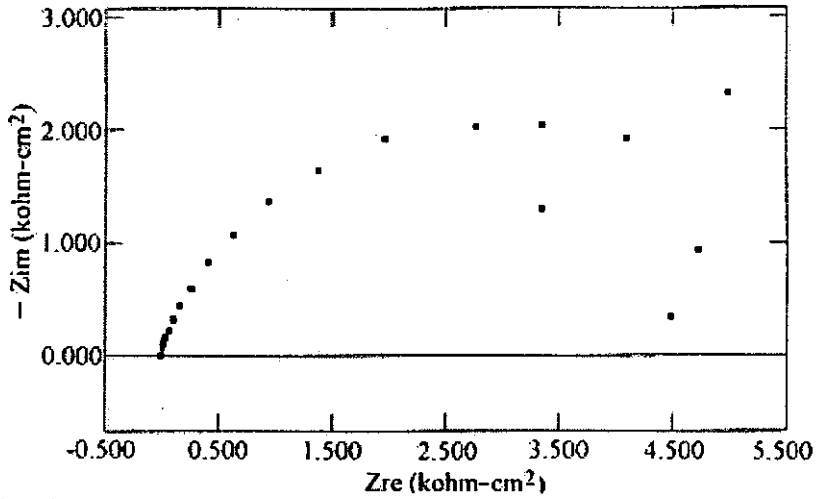

Fig. 5.1 Impedance diagram made on a Pd electrodeposited coating.

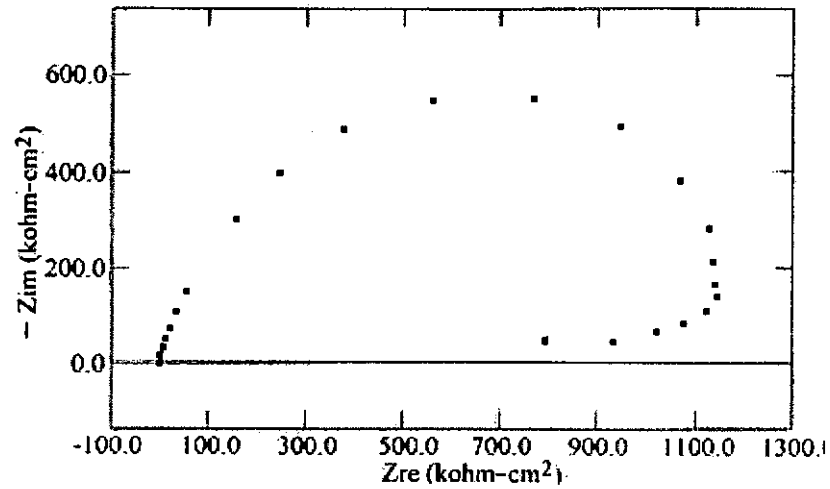

Fig. 5.2 Impedance diagram made on a Co electrodeposited coating.

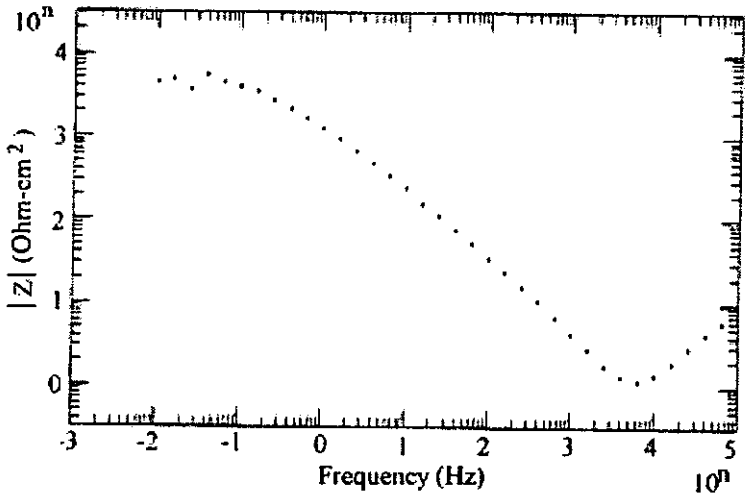

Fig. 5.3 Bode diagram made on a Pd electrodeposited coating.

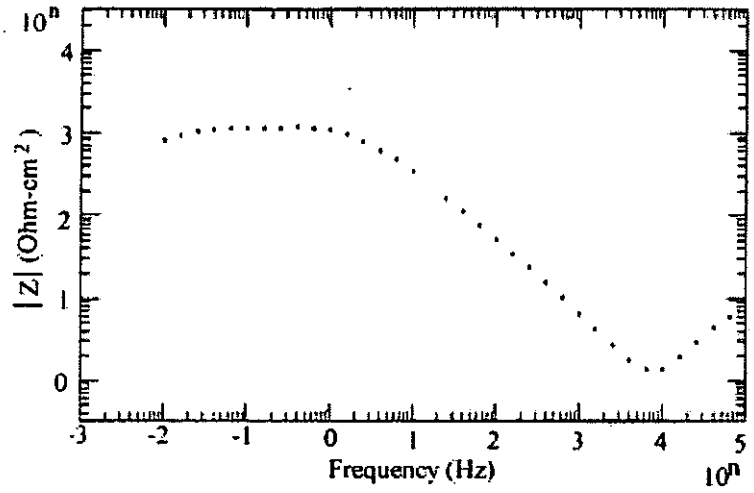

Fig. 5.4 Bode diagram made on a Co electrodeposited coating.

Figures 5.5 to 5.10 show the impedance and Bode diagrams made on three Pd-Fe alloy coatings, which indicate a difficulty in testing the Pd-Fe alloy. The low frequency measurements for the Pd-Fe alloy are scattered and erratic. The calculations of projected centres by permuting data points translate those discontinuities into a large relative standard deviation. The lower polarization resistance to that of Pd calculated for the Pd-Fe alloy is usually explained by the presence of a more active element Fe. The polarization resistance was found to decrease with increasing Fe content in the Pd-Fe alloy.

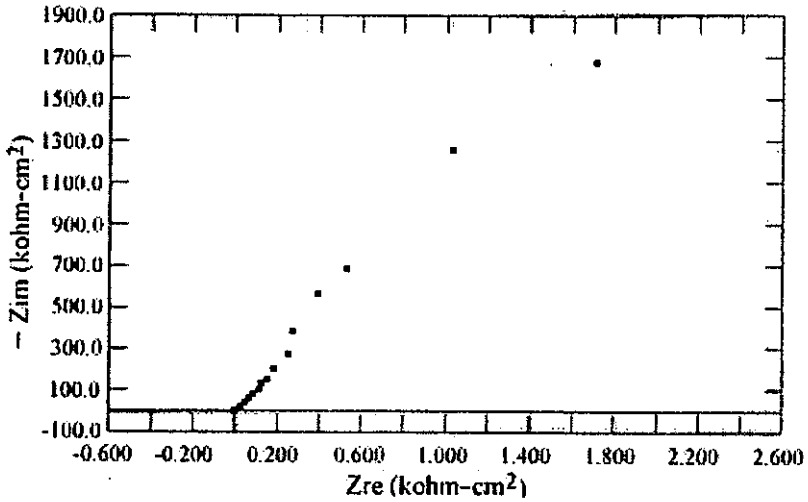

Fig. 5.5 Impedance diagram made on a 75-25 Pd-Fe alloy coating electrodeposited at 1.0A/dm^2

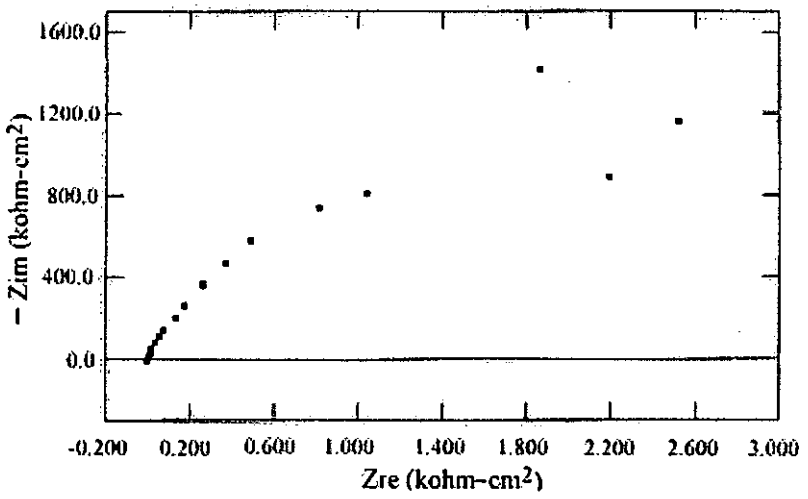

Fig. 5.6 Impedance diagram made on a 70-30 Pd-Fe alloy coating electroplated at 1.6 A/dm^2

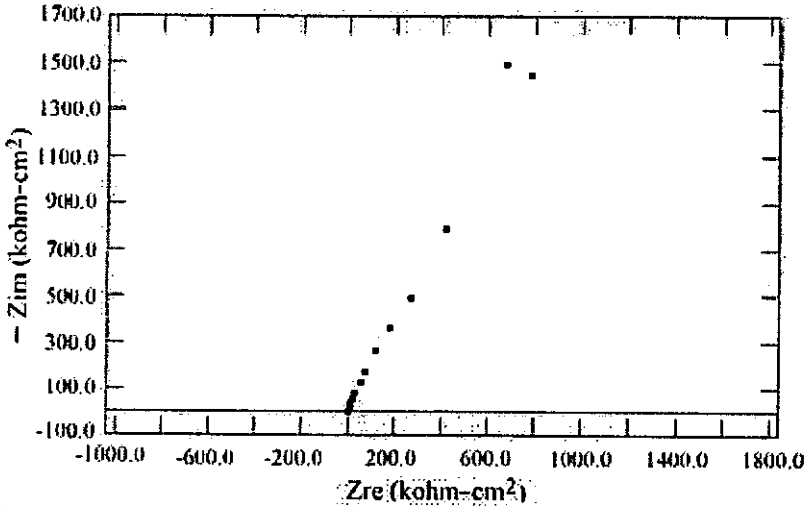

Fig. 5.7 Impedance diagram made on a 67-33 Pd-Fe alloy coating electroplated at 5.2 A/dm^2.

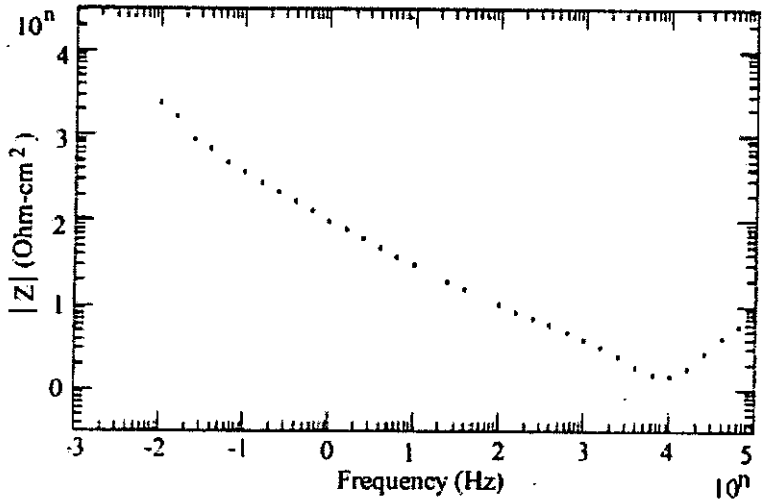

Fig. 5.8 Bode diagram made on a 75-25 Pd-Fe alloy coating electrodeposited at 1.0A/dm^2

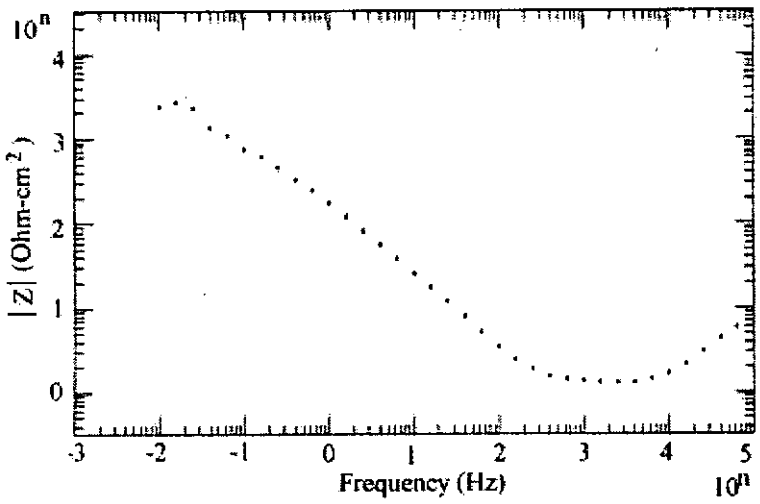

Fig. 5.9 Bode diagram made on a 70-30 Pd-Fe alloy coating electroplated at 1.6 A/dm^2

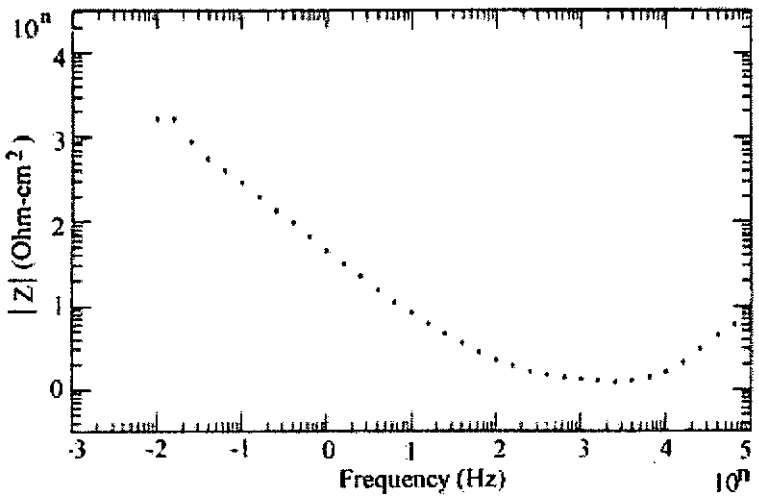

Fig. 5.10 Bode diagram made on a 67-33 Pd-Fe alloy coating electroplated at 5.2 A/dm^2.

A series of measurements are presented in Figures 5.11 to 5.20. These correspond respectively to impedance and Bode plots produced with different Co-W alloys, with W content ranging from 30wt% to 42wt%. The Co-W coatings were electroplated in the baths with different Co/(Co+W) ion ratios and at different current densities. It was found that the polarization resistances of Co-W alloy are smaller than that of the Co coating. It is interesting to note that the polarization resistance calculated for those alloys decrease with increasing W content of the Co-W alloy. Table 5.1 presents the calculated results for different Co-W alloys electroplated under different plating conditions. As reported in the earlier section, microstructure of Co-W coatings is controlled by the bath composition and plating current density (i.e. an amorphous Co-W coating can be obtained by either using a bath with Co/(Co+W) ions ratio of 2/3 or plating at current density of 5.1 A/dm^2). Our impedance measurement results for the Co-W coatings show that the polarization resistances of the Co-W coatings depend on the Co-W coatings composition as well as the microstructure of the coatings (either crystalline or amorphous). The polarization resistance of an amorphous 65-35 Co-W coating (430 ohm-cm^2) has only one-half of the value to that of the crystalline 65-35 Co-W coating (955 ohm-cm^2). It is noted that polarization resistance increases with Co content. However, the polarization resistance of the amorphous 70-30 Co-W coating (910 ohm-cm^2) is still smaller than that of the crystalline 65-35 Co-W coating.

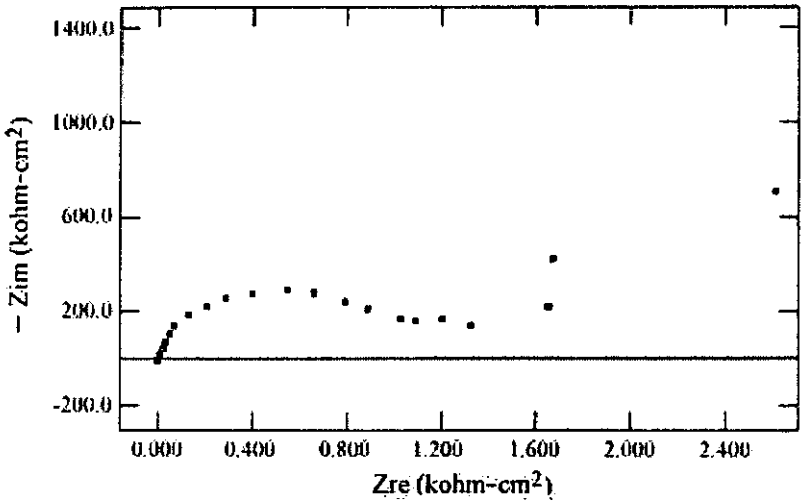

Fig. 5.11 Impedance diagram made on a 65-35 Co-W alloy coating electroplated in a bath with Co/(Co+W) ions ratio 1:2 at 1.0 A/dm^2.

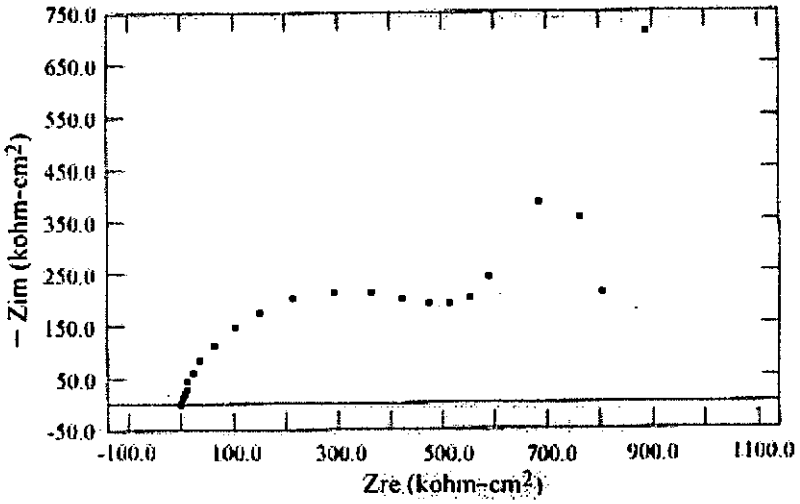

Fig. 5.12 Impedance diagram made on a 60-40 Co-W alloy coating electroplated in a bath with Co/(Co+W) ions ratio 1:2 at 3.0 A/dm^2.

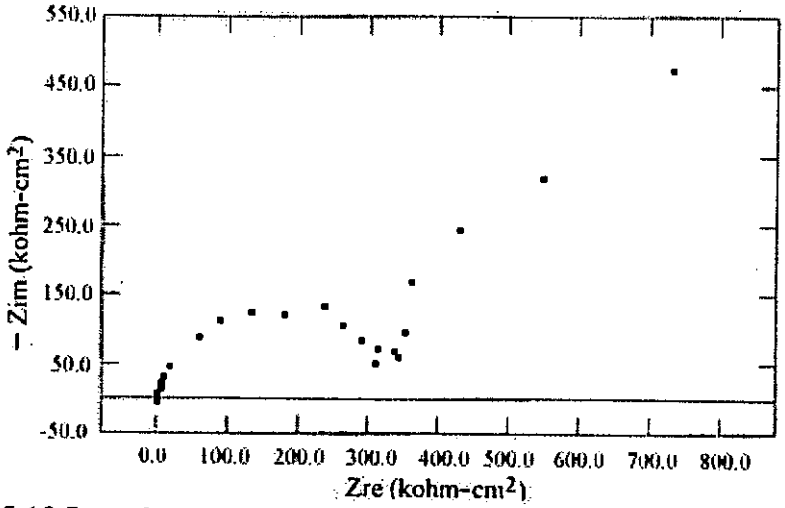

Fig. 5.13 Impedance diagram made on a 58-42 Co-W alloy coating electroplated in a bath with Co/(Co+W) ions ratio 1:2 at 5.0 A/dm^2.

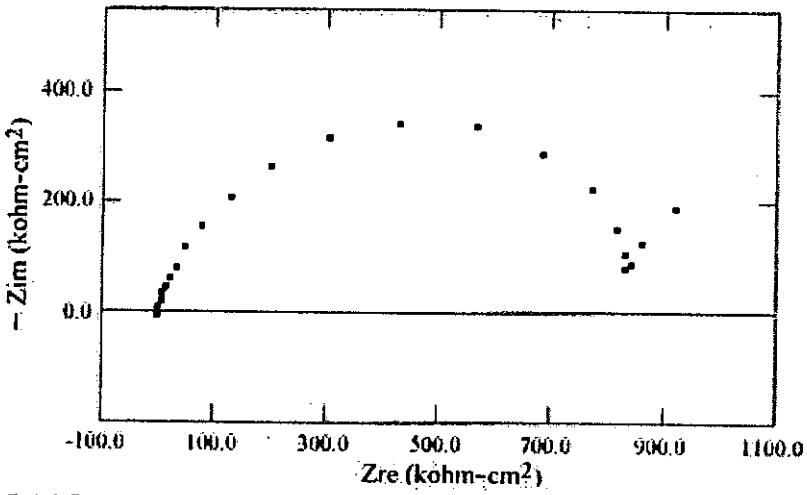

Fig. 5.14 Impedance diagram made on a 70-30 Co-W alloy coating electroplated in a bath with Co/(Co+W) ions ratio 2:3 at 1.0 A/dm^2.

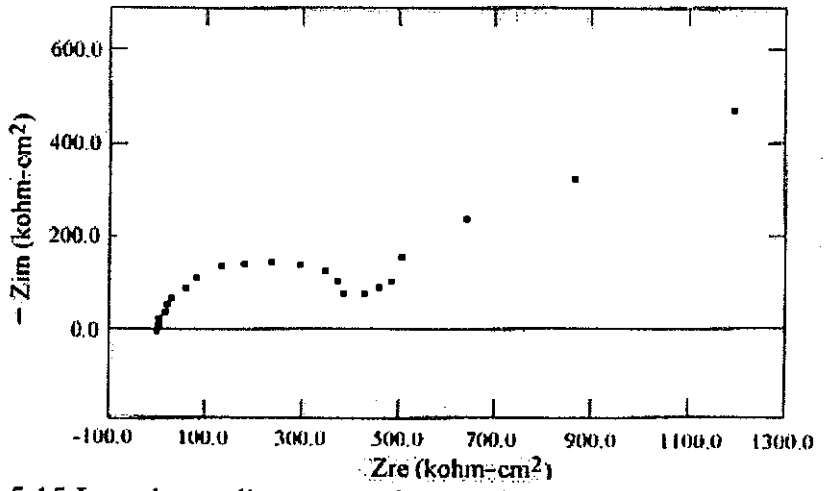

Fig. 5.15 Impedance diagram made on a 65-35 Co-W alloy coating electroplated in a bath with Co/(Co+W) ions ratio 2:3 at 5.0 A/dm^2.

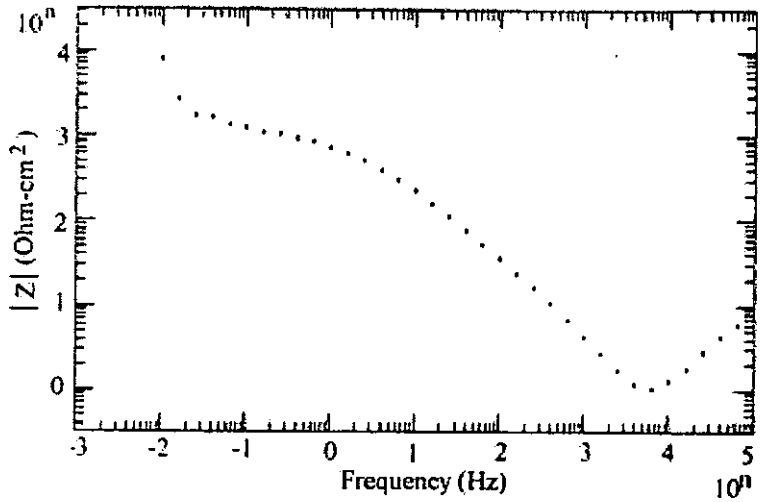

Fig. 5.16 Bode diagram made on a 65-35 Co-W alloy coating electroplated in a bath with Co/(Co+W) ions ratio 1:2 at 1.0 A/dm^2.

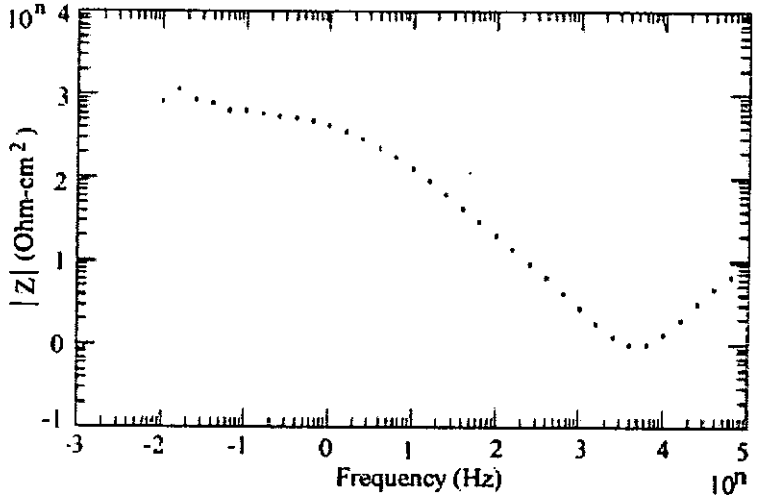

Fig. 5.17 Bode diagram made on a 60-40 Co-W alloy coating electroplated in a bath with Co/(Co+W) ions ratio 1:2 at 3.0 A/dm^2.

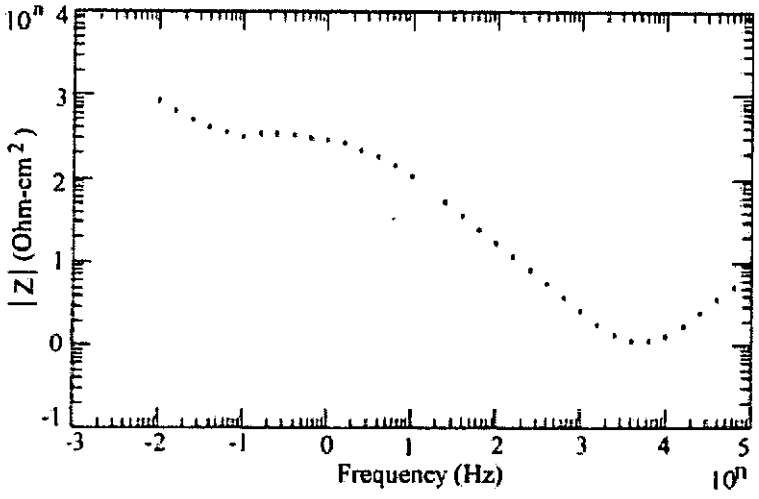

Fig. 5.18 Bode diagram made on a 58-42 Co-W alloy coating electroplated in a bath with Co/(Co+W) ions ratio 1:2 at 5.0 A/dm^2.

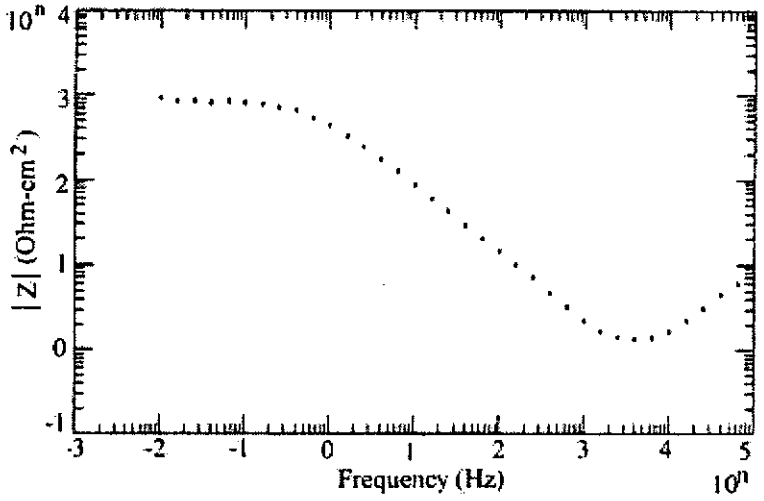

Fig. 5.19 Bode diagram made on a 70-30 Co-W alloy coating electroplated in a bath with Co/(Co+W) ions ratio 2:3 at 1.0 A/dm^2.

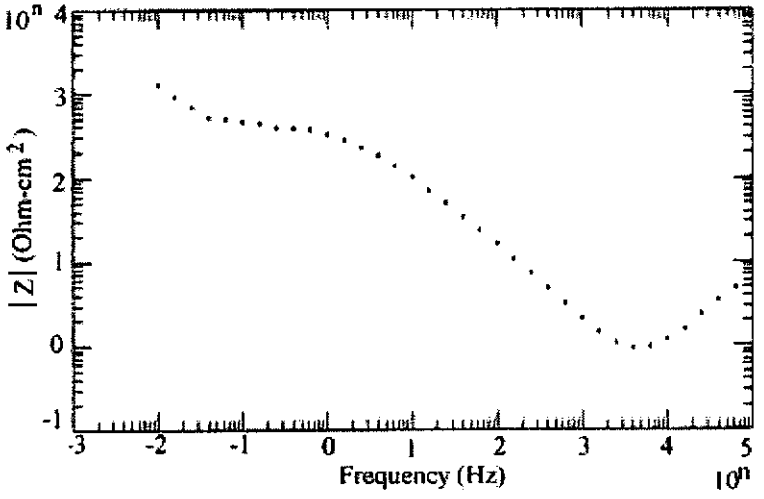

Fig. 5.20 Bode diagram made on a 65-35 Co-W alloy coating electroplated in a bath with Co/(Co+W) ions ratio 2:3 at 5.0 A/dm^2.

Figures 5.11 to 5.15 also imply the presence of oxide on the Co-W coatings in 3% NaCl. The diffusion layer effects cause the low frequency end of the Warburg impedance to bend over the real axis [49]. To account for these, it is necessary to include an additional circuit element, Warburg impedance (W), in series with R_p, as shown in Fig. 5.21. The diffusional impedance effect of the oxide depends on the Warburg coefficient for both anions and cations, σ, and the frequency of the applied ac signal, ω. The Warburg impedance has the complex number form $W = \sigma\, \omega^{-n}(1 - j)$, where $n = 0.5$ for an ideal infinite diffusional impedance [50-51].

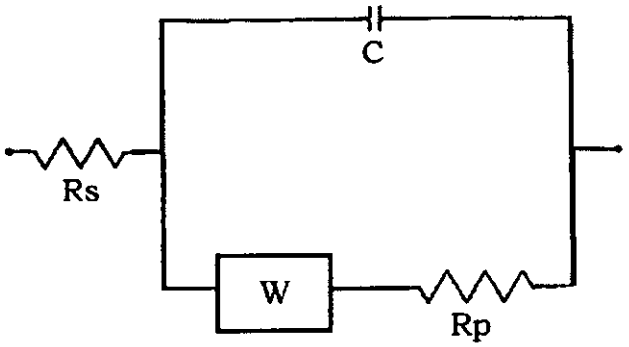

Fig. 5.21 An equivalent circuit including *Warburg* impedance component.

However, in our cases, it is still possible to extrapolate the semicircular region to the real axis and thus determine R_p. Fig. 5.22 illustrates the variation of polarization resistance R_p of different Co-W coatings.

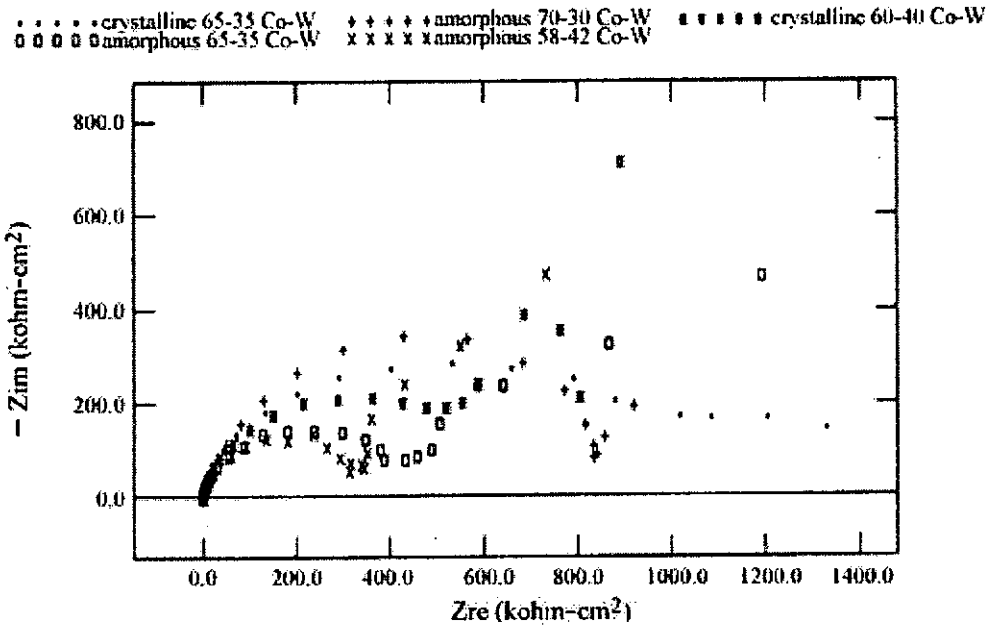

Fig. 5.22 Impedance diagrams made on different Co-W coatings, illustrating the variation of polarization resistance.

Table 5.1 Results of impedance measurements for Co-W alloy coatings electrodeposited under different plating conditions

Co/(Co+W) ions ratio	Current Density (A/dm^2)	Structure	Co-W alloy composition (Co:W)	Polarization Resistance ($ohm\text{-}cm^2$)
1:2	1.0	crystalline	65:35	955
1:2	3.0	crystalline	60:40	600
2:3	1.0	amorphous	70:30	910
2:3	5.0	amorphous	65:35	430
1:2	5.0	amorphous	58:42	350

Impedance measurement results for the columnar and lamellar nickel electrodeposit were illustrated in Figures 5.23 and 5.26 respectively. It can be seen that data points for low frequency measurement never touch the real axis to form a semi-circle. This behaviour was reproduced for many specimens of the same Ni sample, indicating a difficulty in determining the low frequency impedance. However, we can still estimate the polarization resistance of the lamellar and columnar Ni coatings by fitting the high frequency data points with a semi-circle.

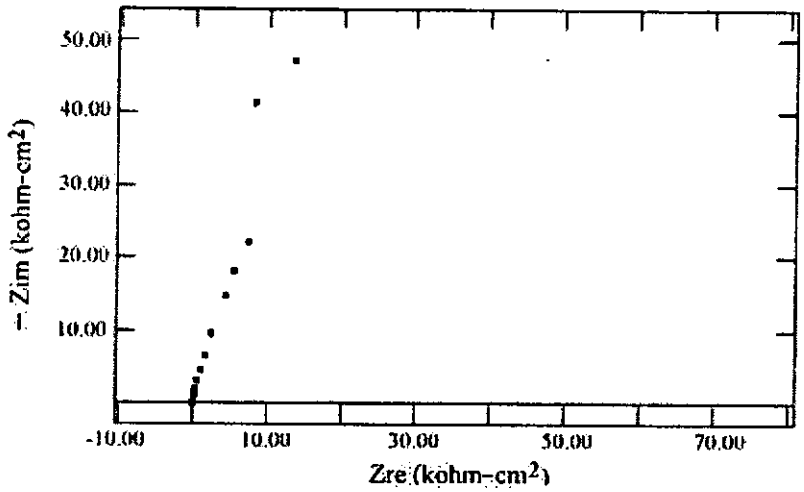

Fig. 5.23 Impedance diagram made on a columnar Ni coating.

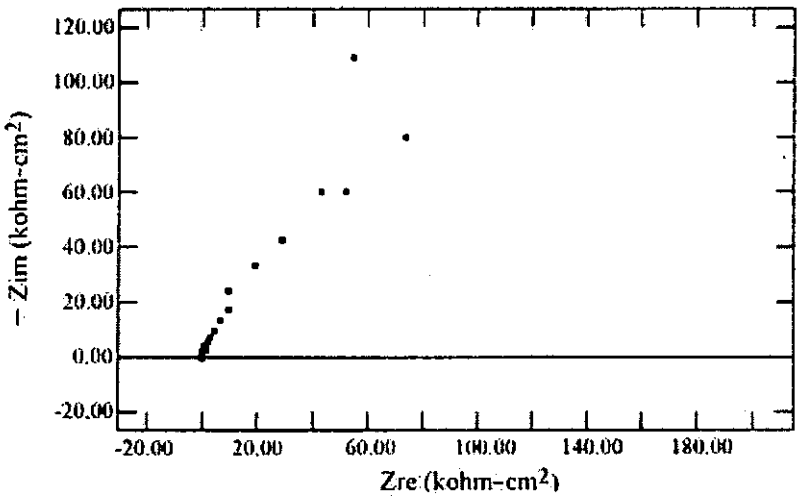

Fig. 5.24 Impedance diagram made on a lamellar Ni coating.

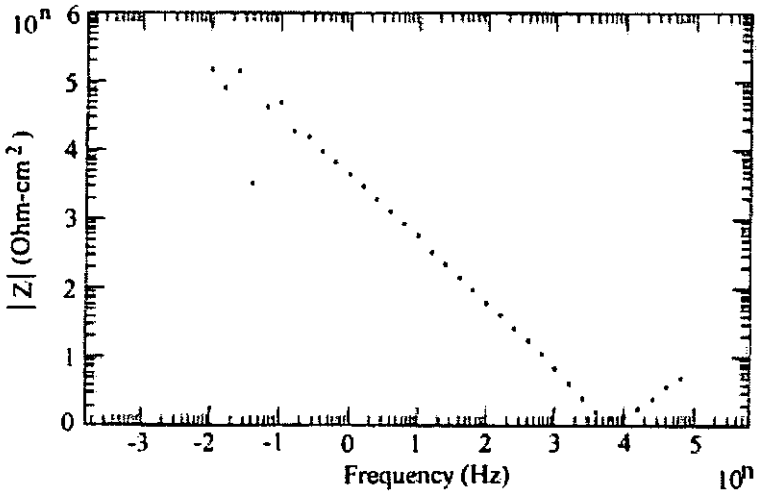

Fig. 5.25 Bode diagram made on a columnar Ni coating.

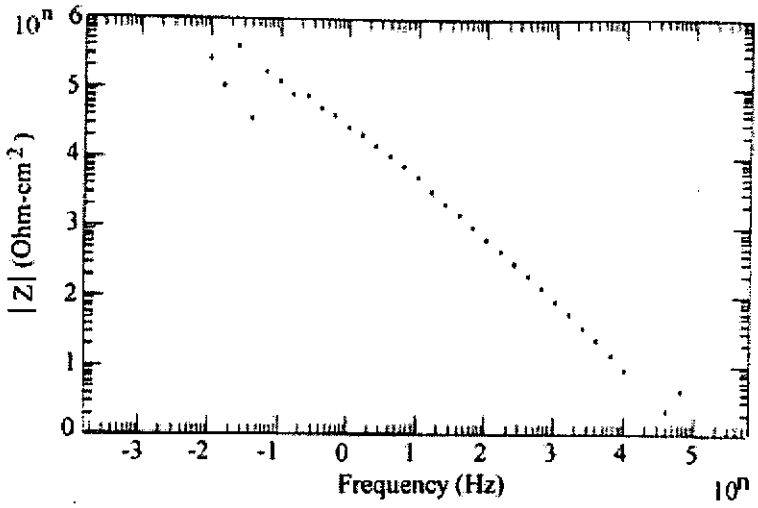

Fig. 5.26 Bode diagram made on a lamellar Ni coating.

Table 5.2 summarizes the impedance measurement results for different electrodeposited coatings.

Table 5.2 Polarization resistances calculated from impedance diagrams of different electrodeposits.

Electrodeposited Coating	Polarization Resistance (ohm-cm^2)
columnar Ni	97.5 k
lamellar Ni	62.0 k
Pd	6.15 k
Co	1.36 k
75-25 Pd-Fe	3.52 k
70-30 Pd-Fe	2.92 k
67-33 Pd-Fe	2.38 k
65-35 Co-W (crystalline)	955
60-40 Co-W (crystalline)	600
70-30 Co-W (amorphous)	910
65-35 Co-W (amorphous)	430
58-42 Co-W (amorphous)	350

5.2 DC Polarization Data Analysis

Figures 5.27 to 5.30 illustrate the potentiodynamic measurement obtained with the columnar and lamellar Ni electrodeposits. Figures 5.27 and 5.29 show the Tafel plots measured on the columnar and lamellar Ni electrodeposits respectively. The resulting potential *versus* current plots of the columnar and lamellar Ni electrodeposits obtained in 3% NaCl at a scan rate of 0.166 mV/s are given in Figures 5.28 and 5.30 respectively. The polarization resistance values ($R_p=\Delta E/\Delta I_{corr}$) are calculated from the linear region of the potential *versus* current plots using the number of data points within ±10mV of the corrosion potential to ensure maximum accuracy. Corrosion current (I_{corr}) and Tafel constants (β_a, β_c) are extracted after performing a nonlinear least squares fit of the data to the Stern-Geary equation [43]:

$$I_{corr} = \frac{\beta_a \beta_c}{2.3(\beta_a + \beta_c)R_p}$$

where β_a and β_c are Tafel proportional constants for anodic (oxidation) and cathodic (reduction) reactions.

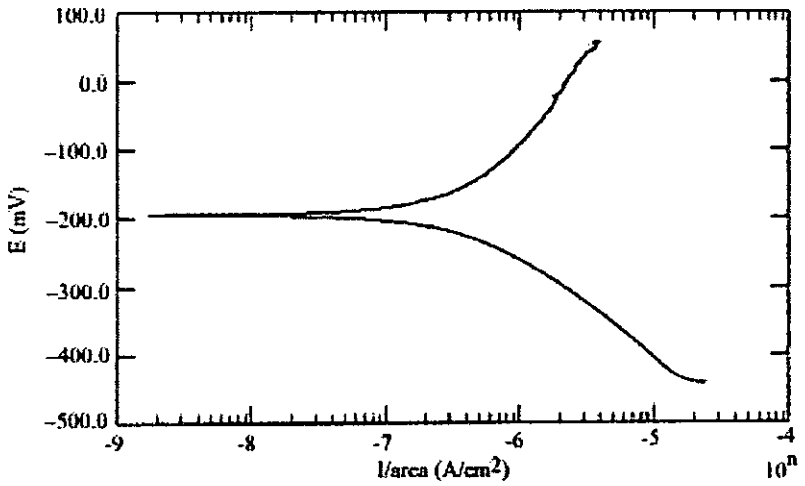

Fig. 5.27 A potential scan with ±250 mV of E_{corr} of the columnar Ni electrodeposit.

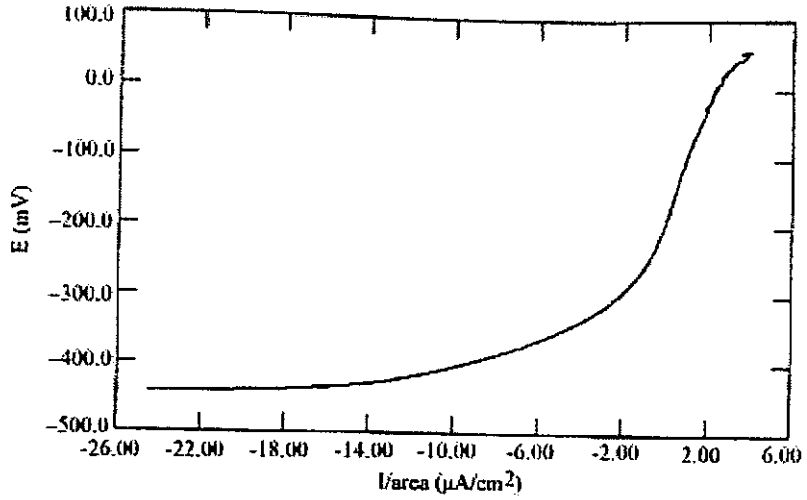

Fig. 5.28 A potential *versus* current plot with ±250 mV of E_{corr} of the columnar Ni electrodeposit. (I_{corr} was determined within ±10mV of the corrosion potential)

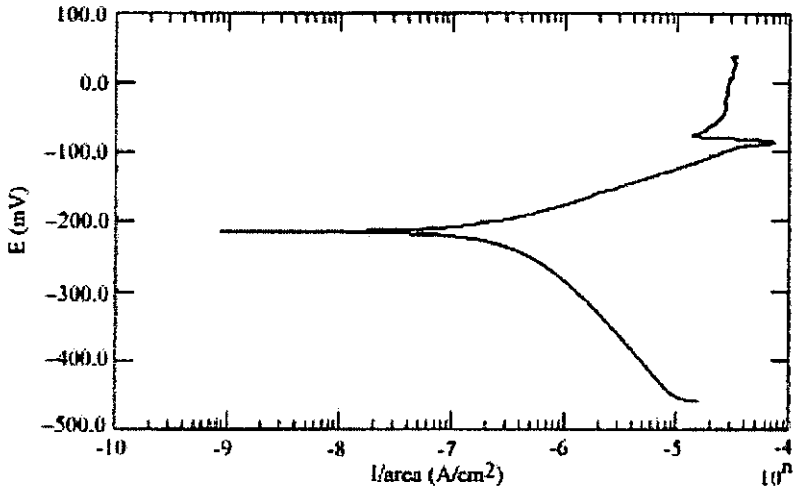

Fig. 5.29 A potential scan with ±250 mV of E_{corr} of the lamellar Ni electrodeposit.

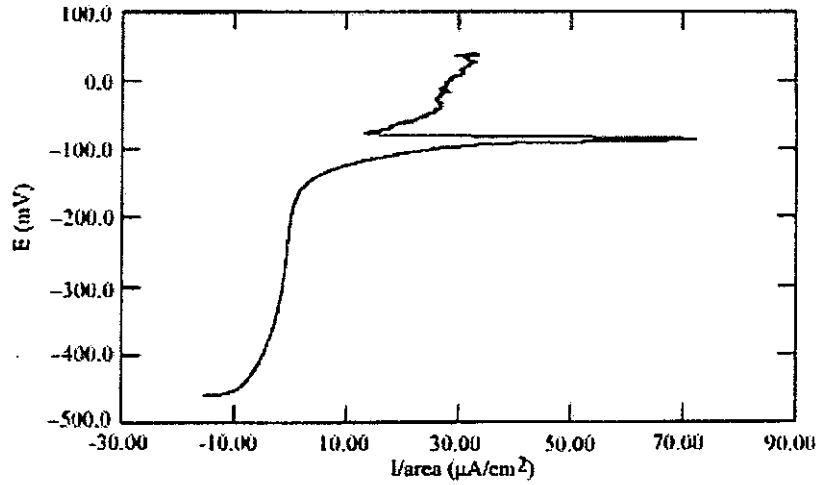

Fig. 5.30 A potential *versus* current plot with ±250 mV of E_{corr} of the lamellar Ni electrodeposit. (I_{corr} was determined within ±10mV of the corrosion potential)

Both columnar and lamellar Ni electrodeposits have relatively high polarization resistance (R_p) and low corrosion current (I_{corr}), compared with other electrodeposited coatings (Pd, Pd-Fe, Co and Co-W).

Figures 5.31 to 5.38 shows Tafel plots and potential *versus* current plots made with Pd, 75-25 Pd-Fe, Co and 65-35 Co-W electrodeposits in 3% NaCl at a scan rate of 0.166 mV/s respectively.

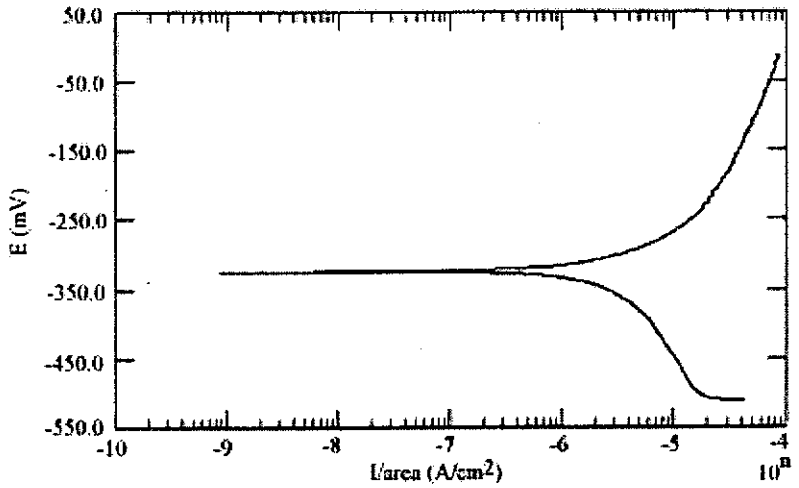

Fig. 5.31 A potential scan with ±250mV of E_{corr} of the Pd electrodeposit.

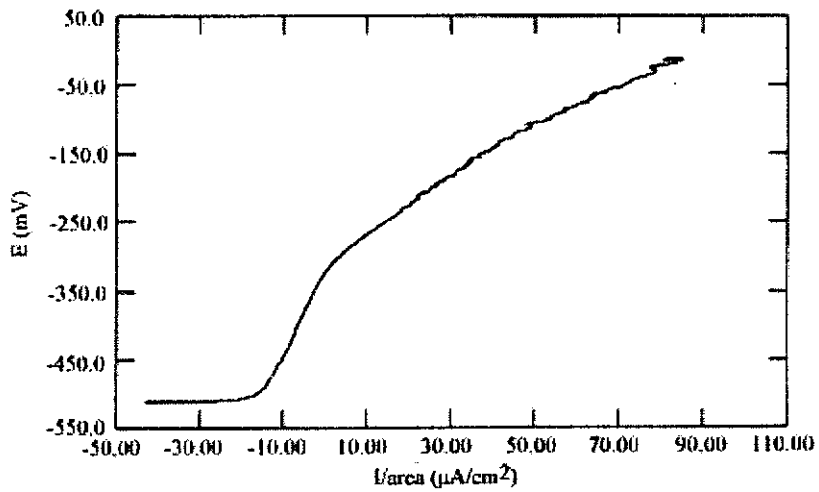

Fig. 5.32 A potential *versus* current plot with ±250mV of E_{corr} of the Pd electrodeposit. (I_{corr} was determined within ±10mV of the corrosion potential)

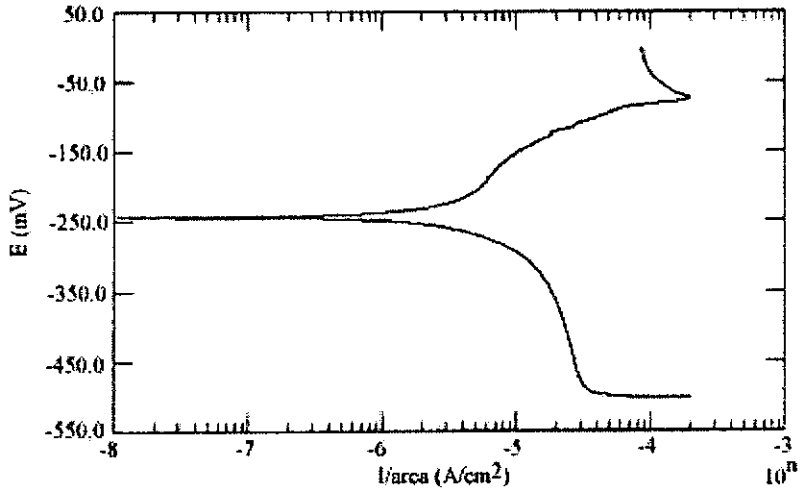

Fig. 5.33 A potential scan with ±250 mV of E_{corr} of the 75-25 Pd-Fe electrodeposit.

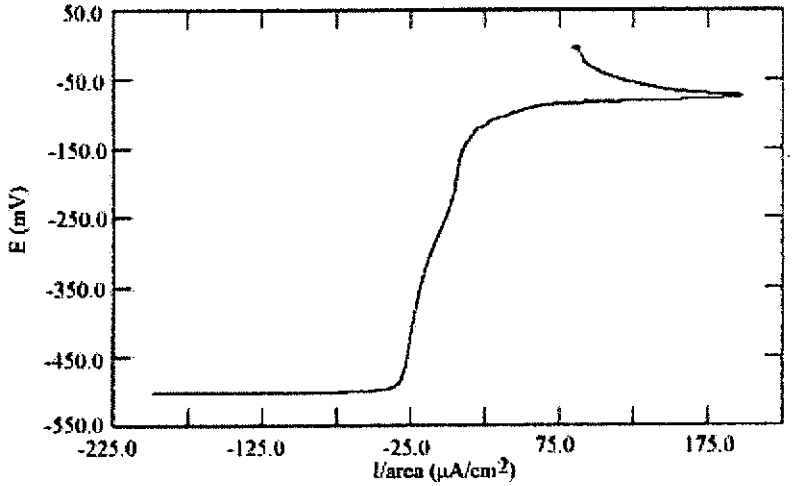

Fig. 5.34 A potential *versus* current plot with ±250 mV of E_{corr} of the 75-25 Pd-Fe electrodeposit. (I_{corr} was determined within ±10mV of the corrosion potential)

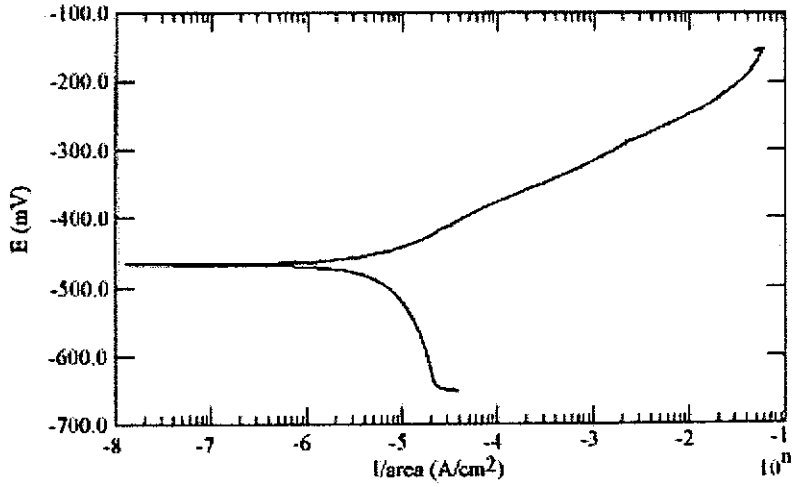

Fig. 5.35 A potential scan with ±250 mV of E_{corr} of the Co electrodeposit.

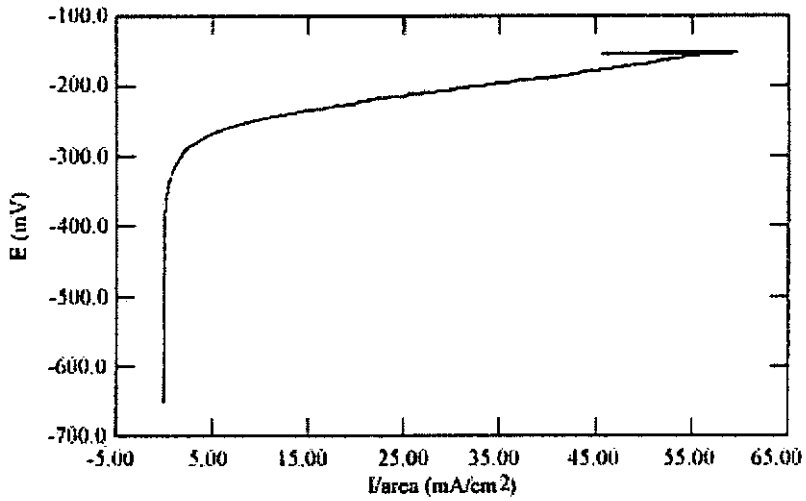

Fig. 5.36 A potential *versus* current plot with ±250 mV of E_{corr} of the Co electrodeposit. (I_{corr} was determined within ±10mV of the corrosion potential)

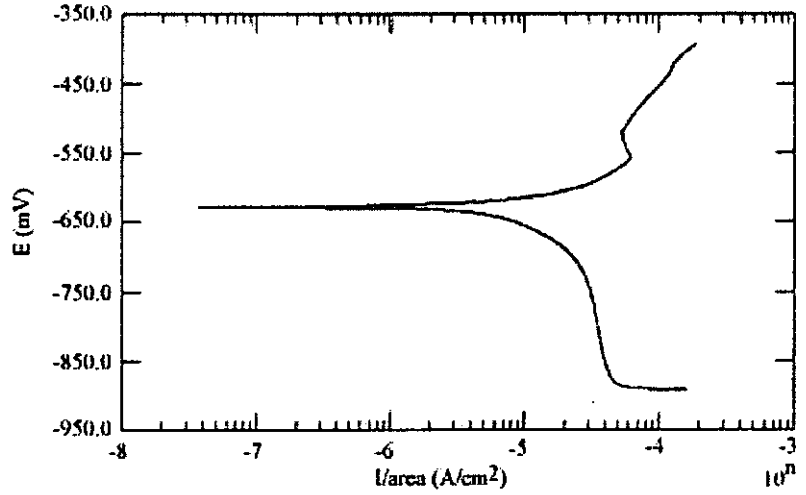

Fig. 5.37 A potential scan with ±250 mV of E_{corr} of the 65-35 Co-W coating electroplated in a bath with Co/(Co+W) ions ratio of ½ at 1 A/dm^2.

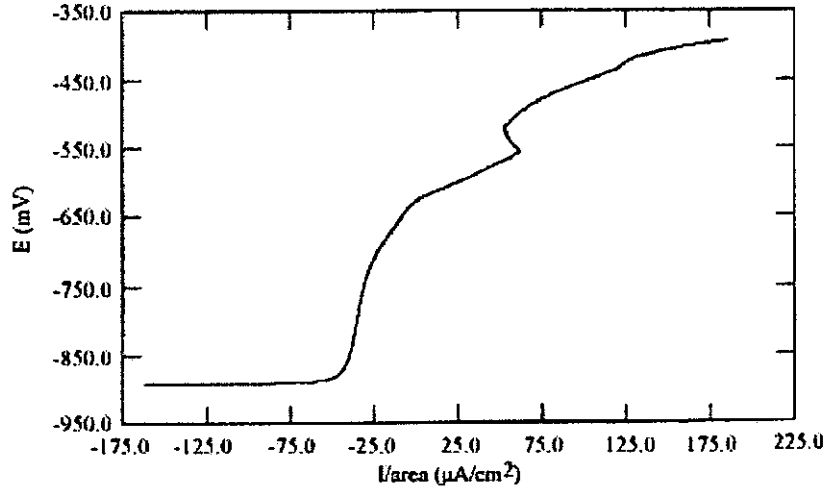

Fig. 5.38 A potential *versus* current plot with ±250 mV of E_{corr} of the 65-35 Co-W coating electroplated in a bath with Co/(Co+W) ions ratio of ½ at 1 A/dm^2. (I_{corr} was determined within ±10mV of the corrosion potential)

The calculated resulting values for polarization resistance (R_p), corrosion potential (E_{corr}), corrosion current (I_{corr}) are given in Table 5.3.

Table 5.3 Calculated values of E_{corr}, R_p and I_{corr} for different electrodeposits.

Specimen	E_{corr}(mV)	R_p(kohm-cm^2)	I_{corr}(μA/cm^2)
columnar Ni	-0.1936	93.91	0.4533
lamellar Ni	-0.21410	64.44	0.4591
Pd	-0.2433	8.57	10.220
75-25 Pd-Fe	-0.3241	5.63	12.520
Co	-0.4670	3.30	8.558
65-35 Co-W	-0.6276	1.55	70.70

The data show that the 65-35 Co-W coating is the most active coating in 3% NaCl which has the most negative E_{corr} (-0.6276 mV), the smallest R_p (1.55 kohm-cm^2) and the largest I_{corr} (70.70 μA/cm^2) among different electrodeposits. There is only small difference in terms of E_{corr}, R_p and I_{corr} between columnar and lamellar Ni coatings. Although Pd gives a higher R_p value compared with 75-25 Pd-Fe and Co coatings, the I_{corr} values among these coatings are similar. To show their different corrosion properties, Tafel plots made with different electrodeposited coatings are illustrated together in Fig. 5.39.

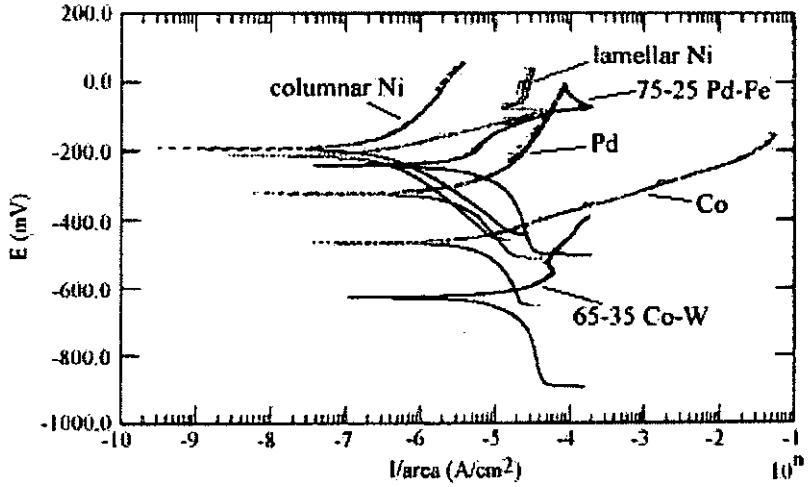

Fig. 5.39 Potential scan with ±250 mV of E_{corr} of different coatings.

It is interesting to note that the polarization resistance calculated for Co-W alloy coating decreases with increasing W content. The E_{corr} value also becomes more negative as the W content in the Co-W alloy increases though their differences are small, as shown in Fig. 5.40. Table 5.4 presents the calculated results for different Co-W alloys electroplated under different plating conditions.

Table 5.4 Results of polarization measurements for Co-W alloy coatings electrodeposited under different plating conditions

Co/(Co+W) ions ratio	Current Density (A/dm^2)	Structure	Co-W alloy composition (Co:W)	Polarization Resistance R_p ($kohm\text{-}cm^2$)	Corrosion Potential Ecorr (mV)
1/2	1.0	crystalline	65:35	1.550	-0.6276
2/3	1.0	amorphous	70:30	1.057	-0.6497
2/3	5.0	amorphous	65:35	0.911	-0.6516
1/2	5.0	amorphous	58:42	0.843	-0.6581

Moreover, crystalline 65-35 Co-W coating gives a higher polarization resistance and less negative E_{corr} value than that of the amorphous 65-35 Co-W coating. Even amorphous 70-30 Co-W coating has a smaller polarization resistance than that of the crystalline 65-35 Co-W coating.

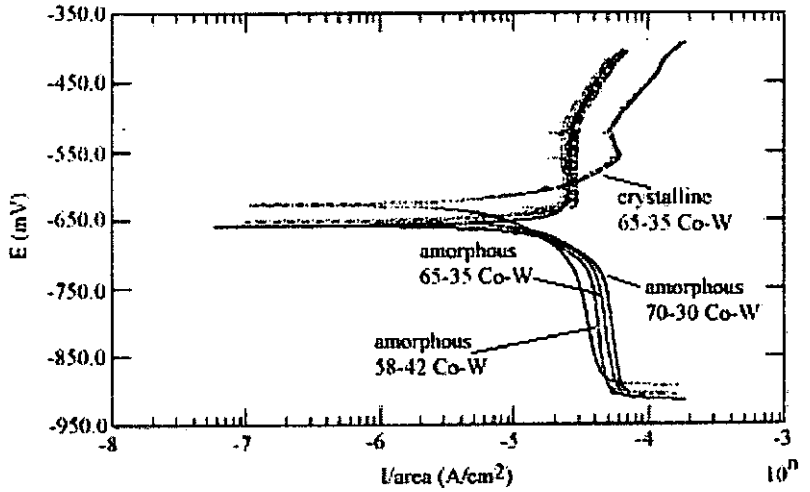

Fig. 5.40 Potential scan with ±250mV of E_{corr} of different Co-W coatings.

Observations from the DC polarization measurements are consistent with those results obtained in the AC impedance analysis. Both DC polarization and AC impedance analysis results show that crystalline 65-35 Co-W coating has a higher polarization resistance (has higher capability to withstand corrosion) to that of amorphous 65-35 Co-W coating. Besides, polarization resistance decreases with increasing W content of the Co-W coating. Table 5.5 summarizes our observations for DC polarization and AC impedance measurements.

Table 5.5 Summary of DC polarization and AC impedance analysis results.

<table>
<tr><td colspan="7">Polarization Resistance (R_p)
←increasing</td></tr>
<tr><td>AC</td><td>Columnar Ni</td><td>Lamellar Ni</td><td>Pd</td><td>75-25 Pd-Fe (R_p increases with Pd content)</td><td>Co</td><td>65-35 Co-W (R_p increases with Co content and crystallinity of the Co-W coating)</td></tr>
<tr><td>DC</td><td>Columnar Ni</td><td>Lamellar Ni</td><td>Pd</td><td>75-25 Pd-Fe</td><td>Co</td><td>65-35 Co-W (R_p increases with Co content and crystallinity of the Co-W coating)</td></tr>
<tr><td colspan="7">Corrosion Potential (E_{corr})
←less negative</td></tr>
<tr><td>DC</td><td>Columnar Ni</td><td>Lamellar Ni</td><td>Pd</td><td>75-25 Pd-Fe</td><td>Co</td><td>65-35 Co-W (E_{corr} becomes less negative with increasing Co content and crystallinity of the Co-W coating)</td></tr>
<tr><td colspan="7">Corrosion Current (I_{corr})
←decreasing</td></tr>
<tr><td>DC</td><td colspan="2">columnar & lamellar Ni</td><td colspan="2">Pd, 75-25 Pd-Fe, Co</td><td colspan="2">65-35 Co-W</td></tr>
</table>

On the whole, a preliminary study on the applications of DC polarization and AC impedance analysis have produced a qualitative picture for the corrosion properties of different electrodeposited coatings. Resulting from the DC polarization and AC impedance measurements, the capability for withstanding corrosion with reference to the polarization resistance of different coatings can be ranked in ascending order as: Co-W, Co, Pd-Fe, Pd, lamellar Ni, columnar Ni.

Chapter 6

Conclusions

6.1 General Comments

An attempt was made to evaluate the diffusion barrier properties of different Ni, Pd, Co, Pd-Fe and Co-W electrodeposited coatings. Most data for the systems involved in this study deal with temperatures ranging from 250 to 800°C. Diffusion barrier properties of some electrodeposits show substantial changes in certain transition temperature ranges. For example, the temperature range 700-750°C indicates a transition between the higher and lower diffusion mechanisms for the copper/nickel couple. Cobalt and cobalt-tungsten alloy coatings are thermally stable at temperatures below 600°C. Their diffusion barrier capabilities decline rapidly at temperatures above 600°C. This observation implies that the effectiveness of a diffusion barrier material depends on the working temperatures required.

Palladium has the poorest diffusion barrier capability among the investigated electrodeposits. However, it still may be effective as a diffusion barrier if the required working temperature is not high (< 250°C). Its barrier property can be improved by alloying with iron as palladium-iron coating. Similarly, the cobalt-tungsten coatings have the higher capability for withstanding copper diffusion than that of the cobalt coatings.

Although palladium-iron coating showed a higher diffusion barrier capability than that of palladium, cracks were generally observed in the palladium-iron coatings. The plating techniques for the palladium-iron coating should be improved in order to obtain the crack-free coating before considering its suitability as a diffusion barrier.

Some investigators [1, 2] reported that negligible interdiffusion between copper and cobalt was observed after heat treatment at temperatures up to 800°C. However, after studying the diffusion experiment of the Cu/Co/Ni systems, this author suggest that copper atoms diffuse through the cobalt barrier via grain boundary diffusion. The earlier observations of negligible interdiffusion between copper and cobalt can be attributed to the limited resolution of the electron probe detector.

On the whole, cobalt-tungsten coatings have shown the highest diffusion barrier capability for copper diffusion and thermal stability among other barrier coatings studied. As the working temperatures for most applications are below 600°C, cobalt-tungsten electrodeposit is suggested to be a potential alternative for nickel as a diffusion barrier coating.

6.2 Main Findings

1. Lamellar Ni and columnar Ni showed similar diffusion barrier properties for Cu diffusion at temperatures above 400°C. Columnar Ni system had a better diffusion barrier capability than that of lamellar Ni at temperatures below 350°C.

2. Interdiffusion coefficients of Cu/Pd system are nearly higher than those of the Cu/Ni system by one order of magnitude (10 times) at all investigated temperatures (250-700°C).

3. Rate of diffusion of Cu for Cu/Pd-Fe system is slower than that of Cu/Pd system at all investigated temperatures (250-500°C). Pd-Fe barrier coating has a better thermal stability than that of Pd, for which the barrier penetration value ($d_{barrier}$)of

Pd-Fe is smaller than that of the Pd barrier after heat treatment at 400°C for 48h for the Cu/Pd-Fe(barrier)/Au system.

4. Results for the diffusion experiments of the Cu/Co/Ni and Cu/Co-W/Ni systems show that Co and amorphous Co-W alloy coating are more effective barrier for Cu diffusion than Ni up to 219 hours at 400°C, while crystalline Co-W alloy coating, composed of 36 wt.% W is a more effective barrier for Cu diffusion than Ni up to 72 hours at 500°C.

5. For the Cu/Co/Ni and Cu/Co-W/Ni systems diffusion experiments, interpenetration of Cu through Co is more pronounced than diffusion of Cu through Ni for temperatures ranging from 500°C to 800°C; and interdiffusion of Cu through Co-36 wt.% W coatings (either amorphous or crystalline) is more pronounced than diffusion of Cu through Ni for temperatures ranging from 600°C to 800°C, whereas crystalline Co-36wt% W is a more effective barrier than Co for Cu diffusion for all investigated temperatures (400-800°C).

6. The good diffusion barrier properties of Co and Co-W coatings (either amorphous or crystalline) are due to their good thermal stability below 500°C. Their effectiveness decline when temperature increases to 600°C or above. These can be attributed to their structural and phase transformations as shown by their changed XRD spectra upon heat treatment.

7. Crystalline Co-W coating plated in a bath with W/(W+Co) ratio of ½ shows better diffusion barrier properties than that of the amorphous Co-W coating plated in a

bath with W/(W+Co) ratio of 2/3 at all investigated temperatures (400-800°C). The amorphous Co-W coating is a more effective barrier than Co at 500°C or below, but it shows a poorer barrier capability than Co at 600°C or above.

8. Diffusion experiment results for different Cu/barrier/Au systems at 400°C for 24 and 48 h respectively confirm that Co-W is the most effective electroplated barrier coating for Cu/Au interdiffusion at 400°C. This result is consistent with our previous evaluation from the diffusion experiments of the Cu/Co/Ni and Cu/Co-W/Ni systems.

9. Diffusion barrier capability for different electrodeposited barrier coatings for Cu/Au interdiffusion at 400°C can be ranked in ascending order as: Pd, Pd-Fe, Ni (lamellar or columnar), Co, Co-W.

10. As a preliminary study on the applications of DC polarization and AC impedance analysis to the characterization of corrosion properties of different electrodeposited coatings in 3% NaCl, their capability for withstanding corrosion with reference to the polarization resistance can be ranked in ascending order as: Co-W, Co, Pd-Fe, Pd, lamellar Ni, columnar Ni. The relatively lower polarization resistance of the Co-W coatings does not imply that such observation may adversely affect their suitability as a diffusion barrier. More in-depth investigation should be taken to evaluate the corrosion processes of different coatings under corrosive environment.

11. Crystalline Co-W coating shows a higher polarization resistance to that of the amorphous one.

6.3 Suggestions for Future Work

The objective of the present project is to investigate the interdiffusion properties between copper substrate and different electroplated coatings. During the research studies, the author has found that the "imperfect" nature of the electroplated coatings, which contains many kinds of defects and impurities, make the interdiffusion behaviour of the systems be difficult to unscramble in details. In order to get more information of the dependence of microstructure and grain size on the diffusion barrier properties of any potential barrier materials, this author hope the following suggestions can help getting a better understanding for the interdiffusion of materials.

1. Interdiffusion of vacuum-deposited thin films systems should be studied in order to get more understanding for the metal-metal interdiffusion processes. Vacuum-deposited films can be prepared with a high degree of purity whereas films deposited by electroplating can contain rather larger concentrations of impurities and defects whose influence on the interdiffusion behavior may be difficult to unscramble. It should be possible, nevertheless, to generalize from the results of clean vacuum-deposited films to the more complicated cases such as electroplated films.

   On the contrary, tedious microsectioning procedures have to be done for the electroplated coatings in order to undergo measurements of diffusion

profiles. Prolonged time is needed for the metal-metal interdiffusion when the annealing temperature is low. For example, it takes more than 2000 hours for the interdiffusion studies of the Cu/Ni couple annealed at 250°C.

For the observation of mass transport on a large scale at low temperatures in thin films by X-ray diffraction analysis [53-55], observable diffusion times can be shortened.

2. It is often stated that the activation energy for grain boundary diffusion in metals is roughly one-half that for lattice diffusion and so the grain boundary diffusion coefficients will be correspondingly higher. The extent to which grain boundary diffusion will contribute to a total diffusion flux will depend on the value of the average grain boundary diffusion coefficient and on how it compares with that of lattice diffusion. It is important to consider diffusion in both grain boundaries and in the grain interiors when estimating the total flux of material transported. Thin film diffusion couples will offer a way of investigating grain boundary diffusion kinetics, because it is possible to find conditions under which the following situation can be observed.

(a) There is little difference in the penetration distance at boundaries and in the bulk lattice, so that $D_{\text{grain boundary}} \approx D_{\text{lattice}}$.

(b) Grain boundary diffusion is much faster than in the bulk.

(c) Penetration only occurs along the grain boundaries, where lattice diffusion is negligible.

Hence, extent of contribution by grain boundary diffusion and lattice diffusion can be separated after considering certain mathematical models of the combination of grain boundary and lattice diffusion [16, 18, 47-48].

3. Because of the mutual insolubility between Co (or Co-W) and Cu, Cu was suggested to diffuse through Co (or Co-W) barrier layer by grain boundary diffusion and accumulated at the interface of Co (or Co-W)/Ni for the diffusion experiment of the Cu/Co/Ni and Cu/Co-W/Ni systems. Cu-Co or Cu-Co-W solid solution was not detected by EDS in our studies. Thin film diffusion couples of the Cu/Co and Cu/Co-W may give more information and insight in considering the existence of any form of lattice diffusion and solid solution in the Cu/Co and Cu/Co-W couples.

4. The effects of electroplating parameters such as current density, temperature, pH, bath composition on the microstructure of the electrodeposits should be studied more systematically. We can determine specific range of plating parameters, which will give the most effective microstructure and composition of the electrodeposit as a diffusion barrier.

5. An investigation correlating the texture (orientation of grains) of the electrodeposited coatings and diffusion barrier properties should be undertaken. This may help in finding specific texture of the electrodeposit which have the best thermal stability and the highest capability to withstand copper diffusion. We can employ the X-ray powder diffraction technique to determine the change of texture of the electrodeposit upon different heat treatment processes. An example of a texture analysis of nickel electrodeposit was put in Appendix III.

6. The potential range used in the potentiodynamic polarization measurement can be increased, for example, ranging from –250 mV with respect to E_{corr} of the specimen to +1.5 V or more. A broader qualitative picture of the specimen in a given solution can be obtained. It helps in detecting any tendency of the specimen to become passivated.

7. For the AC impedance measurements, the diffusion layer effects observed for the Co-W coatings and any other distortion or incompleteness of the semicircle because of other effects in the *Nyquist* plots may be clarified by implementing the more complicated equivalent circuit models describing these processes with the helps of computer simulation.

8. Considering the suitability of a specific electrodeposited coating as a diffusion barrier, a weight loss testing of the Cu/electrodeposited barrier coating/Au specimen under corrosive environment should help us in making a balance between diffusion barrier and corrosion resistance properties. For example, after being immersed in 3% NaCl solution for a prolonged period of time, the solution is taken for atomic absorption spectroscopy analysis (AA). Thus, any barrier material released from the Cu/barrier/Au specimen into the solution can be quantitatively determined.

References

1. Kaja Suryanarayana, PhD. *Thesis*, The Pennsylvania State University (1985).
2. Lucille A. Giannuzzi, James W. Hyres II, Howard W. Pickering and William R. Bitler, Final Report, American Electroplaters' Society Project No. 67 (1989).
3. Fairhurst, S.; Illing, H. P. A., "The toxicity of nickel and its inorganic compounds", *Toxic. Rev.*, **19**, 204 (1987).
4. Coogan, Timothy P.; Latta, Dorothy M.; Snow, Elizabeth T.; Costa, Max, " Toxicity and carcinogenicity of nickel compounds", *Crit. Rev. Toxicol.*, **19(4)**, 341-84 (1989).
5. Common Position (EC) No. 12/94, *Official Journal of the European Communities*, No. C137/60-64, 19 May (1994).
6. I. Boguslavsky, J. A. Abys, E. J. Kudrak, M. A. Williams and T.C. Ong, "Pd-Ni-plated Lids for Frame-Lid Assemblies", *Plating and Surface Finishing*, pp. 72-77, February (1996).
7. E. J. Kudrak, J. A. Abys, V. Chinchankar and J. J. Maisano, "Porosity of Composite Palladium, Palladium-Nickel and Gold Electrodeposits", *Plating and Surface Finishing*, pp. 49-55, February (1992).
8. O. Neukam, Galvanotechnic **61(8)**, 626 (1979).
9. J. L. Martin and M. P. Toben, "Palladium and Palladium Alloy Electrodeposits in the Electronic Industry", *Metal Finishing*, pp. 39-41, January (1990).
10. K Prasad, L Faraone and A G Nassibian, "Investigation of palladium as a barrier to gold diffusion in sintered ohmic contacts to n-GaAs", *Semicond. Sci. Technol.* **4**, 657-662 (1989).

11. N. S. Wheeler and D. S. Lashmore, "Electrodeposited Cobalt-Tungsten as a high-temperature Diffusion Barrier for Graphite-Fiber/Nickel Composites", *Mat. Res. Soc. Symp. Proc.* **318**, 603-608 (1994).

12. U. Admon, M. P. Dariel and E. Grunbaum, "Microstructure of electrodeposited Co-W thin films", *J. Appl. Phys.*, **59 (6)**, 2002-2009, March (1986).

13. S. Nakahara and E. C. Felder, *J. Electrochem. Soc.* **129(1)**, 45 (1982).

14. J. D. Katz, M. S. Thesis, The Pennsylvania State University (1980).

15. Chin-An Chang, "Interactions between Au and Cu across a Ni barrier layer", *J. Applied Physics.*, **60(3)**, 1 August, pp. 1220-1222 (1986).

16. R. Venos, W. Pamler and H. Hoffmann, "Grain Boundary Diffusion in Ni-Cu Multilayer Films", Metallurgical and Protective Coatings, *Thin Solid Films*, **162**, 155-160 (1988).

17. R. Venos and H. Hoffmann, " Surface Accumulation and Monolayer Coverage During Grain Boundary Diffusion in Polycrystalline Cu/Ni Bilayers", *Thin Solid Films*, **174**, 99-104 (1989).

18. K. Roll, "Die Bestimmung Von Konzentrations-Tiefenprofilen In Dunnen Schichten Mit Der Auger-Elektronenspektroskopie", *Thesis*, Universitat Regensburg (1981).

19. Sobha Jayakrishnan and S.R. Natarajan, "Electrodeposition of Palladium from Ammine Complexes", *Metal Finishing.*, February, pp. 81-83 (1988).

20. R. Le Penven, W. Levason, D. Pletcher, "Studies of the electrodeposition of palladium from baths based on $[Pd(NH_3)_2X_2]$ salts, Part I and Part II", *J. Applied Electrochemistry* **20**, 399-404 (1990) and **22**, 421-424 (1992).

21. A. H. Graham, M. J. Pike-Biegunski and S. W. Updegraff, *Plating and Surface Finishing*, **70(11)**, 52 (1983).

22. H. Schmalzried, "Solid State Reactions", (Verlag Chemie, 1981), pp. 87-89.

23. Link ISIS Program, Oxford Instrument (UK) Ltd. (1994).

24. C. S. Barrett, Structures of Metals, 3rd edn., McGraw-Hill, New York, 1966, p. 155.

25. P. Juzikis, M. U. Kittel and Ch. J. Raub, "Electrolytic Deposition of Palladium-Iron Alloys", *Plating and Surface Finishing*, August, pp. 59-62 (1994).

26. S. M. Kim, Mater. Sci. Forum 15-18, 1257 (1987).

27. C. W. Oatley, "The Scanning Electron Microscope", Part 1, (Cambridge University Press, 1972), pp.17-25.

28. S. J. B. Reed, "X-ray Optics and Microanalysis", eds. R. Casting, P. Deschamps and J. Philibert (Paris: Hermann, 1966), pp. 339.

29. M. J. Berger, S. M. Seltzer, Tables of Energy Losses and Ranges of Electrons and Positrons, Nucl. Ser. Rep. No. 39, NAS-NRC Publ. 1133, (Nat. Acad. of Sciences. 1964), pp.205-208.

30. Shinichi Wakabayashi, Takahiro Iijima, Masao Nakazawa, Norio Kaneko and Hiroyuki Nezu, "Diffusion Behavior of Copper Through Electroplated Silver Leadframes", *Plating and Surface Finishing, November*, pp. 63-68 (1993).

31. "Smithells Metals Reference Book", edited by E. A. Brandes and G. B. Brook, (Butterworth, 1992).

32. Yu. M. Polukarov, in Electrodeposition of Alloys, edited by V. A. Averkin, Moscow 1961 (Israel Program for Scientific Translations, Jerusalem, 1964), pp. 52-69.

33. L. S. Palatnik, M. Ya. Fuks, and V. M. Kosevich, "Mechanism of Formation and Substructure of Condensed Films", Nauka, Moscow (1972).

34. J. E. E. Beglin and J. M. Poate, "Interdiffusion in metal-metal systems," *Thin Films Interdiffusion and Reactions*, edited by J. M. Poate, K. N. Tu and J. W. Mayer, (John Wiley & Sons, 1978), pp. 305-358.

35. Peter Madakson and Joyce C. Liu, "Interdiffusion and resistivity of Cu/Au, Cu/Co, Co/Au, and Cu/Co/Au thin films at 25-550°C", *J. Appl. Phys.* **68(5)**, 2121-2126, September (1990).

36. B. S. Bokshtein, I. A. Magidson and I. L. Svetlov, *Phys. Met. Metallogr.* **6(6)**, 81 (1958).

37. Peter Madakson, "Interdiffusion, hardness, and resistivity of Cr/Cu/Co/Au thin films, *J. Appl. Phys.* **70(3)**, 1374-1379 (1991)

38. G. Battaglin, G. Fagherazzi, S. Polizzi, G. Majni and P. Mengucci, "Phase Characterization of Ion-beam-mixed and Thermally Reacted Fe/Pd Thin Film Bilayers", *Materials Science and Engineering, B5* 437-444 (1990).

39. Van Orden, A. C., *CORROSION/91*, Paper 140, National Association of Corrosion Engineers, Houston, TX, (1991).

40. Green, N.D. and Gandhi, R.H., *Materials Performance*, **21(7)**, 34 (1982).

41. Mansfeld. F., "The Polarization Resistance Technique for Measuring Corrosion Currents," *Advances in Corrosion Science and Technology Vol. 6*, M. G. Fontana and R.W. Staehle, Eds., (Plenum Press, New York, 1976). p. 163.

42. Stern, M., *Corrosion*, **14(9)**, 440-444 (1958).

43. Stern, M. and Geary, A. L., *Journal of the Electrochemical Society*, **104**, 56-63, (1957).

44. "Model 352/252 Softcorr II Corrosion Measurement & Analysis Software," EG & G, Princeton, NJ, (1991).

45. Zeller III, R. L. and Savinell, R. F., *Corrosion Science*, **26(8)**, 591-599 (1986).

46. Silverman, D. C., "Simple Models/Practical Answers Using the Electrochemical Impedance Technique," *Corrosion Testing and Evaluation: Silver Anniversary Volume, ASTM STP 1000,* R. Baboian and S. W. Dean, Eds., American Society for Testing and Materials, Philadelphia, pp. 379-395 (1990).

47. D. Gupta, D. R. Campbell and P.S. Ho, Grain boundary diffusion. In J. M. Poate, K. N. Tu and J. W. Mayer (eds.), *Thin Films-Interdiffusion and Reactions* (Wiley, New York, 1978).

48. R. T. P. Whipple, *Philos. Mag.*, **45** 1225 (1954).

49. Sluyters-Rehbach, M., & Sluyters, J. H., *"Electroanalytical Chemistry", Vol. 4,* edited by A. J. Bard, (New York, M. Dekker, 1969).

50. MacDonald, D. D., Liang, R. Y., and Pound, B. G., *Journal of the Electrochemical Society*, **134(12)**, 2981-2986, (1987).

51. MacDonald, D. D. and Macdonald, M. U., *Journal of the Electrochemical Society*, **137(8)**, 2395-2402, (1990).

52. S. S. Lau and R. C. Sun, "Internal Stresses and Interdiffusion of Ti-Pd-Au Films Studied by X-Ray Diffraction Techniques", *Thin Solid Films*, **10** 273-282 (1972).

53. C. R. Houska, "X-Ray Examination of Diffused Films", *Thin Solid Films*, **25** 451-464 (1975).

54. Darrel R. Tenney and Patrick K. Talty, "X-Ray Diffraction Investigation of Bimetallic Diffusion Zones in the Cu-Pd System", *Metallurgical Transactions, Vol. 5, January*, 241-247 (1974).

55. M. Murakami, A. Segmuller and K. N. Tu, "X-Ray Diffraction Analysis of Diffusion in Thin Films", *Analytical Techniques for Thin Films, Treatise on Materials Science and Technology, Vol. 27*, edited by K. N. Tu and R. Rosenberg, (Boston, Academic Press, 1988), pp.201-247.

56. Alloy Phase Diagrams, ASM Handbook Vol. 3, part 2, p.200, The Materials Information Society, (1992).

57. Alloy Phase Diagrams, ASM Handbook Vol. 3, part 2, p.168, The Materials Information Society, (1992).

58. D. R. Marx, W. R. Bitler and H. W. Pickering, "Metallic Barriers for Protection of Contacts in Electronic Circuits from Atmospheric Corrosion", Final Report on AES Project No. 29, *Plating and Surface Finishing, June*, pp. 69-72. (1977).

59. H. J. Bunge, *"Texture Analysis in Materials Science. II Mathematical Methods"*, (Butterworths, London, 1982).

60. Huyser-Gerits and Rieck, *J. Appl. Cryst.*, (7) 286-290, (1974).

Appendix I

Calculation of Interdiffusion Coefficients by Boltzmann-Matano Analysis

Sequence of steps followed in calculating the interdiffusion coefficients:

1. Obtain the concentration-distance profiles of the two interdiffused elements using the EDS detector, in which the relative intensities of the characteristic X-ray of the elements have been converted into atom% using the Link ISIS program. ZAF corrections were made for atomic number, absorption and fluorescence effects. For example, the concentration-distance profiles of a copper/lamellar nickel couple heat-treated at 400°C for 96 hours, are shown in Figure A-1.

2. An average line is drawn for each profile, see Figure A-1.

3. A quadratic equation is curve-fit to the averaged line for the concentration-distance profile of copper. This equation is used as an input function for the Pascal program to manipulate the Boltzmann-Matano solution.

4. The heat treatment time is also input to the program.

5. For the calculation of chemical interdiffusion coefficient at 20% copper, the Matano interface and the slope *dc/dx* at $c = 0.2$ (20%) are calculated by the Pascal program.

6. Diffusivities are then calculated numerically using the Boltzmann-Matano analysis:

$$D_{c=c'_1} = -\frac{1}{2t}\frac{dx}{dc}\bigg|_{c=c'_1} \int_0^{c_1} x\,dc$$

where the integral is solved numerically using Simpson's rule.

7. Results obtained from Boltmann-Matano Analysis for D at 20 atom% copper is 1.95×10^{-14} cm^2/s.

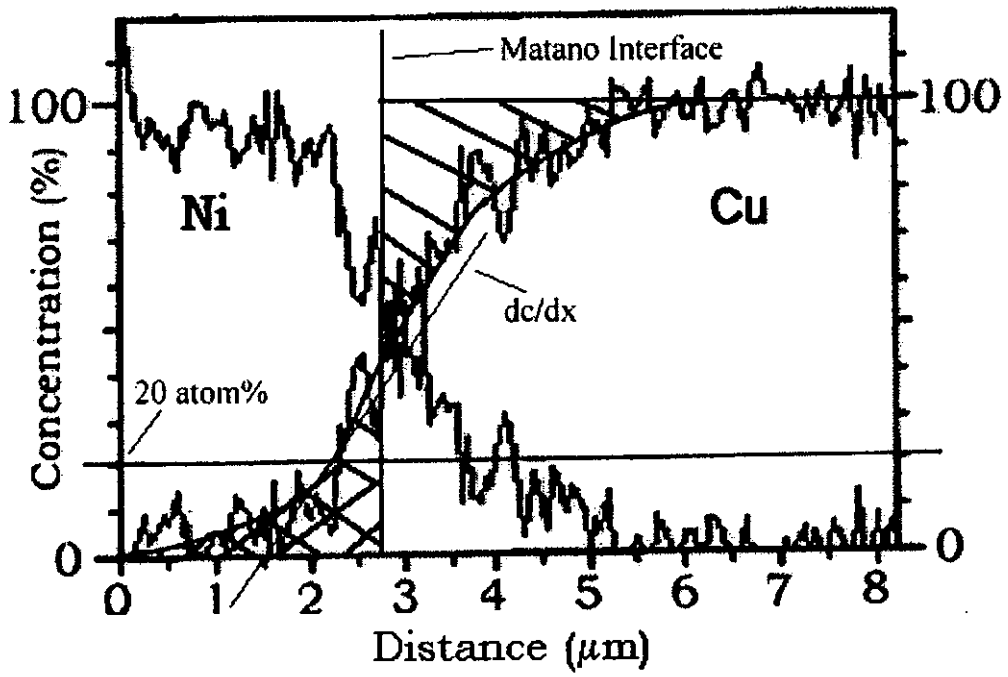

Figure A-1 Concentration-distance profiles of a Cu/lamellar Ni couple After heat treatment at 400°C for 96 hours.

Appendix II

An example of a program computing the Matano Solution:

```
program mantano(input,output);
var
  a,b,c,d,e,f,g,k:real;
  s,l,w,h,u,x:real;
  man,rh,ru,decision,temp,lefttemp,righttemp:real;
  j,n:integer;
  leftintegral,rightintegral:real;
  der,compt,ycompt,diffusion,time:real;
  dv,su,leftsolutionintegral,rightsolutionintegral,solutionintegral:real;
  dertop,derbottom:real;
  function profile(a,b,c,d,e,f,g,k,x:real):real;
  begin
     profile:=(a+c*x+e*x*x+g*x*x*x)/(1+b*x+d*x*x+f*x*x*x+k*x*x*x*x)
  end;
begin
  a:=1.6446725; b:=-0.79406773;c:=2.3808944;d:=0.23942565;
  e:=-2.0572979;f:=-0.031033844;g:=0.51658603;k:=0.0018418369;
  write('Please input starting point');
  read(s);
  write('Please input ending point');
  read(l);
  write('Please input number of divisions');
  read(n);
  lefttemp:=s;
  righttemp:=l;
  man:=l/2;
  repeat
  begin
     {computation of the leftintegral}
     h:=(man-s)/n;
     u:=profile(a,b,c,d,e,f,g,k,s)+profile(a,b,c,d,e,f,g,k,man);
     w:=4;
     for j:=1 to (n-1) do
     begin
        u:=u+w*profile(a,b,c,d,e,f,g,k,s+j*h);
        w:=6-w
     end;
     leftintegral:=(h/3)*u;
     rh:=(l-man)/n; {computation of the rightintegral}
     ru:=profile(a,b,c,d,e,f,g,k,man)+profile(a,b,c,d,e,f,g,k,l);
     w:=4;
     for j:=1 to (n-1) do
     begin
        ru:=ru+w*profile(a,b,c,d,e,f,g,k,man+j*rh);
        w:=6-w
     end;
     rightintegral:=(rh/3)*ru;
     decision:=(l-man)*100-rightintegral;
     temp:=man;
     if leftintegral>decision then
       begin
          man:=(lefttemp+man)/2;
          righttemp:=temp;
```

```
        end;
      if leftintegral<=decision then
        begin
          man:=(righttemp+man)/2;
          lefttemp:=temp;
        end;
  end;
  until (leftintegral/decision>0.995) and (leftintegral/decision<1.005);
  write('The Mantano-interface is at: ');
  writeln(man);
  write('The Mantano-integral is: ');
  writeln(leftintegral);
{ ********************************************************************** }
write('Please input interest composition point: ');
readln(ycompt);
write('Please input annealing time: ');
readln(time);
compt:=0;
repeat
  compt:=compt+0.005;
until (profile(a,b,c,d,e,f,g,k,compt)/ycompt>0.995) and (profile(a,b,c,d,e,f,g,k,compt)/ycompt<1.005);
dertop:=a+c*compt+e*compt*compt+g*compt*compt*compt;
derbottom:=1+b*compt+d*compt*compt+f*compt*compt*compt+k*compt*compt*compt*compt;
der:=(derbottom*(c+2*e*compt+3*g*compt*compt)-
dertop*(b+2*d*compt+3*f*compt*compt+4*k*compt*compt*compt))
/(derbottom*derbottom);
write('Your interest point is at x: ');
writeln(compt);
if compt<man then
begin
  dv:=compt/100;
  su:=profile(a,b,c,d,e,f,g,k,0)+profile(a,b,c,d,e,f,g,k,compt);
  w:=4;
  for j:=1 to 99 do
    begin
    su:=su+w*profile(a,b,c,d,e,f,g,k,j*dv);
    w:=6-w;
    end;
  leftsolutionintegral:=(dv/3)*su;
  rightsolutionintegral:=(man-compt)*ycompt;
  solutionintegral:=leftsolutionintegral+rightsolutionintegral;
end;
if compt>man then
begin
  dv:=(compt-man)/100;
  su:=profile(a,b,c,d,e,f,g,k,man)+profile(a,b,c,d,e,f,g,k,compt);
  w:=4;
  for j:=1 to 99 do
    begin
    su:=su+w*profile(a,b,c,d,e,f,g,k,man+j*dv);
    w:=6-w;
    end;
  leftsolutionintegral:=(dv/3)*su;
  rightsolutionintegral:=(compt-man)*ycompt;
  solutionintegral:=leftintegral+(rightsolutionintegral-leftsolutionintegral);
end;
if (compt/man>0.995) and (compt/man<1.005) then solutionintegral:=leftintegral;
diffusion:=(1/(2*time*60*60))*(1/der)*solutionintegral/100000000;
```

```
write('The solutionintegral is: ');
writeln(solutionintegral);
write('The slope is: ');
writeln(der);
write('The Diffusion coefficient at composition ');
write(ycompt);
write('% is: ');
writeln(diffusion);
end.
```

□

Appendix III

An Example of Texture Analysis of the Nickel Electrodeposit

The metal electrodeposits are often polycrystalline aggregates in which each of the individual grains has an orientation that differs from those of its neighbours. The non-random distributions that occur are called preferred orientations or texture.

Preferred orientations are usually described by means of pole figures. These are simple stereographic projections, which show the distribution of particular crystallographic directions in the assembly of grains that constitutes the metal. For example, a (111) pole figure, showing the positions of the {111} poles for the grain and therefore, the orientation of the grain in the specimen. For a polycrystalline sample all the grains must be considered and three {111} poles must be plotted for each to give the pole figures.

Measuring a pole figure then consists of fixing the wavelength, λ, and the Bragg angle, θ, to examine a single plane, followed by rotation of the sample in numerous orientations covering the hemisphere of the stereographic projection. This rotation is typically performed using an Eulerian goniometer attached to an X-ray diffractometer. (See Figure A-2)

If the resulting poles are distributed uniformly over the area of the projection there is no preferred orientation and the specimen is said to have a random texture. Generally, the poles tend to cluster together in certain areas of the pole figure to produce a texture. The data are collected from many grains simultaneously and to present this in the form of density contours on the pole figure.

Since a pole figure describes the density of only one set of lattice planes as a function of orientation, it must be a projection of the full orientation distribution function. The orientation distribution function (ODF) describes the density of unit cells as a function of orientation in the sample. The unit cell axes and the sample coordinate system are related by three angles, the so-called Euler angles. Figure A-3 shows the physical meaning of the Euler angles. Mathematical methods have been developed which allow a three dimensional ODF to be calculated using numerical data obtained from several pole figures [59-60]. The ODF gives quantitative information about the whole spread of orientations in the texture. Accordingly, as a full mathematical description it can be applied objectively in understanding texture development and in the prediction of anisotropic properties.

The orientation of a unit cell can also be represented by the lattice plane parallel to the surface, and the crystal direction parallel to the rolling direction of the specimen. If the sample surface is parallel to (hkl) and the rolling direction to [uvw], the orientation is annotated as (hkl)[uvw]. There is of course a relationship between the Euler angles (φ_1, φ_2, Φ) and (hkl)[uvw].

$h = n \sin\varphi_2 \sin\Phi$ $\qquad$ $u = m (\cos\varphi_1 \cos\varphi_2 - \sin\varphi_1 \sin\varphi_2 \cos\Phi)$

$k = n \cos\varphi_2 \sin\Phi$ $\qquad$ $v = - m (\cos\varphi_1 \sin\varphi_2 - \sin\varphi_1 \cos\varphi_2 \cos\Phi)$

$l = n \cos\Phi$ $\qquad$ $w = m \sin\varphi_1 \sin\Phi$

where n and m are normalization constants. The relationships between different Euler angles are as follows:

$\phi = \varphi_2 + \pi / 2;$ $\qquad$ $\theta = \Phi;$

$\psi = \varphi_1 - \pi / 2$

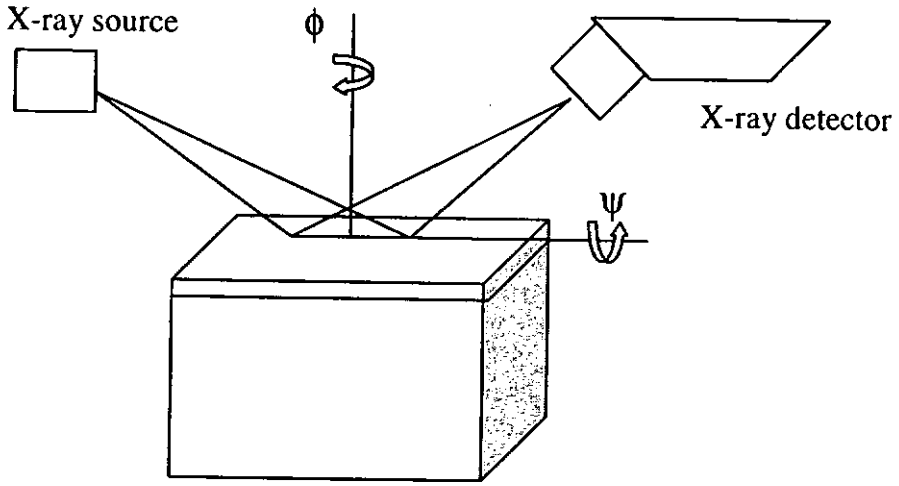

Figure A-2 gives the definition of ψ and ϕ. ψ is the tilt of the sample surface normal with respect to the scattering vector; ϕ is the rotation about the sample surface normal. By scanning the range of ψ from 0 to 90° and ϕ from 0 to 180°, a distribution of plane-normal intensities referred to as a pole figure is measured over the stereographic projection. Changing the Bragg angle θ or the wavelength implies observing a new plane, *d*, and therefore a new pole figure.

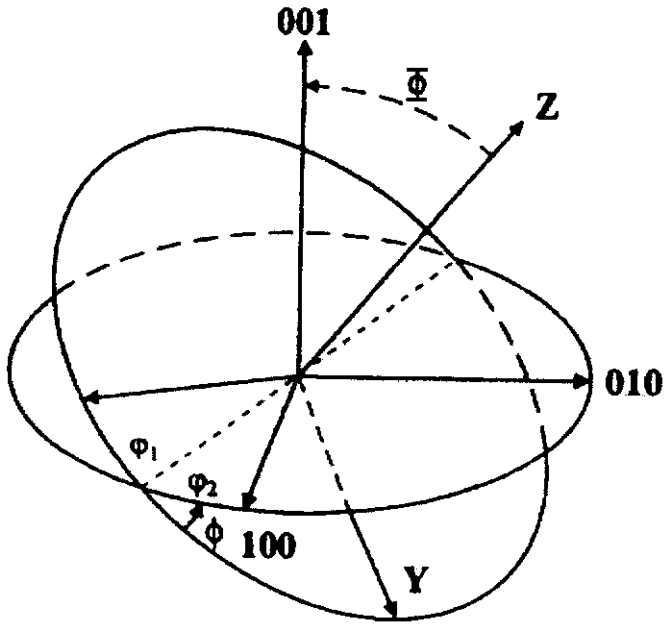

Figure A-3 Physical meaning of the Euler angles as given by Bunge [59]. φ_1 is the rotation of the unit cell about the sample surface normal; Φ is the angle between the sample surface normal and the [001] direction of the unit cell, and φ_2 is the rotation about the [001] direction. There three angles completely describe the orientation of the unit cell in the specimen reference frame. The ODF can be represented by 2D contour plots by slicing the ODF in sections of either Φ, or φ_1, or φ_2.

Figures A-4 to A-6 show the pole figures for the as-deposited nickel coating plated in a Watts bath at 50°C, at 3.6 A/dm^2 pH 3.3 of (111), (220) and (220) reflections. The results are then processed to give ODF of the texture represented by a series of contour plots with different parallel sections (Figure A-7).

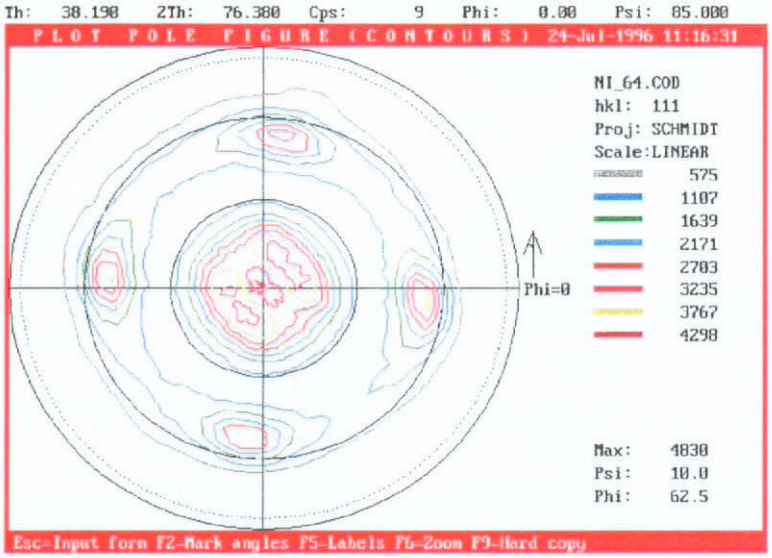

Fig. A-4 (111) Pole Figure of the as-deposited Watts nickel (columnar) electrodeposit.

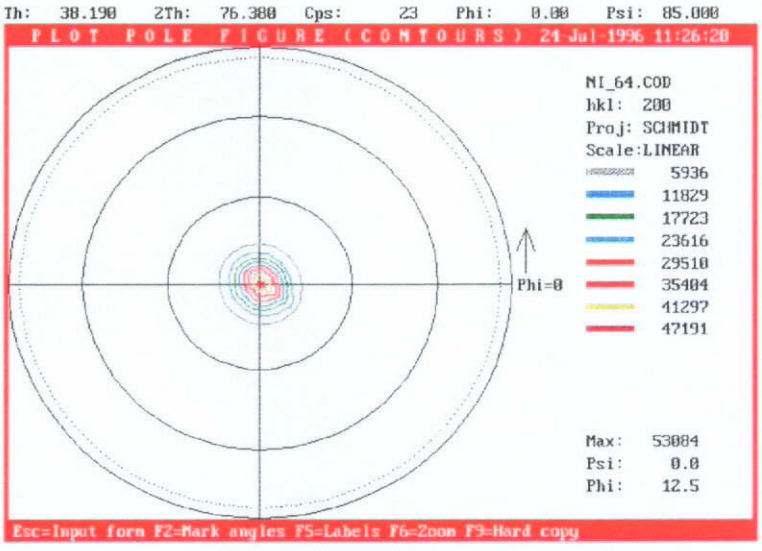

Fig. A-5 (200) Pole Figure of the as-deposited Watts nickel (columnar) electrodeposit.

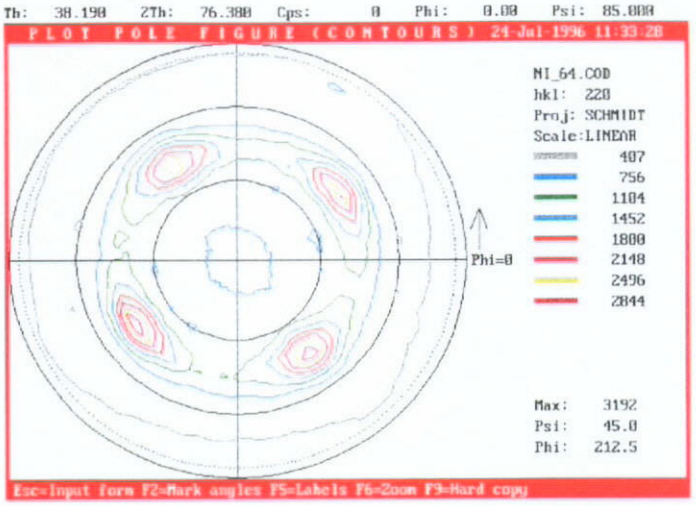

Fig. A-6 (220) Pole Figure of the as-deposited Watts nickel (columnar) electrodeposit.

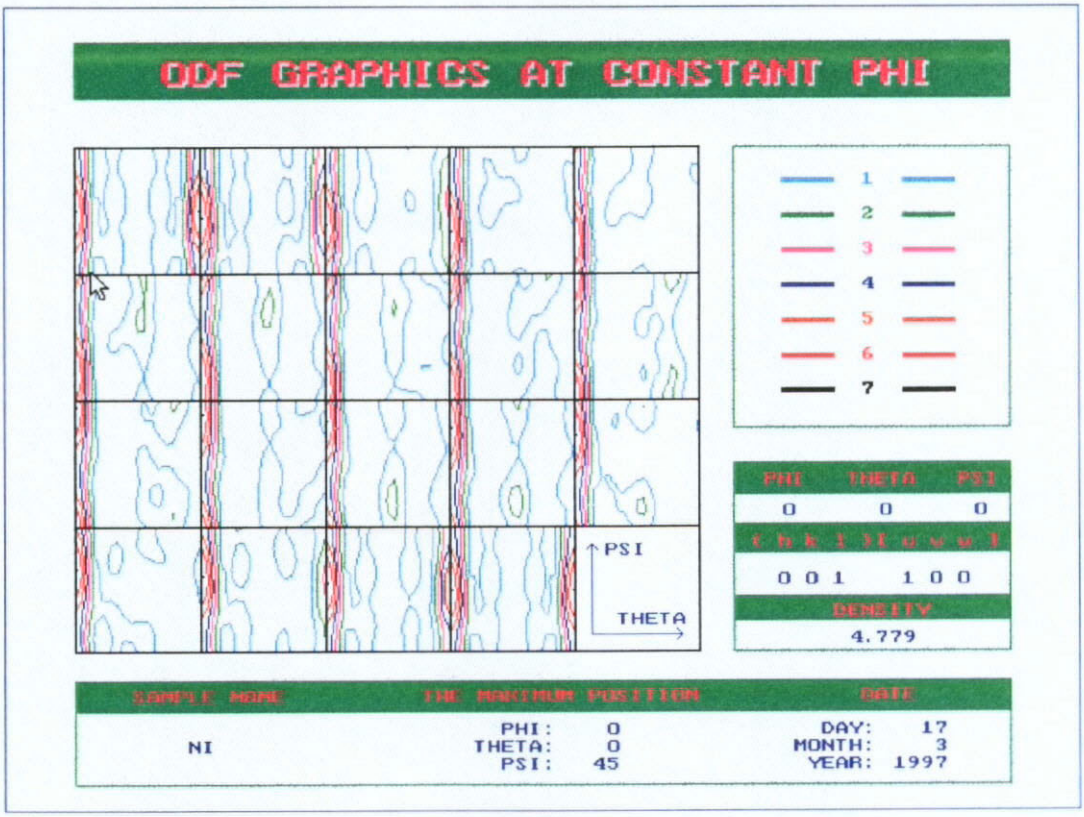

Fig. A-7 ODF obtained from the X-ray technique of the as-deposited Watts nickel (columnar) electrodeposit.

It was found that about 70% of the Watts nickel coating consists of different textured components, exhibiting about 22% of [001]<110>, 20% of [102]<231>, 12% of [212]<120>, 10% of [323]<537> and 6% of [221]<110> texture components.

Figures A-8 to A-10 show the (111), (200) and (220) pole figures for the as-deposited nickel coating plated in a Watts bath with an addition of 1 g/l of 2-butyne-1,4-diol and other plating parameters being changed.

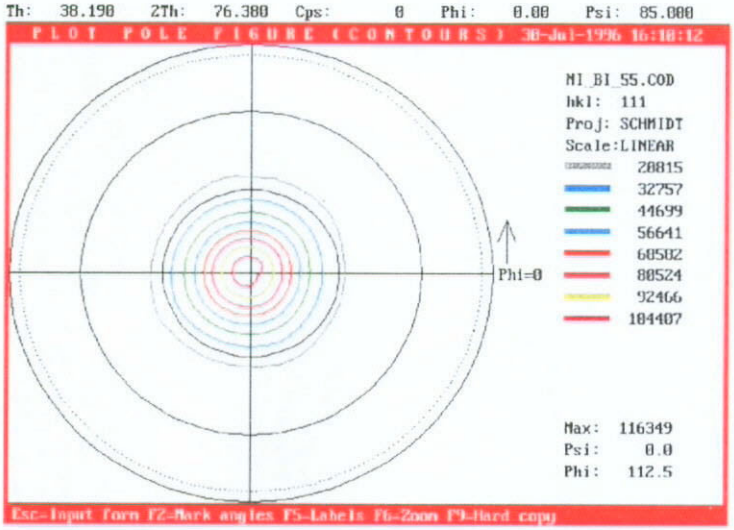

Fig. A-8 (111) Pole Figure of the as-deposited Watts nickel (lamellar) coating plated in a bath with addition of 1 g/l of 2-butyne-1,4-diol.

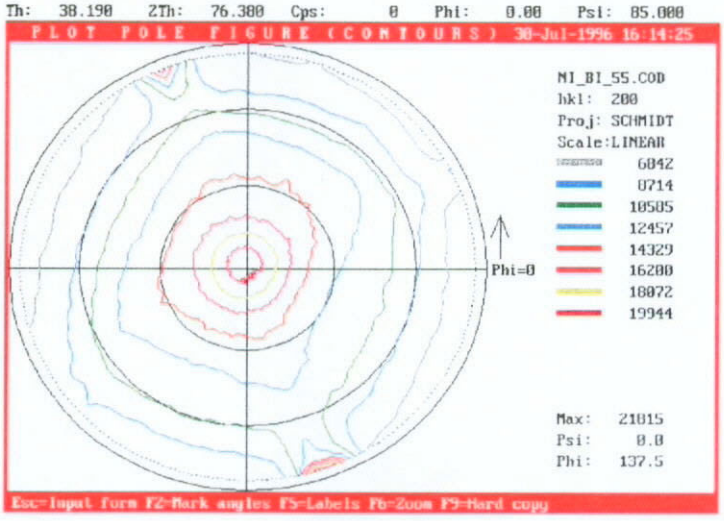

Fig. A-9 (200) Pole Figure of the as-deposited Watts nickel (lamellar) coating plated in a bath with addition of 1 g/l of 2-butyne-1,4-diol.

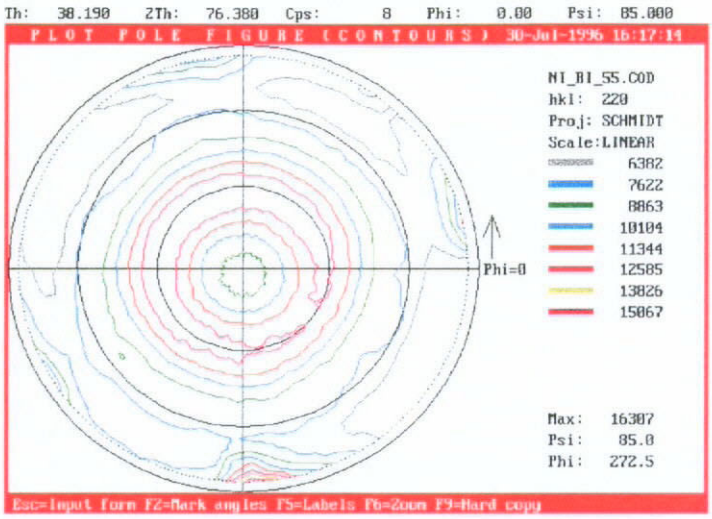

Fig. A-10 (220) Pole Figure of the as-deposited Watts nickel (lamellar) coating plated in a bath with addition of 1 g/l of 2-butyne-1,4-diol.

It is noted that there was substantial modifications of texture by an addition of 2-butyne-1,4-diol to the Watts nickel plating bath, which affected the electrocrystallization mechanisms of Ni.

Thus, an investigation correlating the texture (orientation of grains) of the electrodeposited coatings and diffusion barrier properties may be helpful in finding specific texture of the electrodeposit which have the best thermal stability and the highest capability to withstand copper diffusion.

Publications

Journal Papers:

(1) K. M. Chow, W. Y. Ng and L. K. Leung, "Interdiffusion of Cu substrate/electrodeposits for Cu/Co, Cu/Co-W, Cu/Co/Ni and Cu/Co-W/Ni systems", Surface & Coatings Technology, Vol. 99/1-2, pp. 161-170 (1998)

(2) K. M. Chow, W. Y. Ng and L. K. Leung, "Barrier Properties of Ni, Pd and Pd-Fe for Cu Diffusion", Surface & Coatings Technology (in press) (1998).

Symposium:

(1) K. M. Chow and W. Y. Ng, "Interdiffusion of Cu substrate/Ni couples", 1st International Symposium on Inorganic Chemistry for Chinese Scientists held at The Hong Kong Polytechnic University, 14-19 July, 1996, p. 206 (1997)

(2) K. M. Chow and W. Y. Ng, "Microstructure and interdiffusion studies of Co-W electrodeposit on Cu substrate", 4th Symposium on Chemistry Postgraduate Research in Hong Kong held at The Hong Kong Baptist University, 19 April, 1997, P-21 (1997)